Structure and Dynamics of Chain-Grafted Polymer Nanocomposites

Kim Johnston

Submitted for the degree of Doctor of Philosophy

Heriot-Watt University

Institute of Chemical Sciences

September 2016

ABSTRACT

Polymer nanocomposites are of considerable interest in academia and industry, due to the enhanced properties arising from the addition of nanoparticles to a polymer matrix. Recent developments in controlled radical polymerisations have led to the synthesis of well-defined chain-grafted polymer nanocomposites. Research into the changes in chain conformation and dynamics in these systems is crucial for understanding the effect on macroscopic properties. Therefore, this thesis focuses on an extensive study of the structure and dynamics of these chain-grafted polymer nanocomposites. Two types of nanocomposites were investigated: polymer-silica nanocomposites and polystyrene-fullerene stars. The samples were studied primarily by neutron scattering techniques, along with complementary techniques such as dynamic light scattering (DLS) and rheological measurements.

Small-angle neutron scattering (SANS) data on 6 arm PS-fullerene samples were analysed using the standard star and core-star models. The model fits have shown that the PS-fullerene stars have slightly extended chains around the fullerene core, leading to the stars being larger than expected compared to pure polymer stars. Differential scanning calorimetry (DSC), quasi-elastic neutron scattering (QENS) and rheological measurements showed that PS-fullerene stars have unusual dynamics compared to typical polymer stars, exhibiting total rather than arm molecular weight dependence.

SANS measurements on polymer-silica nanocomposites in solution established that samples prepared with colloidal silica exhibit no change in chain conformation. However, fumed silica nanocomposites show a significant change in the large structure region that could not currently be modelled. QENS measurements on these samples showed that the dynamics of the polymer chains are significantly slowed down by the presence of fumed silica nanoparticles. Using the Time-Temperature Superposition principle (TTS) on the QENS and rheological data on these samples revealed a significant loss of free volume, which is therefore suggested to be the main cause of the decreased chain dynamics. Rheological measurements also confirmed a large increase in viscosity and modulus of dispersed poly(butyl acrylate)-silica nanocomposites. The presence of fumed silica has a greater effect on these properties than colloidal silica.

Finally, a preliminary SANS and microscopy study on two polymer blends containing silica nanoparticles was carried out, establishing that the addition of silica can significantly decrease the miscibility of the blend. The effect of silica on the phase separation temperature is complex, and depends on the concentration of nanoparticles.

ACKNOWLEDGEMENTS

First and foremost, I would like to thank my supervisor, Dr. Valeria Arrighi, for her constant help, support and belief in my abilities throughout my undergraduate and PhD years. Dr. Arno Kraft, my second supervisor, was also invaluable for his assistance, especially in the synthetic part of the project. I would also like to thank our collaborators, Dr. Joao Cabral and Prof. David Bucknall (who recently became a colleague), who provided samples, raw data and their expertise and support for much of the work presented in this thesis.

I would like to thank my family for all their help, especially my mum and dad who have provided me with unconditional love and support throughout my entire life. You may not understand my research, but you understand me and have always believed in me. I would not be the person I am today without your encouragement, and I know I have made both of you very proud. I also have to thank my brothers, Craig and Chris, who have always encouraged me and have been my friends as well as my brothers. To Chris, who will be writing his own PhD thesis soon, I wish you luck.

The acknowledgements would not be complete without thanking the fellow members of my group, Amy and Junjie, and all my friends in the Materials Chemistry office. Special thanks go to Jamie and John, as our lunchtime banter made every day that little bit better.

And last but certainly not least, I would like to thank Victor. For the past ten years you have been a constant pillar of love and support, despite the ocean separating us. As I move forward into the next stage of my life and scientific career, I know you will be right there with me.

DECLARATION STATEMENT

ACADEMIC REGISTRY
Research Thesis Submission

Name*:*	Kim Johnston		
School/PGI:	Institute of Chemical Sciences (ICS)		
Version: *(i.e. First, Resubmission, Final)*	Final	Degree Sought (Award **and** Subject area)	PhD Chemistry

Declaration

In accordance with the appropriate regulations I hereby submit my thesis and I declare that:

1) The thesis embodies the results of my own work and has been composed by myself
2) Where appropriate, I have made acknowledgement of the work of others and have made reference to work carried out in collaboration with other persons
3) The thesis is the correct version of the thesis for submission and is the same version as any electronic versions submitted*.
4) My thesis for the award referred to, deposited in the Heriot-Watt University Library, should be made available for loan or photocopying and be available via the Institutional Repository, subject to such conditions as the Librarian may require
5) I understand that as a student of the University I am required to abide by the Regulations of the University and to conform to its discipline.

**Please note that it is the responsibility of the candidate to ensure that the correct version of the thesis is submitted.*

Signature of Candidate*:*		Date:	

Submission

Submitted By *(name in capitals):*	
Signature of Individual Submitting:	
Date Submitted:	

For Completion in the Student Service Centre (SSC)

Received in the SSC by *(name in capitals):*			
Method of Submission *(Handed in to SSC; posted through internal/external mail):*			
E-thesis Submitted (mandatory for final theses)			
Signature:		Date:	

TABLE OF CONTENTS

LIST OF FIGURES

LIST OF TABLES

LIST OF SYMBOLS AND ABBREVIATIONS

$[\eta]$	Intrinsic viscosity
$<r^2>$	Mean-square end-to-end distance
$<u^2>$	Mean-square displacement
2θ	Scattering angle
A	Surface area
A_2	Second virial coefficient
A300	Aerosil 300 silica nanoparticles
AFM	Atomic Force Microscopy
AGET	Activator Generated by Electron Transfer
AN	Acrylonitrile
ANL	Argonne National Lab
APS	Advanced Photon Source
ATR-FTIR	Attenuated Total Reflection Fourier Transform Infra-Red
ATRP	Atom-Transfer Radical Polymerisation
b	Scattering length
BA	Butyl acrylate
BMPOA	*N*,*N*-bis(2-pyridylmethyl)octylamine
bpy	2,2'-bipyridine
c	Concentration
c^*	Overlap concentration
C60	Fullerene containing 60 carbon atoms
C-F model	Cowie-Ferguson model
CNT	Carbon Nanotubes
C_p	Heat Capacity
D	Diffusion coefficient
DLS	Dynamic Light Scattering
DMTA	Dynamic Mechanical Thermal Analysis
d_R	Tube diameter in the reptation model
DSC	Differential Scanning Calorimetry
DStar	Deuterated polystyrene-fullerene star
DWF	Debye-Waller Factor
$d\Omega$	Solid angle
E'	Storage modulus
E''	Loss modulus
E_a	Activation energy
EDTA	Ethylenediaminetetraacetic acid disodium salt
EG	Ethylene glycol
EISF	Elastic incoherent structure factor
EWS	Elastic Window Scan
F	Shear force
f	Number of arms in a star polymer
f_0	Fractional free volume

$G(r,t)$	Time-dependent pair-correlation function
G'	Dynamic elastic modulus
G''	Dynamic viscous modulus
h	Planck's constant
H5	Cab-O-Sil H5 silica nanoparticles
HStar	Hydrogenated polystyrene-fullerene star
HWHM	Half width at half maximum
$I(Q)$	Measured scattered intensity
$I(Q,t)$	Intermediate scattering function
I_0	Incident flux of neutrons
ILL	Institut Laue-Langevin
IPN	Interpenetrating Network
IR	Infra-Red spectroscopy
k	Wavevector
k_B	Boltzmann's constant
KWW	Kohlrausch-Williams-Watts function
l	Length of one segment of a chain of n segments
LCST	Lower Critical Solution Temperature
M	Molar mass
M_c	Critical molecular weight for entanglement
MDS	Molecular Dynamics Simulations
M_e	Molecular weight of entanglement
Me_6TREN	Tris[2-(dimethylamino)ethyl]amine
MEK	Methyl ethyl ketone (IUPAC name 2-butanone)
MMA	Methyl methacrylate
M_n	Number average molecular weight
M_w	Weight average molecular weight
MWCNT	Multi-Walled Carbon Nanotubes
N	Number of segments
N_A	Avogadro's number
NMP	Nitroxide Mediated radical Polymerisation
NMR	Nuclear Magnetic Resonance spectroscopy
NP	Nanoparticle
NSE	Neutron Spin Echo
ORM	Optical Reflection Microscopy
ORNL	Oak Ridge National Laboratory
OZ	Ornstein-Zernike
$P(Q)$	Form factor
PBA	Poly(butyl acrylate)
PDMS	Poly(dimethyl siloxane)
PMDETA	*N*,*N*,*N'*,*N''*,*N''*-pentamethyldiethylenetriamine
PMMA	Poly(methyl methacrylate)
PS	Polystyrene
PSI	Paul Scherrer Institut

PVME	Poly(vinyl methyl ether)
Q	Momentum transfer
QENS	Quasi-Elastic Neutron Scattering
r^2	End-to-end distance
RAFT	Reversible Addition-Fragmentation chain-Transfer
R_{arm}	Radius of gyration of the arm of a star polymer
R_g	Radius of gyration
R_h	Hydrodynamic Radius
RPA	Random Phase Approximation
R_{star}	Radius of gyration of a star polymer
S	Styrene
$S(Q)$	Structure factor
$S(Q,\omega)$	Energy dependent structure factor
SAN	Poly(styrene-co-acrylonitrile)
SANS	Small-Angle Neutron Scattering
SAXS	Small-Angle X-Ray Scattering
SCPE	Solvent-Chlorinated Polyethylene
SEC	Size Exclusion Chromatograpy
SLD	Scattering length density
S_v	Specific surface area
SWCNT	Single-Walled Carbon Nanotubes
$T(\lambda)$	Sample transmission
TEM	Transmission Electron Microscopy
T_g	Glass Transition Temperature
TGA	Thermal Gravimetric Analysis
THF	Tetrahydrofuran
T_m	Melting temperature
TM-AFM	Tapping mode Atomic Force Microscopy
TMPC	Tetramethyl bisphenol-A polycarbonate
TOF	Time-of-Flight
TTS	Time-Temperature Superposition
UCST	Upper Critical Solution Temperature
V	Scattering volume
V_i	Specific volume of momomeric unit
WANS	Wide-Angle Neutron Scattering
WLF	William-Landel-Ferry
z	Degree of polymerisation
α	Flory expansion parameter
α_f	Degree of thermal expansion
γ	Shear strain
Γ	Half width at half maximum of a Lorentzian function
$\dot{\gamma}$	Strain rate, $d\gamma/dt$
ζ	Friction coefficient
η	Viscosity
$\eta(\lambda)$	Detector efficiency

λ	Wavelength
ξ	Correlation length
ρ	Number density
σ	Scattering cross-section
σ_{abs}	Absorption cross-section
σ_{coh}	Coherent cross-section
σ_{inc}	Incoherent cross-section
σ_{sca}	Scattering cross-section
τ	Shear stress
τ_{KWW}	Characteristic relaxation time
τ_R	Relaxation time
Φ	Volume fraction
χ	Flory-Huggins interaction parameter
ω	Angular frequency

Chapter 1. Introduction

1.1 Polymer Nanocomposites

A polymer is a large macromolecule made up of small monomeric units covalently bonded together. Polymer materials are used in everything from packaging to airplanes and medical applications. However, pure polymers often have insufficient mechanical strength or chemical resistance for some of these applications. A technique that is commonly used in industry is creating a polymer composite by adding a filler material to the polymer, which can drastically affect its properties. Inorganic fillers, such as silica and carbon nanotubes, are used extensively in optical electronics[1], sensors[2], biomedical devices[3] and catalysis[4]. This is because organic/inorganic hybrids combine the advantages of the inorganic material, such as higher mechanical strength, with the flexibility and ductility of the organic polymers. For example, polymer-clay composite films have been developed for use in food packaging as the addition of montmorillonite improved the tensile strength and decreased permeability to oxygen and water of the material[5]. Carbon black is often used as filler in tyres to improve performance and reduce cost. Inorganic fillers can also affect many other properties, such as the density and adhesion of materials[6].

A relatively new class of composites that can provide materials with novel properties are nanocomposites. Nanocomposites contain nanoparticles (NPs) with diameters typically ranging between 1 and 100 nm. Nanocomposites have been known for decades, and one of the first manufactured polymer-nanoparticle composites was a clay-reinforced resin called Bakelite developed in 1909[7] for the preservation of fossils[8]. However, it was not until relatively recently that the technology for production of nanocomposites was improved and more research into the advantages of nanocomposites was carried out[9]. The advantages of nanocomposites over traditional composites is due to the nanoparticles comprising a large surface area and having a high surface-to-volume ratio which results in an even greater effect on the properties of the material. Nanoparticles can also induce different property changes to bulk materials[10], creating a wide range of potential applications.

Nanofillers can have a significant impact on the performance of the material; however changes in rheology and mechanical properties are usually only observed when the nanoparticles are highly dispersed within the polymer matrix[11], which provides the high surface-to-volume ratio needed. Nanoparticles have a tendency to aggregate,

especially during *in situ* polymerisation due to interparticle attractive depletion forces, such as van der Waals and electrostatic interactions, which bring the particles together[12]. This means that producing a homogeneous mixture is very difficult. Therefore alternative methods of producing homogeneous dispersions were developed.

One of the most researched methods in the last decade is grafting polymers from the surface of the particles. This creates core-shell nanohybrids containing an inorganic particle core and a polymeric shell, which further increases the range of applications of nanocomposites[13]. This method increases the dispersion and decreases the amount of possible aggregation of particles, thus offering many advantages over mechanical dispersion and making it an attractive area of research for producing new nanocomposite materials.

In this chapter, we present an introduction to polymer nanocomposites, focusing on the synthetic methods and types of nanocomposites used in this project. The basic theory of the conformation and chain dynamics of polymers is described in order to provide context to the effect of nanoparticles on these properties.

1.1.1 Preparation

1.1.1.1 Dispersed polymer nanocomposites

The majority of polymer composites and nanocomposites are prepared by dispersing the filler particles in the polymer matrix. There are two main categories of dispersion techniques; chemical and physical.

Physical methods of creating dispersions can be as simple as mechanically stirring the mixture. One of the most common mechanical methods of breaking up agglomerated nanoparticles is by bead milling. Bead milling has been used as an effective dispersion technique on many nanocomposites such as polymers with carbon nanotubes[14]. The process involves grinding the particles and passing them through a rotor to disperse them. Another physical method of creating a homogeneous dispersion is ultrasonication, which is usually carried out in a solvent. An ultrasonic horn oscillates the mixture which collapses solvent bubbles. These collapsing cavitation bubbles cause high pressure differences, resulting in turbulence which fractures the solid aggregated particles, breaking them apart and creating a colloidal dispersion[15]. Research on the exact mechanism of this process is still ongoing and there are also many optimisation

parameters of the ultrasonication process, such as time and energy input, that can limit the efficiency of dispersion[16].

In the chemical methods, the surface of the filler is either functionalised using a variety of available methods, such as using chemical reactions to modify the surface chemistry (e.g. treating carbon nanotubes (CNTs) with ammonia to produce a charged group on the surface of the filler[17]), or through addition of surfactants that interact with the filler[18]. Research into chemical dispersion techniques has focused on finding methods of modifying the surface of filler particles without causing degradation of the filler. Surface modification of fillers can also change the polymer-filler interactions and thus change the macroscopic properties of the polymer nanocomposite[19].

When removing the solvent from dispersed polymer nanocomposites, slow evaporation can lead to particle aggregation or segregation. Thus, other methods are often used, such as freeze-drying under vacuum for fast evaporation of solvent and then hot pressing the sample[20].

While dispersion methods have been heavily researched, refined and implemented in research, they are not efficient and will not always produce the desired outcome, *e.g.* bead milling often cannot be scaled up to an industrial scale reaction[21]. Polymer nanocomposites created by dispersion methods are also inherently unstable, as the particles have a tendency to aggregate over time.

1.1.1.2 Grafted polymer nanocomposites

Growing polymer shells from inorganic nanoparticles is being researched extensively[22]. One of the advantages of grafting over dispersing is that grafting allows for precise control over the interparticle distance due to the length of the polymer grafted to it. The interparticle distance can affect some of the properties of the nanocomposite such as mechanical, electronic and optical properties[23]. Grafted nanocomposites can be produced by traditional physisorption techniques, where the polymer is physisorbed onto the surface of the particles and forms a layer on the particles which prevents aggregation[24]. This can be achieved with polyelectrolytes, where the Coulomb interaction between oppositely charged nanoparticles and polyelectrolytes creates a coating of polymer[25]. Other interactions, *e.g.* hydrophobic interactions, can also lead to physisorption onto particles[26].

The second and more common class of grafting techniques is chemical grafting, where covalent links are formed between the polymer and the particle surfaces[13]. These strong covalent bonds produce improved properties in the nanocomposite materials such as improved tensile strength[27]. There are two main types of chemical grafting. The first is a "grafting-from" approach where the polymer is produced *in situ* by chain-growth or surface initiated polymerisation. A polymerisation initiator is immobilised on the surface of the nanoparticles and monomer added to produce polymer chains. The chains form polymer brushes, and various polymerisation techniques have been employed to synthesise polymers in this way. The other method of chemical grafting is the "grafting-to" approach. It relies on having or creating functionalities on the polymers which can react with groups on the nanoparticle surfaces (Figure 1.1).

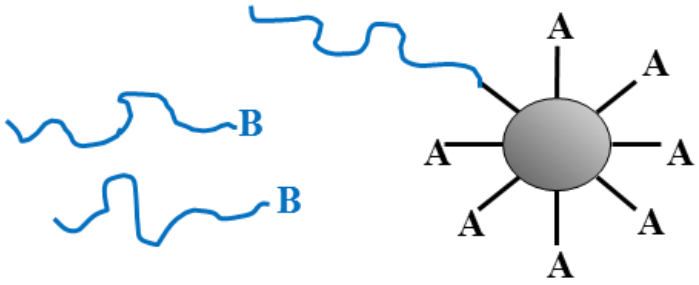

Figure 1.1: Grafting-to approach for grafting polymer chains onto the surface of spherical nanoparticles.

Recently, the synthesis of polymer nanocomposites utilises controlled radical polymerisation techniques. Controlled radical polymerisations are polymerisations where the ability of the chains to terminate themselves has been greatly restricted. This means that the polymerisation continues until all the monomer has been consumed, and thus the molecular weight of the product can be controlled by the monomer and initiator concentration. Controlled polymerisation techniques can be applied to a wide range of monomers to create well-defined polymers with a low polydispersity index (PDI).

There are three commonly used controlled radical polymerisation techniques[28]: atom transfer radical polymerisation (ATRP), reversible addition fragmentation chain transfer (RAFT) polymerisation and nitroxide mediated polymerization (NMP). All of these techniques are being used currently to grow polymer chains from the surface of various inorganic substrates[29]. This project focused on the use of ATRP for growing polymer chains from silica nanoparticles to create polymer nanocomposites with narrow distributions of molecular weight for analysis. This technique was preferred due to a

relatively simple reaction mechanism, more readily available starting materials compared to RAFT and NMP and the successful use of ATRP by the group previously[30, 31].

ATRP is a recent controlled polymerisation technique developed in 1995[32, 33]. The reaction is based upon a transition-metal-catalysed atom transfer radical addition, which is an efficient method of creating a carbon to carbon bond. Initially, the initiator and catalyst system used in ATRP was an alkyl chloride and CuCl/2,2'-bipyridine (bpy) complex[32]. Over the past few years, this has been replaced with CuBr/$CuBr_2$ and other ligands such as *N,N,N',N'',N''*-pentamethyldiethlenetriamine (PMDETA) and tris[2-(dimethylamino)ethyl]amine (Me_6TREN) as these are more reactive and increase the rate of polymerisation[34]. However, it has been found that care must be taken with choice of ligand, as too fast a reaction can cause a loss of control but a very slow reaction is also undesirable.

The proposed mechanism for ATRP has not changed significantly since the technique was first developed. The important step is the atom transfer equilibrium formed between an alkyl halide and a copper complex (Figure 1.2) which controls the polymerisation and is dominated by carbon-halogen bond homolysis, formation of a copper-halogen bond and the redox reaction between the copper complexes. This equilibrium between an 'active' polymer chain and the inactive or 'dormant' form of the polymers, which is weighted towards the dormant form, lowers the concentration of propagating radicals. Thus the amount of chain termination that occurs is greatly reduced and this allows for a controlled polymerisation and molecular weight. Radical exchange processes dominate for tertiary and secondary bromides. However, there is some evidence of an ionic pathway, where the halide anion on the copper species participates in an S_N2 reaction with alkyl halide[35]. This reduces control of the polymerisation and therefore of the molecular weight and PDI of the polymer product.

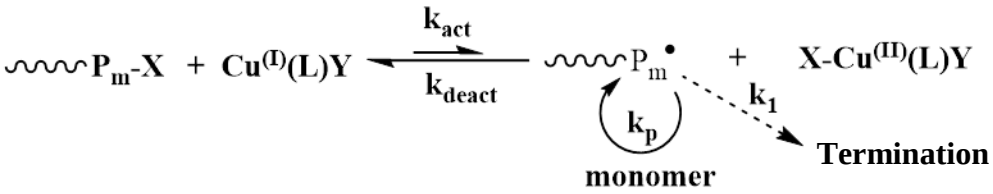

Figure 1.2: Propagation Step of ATRP polymerisation

An alkyl halide initiator can be attached to a nanoparticle via covalent bonding, usually by refluxing the two materials together. ATRP can be used to graft polymers from the surface of the nanoparticles following the general route below (Figure 1.3).

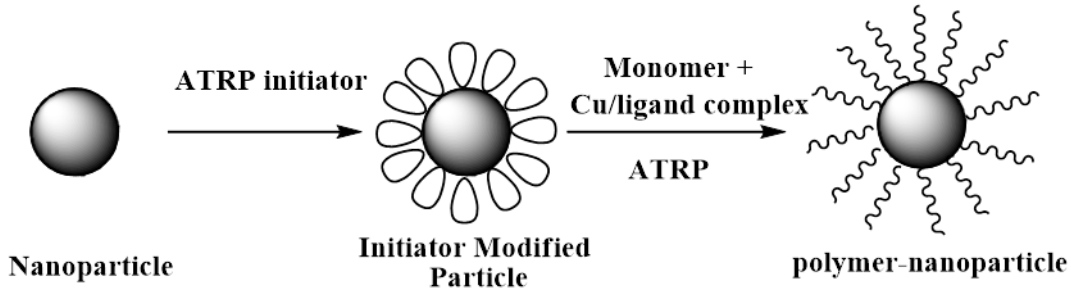

Figure 1.3: Schematic diagram of the preparation of grafted polymer nanocomposites using ATRP.

Grafting polymers using ATRP has been successfully applied to a number of different monomers and substrates. In 2005, El Harrak *et al.* developed a new route for ATRP polymerisation of polystyrene (PS) onto silica nanoparticles.[23] They used small angle neutron scattering (SANS) measurements to characterise the kinetics of the reaction and showed that grafting the polymers from the surface reduced the amount of aggregation compared to bare silica particles.

There are a few disadvantages of the basic ATRP technique. One is the need for stringently oxygen free conditions, as oxidation of the catalyst from Cu(I) to Cu(II) stops the polymerisation. Another disadvantage is the need for relatively high amounts of CuX/ligand catalyst[36]. Removal of the catalyst from the final product requires rigorous purification that is time consuming and produces waste. More complex ATRP techniques were developed in order to overcome these problems. Matyjaszewski *et al.* reported controlled polymerisation of poly(methyl methacrylate) (PMMA) brushes using their newly developed technique, activator generated by electron transfer (AGET) ATRP[37]. In this technique, the catalyst is introduced in its oxidatively stable state, Cu(II), and is activated in situ by a reducing agent such as ascorbic acid, as shown in Figure 1.4. AGET ATRP does not require deoxygenation and can be carried out in the presence of a small amount of copper catalyst, even down to ppm levels and an excess of reducing agent.[38] AGET ATRP from the surface of nanoparticles has been used for a variety of different monomers, such as methyl methacrylate (MMA) and styrene[39].

Another disadvantage of ATRP is macroscopic gelation resulting from unwanted coupling reactions. In order to overcome this, ATRP can be carried out in miniemulsion

conditions. This process prevents macroscopic gelation and cross-linking of polymers by carrying out polymerisation in small, isolated monomer droplets in water. Poly(butyl acrylate)-silica nanocomposites with high conversion and no cross-linking have been produced using this method in the literature[40]. Thus AGET ATRP in miniemulsion is an attractive technique for the synthesis of polymer-silica nanocomposites.

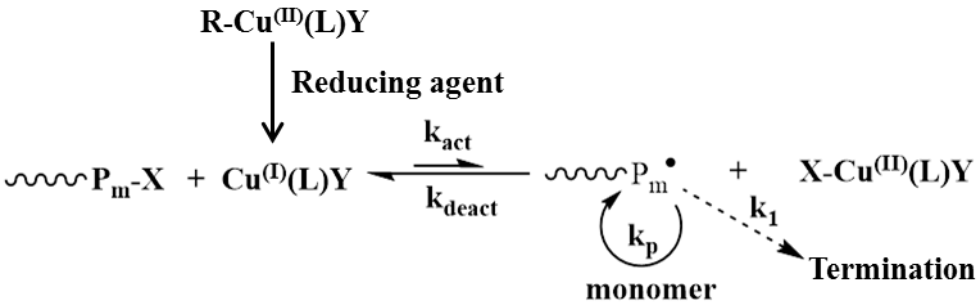

Figure 1.4: Schematic of AGET ATRP mechanism.

1.1.2 Types of nanoparticles

The types of nanoparticles used in polymer nanocomposites range from small inorganic particles (SiO_2, Au, Ag) to organic particles (CNTs, fullerenes). Nanoparticles can also have different shapes, from discrete spherical silica to graphene or silicate sheets. The type, shape and size are significant factors in the effect of the nanofiller on the polymer matrix. There are two nanoparticles used throughout this project: 1) inorganic silica (fumed and colloidal) and 2) organic C_{60} fullerenes.

1.1.2.1 Silica

Silica is commonly used as a filler material as it offers many practical advantages: they are mechanically stable, add good chemical resistance and are relatively inexpensive[41]. Silica is used as a filler material in a variety of everyday products such as shoe soles, adhesives and printing inks[42]. The commercial availability of various silica nanoparticles with a wide range of particle sizes, surface chemistry (hydrophobic or hydrophilic) and aggregation (from colloidal to fumed) makes silica a widely used filler material.

Commercial aggregated silica is produced primarily by two methods, fuming or precipitation. The fuming method produces silica by hydrolysis of chlorosilane ($SiCl_4$) vapour at high-temperatures in an oxygen-hydrogen flame. Precipitated

hydrated silica is produced by treating silicates with mineral acids. Fumed silicas are used extensively in composites due to the effect on mechanical properties of polymeric materials, however these preparation methods do not allow precise control over particle size.

The development of the Stöber synthesis allowed for the preparation of colloidal silica nanoparticles with precise control over the size and distribution[43]. The Stöber synthesis involves the production of spherical silica particles via hydrolysis of tetraethyl orthosilicate (TEOS), as shown in scheme 1.

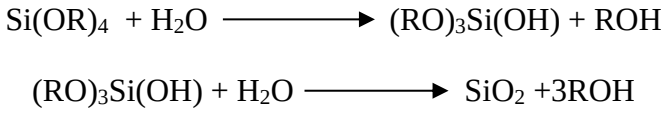

Scheme 1. Synthesis of silica particles using the Stöber method.

An advantage of using silica nanoparticles is the hydroxyl groups present on the surface. These groups can be reacted with organic compounds or polymers in order to use the grafting-to and grafting-from methods discussed in Section 1.1.1.2. Many different polymers have been grafted to and from the surface of silica particles *via* controlled radical polymerisation techniques, such as polystyrene[23, 44, 45], poly(methyl methacrylate)[46], poly(styrene-co-acrylonitrile)[47] and many other polymers[48].

1.1.2.2 Fullerenes

Fullerenes have been used in polymer nanocomposites due to their low density, high tensile strength and commercial availability[49]. There are various types of fullerenes, but the ones most commonly used in polymer nanocomposites are closed cage spherical buckyballs (most common of which is the Buckminsterfullerene, C60) and cylindrical carbon nanotubes (Figure 1.5). Carbon nanotubes have been shown to greatly increase the mechanical strength of a polymer matrix[50].

However, the use of fullerenes in dispersed polymer nanocomposites is often limited[51]. Fullerenes have poor solubility and compatibility with polymers[52] and thus have a tendency to form agglomerates, even at relatively low loadings (~1 wt%)[53]. This is a significant issue for electrical and optical devices, which require a stable dispersion.

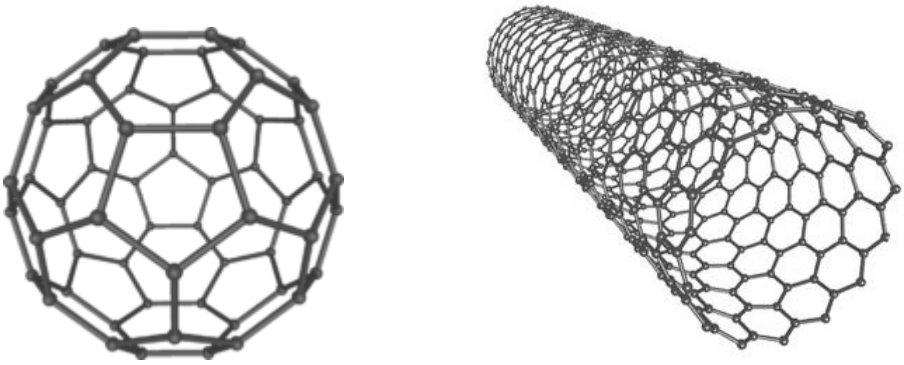

Figure 1.5: Structures of Buckminsterfullerene C60 (left) and carbon nanotubes (right).

In order to overcome this incompatibility, polymer chains have been grafted to the surface of the C60 particles. This creates polymer-fullerene stars. Samulski *et al.* successfully grafted polystyrene chains to fullerene cores in 1992[54], however the samples had a multimodal distribution. Since then, more stringent experimental conditions have been designed in order to create well-defined polymer-fullerene stars. For many years, it was reported that the upper limit of 6 arms was achieved with high purity[55]. However, recently there has been experimental[56] and computational[52] reports that stars with more than 6 arms are possible and that synthesis of polystyrene-fullerene stars results in a mixture of star products that is not detected by traditional size exclusion chromatography (SEC) methods, which would affect the results of the previous studies of these polymer-fullerene stars.

1.1.3 Applications of polymer-silica and polymer-fullerene nanocomposites

The addition of silica not only improves the thermal and mechanical properties, but can also show unique properties that are of interest for many types of applications. Due to silica being chemically inert and optically transparent, polymer-silica is widely used in coatings for polymer films, woods and paper[57]. Polymer-silica hybrids have also been used in membranes, such as poly(phenylene oxide) (PPO)-silica membranes for the separation of H_2 and CO_2,[58] and for removal of heavy metal ions such as cobalt and copper salts from waste water[59]. Some other applications for polymer-silica nanocomposites include optical devices[60], sensors[61, 62] and biomedical devices[3].

Fullerene based nanocomposites are commonly used in organic photovoltaics, transistors and other electronic devices[63] due to their high conductivity. The use of polymer-fullerene hybrids in solar cells[64] is one of the key applications for these types of nanocomposites. Due to the limitations of polymer-fullerene dispersions, grafting

polymer chains to the surface of multifunctional fullerenes has been a subject of recent research for use in such electronic devices and solar cells.

1.2 Polymer Structure[i]

The chemical structure of polymer chains is important for understanding polymer properties. If the polymer chain contains carbon atoms with two different substituents (i.e. asymmetrical C atoms), three stereoisomers are possible: isotactic, syndiotactic and atactic[65]. Several polymers fall into this category, such as polystyrene and poly(methyl methacrylate). The tacticity of polymer chains can affect various properties, such as crystallinity and miscibility[69].

Whilst the chemical structure of the polymer chains plays a significant part, the conformation of the polymer chains can have even greater effects on the polymer physical properties. The conformation of polymers is the overall three-dimensional geometric arrangement of segments or the entire chain. Flexible polymer chains can assume an almost infinite variety of permissible conformations. Therefore a statistical approach to describing polymer conformation is required, using average parameters and distribution functions. The following section describes the theoretical models and parameters used to describe the conformations of linear polymer chains.

1.2.1 Basic theory

A useful parameter for describing the size of a macromolecule is the end-to-end distance. If the bonds of the chain are represented by vectors of length l, then the end-to-end distance is the vector between the two ends of the chain, as shown schematically in Figure 1.6. Due to the number of conformations a chain can adopt, the size of the chain is described by the mean-square end-to-end distance, $\langle r^2 \rangle$, which is dependent on the type of polymer and the chain interactions.

Another measure of the size of a polymer chain commonly used to describe complex polymers is the radius of gyration (R_g or $\langle s^2 \rangle^{1/2}$). The radius of gyration is the root mean square distance of each chain segment measured from its centre of mass, as shown in Figure 1.7. The mean-square radius of gyration can be calculated indirectly from intrinsic viscosity or other dilute solution properties or measured experimentally though scattering experiments[65].

[i] See textbooks [65,66, 67,68] as general references for the following sections

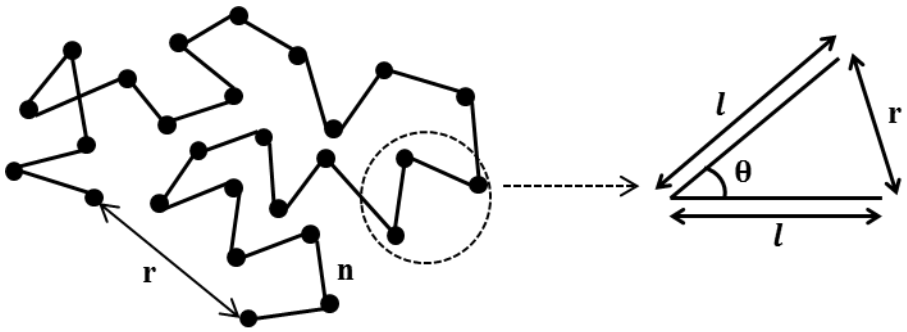

Figure 1.6: The freely jointed or random walk chain model showing the end-to-end distance r for a chain of n segments.

The first and simplest statistical model for a polymer chain is the freely jointed chain model, also known as the random walk model. The chain is treated as a number, *n*, of independent segments that have complete freedom of movement in every direction regardless of the neighbouring bonds. There is no fixed bond angle and there is free rotation around the joints in the chain. Using trigonometry (Figure 1.6), the end-to-end distance for the simplest two-link case can be calculated from the cosine law, leading to the following equation:

$$r^2 = 2l^2 + 2l^2 cos\theta \qquad \textbf{(1.1)}$$

The end-to-end distance, r, can be calculated from random flight statistics. When n is large, Equation (1.1) reduces to[68]:

$$r^2 = nl^2 \qquad \textbf{(1.2)}$$

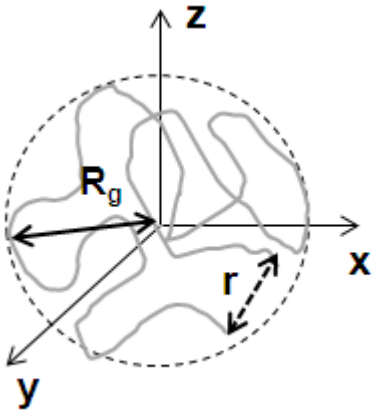

Figure 1.7: Schematic representation of a polymer chain with the end-to-end distance, r, (- - -) and the radius of gyration (—) shown.

Therefore the length of the fully extended chain is equal to nl, and is called the contour length. Using this model, the radius of gyration and mean-square end-to-end distance are related by[70]:

$$R_g{}^2 = \frac{\langle r^2 \rangle}{6} = \frac{nl^2}{6} \quad \textbf{(1.3)}$$

While the freely jointed model is simple, it is also unrealistic. An updated version of the model, called the freely rotating model, uses fixed bond angles to more accurately describe the chemical structure of the chain. For large n, end-to-end distance is calculated by the following equation[69, 71]:

$$r^2 = nl^2 \frac{1 - cos\theta}{1 + cos\theta} \quad \textbf{(1.4)}$$

where θ is the fixed bond angle. For saturated tetrahedral carbon atom, θ is 109.47^o leading to cos θ = 1/3. Therefore, $r^2 = 2nl^2$ and the end-to-end distance is twice as large as the freely jointed model when fixed bond angles are used.

As with the freely jointed model, the freely rotating model is still too simple for real polymer chains. These models do not take into account restrictions that restrict each bond to distinguishable rotational states, i.e. the preferred conformations of the chains. The first simplification is that the preferred conformation of a chain consisting of identical repeating units is one in which all the repeating units adopt the same conformation. In this case, the chain will be a relatively simple geometric pattern, such as a *planar zig-zag* or *helical* structure[72].

In the opposite scenario, each repeat unit is oriented randomly to each other whilst still being bonded. This is known as the *random coil* conformation, though this term refers to the statistical distribution of an array of conformations. In the absence of constraints or interactions, many chains will depart from the preferred conformation and adopt a random coil form.

Additionally, the freely rotating model does not include interactions with neighbouring atoms and other chains that restrict rotation and movement of the segments of the chain. These interactions are divided into two broad groups: 1) short-range interactions which are related to the structural characteristics and occur between neighbouring atoms or groups and 2) long-range interactions between segments in the chain that are far apart in the chain sequence but near each other in space.

Short-range interactions between segments and neighbouring atoms cause steric repulsions of a magnitude proportional to the size of the segment. These repulsions impose restrictions on bond rotations, and in order to minimise these repulsions polymer

chains arrange itself into an expanded coil. Equation (1.4) can be modified for steric repulsion effects[65]:

$$\langle r^2 \rangle_0 = nl^2 \frac{1 - cos\theta}{1 + cos\theta} \cdot \frac{1 - \langle cos\phi \rangle}{1 + \langle cos\phi \rangle} \quad \textbf{(1.5)}$$

where cos ϕ is the average cosine of the angle of rotation of the bonds in the backbone and $\langle r^2 \rangle_0$ is the average unperturbed dimensions where the chains are not affected by external constraints such as interactions with solvent. Cos ϕ is calculated from the potential energy and the Boltzmann distribution of the populations of possible conformers.

Deviations from the freely rotating model due to short-range interactions are often evaluated using a characteristic ratio, C_∞, parameter, which is the ratio of the experimentally or calculated $\langle r^2 \rangle$ value to the theoretically determined value for the freely jointed chain:

$$C_\infty = \frac{\langle r^2 \rangle_0}{nl^2} \quad \textbf{(1.6)}$$

Although taking into account short range interactions leads to a more realistic model for polymer chains, long range interactions are still not accounted for. In the random walk model, a chain is allowed to cross its own path, however this is forbidden in real polymer chains. Any conformations that require self-intersecting chains are therefore not permitted, and this greatly reduces the number of possible chain conformations. This subsequently leads to an increase in $\langle r^2 \rangle$ and R_g as the spatial conformation of chains are perturbed. This is known as the *excluded volume* effect, and has been the subject of numerous studies. In order to describe the extent of expansion caused by this effect, the expansion factor, α, has been introduced by Flory[73]:

$$\langle r^2 \rangle = \alpha^2 \langle r^2 \rangle_0 \quad \textbf{(1.7)}$$

The $\langle r^2 \rangle_0$ value can be calculated from the structural data and statistical information on potentials affecting bond rotation, whereas $\langle r^2 \rangle$ is determined experimentally.

Long-range interactions in polymers are complex and include steric effects as well as van der Waals attractions. In solution, solvent molecule mediated interactions must also be taken into account. Excluded volume effects are therefore important to consider when measuring the structural properties of polymers in solution, and as such will be expanded on in the following section.

1.2.2 Polymer conformation in solution

In solution, the behaviour of polymers is dependent on the concentration. In dilute solution, each chain is isolated and the size is described by the radius of gyration. Dilute polymer solution conformations are primarily dominated by polymer-solvent molecule interactions.

As the concentration increases into the semi-dilute region, the chains begin to overlap and form 'blobs'. Although the blobs are conceptual objects, the size of the blob is estimated by the correlation length, ξ. The concentration at which the solution becomes semi-dilute is called the overlap concentration, c*. As the concentration increases further, we enter the concentrated regime where the chains are now fully overlapping and entangled. The thermodynamics of semi-dilute and concentrated polymer solutions is different than dilute solution properties.

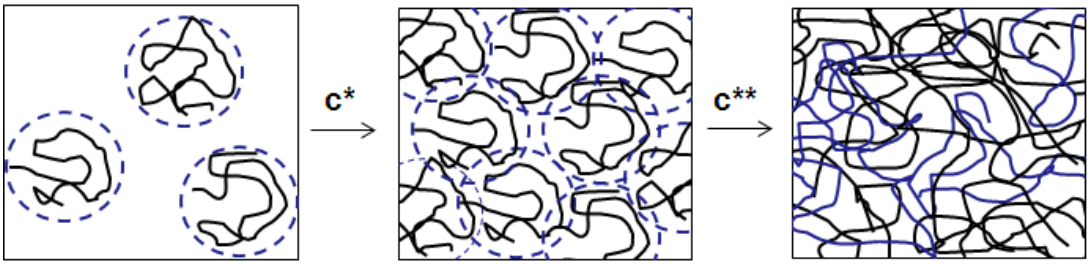

Figure 1.8: Schematic representation of polymer chains in a good solvent under dilute, semi-dilute and concentrated regimes.

Excluded volume effects are an important factor affecting the conformation of polymers in dilute solution. The expansion factor, α, is used to estimate the swelling of a polymer chain in solution, and α^2 varies with temperature depending on the polymer-solvent system. For a given solvent, if $\alpha^2 = 1$ at a given temperature, known as the Θ temperature, the chain becomes ideal and exhibits the same structural behaviour as unperturbed chains, i.e. $\langle r^2 \rangle = \langle r^2 \rangle_0$. At the Θ temperature, the repulsive excluded volume effect is "cancelled out" by the attractive forces between polymer segments when immersed in a poor solvent and thus the polymer chains are unperturbed by long-range interactions. Solvents in which this behaviour occurs are known as Θ solvents. In good solvents, excluded volume effects cause the chains to exhibit expanded self-avoiding walk conformations in dilute solution[74].

Additionally, as the concentration of the solution is increased and polymer chains overlap, chain expansion due to long-range interactions is suppressed. The chains are considered to be ideal Gaussian chains, as expected by Flory[73]. This has been confirmed by neutron scattering experiments on deuterated polymer chains in a melt of the hydrogenated polymer[75, 76].

1.2.3 Branched and star polymer conformation

Polymer chains do not have to be linear and may contain branches. Branched polymers are often difficult to define precisely, making analysis of the conformation and dynamics more difficult. A simple form of a branched polymer is a star polymer. Star polymers consist of a core/centre and arms of the same length (Figure 1.9).

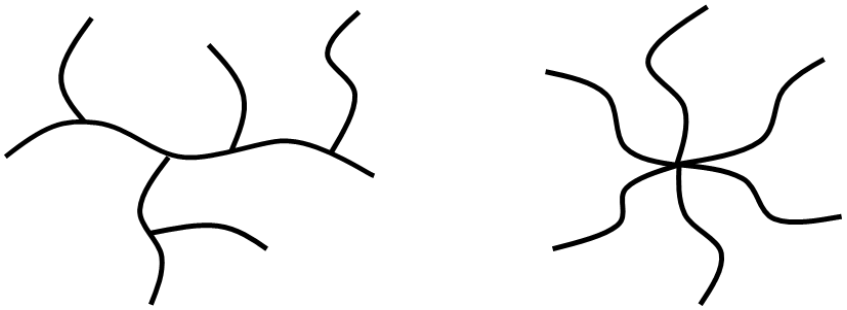

Figure 1.9: Examples of branched polymer architecture: (left) randomly branched chain and (right) a star polymer.

In branched polymer chains, the end-to-end distance cannot be well-defined. Therefore, the radius of gyration is the better measure of the size of branched or star polymers. In order to describe the conformation of branched polymers, the random walk concept was adapted by Zimm and Stockmayer[77]. They assumed that two sub-chains joined at a single point behave similarly to a linear chain and that there are no excluded volume effects. Using these simplifications, a branching factor, g, was introduced:

$$g = \frac{\langle {R_g}^2 \rangle_B}{\langle {R_g}^2 \rangle_L} \quad \textbf{(1.8)}$$

where $\langle {R_g}^2 \rangle_B$ is the mean-square radius of gyration of the branched polymer and $\langle {R_g}^2 \rangle_L$ is the mean-square radius of gyration for the equivalent linear polymer.

The derived equation for g depends on the type of branched polymer. For a randomly branched polymer chain, g depends heavily on the number of branch points. For a single branch point, g is calculated from the following equation:

$$g = \frac{6f}{(f+1)(f+2)} \quad \textbf{(1.9)}$$

where f is the number of branches. For star polymers, g is given by:

$$g = \frac{3f-2}{f^2} \quad \textbf{(1.10)}$$

However, this simple model fails to describe branched polymers for two main reasons. Firstly, the excluded volume effect is more significant in branched polymers due to the increased segment-segment contacts. Secondly, the branching point has many chains attached to a single point, causing spatial crowding[78]. It may be expected that similar effects are seen when the chains are grafted onto a hard core, rather than tethered together to form a 'soft' core.

1.3 Polymer dynamics and rheology[ii]

Due to polymers being macromolecules constructed from small subunits, the dynamics of polymer chains is complex and depends on many factors, such as the molecular weight. In general, polymeric motions can be divided into three broad groups based on the length scale of the motion:

- **Large scale motions**, comprised of the cooperative movements of large sections of the polymer chain or even entire chains. Main chain rotation and translation are large scale and slow motions. The main models used to describe these types of motions are the Rouse and reptation models, which will be described in detail in later sections.
- **Segmental motions** of short segments in the polymer chain backbone. These motions depend primarily on the environment of the segment and are not affected by the overall size of the polymer chains. These motions range from simple torsional libration to relatively large scale rotational behaviour (Figure 1.10).
- **Local scale motions** such as rotations, vibrations and torsions of the side groups (Figure 1.10). The chemical structure of the polymer chains is the determining

[ii] See [65, 79, 80] as general references for the following section

factor in these motions, as the rest of the molecule is considered an inert body that does not affect these motions.

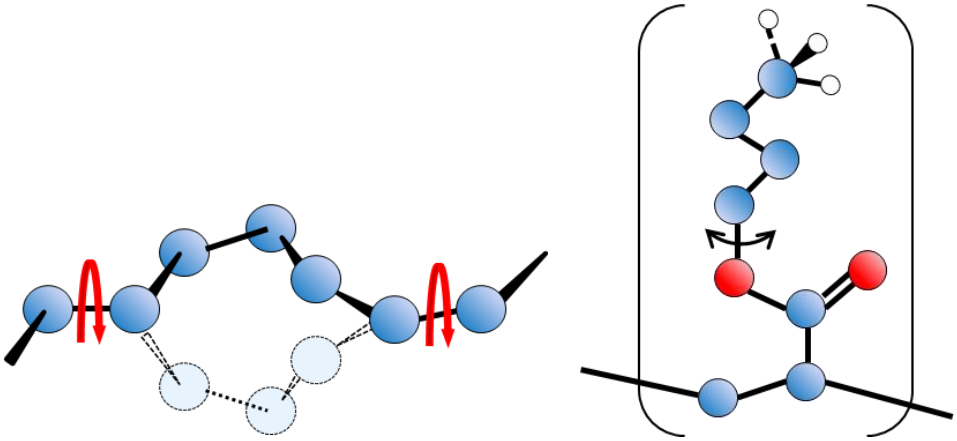

Figure 1.10: Schematic representation of (left) segmental motion and (right) side group rotation in a polymer chain.

The following sections will describe the typical viscoelastic behaviour of polymer chains and then outline the various methods, models and theories used to describe the motions present in a polymer chain.

1.3.1 Viscoelastic behaviour

1.3.1.1 Five regions of viscoelasticity

Polymers are generally viscoelastic materials, showing both elastic and viscous behaviour depending on the state of the material. The physical state of the polymer is related to the extent of the undergoing molecular motions, which are in turn governed by the chain flexibility and the temperature. The types of molecular motions change depending on the current physical state of the polymer, which can be determined by measuring the mechanical behaviour. A typical curve of mechanically measured elastic modulus, E′, against temperature for a linear amorphous polymer is shown in Figure 1.11. There are 5 distinct regions of viscoelasticity that can be identified:

A. **Glassy region**: The polymer is a solid in this region with frozen cooperative molecular motions.
B. **Glass transition**: The transition region between the glass and rubber states. Molecular motions are increasing as the modulus decreases sharply. The glass transition temperature, T_g, is within this region, often cited as the onset of the decrease in the storage modulus.

C. **Rubbery state**: The modulus plateaus as the polymer behaves as a rubber. Chain entanglements in this region prevent liquid flow.
D. **Rubbery flow**: After the rubbery plateau, the modulus begins to decrease again.
E. **Liquid region**: In this region the polymer behaves as a viscous liquid with no evidence of elastic recovery.

Therefore the viscoelastic behaviour of polymer chains is closely related to the polymer dynamics[80]. When a polymer is in the glass region, main chain motion is "frozen in", as the energy required for motions is higher than the thermal energy available and the chains are set into a specific conformation. When the sample is heated, the chain segments can move cooperatively and the sample transitions from the glassy to the rubbery state. In the rubber state, chain entanglements still hinder molecular motions. This transition, known as the glass transition, is a function of molecular motion and measurement of the glass transition temperature, T_g, can in certain circumstances be used to probe changes in molecular motions.

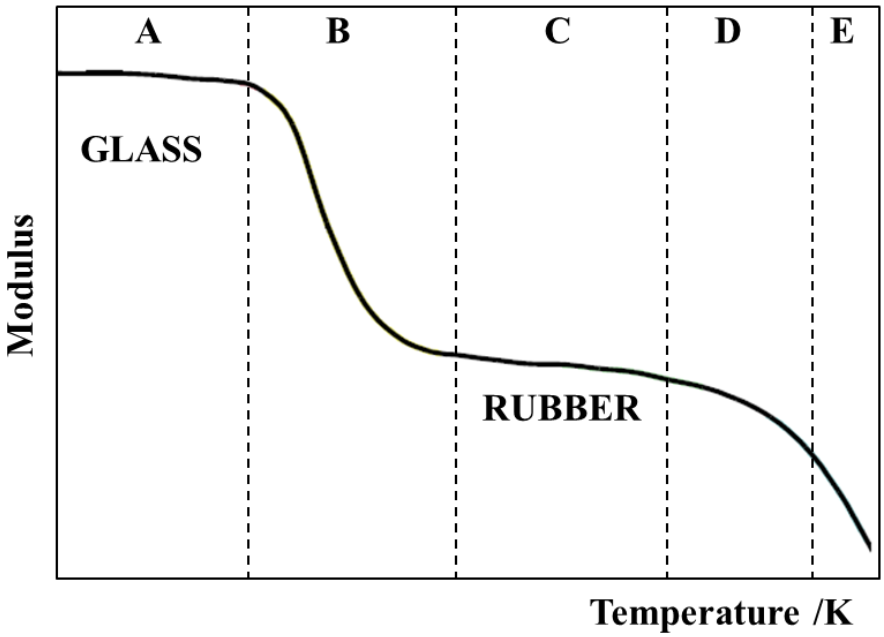

Figure 1.11: The five regions of viscoelasticity for a typical glassy polymer.

In this thesis, the viscoelastic behaviour of grafted and dispersed poly(butyl acrylate) (PBA) nanocomposites were examined using rheological rather than mechanical measurements. Rheology is the study of how materials deform and flow, and therefore can be thought of as the macroscopic dynamics of a material. This is most commonly applied to liquid or liquid-like materials, but can also be applied to the

deformation of solids. Polymeric materials have undergone extensive rheological measurement, as the viscoelastic properties of materials are important in determining the procedures for processing and applications[66].

Rheological oscillatory experiments measure the mechanical relaxation of the behaviour of a polymeric material. In this case, the dynamic storage elastic modulus (G') and dynamic loss modulus (G''), representing the elastic and viscous portions of the chain behaviour respectively, are measured as a function of angular frequency. A schematic diagram for the frequency dependence of a typical polymer melt is shown in Figure 1.12. The three distinct physical states (glass, rubber and viscous liquid) are also observed in this curves, with the order reversed.

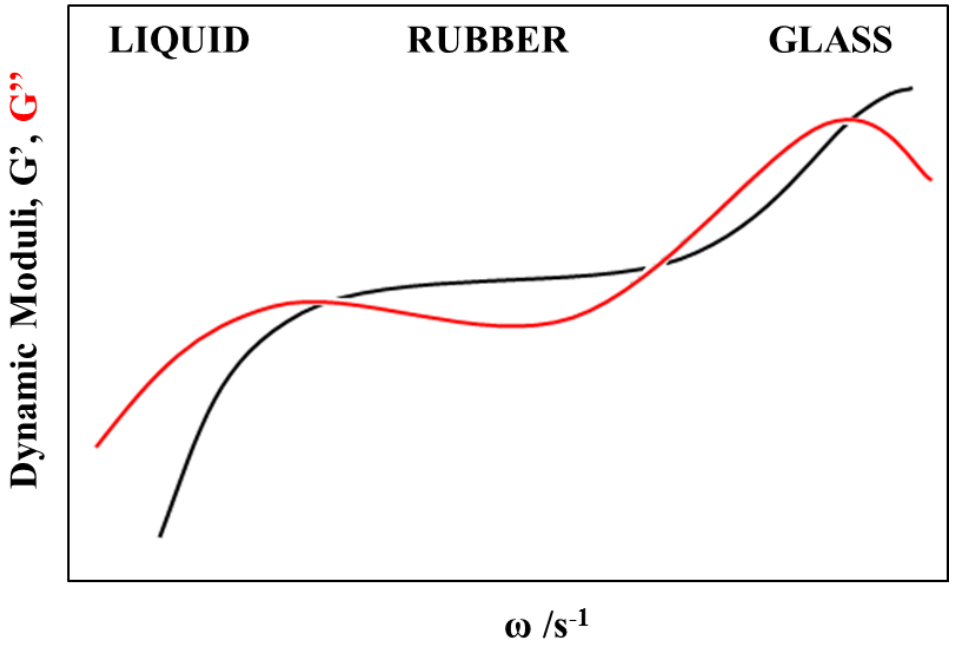

Figure 1.12: Typical dynamic storage modulus (G′) and loss modulus (G″) curves as a function of angular frequency for a linear polymer melt.

At low frequencies, the polymer melt is a viscous liquid as the viscous modulus dominates (G″ > G′). This region is known as the **terminal zone**. The terminal zone corresponds to long-term relaxation processes that are sensitive to the molecular architecture, such as the reptation and chain fluctuation models (see Section 1.3.5 for more details). As frequency increases, both storage and loss moduli increase until the two curves reach a cross over point. At intermediate frequencies, the storage modulus is higher than the viscous modulus (G′ > G″), therefore elastic response dominates in the rubbery plateau region.

As the frequency increases further, the loss modulus, G″, increases to create another cross-over point (G″ > G′), leading to a **transition zone** between the rubber and glass regions. The motions in the transition zone are high frequency, fast motions which are not affected by chain architecture[66]. Finally, in the glassy region, the storage modulus reaches another plateau whereas the loss modulus values start to decrease again leading to dominating elastic response in this region.

1.3.1.2 Viscous Region

Viscometry rheological experiments measure the viscosity, η, of a polymer melt or solution as a function of shear rate or shear stress. The viscosity of a material describes the resistance to deformation and flow by application of a shear stress. Shear stress is defined by the following equation:

$$\tau = \frac{F}{A} \tag{1.11}$$

where F is the shear force per unit area of the surface, A. Shear strain, γ, is given by:

$$\gamma = \tan\theta = \frac{X}{Y} \tag{1.12}$$

where θ is the angle that characterises the deformation and X and Y are the width and height of the deformation. A schematic representation of a shear experiment is shown in Figure 1.13. In these experiments, the bottom plate is stationary while the top plate is moved with a velocity, v_0.

Ideal fluids obey Newton's law and give a linear relationship between shear stress and shear rate:

$$\tau = \eta\dot{\gamma} \tag{1.13}$$

where $\dot{\gamma}$ is the strain rate, dγ/dt. These materials are therefore called Newtonian fluids, and exhibit viscosity that is independent of shear stress or shear rate. The viscosity is therefore defined as:

$$\eta = \frac{\tau}{\dot{\gamma}}\ (Pa.s) \tag{1.14}$$

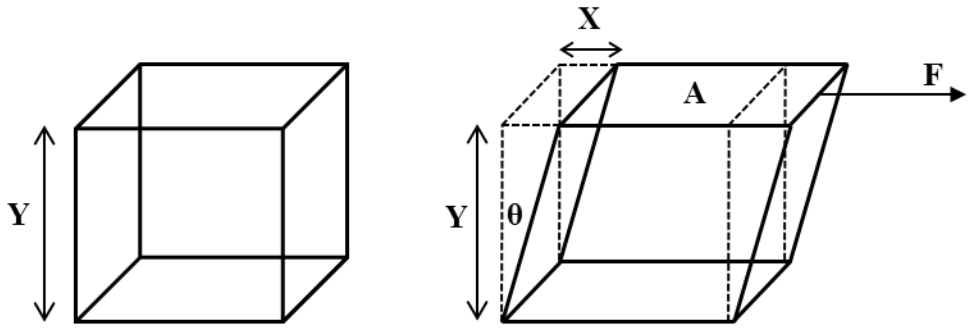

Figure 1.13: Schematic representation of a simple shear experiment.

However, most materials show deviations from this law, and are so termed non-Newtonian. There are two deviations from Newtonian behaviour: shear thickening, where viscosity increases with increasing shear, and shear thinning where the viscosity decreases with increasing shear rate. A typical viscosity curve for a glassy polymer is shown in Figure 1.14. Over the course of a viscometry measurement, initially polymers show Newtonian behaviour at very low rates, then shear thinning and a shear dependent viscosity. At very high shear rates, a second Newtonian plateau region is achieved and viscosity is independent of shear. This behaviour is due to the presence of chain entanglements that restrict flow[65].

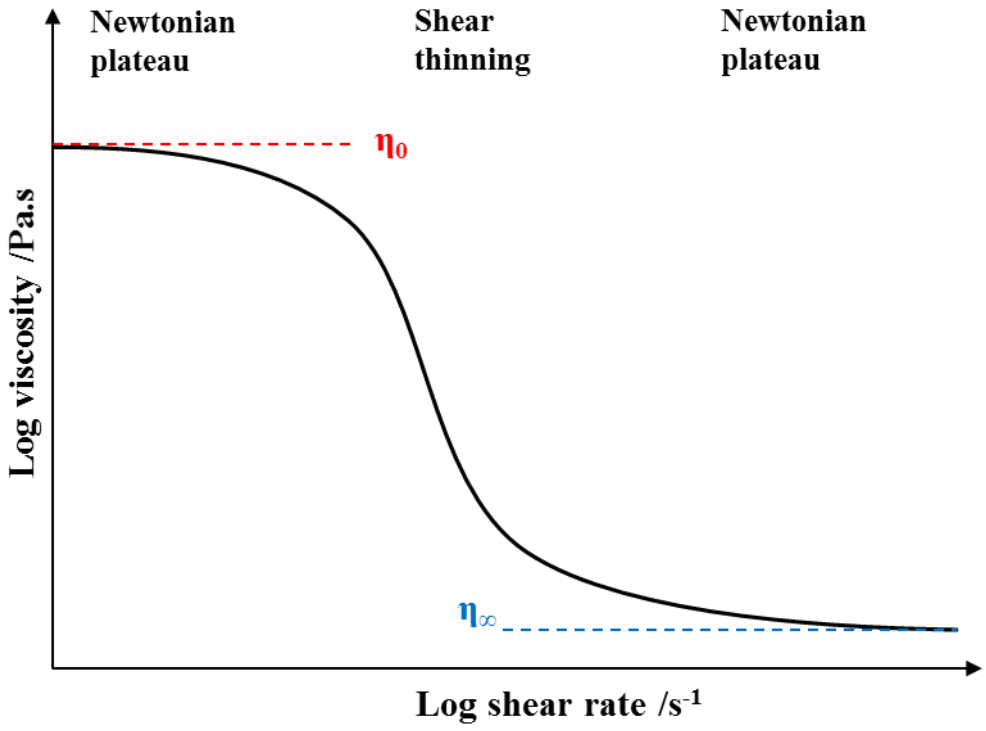

Figure 1.14: A typical viscosity against shear rate curve for an amorphous polymer.

Another important parameter in flow behaviour of polymers is the zero shear rate viscosity, η_0, which is the viscosity at the limit of low shear rate, or the steady state viscosity of the material while at rest (Figure 1.14). The zero shear rate viscosity is extrapolated from measured viscosity in the low shear rate region.

Chain entanglements are important in the understanding of polymer dynamic behaviour and can greatly affect the viscosity of the polymer matrix. Polymer chain entanglements occur when the polymer coils interpenetrate, as shown in Figure 1.15. The molecular weight of entanglement (M_e) is the molecular weight where chains become long enough to entangle, and is determined by measurement of the plateau modulus. The molecular weight dependence of zero shear rate viscosity, η_0, for polymer chains changes at the critical molecular weight for entanglement (M_c) and, theoretically, $M_c \approx 2M_e$. Both of these molecular weight parameters are important factors in polymer dynamics and rheology.

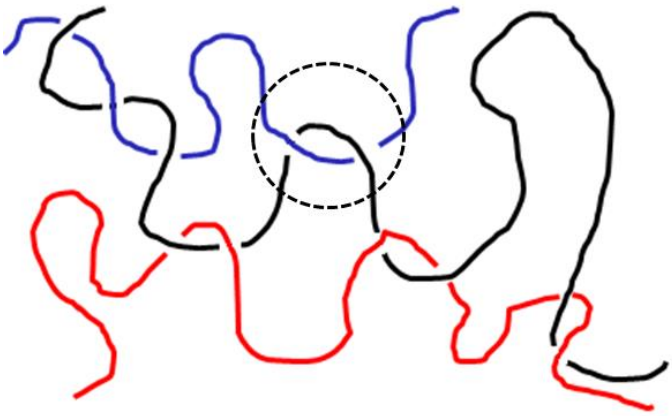

Figure 1.15: Schematic of chain entanglements in a linear polymer melt.

1.3.2 Temperature dependence of relaxations

Polymer chains relieve stress by undergoing relaxation processes. These relaxation processes are labelled in various ways. Often the glass transition is called the α-relaxation and sub-T_g transitions are known as the β and γ-relaxations. Another traditional method is to label the relaxation processes as the α, β and γ-relaxations in order of decreasing temperature.

The temperature dependence of the relaxation processes is an important aspect of polymer dynamics. The activation energy of particular motions can be calculated

from the temperature dependence. The local motions of polymer chains follow Arrhenius dependence, whereas macroscopic motions deviate from this. Segmental motions are modelled by the William-Landel-Ferry (WLF) temperature dependence.

The WLF equation is an empirical expression used to describe the time-temperature behaviour of polymers within the glass transition temperature (T_g) region:

$$\log \alpha_T = -\frac{C_1(T - T_0)}{C_2 + T - T_0} \quad \textbf{(1.15)}$$

where α_T is the horizontal time-scale shift factor, T_0 is the chosen reference temperature and C_1 and C_2 are temperature independent constants, usually treated as adjustable fitting parameters[81]. The WLF equation can also be related to the free volume by the following equations:

$$C_1 = B/2.303 f_0 \quad \textbf{(1.16)}$$

$$C_2 = f_0/a_f \quad \textbf{(1.17)}$$

where f_0 is the fractional free volume, a_f is the degree of thermal expansion and B is a constant (often simplified to unity)[81].

1.3.3 Small scale dynamics below T_g

Below the glass transition, the main chain motion is "frozen in" i.e. the polymer is in the glassy state. However, side groups still undergo rotational, vibrational and librational motions. Methyl group rotations are the most comprehensively studied side group due to their relative simplicity and wide range of torsional potentials depending on the chemical structure of the polymer chain[82]. Long side group motions, such as the side chains in PBA have also been studied, using a variety of techniques such as dielectric relaxation[83] and solid-state NMR[84]. For quasi-elastic neutron scattering (QENS) measurements, long side group chains have to be labelled in order to distinguish their dynamics from the motions of the main chains. In the polymers studied within this thesis, the side groups are generally unlabelled long chains. The only other side group motions of potential interest are the phenyl rings in polystyrene.

There have been many studies of polystyrene's sub-T_g dynamics by various relaxation techniques[85, 86] and by molecular dynamics simulations (MDS)[87, 88]. The phenyl ring side group motions in particular have attracted attention but the results in the literature are inconsistent. Some papers state that up to 100% of the rings are

undergoing 180° rotations ('flipping')[85], whereas others have found the fraction of flipping rings to be less than 3%[88]. The causes of the β and γ-relaxations have been reported to be a variety of motions – from ring flips to ring oscillations to main chain and ring motions[87] and even ring small angle rotations[86]. Recently, Colmenero *et al.* have attributed sub-T_g dynamics of polystyrene to phenyl ring oscillations and state that 180° ring flips do not occur on these time scales[89].

1.3.4 Rouse model

In order to interpret the viscoelastic behaviour of polymer chains, Rouse[90], Zimm[91] and Bueche[92] developed theories based on a model where the chain consists of a series of sub-units. The Rouse model, proposed by Rouse in 1953, is the most widely used for describing the dynamics and viscoelastic behaviour of ideal polymer chains, where only chain connectivity is considered[90]. The polymer chain is described as a series of harmonic springs of length, *l*, between beads, as shown in Figure 1.16. Excluded volume, internal viscosity and hydrodynamic interactions between segments are neglected in this model; interactions between polymer and environment, e.g. solvent, takes place at a finite number of discrete centres along the chain.

In the Rouse model, single chain diffusion is described by Brownian motion, which relates diffusion coefficient, D, of a particle to the viscosity, as the whole chain behaves as a single particle:

$$D = \frac{k_B T}{M\eta} \tag{1.18}$$

where k_B is Boltzmann's constant. The assumption of the lack of internal viscosity effects (i.e. no interaction between segments) and the Brownian motion leads to the derivation of a relaxation time, τ_R:

$$\tau_R = \frac{\zeta l^2 N^2}{3\pi^2 k_B T} \propto M^2 \tag{1.19}$$

where N is the number of segments, ζ is the friction coefficient and l is the average length of a segment.

Although the Rouse model is relatively simple, it has been used successfully to describe the viscoelastic behaviour of polymers[93]. Using the Rouse model, the viscosity and self-diffusion coefficient can be predicted from the following equations[79]:

$$\eta = \frac{\pi^2}{12}\left(\frac{\rho RT}{M}\right)\tau_R \propto M \quad \textbf{(1.20)}$$

$$D = \frac{k_B T}{\zeta N} \propto M^{-1} \quad \textbf{(1.21)}$$

where ρ is the number density of the polymer. The viscosity is proportional to molecular weight for low molecular weight polymers, which has been verified experimentally for polymers at $M < M_c$.[80] Additionally, the temperature dependence of the friction coefficient, ζ, is described using phenomenological expressions such as the WLF Equation (1.11).

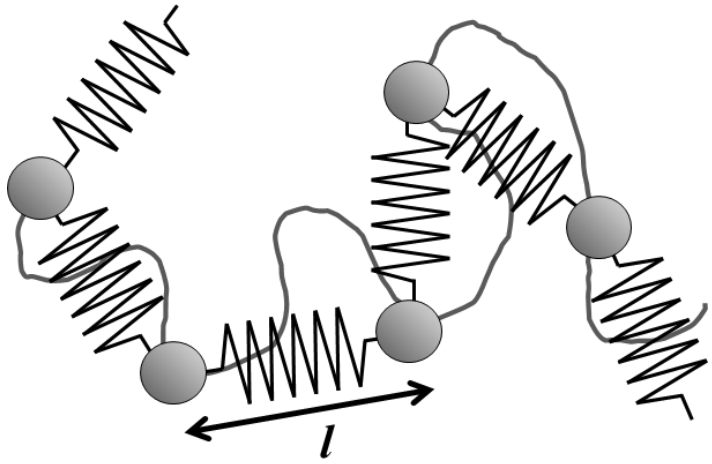

Figure 1.16: Schematic representation of the Rouse model (bead-spring model) for a polymer chain.

In general, the Rouse model applies mainly for short chains below the molecular weight of entanglement. Above M_e, the Rouse model is appropriate only at small relaxation times. At longer times and thus slower motions, chain dynamics are more often described using the reptation model.

1.3.5 Reptation model

The terminal zone of a polymeric material corresponds to the long-time relaxation processes. The two main relaxation processes which are believed to be active in this region are reptation and chain-end fluctuations (Figure 1.17). Both of these models for dynamics use the tube model as the basis for explaining the movements of the polymer chains, i.e. the polymers are confined in polymer tubes due to entanglements restricting molecular motion[94]. The tube diameter, d_R, is the entanglement distance, below which Rouse dynamics are exhibited by the system.

The reptation model for polymers developed by de Gennes[95] was introduced to describe the movement of polymer chains in the presence of fixed obstacles, by describing a tube contour that does not change with time. Over long times, the chains move out of the tube ends in a snake-like motion[96].

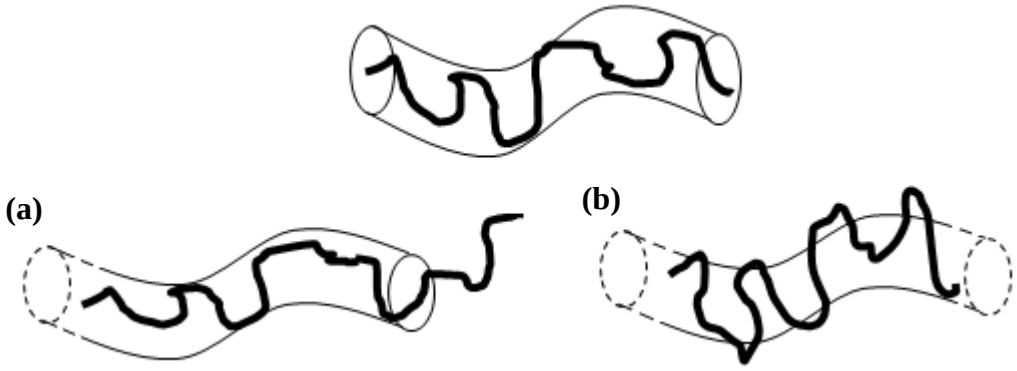

Figure 1.17: Tube model and macromolecular movements of a polymer chain within the model; (a) reptation and (b) chain-end fluctuations.

Reptation theory describes the effect of entanglements on the chain relaxation time, known as the reptation time, τ_r, is the time needed for a chain to move entirely out of the tube[94]:

$$\tau_r = \frac{\zeta l^4 N^3}{\pi^2 {d_R}^2 k_B T} = 3\frac{l^2 N}{{d_R}^2}\tau_R \propto M^3 \qquad \textbf{(1.22)}$$

From this and Equation (1.19), τ_r is proportional to M^3 whereas τ_R is proportional to M^2, therefore τ_r is much larger than τ_R for high molecular weight polymers.

Using the reptation model and above equation, the main features of polymer melt rheology at $M > M_c$ can therefore be described:

$$\eta = \frac{\pi^2}{12}\left(\frac{\rho RT}{M}\right) = \frac{l^2 N}{{d_R}^2}\tau_r \propto M^3 \qquad \textbf{(1.23)}$$

$$D = \frac{k_B T {d_R}^2}{3\zeta N^2 l^2} \propto M^{-2} \qquad \textbf{(1.24)}$$

Theoretically the viscosity varies $\propto M^3$, however experimentally this value has been found to be closer to 3.4 – 3.6 and this has been attributed to tube length fluctuations[79, 80]. The reptation theory was then expanded on by Doi and Edwards[79] and has been applied to both viscoelastic and solution behaviour.

Whilst reptation is the model used for linear polymers, in branched polymers, especially star polymers, the dynamic picture is different. The central branch point prevents linear reptation[97], as the star cannot be easily confined within a tube model and the branches restrict tube mobility. Instead, de Gennes introduced the concept of arm retraction to describe the motions of polymer star arms[98]. The arms, confined in their own tubes, can partially retract down to the centre point of the star and then expand along a different trajectory. Therefore, the dynamics of polymer stars depends on the size of the arm rather than the whole star. This movement is entropically disfavoured[99], therefore stress relaxation time in polymer stars is exponentially slower with increasing arm length.

1.4 Polymer blends[iii]

Polymer blends are a mixture of two or more polymers or copolymers to form a new material. Like the addition of inorganic particles, blending is used to modify the physical behaviour of the polymer components. Polymer blends are used in a variety of applications, from specialised uses such as ion-exchange membranes[103] to general everyday use in appliances, electronics and sporting goods[104]. The addition of nanofillers to polymer blends can be used to further modify the physical properties for industrial applications. Due to this, the effect of nanoparticles on miscibility, morphology and phase separation behaviour of polymer blends is a growing area of research.

The following sections describe the theory of polymer blend miscibility and phase separation. The effect of nanoparticles on the miscibility.

1.4.1 Miscibility

Polymer blends can be divided into three broad categories[102]:

1. Immiscible: Two-phase mixtures. Two glass transitions corresponding to the homopolymers are observed. This is the most common class of blends.
2. Miscible: A homogeneous mixture of polymers which exhibits macroscopic properties expected from a single phase mixture, such as a single glass transition

[iii] See textbook references [100-102] as general references for the following sections.

temperature (T_g). Miscible blends often offer greater control over macroscopic properties than immiscible blends.

3. Compatible: Compatible is an industrial term used primarily to describe immiscible blends that show uniform physical properties and good phase adhesion.

There are various methods for determining the miscibility of a polymer blend. One of the most commonly used methods for probing miscibility is measurement of the T_g using differential scanning calorimetry (DSC)[100].

When a blend is immiscible, DSC traces show two glass transition temperatures corresponding to those of the two polymer components. In a mixture of two completely miscible polymers, a single narrow T_g is observed that is at an intermediate value between the two values for the homopolymers. The simplest equation for calculating the theoretical T_g is the Fox equation[105]:

$$\frac{1}{T_g} = \frac{w_1}{T_{g,1}} + \frac{w_2}{T_{g,1}} \quad \textbf{(1.25)}$$

where w_1 and w_2 are the weight fractions of the polymer 1 and polymer 2 components. Glass transition measurements have many advantages as they are relatively fast (10 – 20 minutes), use small amounts of sample (~10 mg) and give control over the thermal history of the sample. However, this technique does have some limitations, as partially miscible blends appear as a broad T_g and if the polymer components have similar T_g values (<20 ^{o}C difference), then a single broad T_g is often observed even if the blend is immiscible and phase separated.

1.4.2 Phase separation behaviour

The fundamental free energy of mixing governs the behaviour of polymer blends:

$$\Delta G_m = \Delta H_m - T\Delta S_m \quad \textbf{(1.26)}$$

where ΔG_m is the Gibbs free energy of mixing, ΔH_m is the enthalpy of mixing, T is temperature and ΔS_m is the entropy of mixing. A homogeneous mixture is formed when $\Delta G_m \leq 0$, i.e. the Gibbs free energy of the mixture is lower than the sum of the Gibbs free energies of the components. The different phase separation behaviour seen in polymer blends is based on this equation.

There are two main types of phase separation behaviour in miscible one-phase polymer blends[101]: Upper Critical Solution Temperature (UCST) and Lower Critical Solution Temperature behaviour (LCST). Typical phase diagrams for both types of phase behaviour are shown in Figure 1.18. In UCST blends, phase separation occurs with decreasing temperature. This behaviour occurs primarily in low molecular weight non-polar blends where the entropic gain, ΔS_m, is the driving force for mixing. As the temperature increases, ΔS_m increases, therefore leading to a decrease in ΔG_m and blend miscibility.

The other type of phase separation behaviour, LCST, is more commonly observed in polymer blends than UCST behaviour. High molar mass polymers have a small entropic contribution, which generally leads to a positive value of ΔG_m and therefore immiscibility. However, in miscible LCST blends there are specific interactions, such as hydrogen bonding between the polymer components, which result in a large negative ΔH_m value. This leads to a ΔG_m value less than 0 and therefore miscibility. As the temperature increases, these interactions become weaker, ΔG_m increases and thus the blend phase separates. Some polymer blends exhibit both a UCST and an LCST on their phase diagrams, e.g. poly(acrylonitrile-co-styrene)poly(acrylonitrile-*co*-butadiene) blends.

Flory and Huggins[67] proposed a theory to calculate the free energy of mixing of polymer blends. The theory is based on a lattice model, assuming incompressibility and no volume changes upon mixing. The free energy of mixing is given by:

$$\frac{\Delta G_m}{k_B T} = \frac{\phi_1}{z_1} \ln \phi_1 + \frac{\phi_2}{z_2} \ln \phi_2 + \phi_1 \phi_2 \chi \qquad \textbf{(1.27)}$$

where z_i is the degree of polymerisation, ϕ_i is the volume fraction, k_B is Boltzmann's constant and χ is the dimensionless Flory-Huggins interaction parameter. The entropic contribution is given by the first two terms whereas the final term is the enthalpic contribution. In the Flory-Huggins theory, the interaction parameter, χ, is a measure of the polymer-polymer interaction in the blend and is proportional to 1/T. Therefore, for high molecular weight polymer blends where the miscibility of the system is dependent on the enthalpy of mixing, miscibility is usually seen with negative values of χ. Coil expansion is also possible in lower molecular weight blends with a weakly positive parameter, i.e. χ < ½, due to excluded volume effects not considered by the Flory-Huggins equation[106].

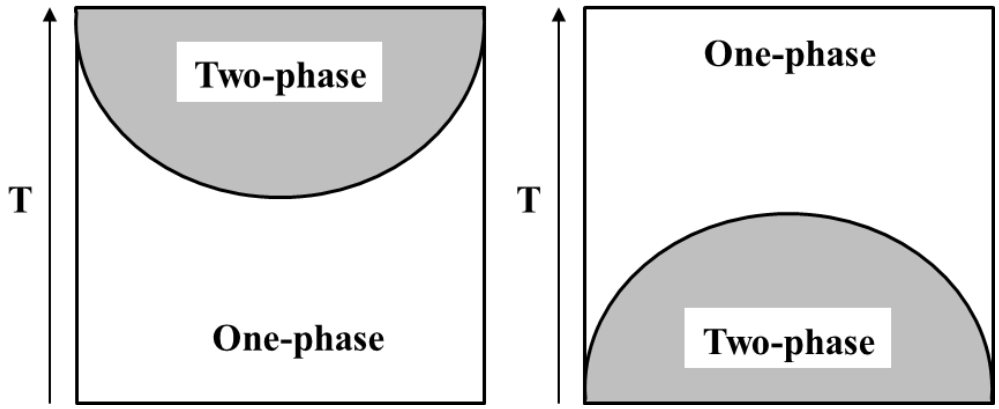

Figure 1.18: Phase diagrams for polymer blends showing (left) LCST and (right) UCST behaviour.

Additionally, previous studies on polymer blends have shown that χ may contain both enthalpic and entropic contributions[107, 108] and thus is often approximated as follows:

$$\chi = \frac{A}{T} + B \tag{1.28}$$

where *A* and *B* are constants that specify the enthalpic and entropic parts respectively. Therefore, in practice χ is generally considered an empirical parameter that includes all deviations from ideal blend behaviour. The inversely proportional temperature dependence is the most common behaviour in mostly UCST type blends such as PS/PMMA[109]. However, other temperature dependences are often observed in LCST or more complex phase behaviours blends[110].

The interaction parameter is considered a complex function[100] that varies with many other parameters such as composition[111], molecular weight, tacticity[112] and even pressure and chain length[101]. These additional contributions are not accounted for in the Flory-Huggins theory and are not completely understood. The χ values are dependent on the system measured and the changes may be related to changes in local energies, packing orientation, polydispersity of components etc.

1.5 Effect of nanoparticles on polymer properties

Nanofillers can have a significant effect on the physical properties of polymers. There are many factors that affect the properties of polymer nanocomposites, such as the nature, size and shape of the fillers, the type of polymer matrix, the dispersion of particles within the matrix and even the preparation method[27]. The reinforcement effects observed in polymer nanocomposites are caused by changes in the microscopic

properties of polymer chains, such as the conformation and the chain dynamics. The following section discusses the existing literature on the effect of nanoparticles on various properties of polymers that were studied during the course of this project, focusing primarily on silica and fullerene containing nanocomposites.

1.5.1 Chain conformation

There has been considerable effort to understand the effect of particles on the structure of the polymer chains. However, the results have often been contradictory and shown to depend on many factors, such as the size of the particles and the concentration. Structural effects caused by nanoparticles have been observed in specific polymer-particle systems. A study by Tuteja *et al.* showed polymer swelling with an increase in R_g of 10 – 20% upon addition of polymer nanoparticles[113]. This has since been attributed to the fact that the nanoparticles were "soft" rather than typical hard spherical inorganic particles[114] as other studies of polymers filled with polymeric nanoparticles have also shown increasing or decreasing R_g values[115]. Deformed and stretched chains have also been observed in polymer-silica nanocomposites using SANS and the effect has been attributed to the formation of a glassy layer around the silica nanoparticles[116]. The loading of nanoparticles is an important factor, as Tung *et al.* observed no change in chain dimensions at < 2 wt% loading of single-walled carbon nanotubes (SWCNT), but observed an increase in R_g at higher nanoparticle concentrations, eventually leading to a 30% increase in R_g at 10 wt% loading[117].

More recently, many studies have shown that polymer chains in nanocomposites are unperturbed by the presence of inorganic filler particles[118-120]. Chevigny *et al*. found typical Gaussian chain behaviour in polystyrene chains grafted from colloidal silica nanoparticles[121]. A SANS and SAXS study of dispersed polystyrene-silica nanocomposites showed that the chains were identical to those of the pure polymer in the intermediate to high Q range (Q is defined in Section 2.2.1). However, at low Q a shoulder peak appears that could not be explained by the authors[122] but has since been attributed to unwanted silica scattering contributions. Similar unexpected small-angle scattering (SAS) signals in the low Q range have been seen in other experiments on polymer nanocomposites, despite being measured under contrast matching conditions to eliminate silica scattering contributions[114]. These papers suggest that any changes in polymer chain dimensions in polymer nanocomposites are caused by other factors, such as poor particle dispersion[120].

The structural behaviour of well-defined polymer-fullerene star nanocomposites has generally been compared to that of pure polymer stars, e.g. polymer star models are used for SANS analysis. Several groups have studied polymer-fullerene stars using various techniques. Weber *et al.* studied PS-C60 stars using dynamic light scattering (DLS) measurements, finding the results to be in agreement with calculations for pure polystyrene stars[55]. Picot *et al.* used SANS to study polystyrene-fullerene stars at various molecular weights and found the stars have radius of gyration values similar to that predicted for typical polystyrene stars[123]. However, Lebedev *et al.* found that the polystyrene-fullerene stars have larger R_g values than those calculated for pure polymer stars, showing the arms are slightly extended[124]. Additionally, many of these studies have used SEC to claim the polymer-fullerene stars are well-defined with no mixtures of stars with different numbers of arms[55, 123], which has since been shown to not necessarily be accurate[56].

1.5.2 Dynamics

The existence of a 'bound layer' is a common explanation for the change in mechanical and structural properties of polymer nanocomposites. Polymer-particle interactions cause greatly reduced mobility in the polymer chains at the surface of the particles, leading to a layer of static chains. This creates regions of different dynamics within the polymer matrix: 1) a region of tightly bound 'immobile' chains and 2) freely moving polymer matrix chains. Additionally, there may also be a third region of loosely bound chains with slightly restricted dynamics. NMR[125, 126], dielectric[127, 128] and QENS studies[129] have identified this behaviour in many types of polymer nanocomposites. A study of polymer-fullerene mixtures[130] found restricted backbone motions relative to the pure polymer due to suppressed chain motions near the particle surfaces. However, other groups have found no change in local dynamics, but instead have seen a suppression of long-range dynamics of the chains[131].

The observed decrease in segmental dynamics has also been attributed to other effects. Decreases in free volume, often related to the agglomeration of nanoparticles or the formation of a polymer-particle network structure, lead to less volume available for chain diffusion and translation[132]. Another suggestion put forward by Fragiadakis *et al.* based on dielectric relaxation measurements is that rather than an immobile layer, the chains around the surface of the particles exhibit different motions to that of the bulk matrix[133]. The chains around the surface of the particles can adopt fewer conformations

and thus has lower configurational entropy than the free polymer chains. This leads to slower molecular motions without the need for a glassy layer model. Gam *et al.* studied chains in the presence of nanoparticles using tracers and found significant slowing down of molecular diffusion, which was most significant in long chain tracer molecules[134]. This was attributed to the loss of chain conformations (and subsequent decrease in entropy) as the molecules diffuse through "bottlenecks" between the particles.

Other studies have found that the chain dynamics of the polymer matrix are unaffected by the addition of nanofillers. Boucher *et al.* observed no change in polymer dynamics when colloidal silica was added to poly (methyl methacrylate), despite observed changes in dynamics related properties such as physical ageing[135]. Holt *et al.* studied poly(2-vinylpyridine)-inorganic oxide nanocomposites and found that even at high loadings (28 vol %), nanoparticles have little effect on the segmental dynamics of the chains despite there being a large change in the rheological properties upon addition of silica[136]. Contradictory literature results on chain dynamics has also been reported in polymer-fullerene nanocomposites. Both accelerated[137] and decelerated[130] dynamics have been reported in polymer-fullerene mixtures.

The type of nanoparticle can therefore also affect the dynamic behaviour. For example, increased chain dynamics have been observed in intercalated polymer nanocomposites containing layered silicate sheets. Confinement effects cause the segmental relaxation process to occur at much lower glass transition for confined chains compared to bulk[138]. There are various proposed explanations for the faster dynamics, including chain cooperativity rearrangements or enhanced mobility in the interphase region next to the surfaces due to parallel orientation of chains near the silicate layer. In other studies where polymer-filler interactions dominate, a slowing down of the relaxation process is seen due to a glassy layer at the surface of the filler[139].

Due to the wide variety of results seen in the literature for dynamics in polymer nanocomposite, universal behaviour has not been established. There are many factors and interactions that can influence the chain dynamics in polymer nanocomposites and thus the dynamic behaviour observed can be specific to certain nanocomposite types[132].

1.5.3 Glass Transition Temperature

As discussed in the previous section, the addition of nanoparticles can affect the chain dynamics, which therefore affects the glass transition temperature. The addition of

nanoparticles to a polymer matrix has been reported to increase and decrease T_g. Molecular dynamics simulations have suggested that the changes in T_g are highly dependent on the polymer-particle interactions: attractive interactions increase T_g while non-attractive interactions can decrease T_g.[140] The addition of nanoparticles on polymers has also been shown to have a non-linear effect on the T_g. Mizuno *et al.* reported increased T_g in polystyrene-silica nanocomposites up to a 20% volume fraction, and then a slight decrease until 50% volume fraction[141].

Other polymer-silica nanocomposites in the literature have shown no change in glass transition temperature[127, 142-144]. In the case of dispersed samples, this has previously been attributed to weak interactions between the polymer and the filler[144]. A lack of restricted chain dynamics upon addition of nanoparticles also can result in no observed change in T_g.[145]

Grafting polymer chains to the surface of nanoparticles can also greatly affect the glass transition temperature. A significantly increased T_g was observed in PMMA chains grafted to ordered mesoporous silica compared to a simple dispersion[146]. The increased T_g was attributed to reduced segmental mobility when chains are grafted. PS-silica nanocomposites were synthesised by Savin *et al.* which showed an increase of 2 – 13 ^{o}C, depending on the molecular weight of the polystyrene chains[45]. Koerner *et al.* also reported an increased T_g in grafted PS-silica compared to the equivalent linear PS[147]. However, the T_g decreases with increasing silica content which suggests there are multiple effects, such as reduced local chain density and constrained cooperativity, on the T_g of these grafted polymer nanocomposites[147].

The effect of fullerenes on the glass transition temperature of polymers has been investigated in a few papers in the literature. PS, PMMA and tetramethyl bisphenol-A polycarbonate (TMPC)-fullerene nanocomposites containing up to 1 wt% fullerenes were analysed by Kropka *et al.*[130] using differential scanning calorimetry (DSC) and dynamic mechanical analysis (DMA). They found a small increase in T_g of ~1 – 4 ^{o}C for all three polymers. Using DSC, Sanz *et al.*[148] found that the addition of fullerenes increased the glass transition temperature up to a loading of 4 wt%. At higher fullerene concentration, the T_g decreased back towards the value for pure polystyrene[148]. They also found that changes in the glass transition are dependent upon fullerene aggregation, as fullerenes could only be sufficient dispersed at concentrations below 1 and 4 wt%.

Some mechanical and DSC studies have observed a second relaxation process occurring in polymer nanocomposites resulting in two glass transitions[149, 150].

Tsagaropoulos and Eisenberg[149, 151] consistently observed a second loss tangent peak in viscoelastic data of a series of uncross-linked polymers. They attributed the additional tan δ maximum to a second glass transition due to the bound layer of chains with restricted mobility observed in many polymer nanocomposites[152]. However, further studies have demonstrated that the existence of a second T_g is not a universal feature of polymer-filler systems. No evidence of a second T_g or large T_g increase have been reported even in highly interacting systems[128].

1.5.4 Physical Ageing

Physical ageing is the slow process of an amorphous material relaxing into its thermodynamic equilibrium state when stored below the glass transition temperature (T_g)[153]. This phenomenon is due to a series of small relaxation events taking place in the amorphous region of glassy polymers. Whilst the chemical structure of the polymer remains unchanged, the change in the packing of the polymer chains leads to a loss of thermodynamic properties such as enthalpy and entropy[154] which typically results to decreased thermal and mechanical properties over time.

The previous sections have shown that the addition of inorganic fillers such as silica to polymers can have a considerable effect on the polymer chain dynamics, which should subsequently lead to significant changes in the physical ageing of the material. However, the exact effect of fillers on the physical ageing of polymers and the mechanism by which this occurs is still under much debate. Some groups have reported decelerated ageing[155], while other studies have shown no change or even accelerated ageing[156] as a result of adding nanoparticles to the polymer matrix. In a recent review of the literature on the physical ageing of polymer nanocomposites[157], the physical ageing has been found to generally correspond to the trend in measured glass transition temperature of the nanocomposite compared to the pure polymer. Polymer nanocomposites showing increased T_g values tend to also show a reduced physical ageing rate, whereas a decreased T_g correlates to accelerated ageing. However, there are exceptions to this, such as PMMA-silica samples where no change in T_g was detected but greatly accelerated ageing was observed[158].

The concentration of nanofillers is an important factor in physical ageing, as the rate of ageing was shown to increase rapidly in PVAc-silica nanocomposites containing larger filler contents[143]. Another factor that can affect the physical ageing of a

nanocomposite is how well dispersed the nanoparticles are. A homogeneous dispersion created by grafting PMMA to carbon nanotubes exhibited a significantly reduced physical ageing rate compared to bulk PMMA and a slightly reduced rate to dispersing carbon nanotubes in PMMA[155].

1.5.5 Viscoelastic behaviour

The rheological properties, such as viscosity, are vitally important for the industrial processing and applications of polymers. Therefore, there has been significant interest in investigating the dynamic moduli and viscosity of polymer nanocomposites.

Generally, nanoparticle fillers have been found to increase the dynamic moduli of the polymer matrix[159-161]. There has been some debate in the literature whether the mechanical reinforcement was primarily caused by large scale agglomerates of fillers[162, 163] or that good dispersion[164, 165] is necessary for reinforcement. More recent literature suggests that it is interparticle interactions, facilitated by bridging chains, which are the dominating factor in reinforcement[166]. Solid-like behaviour in polymer nanocomposites, for example, has often been attributed to the formation of a filler network within the polymer matrix[167, 168]. The formation of a glassy bound layer of chains at the interface between the polymer matrix and the particle due to polymer-particle interactions has also been theorised to be the cause of mechanical reinforcement in polymer nanocomposites[169, 170]. However, Raos *et al.* and other groups have pointed out that it is difficult to separate the contributions from the particle-polymer and particle-particle interactions as they are often correlated[171, 172].

It has also been shown that the size, shape and aggregation of silica nanoparticles are important factors in mechanical reinforcement[172]. Therefore, comparisons of different types of fillers, such as fumed and colloidal silica are crucial for understanding the mechanisms behind this reinforcement. Recently, Zhao *et al.* studied the rheological behaviour of poly(2-vinylpyridine) nanocomposites containing colloidal or fumed silica[173]. They found that fumed silica had a larger effect on the dynamic moduli than colloidal silica and the fumed silica nanocomposites exhibited solid-like behaviour at high loadings. They also compared dispersing PS-grafted silica nanoparticles within linear PS and found a lower percolation threshold (i.e. formation of long-range connectivity), and that grafted nanocomposites showed less mechanical reinforcement than in the dispersed fumed silica nanocomposites.

The earliest studies of the effect of nano-sized fillers on viscosity reported a significant increase upon addition of nanoparticles[174]. The increase in viscosity was observed in many types of polymer nanocomposites, such as gold nanoparticles embedded in poly(tert-butyl acrylate)[175] and poly(propylene)-clay hybrids[176]. The observed increase in viscosity was also consistently larger than that predicted by the known models for composite materials. A significant increase in viscosity is still reported for polymer nanocomposites where strong polymer-particle interactions cause the formation of polymer-particle networks, such as entangled poly(ethylene oxide)-silica melts[177]. As with the dynamic moduli results, the formation of particle-particle networks is a common explanation for increased viscosity seen in polymer nanocomposites[178].

However, new studies on the viscosity of dispersed polymer nanocomposites containing spherical particles have shown decreased viscosity compared to the pure polymer. The decrease in viscosity has been related to weak polymer-particle interactions and an increase in free volume upon addition of nanoparticles[179]; however Mackay *et al.* predicted that the observed decrease has a more complex nature[180]. Tuteja *et al.* studied polystyrene nanoparticles dispersed in linear polystyrene chains[181], and found that the viscosity of the resulting blend is reduced when the interparticle gap is smaller than the linear polymer and that this is only seen when the chains are sufficiently entangled to cause confinement effects. Tuteja and Mackay also studied polystyrene-fullerene dispersions and found a similar decrease in viscosity[51]. They postulate that a decrease in viscosity in polymer nanocomposites with spherical nanoparticles is observed under two conditions: the polymer chains are entangled and the average distance between nanoparticles is less than two times the radius of gyration of the polymer.

A similar decrease in viscosity was observed by Jain *et al.* in polypropylene-silica dispersions[182]. The authors attributed this to selective adsorption of high molecular weight polymer chains on the surface of the colloidal silica, leaving the lower molecular weight chains to form the surrounding swollen matrix.

Overall, the effect of fillers on the viscosity of the polymer matrix is still not completely understood, and both increasing and decreasing viscosity have been observed due to different factors that can arise in polymer nanocomposites (e.g. polymer-particle interactions versus free volume increases). Additionally, separating the

contributions from interparticle interactions from the polymer-particle interactions is non-trivial in both viscosity and dynamic moduli measurements.

1.5.6 Polymer blend miscibility

There is extensive literature on the thermal and mechanical properties of polymer nanocomposites, but there are far fewer systematic studies on the phase behaviour of polymer blends containing nanoparticles. Studies have shown that addition of fillers can increase[183, 184] or decrease[185] the phase separation temperature. The filler particles also often have stronger interactions with one of the polymers in the blend. For example, carbon black filler in poly(vinylidene fluoride) (PVDF)/PMMA blends interacts preferentially with PVDF, leading to composition fluctuations[186]. Attempts to computationally model the interactions between the polymer components and nanoparticles have shown that the size of the particles relative to the polymer chain is an important factor in the effect on blend miscibility[187]. Smaller nanoparticles reduce unfavourable polymer-polymer interactions and lead to increased miscibility.

The work on polymer blends presented in this thesis will focus primarily on PMMA/SAN and PMMA/SCPE blends containing silica nanoparticles. The miscibility of PMMA/SAN blends has been studied extensively in the literature over the past few decades[168, 188-190]. There are also a few literature papers of the effects of nanoparticles on this blend, primarily studied using various microscopy techniques. Chung *et al.* studied dispersions of colloidal silica in PMMA/SAN and found that silica is evenly dispersed in the one-phase system, but migrate into the PMMA rich zones after phase separation[191]. The presence of silica also slowed down domain growth in the sample. Rheological measurements on dispersed PMMA/SAN/silica blends to create a binodal phase diagram showed an increase in phase separation temperature, especially for compositions with high amounts of SAN[183]. This was attributed to the migration of silica into the PMMA rich zones, an effect observed only when PMMA is the minor phase[192].

Most phase separation studies of blends with nanoparticles use rheological methods[183, 193] or cloud-point, microscopy and turbidity methods[185]. The use of more extensive techniques, such as small-angle neutron scattering (SANS), to study the phase boundaries and one-phase and two-phase behaviour has been limited[194]. Additionally, there are only a handful of studies on the effect of grafting polymer chains on polymer

blend miscibility, mainly focused on PS/PVME blends with PS grafted to various nanoparticle fillers such as silver[195] and MWCNTs[196]. These papers are recently published, showing that this is a current area of research. More studies are required to fully understand the effect of grafting on polymer blends miscibility[197].

1.6 Aims of Project

Grafting chains from the surface of silica nanoparticles is a newly developed technique that has gained much interest recently due to the ability to create stable dispersions and increase the strength of the polymer-particle interactions. The effect of grafting chains onto fillers on the structure and dynamics of polymer chains is still an open question in material science, and there are few comparisons of grafted and dispersed polymer nanocomposites in the literature.

The aim of this work is to study the structure and dynamics of chain-grafted polymer nanocomposites in comparison to pure polymers and particle dispersions. Understanding the changes in conformation and local chain dynamics is crucial for explaining the macroscopic effects, such as mechanical reinforcement. Two types of silica nanoparticles were used in this work (colloidal and aggregated) in order to study the effect of differently structured nanoparticles, as the size, shape and aggregation of the filler has been shown to have a significant effect on mechanical properties of polymer nanocomposites.

The two main techniques used to study the structure and dynamics of chain-grafted polymer nanocomposites are small-angle neutron scattering (SANS) and quasi-elastic neutron scattering (QENS). Other measurements, such as dynamic light scattering and comprehensive rheological experiments are used to complement the results from these two techniques.

In this thesis, the structure and dynamics of two types of polymer nanocomposites are presented; well-defined 6-arm polystyrene-fullerene stars and polymer-silica nanocomposites. The polymer-silica nanocomposites contain polymer chains of well-defined length and molecular weight but not grafting density.

This thesis is structured as follows:

- The theoretical background and basic concepts of neutron scattering are summarised in **Chapter 2**. In particular, a detailed description of the theory, experimental and the two neutron scattering techniques used in this project, quasi-elastic neutron scattering (QENS) and small-angle neutron scattering (SANS), are provided. Finally, a summary of the neutron sources and instrumentation used throughout this project is given.
- **Chapter 3** contains the details of the materials, synthesis and various characterisation methods used.
- The results of structural studies using SANS and DLS measurements on nanocomposites are given in **Chapter 4 and 5**. Two types of nanocomposites are discussed: well-defined PS-fullerene stars are discussed in in Chapter 4 whilst Chapter 5 covers the measurements on various polymer-silica nanocomposites.
- The effect of fillers on the dynamics of polymer chains is discussed in **Chapter 6.** The first part of the chapter contains the results and discussion of the local chain dynamics, rheology and physical ageing of polymer-silica nanocomposites, the second part focuses on the chain dynamics and rheology of polystyrene-fullerene stars.
- **Chapter 7** covers preliminary results on the incorporation of fillers and polymer nanocomposites in polymer blends. A brief introduction on polymer blend phase separation theory is presented in this chapter. Microscopy, glass transition and SANS measurements were carried out on two blends: PMMA/SAN and PMMA/SCPE. The effect of silica nanoparticles on the phase separation of these blends was studied.
- Finally, **Chapter 8** contains the conclusions and potential future work arising from the work presented in this thesis.

Chapter 2. Neutron Scattering Theory and Instrumentation

The structure and dynamics of polymers have been studied extensively using a range of techniques: neutron magnetic resonance, X-Ray scattering, dielectric spectroscopy, light scattering and neutron scattering. Neutron scattering can be advantageous over other scattering techniques due to the unique properties of neutrons and has rapidly become an important technique in a wide range of applications, especially in the field of polymer conformation and dynamics.[iv]

In this Thesis, the structure and dynamics of polymer-silica and polystyrene-fullerene nanocomposites have been investigated primarily through neutron scattering. Two neutron scattering techniques were used for this work: Small-Angle Neutron Scattering (SANS) for structural studies and Quasi-Elastic Neutron Scattering (QENS) for measuring polymer chain dynamics. This chapter provides an overview of the neutron scattering theory required for understanding the work presented, with emphasis on the theory and instrumentation for SANS and QENS experiments.

2.1 Neutron properties

Neutrons are one of the fundamental particles that make up all matter. The basic properties of neutrons are listed in Table 2.1. Neutron scattering techniques are invaluable for analysing materials due to the combination of these basic properties of the neutron:

1. It has an energy range in the order of a few meVs to eV, which is comparable to the intermolecular energies in condensed phases. Thus the neutron scattering technique can probe processes such as quantum tunnelling (μeV) to molecular translations, rotations and vibrations and even eV transitions in the electronic structure of the material.
2. Low energy neutrons can be considered as plane waves with a wavelength of ~1.8Å, which is similar to the molecular dimensions or spacings within a solid. This allows for diffraction measurements to be performed without needing heavy atoms in the molecule unlike X-Ray diffraction measurements.
3. Another important property is the neutrality of the neutron particle and a negligible, if not zero, electric dipole moment. This results in the interaction between the neutron and the nucleus of the atom being weak, which allows for

[iv] See textbook references [198-202] as general references for the following chapter

deeper penetration of the material. Electron and proton alternatives are charged particles that experience a strong Coulomb interaction with the surface of the material being probed, meaning that only shallow penetration and thus surface studies can be performed.

Neutrons have a spin of 1/2, and therefore can interact with unpaired electrons in the materials via dipole-dipole coupling. Whilst this is useful for researching magnetic properties of materials, for polymeric studies this magnetic interaction is generally ignored and only non-magnetic interactions are considered.

Table 2.1: Neutron Properties

Mass	1.675×10^{-27} kg
Charge	0
Spin	½
Magnetic moment	$-1.913\mu_N = -9.65 \times 10^{-27}$ J T^{-1}

Additionally, due to wave-particle duality, neutrons can be considered as a plane wave, with a wavevector $\boldsymbol{k}$ given by[v]:

$$\boldsymbol{k} = \frac{2\pi m}{h}\boldsymbol{v} \tag{2.1}$$

and wavelength:

$$\lambda = \frac{h}{mv} = \frac{2\pi}{|\boldsymbol{k}|} \tag{2.2}$$

where h is Planck's constant, m is the mass of a neutron, v is the velocity of the neutron and v is the magnitude of the velocity. Wave-particle duality also allows us to calculate the kinetic energy and the de Broglie wavelength from the following equations

$$E = \frac{1}{2}mv^2 = \frac{h^2}{2m\lambda^2} = = \frac{3}{2}k_B T \tag{2.3}$$

$$\lambda = \frac{h}{\sqrt{3mk_B T}} \tag{2.4}$$

where k_B is the Boltzmann constant and T is the temperature in Kelvin.

Neutrons are divided into three categories according to their energy and wavelength: hot neutrons, thermal neutrons and cold neutrons (Table 2.2). Neutrons

[v] Vectors are indicated in bold and relative moduli in plain text.

produced by a reactor or pulsed source are hot neutrons with high energy and velocity, thus these neutrons must be slowed down by a moderator before being used for scattering experiments. Thermal neutrons are most often used for scattering, although cold neutrons are often required for better spatial resolution in scattering experiments.

The temperature of the moderator determines the distribution of the neutrons, and this can be changed for different types of experiments. Moderators contain a high concentration of light elements such as hydrogen and deuterium. Each facility uses different materials, such as water (313K) and supercooled H_2 gas, heavy water (323 K) and liquid deuterium (25 K).

Table 2.2: Energy and wavelength of the three categories of neutrons.

Neutron	Temperature /K	Energy /meV	Wavelength /nm
Hot	1000 – 6000	100 – 500	0.04 – 0.1
Thermal	60 – 1000	5 – 100	0.1 – 0.4
Cold	1 – 120	0.1 – 10	0.4 – 3

2.2 Scattering experiment basics

Neutron scattering experiments have a similar basic schematic diagram to other scattering experiments, such as X-ray and electron scattering. A source emits incident particles which are fired towards the sample. Whilst the majority of the emitted particles are transmitted, a fraction of the particles are scattered which are then collected by a detector and the resulting pattern analysed. The schematic of a standard neutron scattering experiment is shown below (Figure 2.1).

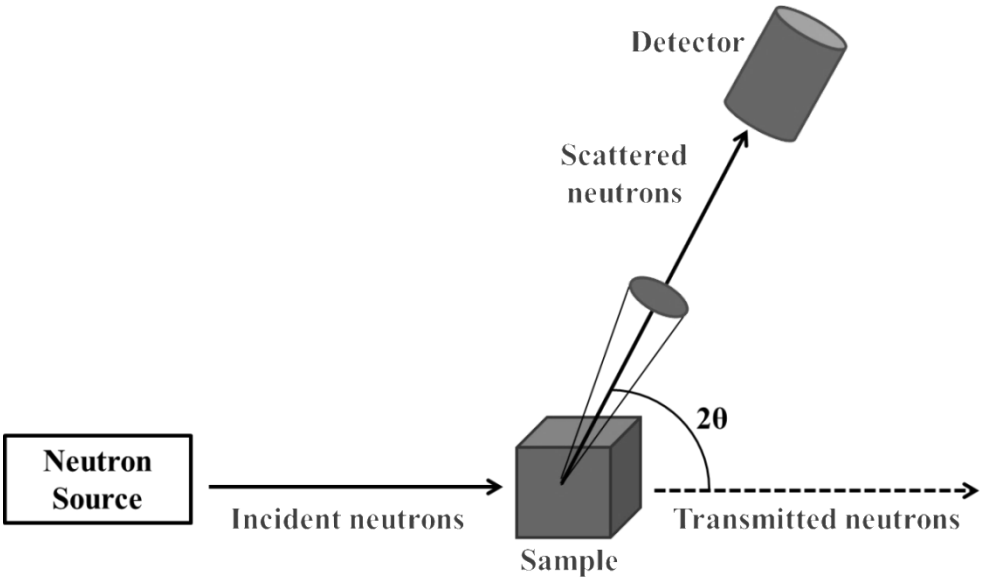

Figure 2.1: Schematic of a standard neutron scattering experiment.

Neutrons are produced by a neutron source, as detailed in Section 2.5.1. A monochromator allows neutrons with a specific energy/wavelength only to pass through and hit the sample. The majority of the neutrons are transmitted, however a fraction are scattered by the sample at a scattering angle, 2θ, and are picked up by a detector within a solid angle $d\Omega$. In general, the scattering intensity is measured as a function of energy and scattering angle.

There are three main types of neutron scattering experiments:

1. Elastic neutron scattering, where there is no energy exchange between neutrons and sample. This type of scattering is related to the correlation of scattering centres, and thus gives information on the structure of the material. Small-Angle neutron scattering (SANS) is an elastic scattering technique that is used to analyse the structure and conformation of materials such as polymers.
2. Inelastic neutron scattering, where there is energy exchange between the neutrons and sample. This scattering gives rise to discrete peaks in the energy spectrum. Inelastic scattering gives information on quantised motions, such as the vibrational and rotational modes of the sample.
3. Quasi-elastic neutron scattering (QENS), where there is a small energy exchange between the neutron and nuclei upon scattering. This results in a broadening of the elastic peak.

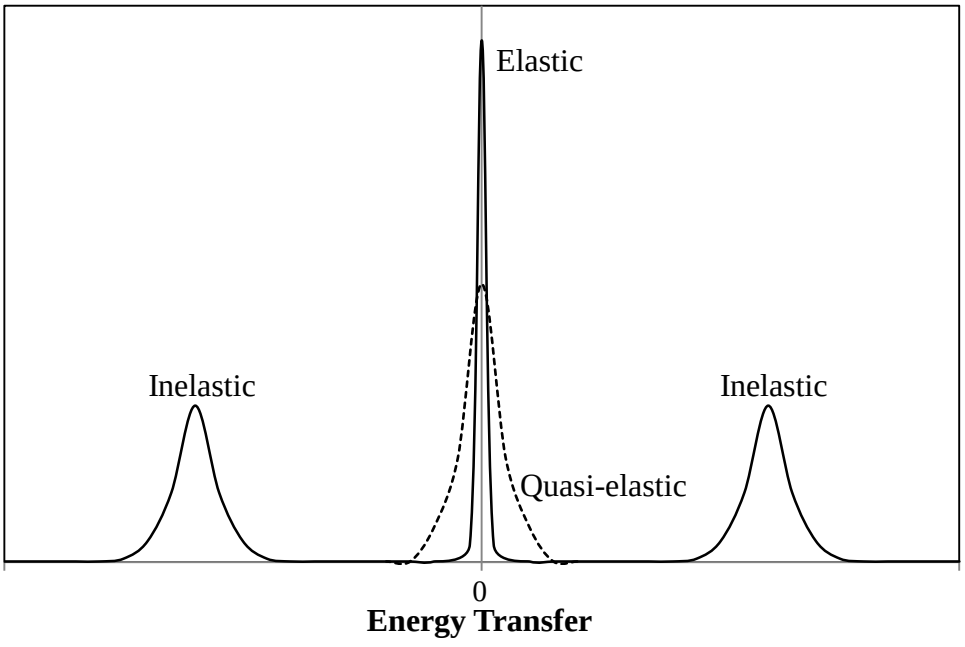

Figure 2.2: Representation of elastic, quasi-elastic and inelastic neutron scattering.

2.2.1 Momentum & energy transfer

Structural and dynamic information can be extracted from the scattered intensity as a function of the momentum transfer, *Q*. The momentum transfer is also the wavevector change, and so can be calculated from the incident and scattered wavevectors, k_f and k_i, respectively:

$$\boldsymbol{Q} = \left|\boldsymbol{k}_f - \boldsymbol{k}_i\right| \tag{2.5}$$

This is shown schematically in Figure 2.3:

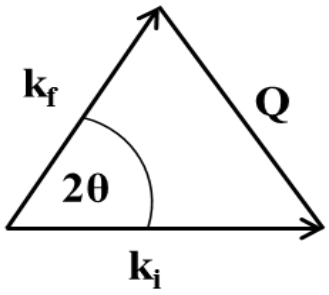

Figure 2.3: Definition for the momentum transfer, *Q*, in a scattering experiment from the incident wavevector, k_f, and scattered wavevector, k_i.

Inelastic scattering occurs when neutrons are scattered from molecules undergoing motions such as translation, vibration or rotation. The energy transfer is calculated from the change in kinetic energy using the following equations:

$$E_i = \frac{\hbar^2 {k_i}^2}{2m} \tag{2.6}$$

$$E_f = \frac{\hbar^2 {k_f}^2}{2m} \tag{2.7}$$

$$\Delta E = E_f - E_i = \hbar\omega = \frac{\hbar^2 (k_f - k_i)^2}{2m} \tag{2.8}$$

where ω is the angular frequency. Using Equation (2.1) and ħ = h/2π, the momentum transfer for inelastic scattering is:

$$\hbar Q = \hbar k_f - \hbar k_i \tag{2.9}$$

$$Q = \left(k_i^2 + k_i^2 - 2k_i k_f \cos(2\theta)\right)^{\frac{1}{2}} \tag{2.10}$$

The scattering is elastic when there is no or negligible energy change and therefore no wavelength change, i.e. $k_f = k_i$. This reduces the previous equation to the following equation for the momentum transfer:

$$Q = \frac{4\pi}{\lambda} sin\theta \tag{2.11}$$

Using Bragg's law,

$$d = \frac{2\pi}{Q} \tag{2.12}$$

which shows the inverse relationship between distance (d) and Q and thus scattering within small dimensions occurs at high Q and vice versa. This allows for selecting the Q range appropriate for the length scale to be investigated.

2.2.2 Cross section & scattering length

When a neutron collides with a nucleus, it can be either scattered or absorbed. The scattering cross section, σ_{sca}, and the absorption cross section, σ_{abs}, which is wavelength dependent, are defined as:

$$\sigma_{sca} = \frac{I_{sca}}{I_0} \tag{2.13}$$

$$\sigma_{abs} = \frac{I_{abs}}{I_0} \tag{2.14}$$

where I_{sca} is the number of scattered neutrons, I_{abs} is number of absorbed neutrons and I_0 is the incident flux of neutrons. The total cross section is the sum of the absorbed and scattered cross sections. The scattering cross section gives the probability of a neutron being scattered into one steradian per unit flux.

The neutron wavelength is orders of magnitude larger than the size of the nucleus it collides with. Therefore these nuclei are considered point scatterers and as a source for scattered waves. The scattered wave is characterised by the scattering length, b, which is unique to each type of nucleus (Table 2.3). The cross sectional area of nuclei is often given in the units of barns, which is equal to 10^{-28} m^2 or 100 fm^2, which is the SI unit. The scattering cross section is related to the scattering length through the following equation:

$$\sigma = 4\pi b^2 \tag{2.15}$$

Table 2.3: Scattering length and scattering cross section values for elements used in this project[203]

Element	b /fm	σ_{coh} /barns	σ_{inc} /barns	σ_{sca} /barns	σ_{abs} /barns
^{1}H	-3.74	1.76	80.26	82.02	0.33
^{2}H (D)	6.67	5.59	2.05	7.64	0.0005
C	6.65	5.55	0.001	5.55	0.0035
N	9.36	11.01	0.5	11.51	1.9
O	5.80	4.23	0	4.23	0.0002
Si	4.15	2.16	0.004	2.17	0.171

The cross sections listed in Table 2.3 only consider the scattering from a single neutron. However, the neutron-nucleus interaction also depends on the type of nucleus and the total spin-state of the neutron-nucleus system. Neutrons have a spin of ½, thus a neutron colliding with a nucleus of spin I will have a total spin of either I + ½ or I – ½. It follows that the scattering length in a sample varies, due to random nuclear spin and the presence of isotopes. The scattering intensity therefore contains a component arising from interference effects between waves scattered from different nuclei containing structural information, i.e. coherent scattering, and another from the randomness i.e. incoherent scattering.

Assuming no correlation between the *b* values of different nuclei, we can define two mean square values:

$$\langle b_i b_k \rangle = \langle b^2 \rangle \qquad \text{for j = k} \tag{2.16}$$

$$\langle b_i b_k \rangle = \langle b \rangle^2 \qquad \text{for j} \neq \text{k} \tag{2.17}$$

The average $\langle b \rangle$ of *b* over all spin states and isotopes is called the coherent scattering length (Equation (2.17)). The incoherent scattering length is the root mean square deviation of *b* from $\langle b \rangle$. This allows us to separate the total cross section into a coherent cross section, related to the mean value of the scattering length:

$$\sigma_{coh} = 4\pi \langle b \rangle^2 \tag{2.18}$$

and an incoherent cross section that occurs when there is variation in scattering length from the mean value:

$$\sigma_{inc} = 4\pi (\langle b^2 \rangle - \langle b \rangle^2) \tag{2.19}$$

The incoherent cross section has a value of zero if the nuclear spin is zero and the sample is heterogeneous. In the case of hydrogenated polymers, hydrogen has the largest incoherent cross section with respect to any other atom and therefore the scattering is almost entirely incoherent.

Neutron scattering experiments measure the double differential cross section, which is the probability of neutrons with incident energy *E* being scattered into the solid angle and this can be shown as:

$$\frac{\partial^2\sigma}{\partial\Omega\partial E} = \frac{1}{h}\frac{\partial^2\sigma}{\partial\Omega\partial\omega} \tag{2.20}$$

The double differential cross section can be related to the structure and motion of the scattering nuclei through quantum physics. The double differential cross section for a system of *N* nuclei can be written in terms of position $r_j(t)$ of all nuclei as a function of time, *t*:[204]

$$\frac{\partial^2\sigma}{\partial\Omega\partial E} = \frac{1}{2\pi}\frac{k_f}{k_i}\sum_j\sum_k b_j b_k \int_{-\infty}^{\infty} \langle e^{-i\boldsymbol{Q}\boldsymbol{r}_j(t)} e^{-i\boldsymbol{Q}\boldsymbol{r}_k(0)}\rangle\, e^{i\omega t} dt \tag{2.21}$$

where the angular brackets indicate a thermal average value. Using the mean square values defined in Equations (2.16) and (2.17), Equation (2.21) can be rewritten as:

$$\begin{aligned}\frac{\partial^2\sigma}{\partial\Omega\partial E} = {} & \frac{\langle b^2\rangle}{2\pi}\frac{k_f}{k_i}\sum_j \int_{-\infty}^{\infty} \langle e^{-i\boldsymbol{Q}\boldsymbol{r}_j(t)} e^{-i\boldsymbol{Q}\boldsymbol{r}_j(0)}\rangle\, e^{i\omega t} dt \\ & + \frac{\langle b\rangle^2}{2\pi}\frac{k_f}{k_i}\sum_j\sum_k \int_{-\infty}^{\infty} \langle e^{-i\boldsymbol{Q}\boldsymbol{r}_j(t)} e^{-i\boldsymbol{Q}\boldsymbol{r}_k(0)}\rangle\, e^{i\omega t} dt\end{aligned} \tag{2.22}$$

Using the definition of coherent and incoherent scattering lengths, the differential scattering cross section can then be separated into two terms, one for the coherent scattering and one for the incoherent scattering:

$$\frac{\partial^2\sigma}{\partial\Omega\partial E} = \left(\frac{\partial^2\sigma}{\partial\Omega\partial E}\right)_{coh} + \left(\frac{\partial^2\sigma}{\partial\Omega\partial E}\right)_{inc} \tag{2.23}$$

$$\left(\frac{\partial^2\sigma}{\partial\Omega\partial E}\right)_{coh} = \frac{{b^2}_{coh}}{2\pi}\frac{k_f}{k_i}\sum_j\sum_k \int_{-\infty}^{\infty} \langle e^{-i\boldsymbol{Q}\boldsymbol{r}_j(t)} e^{-i\boldsymbol{Q}\boldsymbol{r}_k(0)}\rangle\, e^{i\omega t} dt \tag{2.24}$$

$$\left(\frac{\partial^2\sigma}{\partial\Omega\partial E}\right)_{inc} = \frac{{b^2}_{inc}}{2\pi}\frac{k_f}{k_i}\sum_j \int_{-\infty}^{\infty} \langle e^{-i\boldsymbol{Q}\boldsymbol{r}_j(t)} e^{-i\boldsymbol{Q}\boldsymbol{r}_j(0)}\rangle\, e^{i\omega t} dt \tag{2.25}$$

The coherent scattering depends mainly on the correlation between the positions of different nuclei at different times, and in a dynamic experiment this gives information about the relative motion between nuclei *j* and *k*. The incoherent scattering depends on the correlation between positions of the same nuclei at different times, and therefore does not contain any information on the dynamics or structure of the sample.

2.2.3 Correlation functions

The thermal averages expressed in Equation (2.22) can be expressed in terms of correlation functions which were proposed by van Hove[204]. These functions give meaning to the scattering cross sections and can be used to calculate various properties of the scattering system. Firstly, we define the intermediate scattering function, $I(Q,t)$:

$$I(Q,t) = \frac{1}{N}\sum_{j,k} \langle e^{-i\boldsymbol{Q}\boldsymbol{r}_j(0)} e^{\ i\boldsymbol{Q}\boldsymbol{r}_k(t)} \rangle \tag{2.26}$$

where N is the number of scattering nuclei in the system. The intermediate scattering function is the spatial Fourier transform of the van Hove function. The inverse Fourier transform of $I(Q,t)$ is called the time-dependent pair-correlation function, $G(\boldsymbol{r},t)$. The pair correlation function is the probability density for finding an atom at time t at a distance r from the atom at $t = 0$.

$$G(\boldsymbol{r},t) = \frac{1}{(2\pi)^3}\int I(Q,t)e^{-i\boldsymbol{Q}\boldsymbol{r}}dQ \tag{2.27}$$

The scattering function is defined as:

$$S(\boldsymbol{Q},\omega) = \frac{1}{2\pi}\int_{-\infty}^{\infty} I(Q,t)e^{-i\omega t}dt \tag{2.28}$$

The Fourier transform $F(y)$ of a one-dimensional function $f(x)$ is related to the same function by[198]:

$$\begin{aligned} F(y) &= \frac{1}{2\pi}\int_{-\infty}^{\infty} f(x)e^{-ixy}dx \\ f(x) &= \int_{-\infty}^{\infty} F(y)e^{ixy}dx \end{aligned} \tag{2.29}$$

and the Fourier transform $F(\boldsymbol{s})$ for a three-dimensional function $f(\boldsymbol{r})$ is given by:

$$F(s) = \frac{1}{(2\pi)^3}\int_{-\infty}^{\infty} f(r)e^{-i\boldsymbol{s}\boldsymbol{r}}d^3r$$

$$f(r) = \int_{-\infty}^{\infty} F(s) e^{isr} d^3 s \tag{2.30}$$

Therefore, we can relate I(Q,t), G(r,t) and S(Q,ω) as follows:

$$I(Q,t) = \int G(r,t) e^{iQr} dr \tag{2.31}$$

$$S(Q,\omega) = \frac{1}{2\pi} \int_{-\infty}^{\infty} \int_{V} G(r,t) e^{i(Qr-\omega t)} dr dt \tag{2.32}$$

where *V* is the scattering volume[200]. Equation (2.32) shows that the scattering function *S(Q,ω)* is related to the pair correlation function. The incident particles can be considered as waves which interfere with the waves scattered by particles within the measured system. The phase difference between the two waves depends on the position of one particle at time *t* and the other particle at time 0, therefore the scattering depends on the pair correlation function, *G(**r**,t)*.

The above equations are used for coherent scattering as they arise from wave interference resulting from scattering from different nuclei. The incoherent scattering from the same nuclei is defined using the self-intermediate scattering function, self-correlation function and the incoherent scattering function:

$$I_s(Q,t) = \frac{1}{N} \sum_{j} \langle e^{-i\boldsymbol{Q}\boldsymbol{r}_j(0)} e^{-i\boldsymbol{Q}\boldsymbol{r}_j(t)} \rangle \tag{2.33}$$

$$G_s(\boldsymbol{r},t) = \frac{1}{(2\pi)^3} \int I_s(Q,t) e^{-i\boldsymbol{Q}\boldsymbol{r}} dQ \tag{2.34}$$

$$\begin{aligned} S_{inc}(\boldsymbol{Q},\omega) &= \frac{1}{2\pi} \int_{-\infty}^{\infty} I_s(Q,t) e^{-i\omega t} dt \\ &= \frac{1}{2\pi} \int_{-\infty}^{\infty} \int_{V} G_s(r,t) e^{i(Qr-\omega t)} dr\, dt \end{aligned} \tag{2.35}$$

The double differential cross section (Equation (2.23)) can then be rewritten as follows using Equations (2.24), (2.25) and the above definitions for coherent and incoherent scattering functions:

$$\frac{\partial^2 \sigma}{\partial \Omega \partial E} = \frac{1}{2\pi} \frac{k_f}{k_i} N [b^2{}_{coh} S_{coh}(Q,\omega) + b^2{}_{inc} S_{inc}(Q,\omega)] \tag{2.36}$$

The static approximation is applied when there is no energy change in the scattering event, i.e. elastic scattering. This means that the time dependence of the

system is disregarded. The double differential scattering cross section is reduced to $\delta\sigma/\delta\Omega$ and consists of a coherent and incoherent scattering part. In the static approximation, the static intermediate function and the static pair-correlation function are expressed as:

$$I(Q) = \frac{1}{N}\sum_{j,k}\langle e^{-i\boldsymbol{Q}\boldsymbol{r}_j} e^{\ i\boldsymbol{Q}\boldsymbol{r}_k}\rangle \tag{2.37}$$

$$G(\boldsymbol{r}) = \frac{1}{(2\pi)^3}\int I(Q)e^{-i\boldsymbol{Q}\boldsymbol{r}}dQ \tag{2.38}$$

The coherent scattering equation becomes:

$$\left(\frac{\partial^2\sigma}{\partial\Omega\partial E}\right)_{coh} = \frac{{b^2}_{coh}}{2\pi}\frac{k_f}{k_i}NS_{coh}(Q) \tag{2.39}$$

where $S_{coh}(Q)$ is the static coherent scattering function or structure factor.

In summary, in inelastic scattering the incoherent intensity is proportional to the space and time Fourier transforms of the pair-correlation function, *G(r,t)*. The coherent intensity of inelastic scattering is proportional to the Fourier transform of the time-dependent pair correlation function, *G(r,t)*. And finally, in elastic scattering the scattered intensity is proportional to the spatial Fourier transform of the static pair-correlation function, *G(r)*. Thus inelastic scattering gives information on dynamics of the system, whereas elastic scattering gives structural information.

2.3 Small-Angle Neutron Scattering (SANS)

Small Angle Neutron Scattering (SANS) has been shown to be a powerful technique for studying structure at length scales of nm to μm, which correlates with the atomic and molecular dimensions found in complex fluid systems[205]. Neutron radiation fired at a sample is elastically scattered and the resulting pattern can be analysed to provide a variety of different structural information present within a sample, from large scale molecular weight to local structure and chain statistics. This technique has been used extensively to probe structural information for pure polymers in dilute and concentrated solutions and in the bulk[200].

Recently, SANS experiments have been used to elucidate the changes in structure of polymer nanocomposites where the chains have been grafted to the surface

of the filler material such as polystyrene chains grafted to fullerene cores[206] and polymer chains grafted to silica[23, 121].

2.3.1 Overview

The measured scattered intensity, *I(Q)*, in a SANS experiment is related to the scattering cross section, δσ/δΩ, by the following equation:

$$I(Q) = I_0(\lambda) d\Omega \eta(\lambda) T(\lambda) V, \frac{\partial \sigma}{\partial \Omega}(Q) \quad \textbf{(2.40)}$$

where $I_0(\lambda)$ is the incident flux, $d\Omega$ is the solid angle, η(λ) is the detector efficiency, $T(\lambda)$ is the sample transmission and *V* is the volume of the sample illuminated by the neutron beam. $I_0(\lambda)$, $d\Omega$ and $\eta(\lambda)$ are instrument specific, the other terms are sample dependent and the scattering cross section is specific to SANS measurements. *I(Q)* is then calibrated to obtain data in absolute units, and contains all the information on the size, shape and interactions within the sample.

Neutron scattering from a sample consists of a coherent and an incoherent contribution. Coherent scattering arises from interference effects from waves scattered from different nuclei and contains the structural information. Incoherent scattering is independent of the scattering vector and gives no structural information. Subsequently, incoherent scattering is treated as a flat background that must be subtracted from the scattered intensity to obtain the coherent scattering intensity only. The various methods used for incoherent background subtraction are detailed extensively in Section 2.3.2.

Highly hydrogenated samples such as polymers have a high incoherent cross section and a low coherent cross section, leading to measurements with a high background and difficulty in extracting the structural information. By replacing the hydrogen atoms with deuterium, the coherent cross section is much higher, thus deuterated polymers are often used for SANS measurements. Deuterated components are dispersed in a hydrogenated medium, either hydrogenated polymer chains or solvent. Assuming an identical unit volume of the two components, the coherent differential cross section for a mixture containing hydrogenous and deuterated polymer chains is given by[200]:

$$\left(\frac{d\Sigma(Q)}{d\Omega}\right)_{coh} = (b_D - b_H)^2 S(Q) \quad \textbf{(2.41)}$$

where b_D and b_H are the scattering lengths of the deuterated and hydrogenated units respectively and *S(Q)* is the structure factor. In the small angle regime, the scattering unit for a polymer molecule is the monomer repeating unit.

The assumption that the scattering units have the same volume is correct when the system consists of a mixture of polymer chains with the same properties other than scattering length. If this is not the case then the scattering length will have to be adjusted by multiplying b_H or b_D by the ratio between the partial molar volumes of species H and D. This is used for polymer solutions containing a deuterated polymer and hydrogenated solvent or vice versa.

The structure factor, *S(Q)*, is made up of two components (Equation (2.42)): an intramolecular term, the form factor *P(Q)*, and an intermolecular factor *R(Q)*. *P(Q)* is the intramolecular interference due to the scattering by individual molecules and *R(Q)* arises from the interference between waves scattered by different molecules. *P(Q)* and *R(Q)* are normalised so that *P(Q=0)* and *R(Q=0)* are both equal to unity:

$$S(Q) = N_D z^2 P(Q) + N_D^2 z^2 P(Q) \tag{2.42}$$

where N_D is the number of deuterated chains per unit volume and z is the degree of polymerisation and:

$$P(Q) = \frac{1}{z^2} \sum_{i\alpha}^{z} \sum_{j\alpha}^{z} \langle e^{-\imath \boldsymbol{Q} \boldsymbol{r}_{ij}} \rangle \tag{2.43}$$

$$R(Q) = \frac{1}{z^2} \sum_{i\alpha}^{z} \sum_{j\beta}^{z} \langle e^{-\imath \boldsymbol{Q} \boldsymbol{r}_{i\alpha j\beta}} \rangle \tag{2.44}$$

By combining Equation (2.41) and (2.42), the coherent differential cross section for identical deuterated and hydrogenated chains can be written as:

$$\left(\frac{d\Sigma(Q)}{d\Omega}\right)_{coh} = I(Q) = (b_D - b_H)^2 N z^2 x(1-x) P(Q) \tag{2.45}$$

where N is the total number of chains per unit volume and x is the molar fraction of deuterated chains.

The scattering length density (SLD) is the scattering length per unit volume of the molecule and is useful for comparing the scattering properties of different samples. For a polymer, the molecule is the monomeric unit and is defined as follows:

$$\rho_{bi} = \frac{\Sigma b_i}{V_i} = \frac{\Sigma b_i \rho N_A}{m_o} \quad \textbf{(2.46)}$$

where Σb_i is the sum of the scattering lengths of all the constituent atoms in the monomer unit, V_i is the specific volume of the monomeric unit, m_o is the molar mass of the repeat unit, N_A is Avogadro's number and ρ is the density of the polymer. ρ_{bi} has dimensions of length^{-2} and is normally quoted in 10^{10} cm^{-2} or 10^{-6} Å^{-2} and can be a negative value when the molecule/polymer contains a large number of hydrogen atoms. Neutron contrast in SANS experiments originates from the differences in the scattering length densities of the deuterated and hydrogenated components.

2.3.2 Incoherent background subtraction

Background intensity resulting from incoherent scattering in the sample must be subtracted from the sample intensity in order to carry out quantitative analysis. Therefore, it is essential that the level of incoherent scattering be estimated as accurately and systematically as possible in order for good quality data analysis. There are many literature methods for subtracting the incoherent background, with varying advantages and disadvantages to each.

For deuterated polymer chains in very dilute solution (c << c*), subtracting the solvent is usually sufficient to remove the background incoherent scattering[207]. However, in more concentrated solutions and hydrogenated polymer chain solutions, there may be additional incoherent scattering from the chains that must be subtracted before analysis.

One method is fitting the data to the form factor model with an adjustable background constant as an added variable, allowing the program used to fit the background to obtain the best value. However, this method is not systematic, and in practice often proved unreliable. Background levels were often underestimated or overestimated, leading to negative and unphysical background intensity values.

Another method for determining the incoherent background is by subtracting the scattered intensity value at high Q, where the coherent scattering contribution generally is negligible in soft condensed matter and thus the scattering can be assumed to be mainly incoherent[207]. However, this method has a number of problems: 1) the scattering at high *Q* may still contain some coherent scattering, 2) the incoherent scattering may

not be *Q* independent and 3) the background will be overestimated if the scattering intensity has not reached a constant value at the highest *Q* range of the instrument used.

A commonly used method used is the transmission method proposed by Hayashi *et al.*[208], which uses the incoherent cross section of hydrogen, σ_{inc}^{H}, to calculate the scattering from a hydrogenous polymer. The incoherent transmission value can be calculated by the following equation:

$$T_{inc}^{cal} = exp(-\sigma_{inc}^{H} N_H t_H) \tag{2.47}$$

where T_{inc}^{cal} is the calculated transmission, N_H is the number of protons per unit volume and t_h is the sample thickness. The incoherent scattering is assumed to be equally distributed over 4π steradians and proportional to (1 -T_{inc}^{cal}) and:

$$I_{H,inc} = \Phi_0 A_S \frac{1 - T_{inc}^{cal}}{4\pi} = \Phi_0 A_S \frac{1 - \exp(\sigma_{inc}^{H} N_H t_h)}{4\pi} \tag{2.48}$$

The measured experimental transmission value (T_{inc}^{exp}) can be used instead of the calculated value and the incoherent scattering contribution can be calculated by the following equation:

$$I_{H,inc}^{m} = \Phi_0 A_S \frac{1 - T_{inc}^{exp}}{4\pi} = \Phi_0 A_S \frac{1 - \exp(\sigma_{inc}^{m} N_H t_h)}{4\pi} \tag{2.49}$$

where Φ_0 is the incident beam intensity per unit area, A_s is the sample area, σ_{inc}^{m} is the measured incoherent scattering cross section, N_H is the number of protons per unit volume and t_h is the sample thickness. This method is only suitable for fixed wavelength instruments as transmission is wavelength dependent. Data analysis on experiments carried out on SANS instruments which use a variable wavelength when measuring the scattering intensity, such as LOQ at ISIS, cannot use any subtraction methods based on a constant transmission value.

If the samples being measured are H/D mixtures, the incoherent scattering intensity can be calculated using the following methods. One method is closely related to the transmission method and uses the following relationship to determine incoherent scattering[208]:

$$I_{inc} = \frac{1 - \exp(-\sigma_{inc}^{H} N t_s)}{1 - \exp(-\sigma_{inc}^{H} N_H t_H)} I_{H,inc} \tag{2.50}$$

where N is the number of protons per unit volume in the mixture and t_s is the sample thickness. This form has the same problem as Equation (2.48), as it uses the calculated values of incoherent cross sections for bound atoms, which does not take into account that incoherent cross section is proportional to wavelength[209]. Thus, lower errors can be achieved by using the measured values for transmission and the equation rewritten in the following form:

$$\left(\frac{d\Sigma}{d\Omega}\right)_{i,s} = \frac{1-T_s}{1-T_H}\frac{t_H T_H}{t_s T_s}\left(\frac{d\Sigma}{d\Omega}\right)_{i,H} = B\left(\frac{d\Sigma}{d\Omega}\right)_{i,H} \quad \textbf{(2.51)}$$

where T_s and t_s are the transmission and thickness and T_H and t_H are the transmission and thickness of the hydrogenated polymer. As with the transmission method for pure polymers, this method is only suitable for fixed wavelength instruments such as the SANS instrument D22 at ILL.

The other main method for H/D mixtures is to calculate the incoherent scattering as a proportion of the normalised incoherent scattering cross section (cm^{-1}) of the pure deuterated polymer, $(d\Sigma/d\Omega)_{i,D}$, and the hydrogenous polymer, $(d\Sigma/d\Omega)_{i,H}$ in the mixture[210]:

$$\left(\frac{d\Sigma}{d\Omega}\right)_{i,s} = \Phi\left(\frac{d\Sigma}{d\Omega}\right)_{i,D} + (1-\Phi)\left(\frac{d\Sigma}{d\Omega}\right)_{i,H} \quad \textbf{(2.52)}$$

where Φ is the volume fraction of the deuterated component. This linear combination method is also suitable for H/D mixtures where one of the components is the solvent, i.e. hydrogenous chains in deuterated solvent or vice versa. When a fully deuterated polymer sample is used, the incoherent background is often considered negligible and the first term of the above equation is omitted.

2.3.3 Form Factors and Models for Polymer Analysis

The scattering of molecules in SANS experiments are represented by the form factor *P(Q)*, which depends on the size and shape of the molecules. SANS data cannot give information directly on the conformation, instead a suitable model has to be applied to the data. Various analytical expressions have been developed to describe the form factors of scattering objects of a variety of shapes, from simple (spheres, rods) to far more complex expressions (core-shell). Choosing the correct model for data analysis requires some idea of the structure of the material, often through other experimental techniques and computational modelling.

The simplest model is that of a monodisperse sphere[211]:

$$P(Q) = \left[\frac{3(\sin(QR) - QRcos(QR)}{(QR)^3}\right]^2 \quad \textbf{(2.53)}$$

In the work presented in this thesis, polymer nanocomposites and corresponding linear polymer chains are analysed by neutron scattering. For linear polymers, the standard Gaussian polymer chain form factor using the Debye formula[200] (Equation (2.54)) is used to fit the variation in scattered intensity:

$$P(Q) = \frac{2}{x^2}[x - 1 + \exp^{-x}] \quad \textbf{(2.54)}$$

where $x = q^2R_g^2$, and R_g is the radius of gyration of a single chain. Excluded volume effects are not considered by the simple Debye formula, thus an additional Flory exponent, *v*, in an adjusted equation for linear polymers was introduced by Benoit[212]:

$$P(Q) = 2\int_0^1 dx\,(x-1)\exp\left[-\frac{Q^2a^2}{6}n^{2\nu}x^{2\nu}\right] \quad \textbf{(2.55)}$$

This expression was then converted into an analytical form by Hammouda[213]. This model is included in the analysis program SasView under PolymerExclVol using the form factor[214]:

$$P(Q) = \frac{1}{\nu X^{1/2\nu}}\gamma\left(\frac{1}{2\nu}, X\right) - \frac{1}{\nu X^{1/\nu}}\gamma\left(\frac{1}{\nu}, X\right) \quad \textbf{(2.56)}$$

where $X = (Q^2R_g^2(2\nu+1)(2\nu+2))/6$ and $\gamma\left(\frac{1}{\nu}, X\right)$ is the incomplete gamma function:

$$\gamma\left(\frac{1}{\nu}, X\right) = \int_0^X e^{-y}y^{x-1}dy \quad \textbf{(2.57)}$$

When the polymer acts as Gaussian chains ($\nu = 0.5$), this model simplifies to the Debye equation (2.54).

More complex models are required for polymer nanocomposite materials which contain more than one component. Model polymer nanocomposites with well-defined numbers and molecular weights of arms have been considered as star polymers with a hard centre in the literature[123]. The typical model used to fit the form factor of star polymers is the Gaussian star form factor[215] described by the Benoit function:

$$P(Q) = \frac{2}{fv^4}\left[v^2 - 1 + \exp^{-v^2} + \frac{f-1}{2}\left[1 - \exp^{-v^2}\right]^2\right] \quad \textbf{(2.58)}$$

$$v = \sqrt{\frac{f}{3f-2}}\, QR_{star} \quad \textbf{(2.59)}$$

where f is the number of arms and R_{star} is the radius of gyration of the star. The radius of gyration of a single arm, R_a can be calculated from R_{star} using the following relationship[216]:

$$R_a = \sqrt{\frac{f}{3f-2}}\, R_{star} \quad \textbf{(2.60)}$$

2.3.4 Guinier, Kratky and Zimm Plots

A double logarithm or log-log plot of the experimental data is a useful method of determining Q dependence and therefore choosing an appropriate model for the data analysis. Three regions can be distinguished on a log-log plot (Figure 2.4).

1. The low-Q Guinier region, which consists of a plateau at low Q that depends on concentration, M_w and degree of aggregation.
2. An exponential decay at intermediate Q called the intermediate-Q Guinier region. Using Guinier's law[211] (Equation (2.61) below), a plot of $\log(d\Sigma(Q)/d\Omega)$ against Q^2 in the Guinier region gives a straight line with a slope of $-(R_g^2/3)$. This is known as a Guinier plot. Thus this region allows us to determine the size of the polymer chains.
3. Finally, the high Q region, with a linear decay of the scattered intensity. The slope is usually quoted as Q^{-n}, and gives an indication of the behaviour of the polymer chains in solution: n=2 for Gaussian chains in a dilute environment, 5/3 for fully swollen chains and 3 for collapsed polymer chains.

Thus, a double logarithm plot can be used to determine molecular weight, radius of gyration and potential solution behaviour of the chains.

$$I(Q) = I_0 exp\left(-\frac{Q^2 R_g^2}{3}\right) \quad \textbf{(2.61)}$$

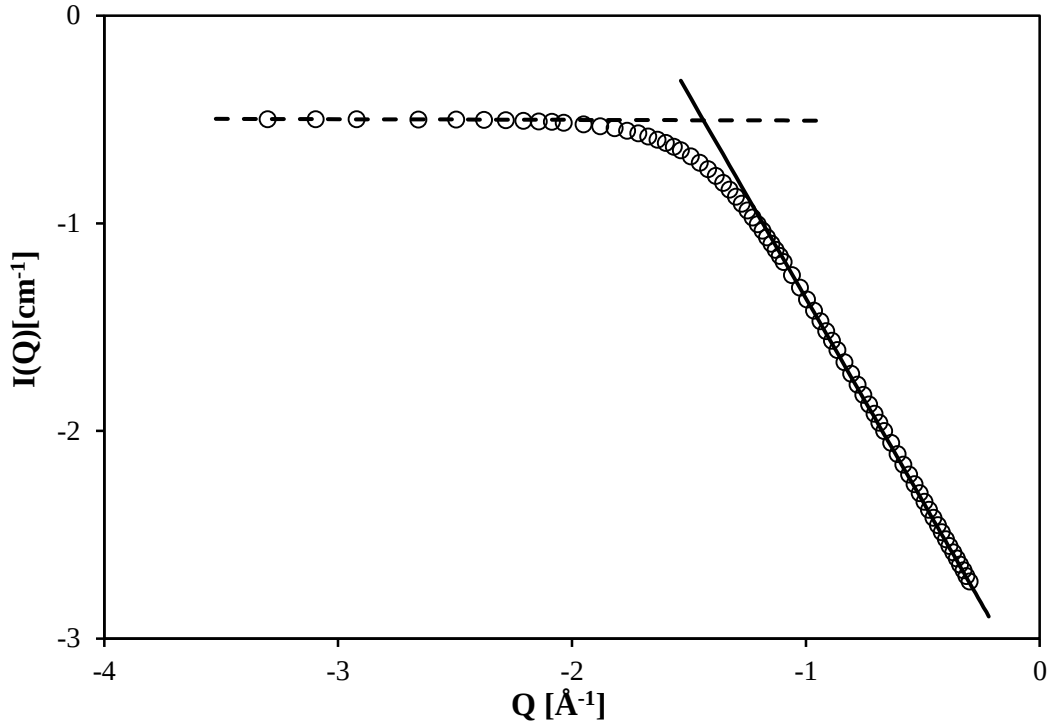

Figure 2.4: Schematic of a log-log plot showing the three distinct regions of scattered intensity. The dashed line represents the slope of the Guinier region, whereas the solid line represents the slope of the high *Q* region.

Another common method used to determine the radius of gyration is to use the Zimm equation and plot. At low *Q* (within the Guinier range), the Debye model can be reduced to the Guinier equation (2.61). Expanding the form factor into a power series leads to the following equation[217]:

$$\frac{1}{P(Q)} = \left[1 + \frac{Q^2 R_g^2}{3} + \dots\right] \tag{2.62}$$

Combining Equations (2.62) and (2.45) allows for calculation of R_g by plotting the inverse of the scattered intensity against Q^2. This is called a Zimm plot and was originally developed for light scattering measurements but has since been used for neutron scattering data analysis:

$$\begin{aligned} I(Q)^{-1} &= [(b_D - b_H)^2 N z^2]^{-1}\left[1 + \frac{Q^2 R_g^2}{3} + \ \dots\right] \\ &= \frac{{m_0}^2}{(b_D - b_H)^2 M \rho N_A}\left[1 + \frac{Q^2 R_g^2}{3} + \ \dots\right] \end{aligned} \tag{2.63}$$

where the degree of polymerisation, *z*, has been substituted by molar mass over mass of monomer or repeat unit (M/m_0) and the total number of molecules, *N*, by ($N_A\rho/M$),

where ρ is the density. The resulting straight line has a slope related to the radius of gyration and the intercept at Q=0 can be used to determine molar mass:

$$intercept = \left(\frac{m^2}{(b_D - b_H)^2 \rho N_A}\right)\frac{1}{M}$$
$$slope = \left(\frac{intercept}{3}\right)R_g^2 \quad \textbf{(2.64)}$$

The scattering function from a polymer in solution is affected by the concentration. According to Zimm[217] and using a virial expansion,[200] the scattered intensity as a function of Q and c can be given as:

$$\frac{Kc}{I(Q=0)} = \frac{1}{MP(Q)} + 2A_2c + \ \ldots \quad \textbf{(2.65)}$$

where K is a constant, c is the concentration, A_2 is the second virial coefficient which characterises the average interparticle interactions. The value of A_2 can be extracted from a Zimm plot of $c/I(Q)$ against c.

The above equations and the Zimm plot apply in the low Q range. In the high Q range ($Q \geq 5/R_g$), a Kratky plot gives detailed information on the chain architecture[218]. A Kratky plot is a plot of $I(Q)Q^2$ against Q , which for a linear chain should reach a plateau value with increasing Q as the Debye equation (2.54) for a linear chain can be approximated to:

$$I(Q) = \frac{(b_D - b_H)^2 \rho N_A M}{m^2 Q^2 R_g^2} \quad \textbf{(2.66)}$$

Deviations from this behaviour have been seen in cyclic[219], branched[220], star and ring[200] polymers, e.g. a 'hump' is seen at intermediate Q values before the plateau of the linear polymers. As such, the shape of the Kratky plot can be used to determine the architecture of the polymer chains. However, high Q data has a high scattering intensity and is noisy compared to low Q data and thus distinguishing between different Kratky plots can be difficult.

2.3.5 Contrast Matching

Contrast matching is a useful technique for analysing objects with two or more distinct subunits that have different scattering length densities, such as core-shell particles. This technique relies on hydrogen and deuterium atoms having different scattering length

values (-3.74 and 6.67 fm respectively). Replacing hydrogen atoms with deuterium greatly changes the SLD value with generally negligible effects on the physical chemistry of the molecule[199]. Therefore, the SLD of a component can be systematically varied by selective deuteration, and the point at which the SLD of one component is equal to the SLD of another is called the contrast match point.

An example of a contrast matching experiment of a ternary core-shell particle is shown in Figure 2.5. By matching the SLD of the solvent to one of the components and making it essentially invisible (e.g. the core in Figure 2.5 (b) and the shell in Figure 2.5 (c)), the scattering from the other component can be analysed as if it were in a binary mixture[199]. This allows us to measure the scattered intensity resulting from each component separately as well as the total scattered intensity (Figure 2.5(a)).

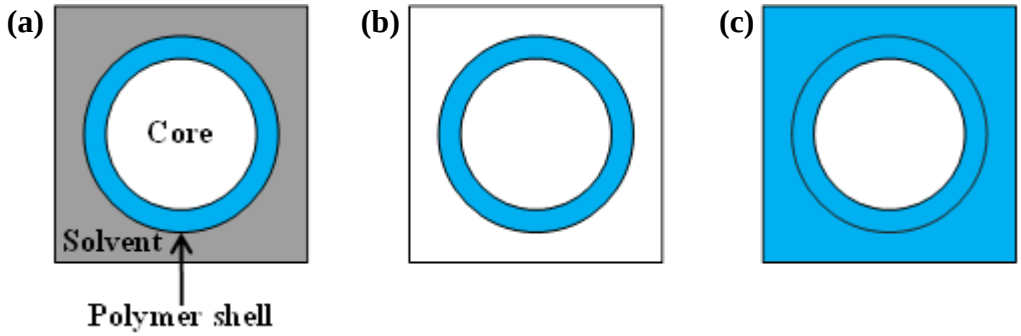

Figure 2.5: An illustration showing the different contrast matching conditions (a) core, shell and solvent SLD are all different, (b) solvent matches the core and (c) solvent matches the polymer shell

The easiest and least expensive way to perform a contrast matching experiment is to use a mixture of deuterated and hydrogenated solvent. Approximate contrast matching conditions can be determined using the calculated scattering length densities (Equation (2.46)) of the components and the deuterated and hydrogenated solvent. The polymer chains can also be partially or fully deuterated for contrast matching experiments, however deuterated polymers and monomers are expensive and deuteration methods for monomers and polymers are often time consuming and difficult. However, the advantage of using deuterated polymers is that the scattering is mostly coherent, rather than mostly incoherent as it is in hydrogenated polymers. Additionally, neutron experiments are generally non-destructive, allowing for recovery of the deuterated polymers.

In this project, contrast matching was used in SANS measurements of polymer-silica samples to remove the silica scattering contribution and thus analyse the

scattering from the polymer chains alone (Figure 2.5(b)). This technique has also been used in the literature of similar dispersed nanocomposites to monitor the silica nanoparticle dispersion by contrast matching the chains to the solvent[121].

2.3.6 Polymer Blend analysis

The final part of the work presented in this thesis is a study of the structure and phase separation in polymer blends containing nanofillers. The analysis on one-phase blends will focus on the Random Phase Approximation (RPA) developed by de Gennes[221] whereas two-phase blends are analysed using the Debye-Bueche[222] or Porod models[223].

Equation (2.45) gives the coherent scattered intensity when the hydrogenated and deuterated chains are identical. If the two components are different polymers with different molecular weights and degree of polymerisation, as in a polymer blend, the equation can be generalised to:

$$\frac{(b_D - b_H)^2}{I(Q)} = \frac{1}{N_H z_H^2 P_H(Q)} + \frac{1}{N_D z_D^2 P_D(Q)} \tag{2.67}$$

This equation assumes that the volumes for the two monomers are equal, however that might not be the case with two different monomers. Thus, ($b_D - b_H$) can be replaced by:

$$\Delta b_{eff} = \nu_0 \left(\frac{b_H}{\nu_H} - \frac{b_D}{\nu_D}\right) \tag{2.68}$$

where ν_H and ν_D are the volumes of the H and D monomer respectively and ν_0 is the reference volume:

$$\nu_0 = \sqrt{\nu_H \nu_D} \tag{2.69}$$

Assuming the density of the polymer remains the same upon mixing, the scattering unit volumes can be calculated as follows:

$$\nu_H = \frac{m_H}{\rho_H N_A}$$
$$\nu_D = \frac{m_D}{\rho_D N_A} \tag{2.70}$$

where m_H and m_D are the molar mass of the H and D monomer respectively.

The effect of deuteration on the thermodynamics of H/D mixtures and interactions between the two components must also be taken into account[200]. Therefore Equation (2.67) is modified as follows:

$$I(Q) = \frac{\left(\Delta b_{eff}\right)^2}{v_0}\left[\frac{1}{N_H z_H^2 P_H(Q)} + \frac{1}{N_D z_D^2 P_D(Q)} - 2\chi\right]^{-1} \quad \textbf{(2.71)}$$

where the form factors for the polymers, $P_H(Q)$ and $P_D(Q)$, are appropriate model functions and χ is the polymer-polymer interaction parameter.

RPA analysis is only appropriate for blends in the one-phase region. When the blend has phase separated, other models are used to describe the scattering. One of these, the Debye-Bueche model[222] describes the scattering behaviour of a two-phase system using a two-point correlation function:

$$\gamma(r) = \frac{\langle \rho_A \rho_B \rangle}{\langle \rho^2 \rangle} \quad \textbf{(2.72)}$$

where ρ_A and ρ_B are the local deviations of the SLD from the average value $\langle \rho^2 \rangle$ at points A and B, separated by distance r. If the two phases are randomly distributed and have irregular shape and size, the correlation function is given by:

$$\gamma(r) = exp\left(-\frac{r}{\zeta}\right) \quad \textbf{(2.73)}$$

where ζ is the correlation length.

By Fourier transforming the exponential correlation function, the differential cross section is obtained[224]:

$$\frac{d\Sigma(Q)}{d\Omega} = \frac{K\langle \rho^2 \rangle \xi^3}{(1 + Q^2\xi^2)^2} \quad \textbf{(2.74)}$$

where $K = 8\pi\Phi(1\text{-}\Phi)$ and Φ and $(1\text{-}\Phi)$ are the volume fractions of the two components. A plot of inverse square root of the differential cross section against Q gives a straight line, from which the correlation length can be derived.

In two-phase systems with sharp boundaries, the high Q scattering follows Porod's law with a Q^{-4} dependence:

$$I(Q) = \frac{2\pi\ \Delta\rho\ S_v}{Q^4} + bkg \quad \textbf{(2.75)}$$

where $\Delta\rho$ is the contrast factor and S_v is the specific surface area (surface area/volume). Deviations from Porod's law occurs when the phase boundaries are diffuse.

2.3.7 Small-Angle X-Ray Scattering (SAXS)

SAXS is comparable technique to SANS, due to X-rays having some similar properties to neutrons, such as a wavelength (~1Å) comparable to interatomic distances. However, there are key differences between the X-rays and neutrons that often result in SAXS and SANS being complementary techniques to each other[199]. For example, X-ray sources have higher fluxes than neutron sources, and X-rays are sensitive to inhomogeneities in electron density rather than nuclei density fluctuations. One of main differences is the energy of the particles. X-Rays have a higher energy (~10 keV) than neutrons (~10 meV), which is an important factor in inelastic scattering.

A disadvantage of SAXS is that there is no contrast between H and D atoms as is seen in neutron scattering, as the X-ray scattering length is correlated to the atomic number. The use of H/D labelling is often crucial in polymer nanocomposites experiments for measuring the different components of the samples separately by contrast matching experiments. Labelling of samples for SAXS measurements involves heavy metal atom labels, which can change the properties of the sample. A combination of SANS and SAXS measurements can provide a more complete structural study than either technique alone.

2.4 Quasi-elastic Neutron Scattering (QENS)

Quasi-elastic neutron scattering (QENS) is a powerful technique for studying the dynamics of polymers on molecular length scales (1 to 10 Å) and microscopic times (ps to ns). This allows us to probe dynamic processes such as side group rotations. Neutron scattering allows for measuring both protonated and partially or fully deuterated polymer chains in order to study a variety of different molecular motions. QENS has been used extensively to study polymer chains, initially focusing on polymers in dilute and concentrated solutions[200]. Polymer nanocomposites are a more recent area of research, with most studies concentrating on dispersed polymer nanocomposites[129, 130] and a few more recent studies on grafted nanocomposites[225].

2.4.1 Overview

The various motions of polymer chains occur over a large range of time scales, from slow reorientation of chains above the glass transition temperature to the torsion and vibration of side groups (~10^{14}Hz). Quasi-elastic neutron techniques are used to

investigate the upper end of the frequency range (>10^7Hz) to measure vibrations and rotations of the side groups, and high frequency motions of the backbone[200]. Neutron Spin Echo (NSE) experiments can further expand the range of motions that can be investigated using neutron techniques.

Molecular vibrations give rise to discrete peaks in the inelastic spectrum; however rotations and translations have small energy exchanges which occur as a broadening of the elastic peak.

QENS measurements measure the scattering intensity as a function of energy transfer and scattering vector, $S(\boldsymbol{Q},\omega)$. For hydrogenated polymers, QENS measurements are dominated by the incoherent scattering of hydrogen. QENS spectra are therefore analysed by using a suitable model function and fitting to the data. The measured scattering law, $S_{meas}(\boldsymbol{Q}, \omega)$, is a convolution of the resolution function of the spectrometer with the simple scattering vector:

$$S_{meas}(\boldsymbol{Q},\omega) = R(\boldsymbol{Q},\omega) \otimes S(\boldsymbol{Q},\omega) \quad \textbf{(2.76)}$$

There are three main time and length scales that can be measured by neutron scattering:

1. Short time scales (ps to ns) and lengths (~1 – 10 Å): at these lengths, local bond dynamics are observed.
2. Intermediate lengths (20 – 100 Å) and times (>1ns): This regime is characterised by the Rouse dynamics as the chemical structure of the chain is no longer important and only the topology of the chains is considered. QENS measurements are confined to the shorter length scale motions in this region, whereas NSE has access to the larger length scale motions.
3. Longer times and lengths: Interpenetration of the polymer coils confines topology and causes entanglement constraints. This leads to the reptation process (Section 1.3.5) which can be observed by NSE techniques.

The following sections discuss the theory and models behind the analysis of the dynamics of polymer chains using QENS, starting with the separations of the different motions.

2.4.2 Separation of Motions

A typical spectrum resulting from a QENS experiment consists of three components: (1) an elastic peak resulting from the slow motions that cannot be resolved by the

instrument, (2) a quasielastic broadened peak resulting from the molecular motions resolved by the instrument and (3) a flat background caused by the motions that are too fast to be detected by the instrument.

For the quasielastic and inelastic components caused by motions, the translational, rotational and vibrational motions of polymer chains can be separated by expressing the time dependent position vector, ***R(t)***, in terms of three component vectors:

$$\boldsymbol{R}(t) = \boldsymbol{c}(t) + \boldsymbol{r}(t) + \boldsymbol{u}(t) \quad \textbf{(2.77)}$$

where *c(t)* describes the position of the centre of mass, *r(t)* is for rotations around the centre of mass and *u(t)* is the displacement of the nucleus from its average position.

Assuming dynamic independence of the motions, thermal averaging over the different motions can be made separately and the intermediate scattering law can be written as a product of the intermediate scattering functions associated with each component of the motions:

$$I_{inc}(Q,t) = I_{tr}(Q,t) \times I_{rot}(Q,t) \times I_{vib}(Q,t) \quad \textbf{(2.78)}$$

If the motion of the scattering nucleus is well located or restricted, such as reorientation of molecules around their centre of mass, then the incoherent intermediate scattering function tends to a non-vanishing value. It is therefore possible to separate the intermediate scattering function into a time-independent part, $I_{inc}(Q,\infty)$, and a time dependent part, $I^{*}_{inc}(Q,t)$. This separation is crucial, as the time-independent part is a constant term and as such gives rise to a purely elastic component when the raw data is Fourier transformed:

$$I_{inc}(Q,t) = I_{inc}(Q,\infty) + I^{*}_{inc}(Q,t) \quad \textbf{(2.79)}$$

The elastic component of the QENS spectra is called the Elastic Incoherent Structure Factor (EISF). Samples with translational disorder do not show any elastic peak, thus the presence of an elastic peak shows that there are scattering centres within the sample that are localised in space.

If the intermediate scattering function shows a simple exponential decay with characteristic time, τ, then the Fourier transform is represented by a Lorentzian function. The half width at half maximum (HWHM) of the Lorentzian in energy units is equal to

1/τ. Therefore the width and shape of the quasielastic peak is directly related to the characteristic time of the relevant motions of the polymer chains.

The Fourier transform of the intermediate scattering function leads to the incoherent scattering function, $S_{inc}(Q,\omega)$, which can be given by the convolution product of the scattering functions of the different motions:

$$S_{inc}(Q,\omega) = S_{tr}(Q,\omega) \otimes S_{rot}(Q,\omega) \otimes S_{vib}(Q,\omega) \quad \textbf{(2.80)}$$

The thermal averages for $S_{tr}(Q,\omega)$ and $S_{rot}(Q,\omega)$ can be evaluated with classical mechanics, however $S_{vib}(Q,\omega)$ is calculated from quantum mechanics. $S_{vib}(Q,\omega)$ can be separated into an elastic and an inelastic component:

$$S_{vib}(Q,\omega) = e^{-2W(Q)}\left(\delta(\omega) + S_{vib}^{inel}(Q,\omega)\right) \quad \textbf{(2.81)}$$

The calculation of the elastic component leads to the Debye-Waller effect. The Debye-Waller factor is introduced in the above equation:

$$2W(Q) = \langle u^2 \rangle Q^2 \quad \textbf{(2.82)}$$

where $\langle u^2 \rangle$ is the mean square displacement of the scattering nuclei under the effect of internal molecular vibrations. The function $S_{vib}^{inel}(Q,\omega)$ is related to the density of states for lattice vibrations and gives rise to scattering with energy transfer values up to 20 meV. In the quasi-elastic region, the Debye-Waller effect is often weak and leads to the flat background seen in the spectra[201].

Due to motions occurring on different time and length scales, the separation and analysis of the different motions is achieved by measuring the sample at various *Q* and energy ranges on different instruments. Measuring the sample at different temperatures on a single instrument and using Time-Temperature Superposition (TTS) or Elastic Window Scans (EWS) measurements can separate out the different motions that occur in different temperature ranges, which will be explained further in the next Sections.

2.4.3 Elastic Window Scans

Elastic Window Scan (EWS) is a technique that measures the decrease of elastic intensity as a function of temperature and momentum transfer, *Q*. The data is collected by integrating scattered intensity within a narrow energy interval around the elastic peak (Figure 2.6)[226, 227]. More recently, studies are also integrating the scattered intensity in

the wings of the quasi-elastic broadening as more information can be obtained from the full spectrum than from the elastic intensity alone[228]. High resolution QENS instruments such as IN10 and IN16B at ILL are often used for this type of experiment due to their narrow energy window and high energy resolution.

The scattered intensity measured in QENS experiments is composed of different rotational, vibrational and translational motions. The contribution from these motions can be observed at different temperatures in elastic window scan measurements.

At very low temperatures (<50 K), the scattered intensity arises from inelastic intramolecular vibrations as molecular motion is "frozen in". These motions are taken into account by the Debye-Waller factor. As the temperature increases below the glass transition temperature (T_g), side group rotations and other local motions are observed, causing a broadening in the elastic peak. As the temperature approaches T_g, segmental main chain motions appear as a decrease in the elastic intensity. Finally, above T_g there is a significant loss of elastic intensity as the polymer starts to flow and the molecular motions become faster and contribute to inelastic rather than elastic scattering.

Figure 2.6 shows that the quasielastic broadening increases and the peak height (and thus elastic scattering intensity) decreases as temperature increases. The elastic scattering, $S_{inc}(Q,\omega=0)$ is a function of temperature, and the temperature dependence of the scattered intensity can be determined. Therefore, elastic window scans can give information on the different motions of polymer chains through measurement and analysis of the temperature dependence of the elastic scattering intensity.

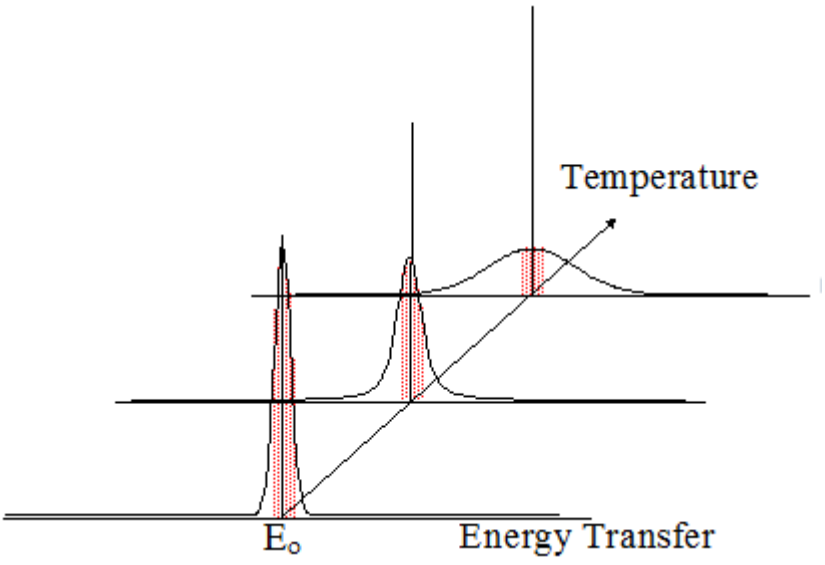

Figure 2.6: Representation of the integration of scattered intensity within a narrow energy interval around E_0 to create an elastic window scan data set.

2.4.4 Side Group Rotation

Side group rotations and vibrations can also be analysed by QENS due to their large amplitude and the possibility of selective deuteration. This is useful because torsions and vibrations of polymer side-groups such as methyl groups can be difficult to study by conventional light-spectroscopy. The most commonly measured side-group motion is methyl group rotations and torsions and they have been studied extensively in a variety of polymers; PMMA[229], PDMS[230], PVME[231] etc.

The rotational motion of side groups is influenced by the interactions with neighbouring atoms and groups. Assuming a particle can be rotated into two positions, 1 or 2, when rotating it must 'jump' through an energy barrier from 2 to 1 or 1 to 2. If there are more preferred orientations then there are more potential energy barriers the molecules can jump over. If the potential energy barrier is large compared to the rotational energy levels then the molecule is trapped in its orientation and only small angular oscillations called librations occur. A schematic representation of this jump model for 3 potential orientations is shown in Figure 2.7. As the temperature increases, the molecules have more energy and thus they can jump over the energy barriers and rotation of the side group occurs.

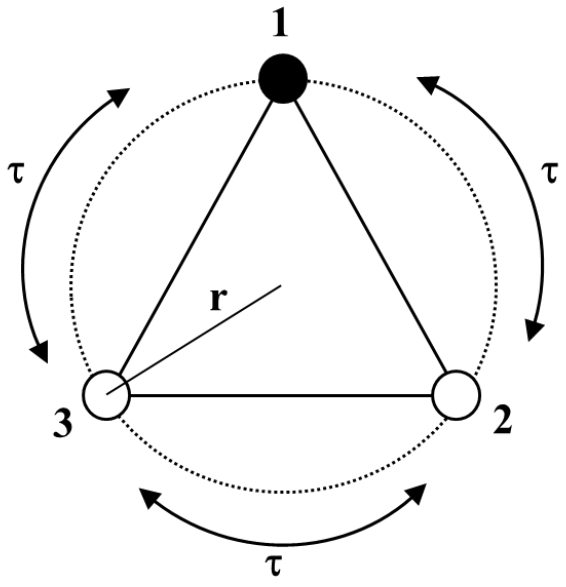

Figure 2.7: Schematic representation of the jump model of a particle rotating through 3 equivalent sites on a circle.

The common model used to describe this rotational motion assumes instantaneous jumps decoupled from the side group librations. The characteristic or

correlation time, τ, is the average time between two successive jumps and the rate constant, i.e. the probability of reorientation per unit time, is defined as $\Gamma = 1/\tau$. The temperature dependence of τ follows an Arrhenius law:

$$\tau = \tau_\infty e^{E_a/k_B T} \tag{2.83}$$

where E_a is the activation energy and τ_∞ is a constant defined as:

$$\tau_\infty = \lim_{T\to\infty} \tau \tag{2.84}$$

In order to study side group rotations, samples are studied at or below glass transition temperature. This freezes the main chain backbone in order to reduce main chain motions which broaden the quasieleastic spectra. At temperatures well below T_g, the scattering function is given by:

$$S_{inc}(Q,\omega) = \big(A_0(Q)\delta(\omega) + S_{qel}(Q,\omega)\big) \otimes R(Q,\omega) \tag{2.85}$$

where $A_0(Q)$ is the elastic incoherent structure factor (EISF), $S_{qel}(Q,\omega)$ is the quasielastic scattering function and $R(Q,\omega)$ is the instrument resolution. The full width at half maximum (FWHM) is used as a measure of the instrument resolution as it determines the lower limit of the observable energy transfers. If vibrational motions are considered, a Debye-Waller factor is introduced to the above equation, causing a decrease in both elastic and quasielastic scattered intensity.

The quasielastic contribution is usually expressed by a Lorentzian function, as mentioned in Section 2.4.2 for Fourier transforms of exponential decays, thus the quasielastic component can be expressed as follows:

$$S_{qel}(Q,\omega) = (1 - A_0(Q))L(\omega) = (1 - A_0(Q))\frac{1}{\pi}\frac{\Gamma}{\Gamma^2 + \omega^2} \tag{2.86}$$

where Γ is the HWHM of the Lorentzian function. However, the side groups of polymer chains are not all in the same local environment due to the amorphous nature of polymers[231]. The lack of regularity of the main chain conformation and different local packing conditions leads to a distribution of jumping rates or correlation times. A single Lorentzian is insufficient to describe the different environments, and so is replaced by a distribution of Lorentzian functions, most commonly the log-Gaussian distribution[231]:

$$S_{qel}(Q,\omega) = (1 - A_0(Q))\sum_{i=1}^{N} g_i L_i(\omega) \tag{2.87}$$

with $\sum_{i=1}^{N} g_i = 1$. The log-Gaussian distribution has a weight equal to σ:

$$g_i = \frac{1}{\sqrt{2\pi}\sigma} exp\left[\frac{1(ln\Gamma_i - ln\Gamma_0)^2}{2\sigma^2}\right] \quad \textbf{(2.88)}$$

where Γ_0 is the HWHM of the most probable Lorentzian component. L_i is a Lorentzian function with HWHM equal to Γ_i:

$$L_i = \frac{1}{\pi}\frac{\Gamma_i}{\Gamma_i^2 + \omega^2} \quad \textbf{(2.89)}$$

If the side group chains contain long alkyl chains, such as in poly(butyl acrylate), it may not be possible to separate the side group rotations from the main chain segmental motions in the QENS and EWS spectra. In that case, only the overall dynamics of the system can be considered and analysed.

2.4.5 Main Chain Motion

The motion of the main chain can be also analysed by quasi-elastic neutron scattering. These experiments are carried out above the T_g, where conformational rearrangements occur. Different regions of large scale main chain dynamics can be distinguished:

1. The motion of the polymer chain as a whole can be observed at small scattering vectors (Q), i.e. $Q < 1/R_g$ where chain diffusion dominates. The HWHM of the quasielastic peak varies with Q^2 with a diffusion coefficient, i.e. $\Gamma = DQ^2$. This range is only measurable in neutron scattering for small polymer chains.
2. At larger values of Q, $1/R_g < Q < 1/l$, where l is the length of a segment in the Rouse model. In this region, the internal motions of the polymer chains are observed, and the HWHM of the quasielastic peak is proportional to Q^4 according to the Rouse model (See Section 1.3.4 and ref [94] for more details).
3. If the polymer chains are larger than the molecular weight of entanglement, M_e, deviations from the Rouse dynamics are expected for distances larger than the diameter of the tube. The HWHM being proportional to Q^4 is expected for $1/R_e < Q < 1/l$ where R_e is the entanglement length. At shorter length scales (i.e. $Q > 1/l$), more deviations from the Rouse model are observed and various relaxation processes and the stiffness of polymer chains need to be considered[232].

The scattering law corresponding to Rouse motion was calculated by de Gennes[93]. For Brownian motion of a point in a chain constrained by attachment to neighbouring atoms, the time dependent intermediate scattering function is calculated by:

$$I(Q,t) = e^{-\left(\frac{t}{\tau_R}\right)^{1/2}} \quad \textbf{(2.90)}$$

where τ_R is the relaxation time. The $t^{1/2}$ dependence gives a non Lorentzian shape in $S_{inc}(Q,\omega)$ in the energy domain. As mentioned earlier, the width of the quasielastic broadening is predicted to vary with Q^{-4} dependence.

However, deviations in the Rouse model have been observed in various polymers[233, 234] often due to topological constraints or polymer chain interactions[235]. To account for deviations from the Rouse model, the stretched exponential or Kohlrausch-Williams-Watt (KWW) function is used to characterise the time decay of the incoherent intermediate scattering function:

$$\phi(t) = e^{-(t/\tau_{KWW})^{\beta}} \quad \textbf{(2.91)}$$

Therefore, the intermediate scattering function is expressed as:

$$I(Q) \propto exp\left[\frac{t}{\tau_{KWW}(Q)}\right]^{\beta} \quad \textbf{(2.92)}$$

where t is time (ns), τ_{KWW} is the characteristic relaxation time which is Q dependent, and β is the stretched exponent ($0<\beta<1$) which characterises the relaxation time distribution. The Q dependence of the relaxation time is expressed by a power law $\tau_{KWW} \propto Q^{-n}$, and typical n values for polymer chains are 5/3 to 4.[66] Higher n values show more diffusive dynamic processes. The KWW function generalises the result of the original Rouse model and can be used to fit the intermediate scattering function results obtained from QENS experiments[236].

2.4.6 Analysis of QENS data

In order to extract dynamic information on the polymer chains, an appropriate choice of model function is required to provide an expression for the incoherent scattering law, $S_{inc}(Q,\omega)$, in terms of molecular parameters. This function is then convoluted with the instrumental resolution and fitted to the experimental data. Instead of directly analysing the dynamic incoherent structure factor $S_{inc}(Q,\omega)$, it is often easier to compute and analyse the intermediate scattering function $I_{inc}(Q,t)$ by Fourier transforming the experimental data and dividing by the Fourier transform of the resolution function. The relationship between $S_{inc}(Q,\omega)$ and intermediate scattering function is:

$$S_{inc}(Q,\omega) = \frac{1}{2\pi}\int I_{inc}(Q,t)e^{(-i\omega t)}dt \quad \textbf{(2.93)}$$

with:

$$I_{inc}(Q,t) = \frac{1}{N}\sum \langle e^{\boldsymbol{iQ}R_i(t)}e^{-\boldsymbol{iQ}R_i(0)}\rangle \quad \textbf{(2.94)}$$

where the brackets indicate thermal averaging and $R_i(t)$ and $R_i(0)$ are the position of the nuclei at time t and t=0, respectively. By describing the positions of the scattering nuclei within a sample, $S_{inc}(Q,\omega)$ and $I(Q,t)$ give dynamic information on the system.

The intermediate scattering function is then analysed using the KWW function. In order to analyse the QENS data collected in the energy or frequency domain, the Fourier transform of the KWW function is required. Arrighi *et al.* developed an algorithm for computing the Fourier integral of the KWW function to carry out analysis of the QENS data in the energy domain[237]. However, in this project all analysis and fitting was carried out in the time domain by using Excel to Fourier transform the raw QENS data.

2.5 Neutron Sources and Instrumentation

A neutron source is a device that emits neutrons, and specifically designed large scale neutron reactors are required for scattering experiments. Research facilities have been built up around these reactors, providing a variety of instruments and techniques for analysis. The three facilities used for data collected in this thesis were ISIS at the STFC Rutherford Appleton Laboratory in the UK, the Institut Laue-Langevin (ILL) in France and the Paul Scherrer Institut (PSI) in Switzerland. Each facility has a wide variety of instruments available, and the instruments used for this project were the SANS instruments LOQ, SANS2D (ISIS), D22 (ILL) and SANS-II (PSI), and the QENS instruments IRIS (ISIS), IN16 and IN16B (ILL).

2.5.1 Neutron Sources

There are two main types of neutron sources for neutron scattering experiments: spallation sources and continuous reactor sources.

A continuous neutron source produces neutrons by a fission chain reaction using uranium enriched with its ^{235}U isotope as the principal raw material. A stray neutron is

absorbed by the uranium, causing it to become unstable and break up, releasing an average of 2-3 neutrons per event. A possible mechanism for one such event is shown below[198]:

$$n + {}^{235}U \rightarrow {}^{236}U^{*} \rightarrow {}^{134}Xe + {}^{100}Sr + 2n \quad \textbf{(2.95)}$$

These neutrons are thermalized in a moderator and emitted with a broad range of wavelengths. The wavelength used for the experiment is selected using one of three methods; 1) by Bragg scattering using a crystal monochromator, 2) by velocity selection using a mechanical chopper or 3) by time-of-flight. Time-of-flight methods determine the energy of neutrons by measuring the time the neutron takes to travel a set distance. High energy neutrons are faster than low energy neutrons.

This neutron fission chain reaction means continuous reactor sources are capable of producing high flux neutron beams; however the drawback is the production of heat within the reactor. The ILL (France) uses a continuous reactor source, and currently produces the most powerful continuous neutron flux. It operates at a thermal power of 58.3 MW and produces a flux of 1.5 $x10^{15}$ neutrons s^{-1} cm^{-2}.

Spallation neutron sources are the alternative to continuous fission reactor sources, and have become increasingly important in recent years[198]. Spallation sources are considered more environmentally friendly because they do not require uranium fission fuel. Instead of using fission to create neutrons, a heavy metal sample is bombarded with high energy protons (~1 GeV) that have been accelerated using a particle accelerator. Neutrons and protons are expelled from the nuclei, and this process is called spallation. This method produces a high yield of approximately 30 neutrons per proton and the heat dissipated per neutron is much lower than that produced by a continuous fission reactor[200]. The neutrons expelled have energies of ~1 meV and for scattering purposes are slowed down using a monochromator. This creates a white beam of neutrons with a range of wavelengths, allowing for the use of fixed geometry instruments.

ISIS uses a pulsed spallation source, using ^{183}Ta as the heavy metal for neutron production. The peak flux achieved is 4$x10^{16}$ cm^{-2} s^{-1}, but the time average flux is much lower (~2 $x10^{13}$), and that is one of the disadvantages of the pulsed spallation source. The PSI facility in Switzerland uses the first continuous spallation source in the world (SINQ), utilising a cyclotron as its particle accelerator to produce a continuous beam of

protons. This gives a high time averaged flux (~$1x10^{14}$), but results in a high background and no time structure.

2.5.2 SANS instruments

Small-Angle Neutron spectrometers measure the elastic intensity resulting from neutron scattering at small angles. This requires high *Q* resolution and the wavelength and scattering angle have to be well-defined to collect useful data. The design of the SANS instruments for use on continuous and on spallation sources are different.

SANS instruments on continuous neutron sources typically have a beam collimation system inside an evacuated pre-sample flight path. This collimation system is a set of pinholes that converges the neutron beam on the sample. The length of the collimator is adjustable, thus the source-to-sample distance can be changed as needed. After the sample, there is another evacuated cylindrical tube, containing an area detector. The sample-to-detector distance is adjusted by moving the detector in this evacuated tube. This distance determines the *Q* range of the experiment, thus the sample is often measured at more than one distance in order to extend the *Q* range of the data collected. Finally, a set of beam stops are used to prevent the main beam from hitting the detector and damaging it with overexposure.

On pulsed spallation neutron sources, SANS instruments are configured to use a white beam of neutrons containing a range of wavelengths, using mirrors to remove short wavelengths. This means that a large *Q* range and good *Q* resolution can be achieved without changing the sample-to-detector distance, as is needed in the continuous source instruments. The disadvantage of such SANS instruments is the data reduction and analysis is more complex, as many corrections are wavelength dependent (transmission, normalisation, incoherent background subtraction) and so cannot be calculated as easily as with fixed wavelength instruments.

SANS data presented in this thesis were collected on four different instruments: LOQ, D22, SANS-II and SANS2D. The specifications for each instrument are listed in Table 2.4 and Table 2.5.

LOQ (Figure 2.8) is a relatively simple fixed geometry instrument on the pulsed spallation source at ISIS that uses a white neutron beam and time-of-flight analysis to separate neutrons of different wavelengths. The moderator to sample distance is fixed at

10.87 m and the sample-to-detector distance is 4.28 m. This allows or a wide range of *Q* values in a single measurement without the need to reconfigure the instrument. An in-situ magnetic field of c.a. 1.0 Tesla can be applied perpendicular to the neutron beam during the experiment for magnetic property measurements. LOQ can typically be used to probe the structure and conformation of polymers on length scales of 1 to 100 nm, although highly anisotropic systems can be analysed up to length scales of 400 nm.

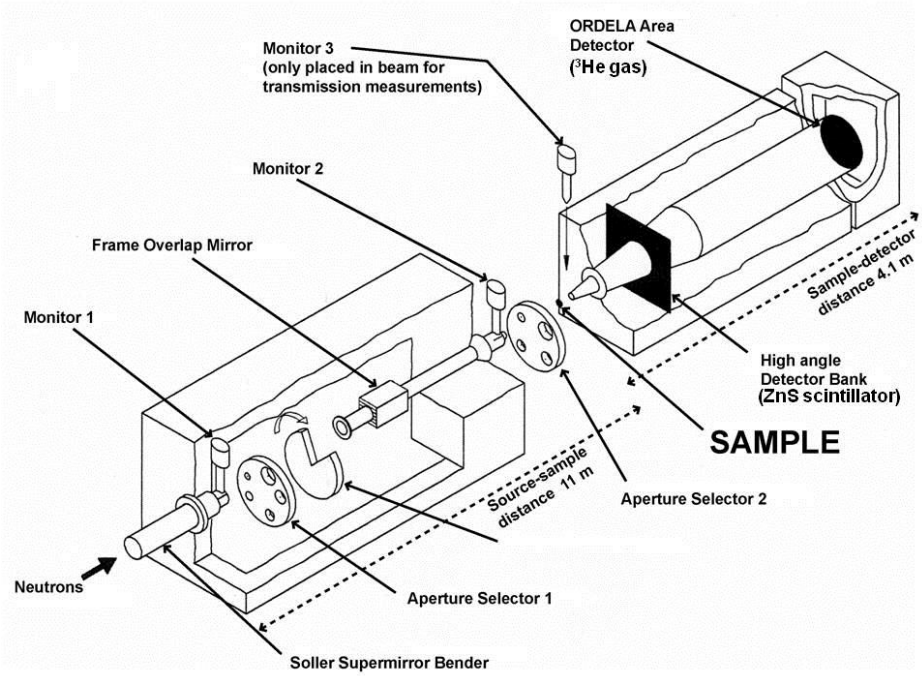

Figure 2.8: Schematic Diagram of the LOQ spectrometer at ISIS[238].

SANS2D is another time-of-flight SANS instrument at ISIS, one designed to be a more flexible and higher throughput instrument than LOQ. The diagram of SANS2D is shown below (Figure 2.9). SANS2D combines the advantages of a white beam instrument with two moveable area detectors. As per continuous source instruments, these detectors can be moved to extend the *Q* range of the instrument, giving an overall *Q* range for the instrument of 0.002 to 3 Å. This means that SANS2D can examine the size and shape of polymers on a scale of 0.25 to 300 nm. SANS2D also has a larger flux at the sample than LOQ, meaning shorter experiment times for the same amount of scattered intensity collected.

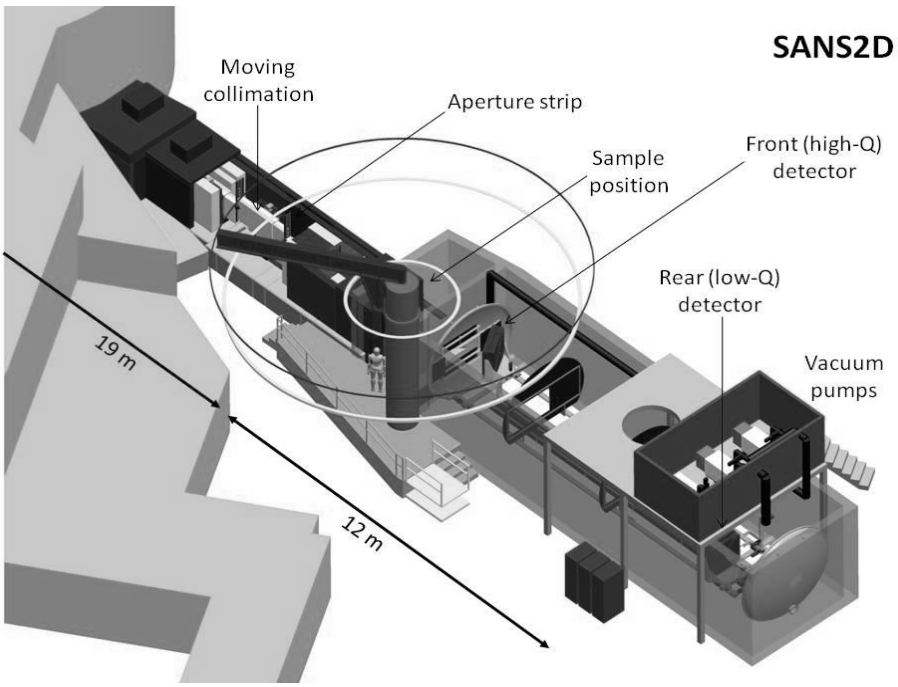

Figure 2.9: Schematic Diagram of the SANS2D SANS spectrometer at ISIS[239].

D22 is a SANS instrument at ILL that has the highest flux at the sample and a wavelength range of 4 to 40 Å, as such is often used to measure weakly scattering samples and for real-time experiments. A schematic is shown in Figure 2.10. A narrow wavelength band is selected by a velocity selector, which can be rotated to collect shorter wavelength neutrons or tune the wavelength resolution. The neutron beam then enters the collimation system consisting of 8 segments, which can be adjusted to change the source-to-sample distance. The beam then passes through a diaphragm and hits the sample. The moveable area detector is the largest of all the SANS instruments with an active area of 102 x 98 cm^2. The detector can be moved to create sample-to-detector distances between 1 to 17.8 m, thus covering a total Q range of 0.0004 to 0.44 Å (no detector offset) or 0.85 Å (with detector offset).

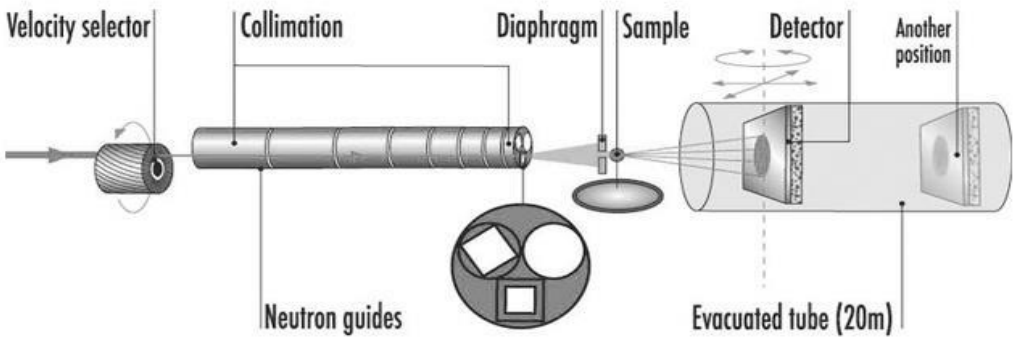

Figure 2.10: Schematic Diagram of the D22 SANS spectrometer at ILL[240].

The final instrument used, SANS-II, is installed at PSI (Switzerland). Based on a continuous spallation source, its design is similar to the instruments found on continuous fission reactor sources, as shown in Figure 2.11. The neutron wavelength is determined by a mechanical velocity selector then passed through a collimator with 5 sections which can be adjusted from 2 - 6 m in length. The moveable detector can change the sample to detector distance from 1.1 to 6 m, giving a *Q* range of 0.002 to 0.35 $Å^{-1}$ using 3 instrument settings.

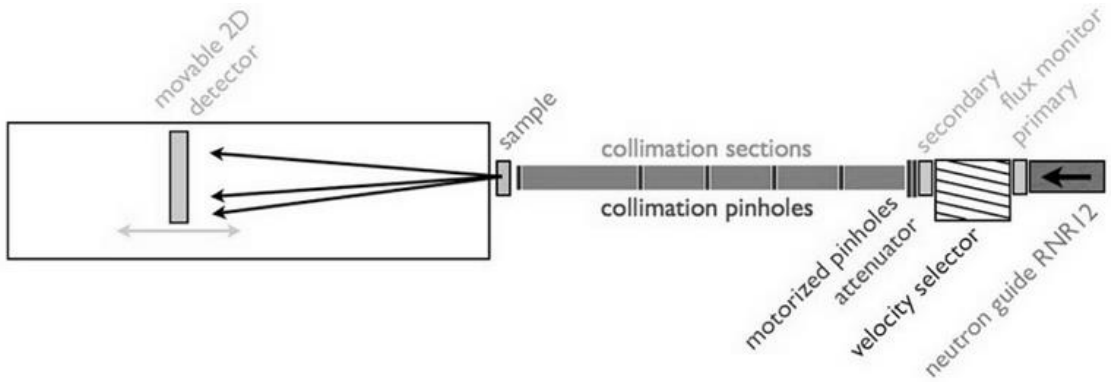

Figure 2.11: Schematic Diagram of the SANS-II SANS spectrometer at PSI[241].

Table 2.4: Specifications of variable wavelength SANS instruments: LOQ and SANS-2D

Instrument	LOQ	SANS2D
Flux /n cm^{-2} s^{-1}	$2x10^5$	$>10^6$
Incident Wavelength /Å	2.2 – 10 (25 Hz)	2.0 – 14 (10 Hz)
Q range /$Å^{-1}$	0.006 – 0.28	0.002 – 3
Beam size at sample	2-20 mm diameter	2-15 mm diameter
Detector Type	^{3}He-CF_4 filled ORDELA	^{3}He-CF_4 filled ORDELA x 2
Detector Area /cm^2	64 x 64	96.5 x 96.5
Detector Resolution /mm^2	5 x 5	5 x 5

Table 2.5: Specifications of fixed wavelength SANS instruments: D22 and SANS-II

Instrument	D22	SANS-II
Flux /n cm^{-2} s^{-1}	$1.2x10^8$	$3x10^4$
Incident Wavelength /Å	4.5 - 40 (fixed variable)	4.5 – 20 (fixed variable)
Q range /$Å^{-1}$	0.0004 – 0.44 (0.85)	0.002 – 0.35
Beam size at sample	10 – 300 mm diameter	
Detector Type	^{3}He CERCA	^{3}He
Detector Area /cm^2	102 x 98	64 x 64
Detector Resolution /mm^2	7.5 x 7.5	4.5 x 4.5

2.5.3 QENS instruments

The QENS data on poly(butyl acrylate)-silica nanocomposites was collected previously by Natalie Grima on two instruments: (1) IN16 (Institut Laue-Langevin ILL, France) and (2) IRIS (ISIS, Rutherford Appleton Laboratory, UK). The details of these instruments are listed in Table 2.6.

IN16 was a high-resolution backscattering spectrometer at ILL and was the most sensitive backscattering spectrometer before decommission; a schematic diagram is shown below (Figure 2.12). This instrument uses two neutron optical devices (graphite deflectors) to optically focus the neutron beam, increasing the flux by up to a factor of 5. The graphite double deflector system selects roughly the desired wavelength of neutrons. The neutrons are then transmitted to a moving crystal monochromator in nearly perfect backscattering geometry, which selects the neutrons with the desired wavelength. IN16 uses two monochromators: Si(111) reflection in high and low resolution and a Si(311) reflection (a $Si_{1-x}Ge_x$ monochromator was planned but never implemented). Using Si(311), a resolution of ~2.5 μeV is obtained for this instrument. For quasi-elastic scattering, the monochromator and analyser crystals are the same material, and the same lattice spacing and orientation are used. The monochromator is sitting on top of a Doppler drive, which can used to change the incident energy of the neutrons by Doppler shifting.

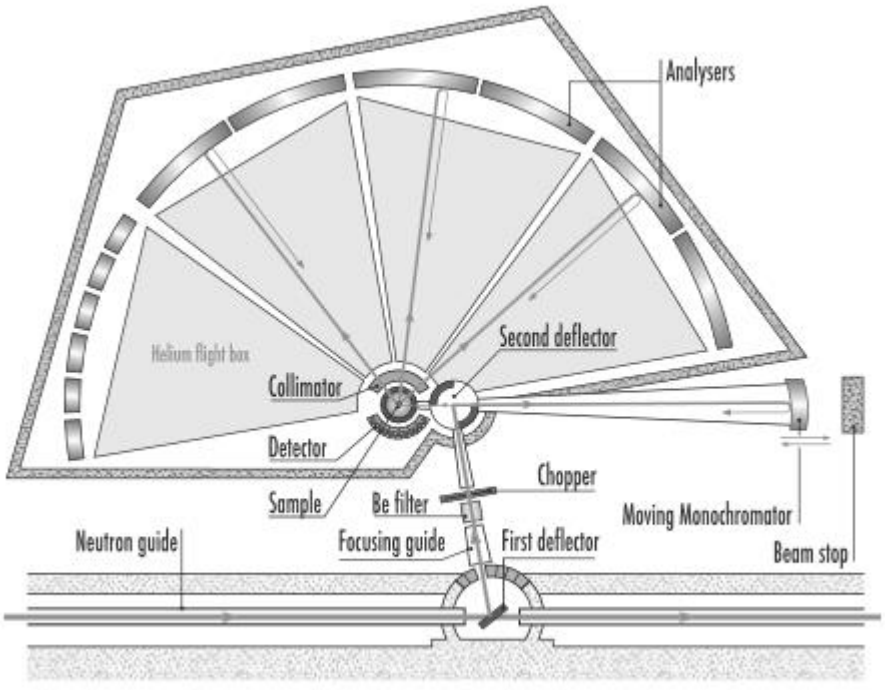

Figure 2.12: Schematic diagram of IN16 backscattering spectrometer[242].

IRIS (ISIS) is a high resolution quasi-elastic and inelastic scattering neutron spectrometer. The instrument is based on a pulsed neutron source, allowing for the collection of data in a wide energy window and *Q* range at a single instrument configuration. IRIS is a time-of-flight inverted-geometry instrument, using the creation time of the pulses of neutrons to start the TOF clock. This allows all of the neutrons to be used in the scattering experiment, whereas traditional TOF instruments can only use a fraction of the neutron beam.

A diagram of the instrument is shown in Figure 2.13. Neutrons leave the moderator and pass through two disc-choppers, which define the wavelength range for the experiment. The wavelength selection defines the energy resolution and transfer range in the experiment. The scattered neutrons are analysed by two analyser arrays; pyrolytic graphite (PG) and muscovite mica (Mica) with detector banks containing 51 detectors. These analysers can be operated simultaneously or separately, giving IRIS a wide *Q* range with a high resolution.

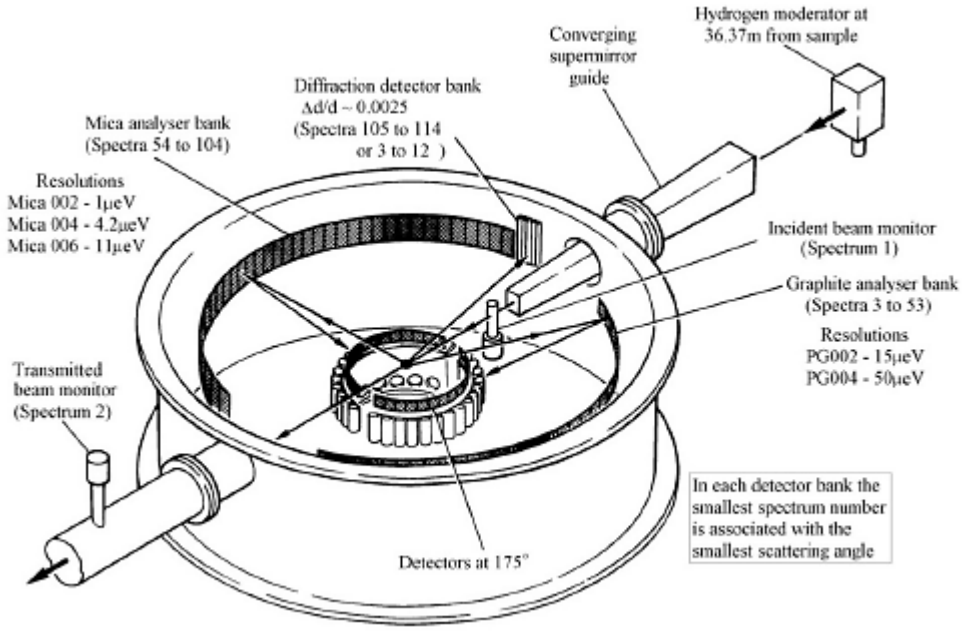

Figure 2.13: Schematic diagram of IRIS spectrometer at ISIS[243].

QENS measurement results on polystyrene-fullerene star systems were carried out on the new IN16B instrument (ILL, France), an upgraded version of IN16, which was shut down in August 2013. This instrument has a similar set-up to IN16, shown in Figure 2.12, and the specifications are listed in Table 2.6. The main upgrade is the use

of a Phase Space Transformation (PST) chopper at the end-of-guide position, which converts a wide wavelength band to a narrow one and then deflects these neutrons to the backscattering monochromator. This, in combination with a new neutron guide focusing optics that guides the neutrons to the PST chopper, results in an increase of flux of a factor of 10. The analyser solid angle is doubled compared to IN16 and new GaAs monochromators and analysers are planned to increase the measureable *Q* range.

Table 2.6: Instrument specifications for IRIS, IN16 and IN16B

Instrument	**IRIS**				
Analyser	PG (002)	PG (004)	Mica (002)	Mica (004)	Mica (006)
Analysing Energy /meV	1.84	7.38	0.207	0.826	1.86
Energy Transfer /meV	-0.4 to 0.4	-3.5 to 4.0	-0.02 to 0.02	-0.15 to 0.15	-0.4 to 0.4
Scattering Angle /deg	25 – 160	25 – 160	25 – 155	25 – 155	25 – 155
Momentum transfer /Å^{-1}	0.42 to 1.85	0.84 to 3.70	0.13 to 0.62	0.26 to 1.24	0.40 to 1.87
Energy Resolution /μeV (FWHM)	17.5	54.5	1.0	4.5	11.0
Instrument	**IN16**				
Monochromator	Si (111) high res	Si (111) low res	Si (311)		
Analyser	Si (111)	Si (111)	Si (311)		
Flux at sample	~ 2 x 10^4	~ 5 ± 4 x 10^4	5 x 10^3		
Incident wavelength /Å	6.271	6.271	3.275		
Energy Transfer /μeV	-15 to 15	-15 to 15	-28 to 28		
Energy Resolution /μeV (FWHM)	0.3 – 0.4 (Lorentzian)	0.9 (Gaussian)	~2.5		
Elastic *Q* range /Å^{-1}	0.02 to 1.9	0.02 to 1.9	1.7 to 3.7		
Instrument	**IN16B**				
Monochromator	Si (111) high res	Si (111) low res	Si (311)		
Analyser	Si (111) polished	Si (111) polished	Si (311)		
Flux at sample	t.b.d.	~ 6 x 10^5	1.2 x 10^5		
Incident wavelength /Å	6.271	6.271	3.275		
Energy Transfer /μeV	-31 to 31	-31 to 31	-59 to 59		
Energy Resolution /μeV (FWHM)	~0.35	~0.85	~2.0		
Elastic *Q* range /Å^{-1}	0.1 to 1.8	0.1 to 1.8	0.7 to 3.5		

Chapter 3. Experimental and methodology

3.1 Materials

2,2,2-Trichloroethyl chloroformate, ascorbic acid, Brij 98 [polyoxyethylene(20) monooctadecyl ether, M_n = 1150 g mol^{-1}], butyl acrylate (BA, +99%), methyl methacrylate (MMA, 99%), methyl methacrylate-d_8 (99%), styrene (>99%), *N*,*N*,*N'*,*N''*,*N''*-pentamethyldiethylenetriamine (PMDETA), tin(II) 2-ethylhexanoate ($Sn(EH)_2$, ~95%) and 2-butanone/methyl ethyl ketone (MEK) were purchased from Aldrich, copper(II) chloride, tetrabutyl-ammonium fluoride (TBAF), 2-bromoisobutyrylbromide and triethylamine from Lancaster, 3-aminopropyl triethoxysilane (98%) and hexadecane from Fluka, tris(2-dimethylamino)ethyl)amine (Me_6TREN), ethylene glycol 99% (EG) from Alfa Aesar and ethylenediaminetetraacetic acid disodium salt (EDTA) from Acros. Toluene, tetrahydrofuran (THF), and methanol were obtained from Fisher Scientific. Bis(2-pyridylmethyl)octylamine (BPMOA) was synthesised by a literature procedure.[244, 245]

The monomers butyl acrylate (BA), methyl methacrylate (MMA), methyl methacrylate-d_8 and styrene (S) were purified by extraction with approximately 20 ml of 0.1 M aqueous NaOH three times to remove the inhibitor. The monomers were then washed with 0.1 M aqueous HCl and water until neutral to litmus. After drying over anhydrous $MgSO_4$, the monomers were filtered, degassed and stored at 3 °C.

Different types of silica nanoparticles were used throughout this research. The various properties and sources of the silica are listed in Table 3.1.

Table 3.1: Various properties of the silica particles used throughout the project.

Silica Name	Type of silica	Surface Area /m^2g^{-1}	Particle diameter	Source
MEK-ST	Colloidal	155	10-15 nm	Nissan Chemical
LUDOX-AM	Colloidal	198-255	12-15 nm	Sigma-Aldrich
Cab-O-Sil H5 (H5)	Aggregated	300	7 nm (0.2-0.3 µm aggregates)	Cabot
Aerosil 300 (A300)	Aggregated	300	7 nm (0.2-0.3 µm aggregates)	Evonik (formerly Degussa-Huls)

Some of the polymer-silica nanocomposites samples analysed in this thesis were synthesised previously using the synthesis methods listed in Section 3.2. by other students in the Polymer group, Dr. Moussa Khlifa[31], Natalie Grima[30] and Gavin Ross.

3.2 Synthesis of Polymer Nanocomposites

3.2.1 Synthesis of Atom Transfer Radical Polymerisation (ATRP) Initiators

3.2.1.1 Preparation of *O*-2,2,2-Trichloroethyl *N*-(3-Triethoxysilylpropyl) carbamate (Trichloroethyl Carbamate Initiator)

A mixture of 3-aminopropyltriethoxysilane (13.6 mL, 12.9 g, 58.4 mmol), 2,2,2-trichloroethyl chloroformate (7.9 mL, 12 g, 58 mmol), and triethylamine (10.0 mL, 7.26 g, 71.7 mmol) in toluene (100 mL) was stirred at 40 °C for 4 hours. The mixture was filtered to remove triethylammonium chloride. The filtrate was concentrated in vacuum to give a brown oil (20.9 g, 90%). The crude product was further purified by vacuum distillation (Kugelrohr, 205 °C/0.4 mbar) to yield trichloroethyl carbamate initiator as a colourless liquid.

3.2.1.2 Preparation of 2-bromo-2-methyl *N*-(3-triethoxysilylpropyl) propionamide (2- bromoisobutyryl initiator)

A mixture of 3-aminopropyltriethoxysilane (6.98 mL, 6.63 g, 29.95 mmol), and triethylamine (5.48 mL, 3.94 g, 38.95 mmol) in toluene (50 mL) was placed in a flask with a dropping funnel fitted with a drying tube attached. The solution was cooled with an ice bath, then 2-bromoisobutyrylbromide (3.89 mL, 7.23 g, 31.45 mmol) was added drop-wise over 15 min. The mixture was left in the ice bath for 10 min and then heated at 40 °C for 90 min. The reaction mixture was then filtered under vacuum and the filtrate was concentrated in vacuum to give a dark brown oil. The crude product was further purified by vacuum distillation (Kugelrohr, 250 °C/0.5 mbar) to yield the 2-bromoisobutyryl initiator as a light brown liquid.

3.2.2 Preparation of Initiator functionalised silica nanoparticles

A mixture of dry Cab-o-sil H5 silica (~5 g), initiator ($7x10^{-4}$ mol) and toluene (90 mL) was heated at 100 ºC for 17 hours. Functionalised silica particles were concentrated by centrifugation (4000 rpm, 20 min) and the supernatant layer was decanted off. The gel

layer was dispersed in THF and the centrifugation process was repeated four times. The remaining gel was dried at 60 ºC for 48 hours.

For colloidal silica MEK-ST, the silica dispersion (5 g of 30 wt % SiO_2 in methyl ethyl ketone) was mixed with initiator (0.5 mL) and gently refluxed at 70 ºC for 24 hours. Elemental analysis was used to confirm the presence of the initiator on the surface of the particles.

3.2.3 Typical ATRP synthesis of PMMA-silica in mini-emulsion

The synthesis of poly(methyl methacrylate) (PMMA)-grafted polymer nanocomposites was adapted from a procedure in the literature[246]. Copper (II) chloride (5.1 mg, 38 µmol), BPMOA (38 µL, 38 µmol), inhibitor-free methyl methacrylate (4.00 mL, 38 mmol) and deionised water (3 mL) were stirred in a Schlenk flask at 50 ºC for 15 minutes. The mixture was then cooled in an ice bath and a solution of Brij 98 (115 mg) in deionised water (17 mL), hexadecane (0.23 mL) and trichloroethyl carbamate-initiator silica nanoparticles (0.61 g) were added to the Schlenk flask. The solution was then sonicated in an ultrasonic bath for 15 minutes. The homogenised mini-emulsion was deoxygenated with nitrogen for 30 minutes before being heated to 70 ºC in a polyethylene glycol bath. An aqueous solution of ascorbic acid (10.0 mg, 57 µmol, dissolved in 1.0 mL of deionised water) was added. The polymerisation was stopped after 120 min by opening the sealed flask to air. An aqueous solution of EDTA (15.5 mg in 3 mL of deionised water) was added in order to remove the copper catalyst complex. The mixture was added into methanol drop-wise and allowed to precipitate for 30 min. The supernatant was removed by filtration. The crude product was purified by Soxhlet extraction with THF (100 mL, 12 hours at 90 °C) to remove any unattached polymer chains. The collected polymer-silica composite was then dried at 110 ºC for 48 hours, then at 160 ºC in the vacuum oven for 24 hours to remove all traces of solvent.

3.2.4 Typical ATRP synthesis of PBA-silica in mini-emulsion

Copper (II) bromide (5.1 mg, 38 µmol), PMDETA (8 µL, 38 µmol), inhibitor-free butyl acrylate (5.40 mL, 38 mmol) and deionised water (3 mL) were continuously stirred in a Schlenk flask at 50 ºC for 15 minutes. The mixture was then cooled in an ice bath and a solution of Brij 98 (115 mg) in deionised water (17 mL), hexadecane (0.23 mL) and 2-bromoisobutyryl-initiator silica nanoparticles (0.61 g) were added to the Schlenk

flask. The solution was then sonicated in an ultrasonic bath for 15 minutes. The homogenised mini-emulsion was deoxygenated with nitrogen for 30 minutes before being heated to 70 ºC in a polyethylene glycol bath. An aqueous solution of ascorbic acid (10.0 mg, 57 μmol, dissolved in 1.0 mL of deionised water) was added. The polymerisation was stopped after 6 hours by opening the sealed flask to air. An aqueous solution of EDTA (15.5 mg in 3 mL of deionised water) was added in order to remove the copper catalyst complex. The solid was precipitated by adding to methanol drop-wise, and then the supernatant was removed by filtration. The crude product was purified by Soxhlet extraction with THF (100 mL, 12 hours at 90 °C) to remove any unattached polymer chains. The collected polymer-silica composite was then dried at 100 ºC for 24 hours, then at 160 ºC in the vacuum oven for 24 hours to remove all traces of solvent. DLS measurements on the mini emulsion stability are shown in Appendix A.

3.2.5 Typical ATRP synthesis of PS-silica

The synthesis of PS-silica samples used a different ATRP method adapted from the literature on ATRP synthesis of poly(styrene-co-acrylonitrile)[47].

Initiator modified silica nanoparticles (0.20 g, 18.8 μmol) were dispersed in anisole (6 mL) with stirring for 12 hours in a Schlenk flask. Styrene (~2.4 mL, 21 mmol) was added, and then a solution of $CuCl_2$ (0.21 mg, 0.94 μmol) and Me_6TREN (0.39 μL, 0.94 μmol) complex in anisole (0.75 mL) were added. The mixture was degassed by three freeze-pump thaw cycles, then a solution of $Sn(EH)_2$ (5.00 μL, 15.41 μmol) and Me_6TREN (6.50 μL, 15.4 μmol) in anisole (0.5 mL) was added. The Schlenk flask was then transferred into a thermostatic oil bath at 70 ºC. The reaction was stopped after 24 hours by exposing the catalyst to air. The product was precipitated into methanol (700 mL) over 30 minutes then the supernatant removed by filtration. The precipitate was dried in a vacuum oven at 160 ºC. The process was repeated several times with different amounts of colloidal and aggregated silica initiator particles to collect several samples. DLS measurements on the mini emulsion stability are shown in Appendix A.

3.2.6 Preparation of polymer-silica dispersions

A 5-10 wt% polymer solution in toluene was prepared and stirred, then fumed silica particles (Cab H5 and A300, 10, 20, 30 wt %) were added. The flask was sealed to

prevent solvent evaporation and stirred for 48 hours. The solvent was then allowed to evaporate at room temperature for 24 hours, and then the residue dried in a vacuum oven at 160 ^{o}C for a further 24 hours. Nanocomposites containing colloidal MEK-ST and Ludox particles were prepared in MEK and THF respectively.

3.2.7 Preparation of polymer blends

PMMA and poly(styrene-co-acrylonitrile) (SAN) or solvent-chlorinated polyethylene (SCPE) were dissolved in MEK (10 mL) and continuously stirred for 2-3 hours. The details of the pure polymers used are given in Table 3.2. The calculated amount of silica nanoparticles was added and the solutions were stirred for a further 24 hours. The sample vials were opened and the solvent left to evaporate slowly for 24 hours. Samples were then dried at 74 ^{o}C in the oven overnight. After this they were transferred to the vacuum oven and dried at 70 ^{o}C for 48 hours to remove any remaining solvent. All blend compositions (by weight fraction) prepared are listed in Table 3.3 below.

The study on polymer blends was done in collaboration with Ellie Campbell, an undergraduate project student, who ran some of the glass transition measurements and assisted with preliminary analysis on the SANS data for the PMMA/SCPE blends.

Table 3.2: Molecular weight information for the pure polymers used in blends

Polymer	M_w / g mol^{-1}	M_n /g mol^{-1}	PDI
PMMA	90,000	45,000	2.00
d_8PMMA	82,100	31,300	2.62
Grafted-PMMA 6.1 MEK-ST*	37,800	36,000	1.05
Grafted-d_8PMMA 17.3 MEK-ST	34,400	31,000	1.11
d_5PMMA^{iso}	250,000	167,000	1.50
d_5PMMA^{syn}	250,000	167,000	1.50
SAN^{26}	68,600	34,300	2.00
SCPE^{63}	207,000	128,600	1.61

Notation: $d_{\#}$ = number of deuterium atoms, ##.# = wt % of silica measured by elemental analysis. Syn = syndiotactic, iso = isotactic, SCPE$^{\#\#}$ = percentage chlorinated, SAN$^{\#\#}$ = percentage AN in copolymer. Unless otherwise stated, the PMMA samples are atactic. Samples labelled with * were synthesised by Dr. Moussa Khlifa.

Table 3.3: Polymer blend composition for microscopy and neutron scattering measurements

Blend	Composition		
PMMA/SAN/MEK-ST	30/70/0 50/50/0 70/30/0	30/70/1 50/50/1 70/30/1	30/70/5 50/50/5 70/30/5
d_8PMMA/SAN/MEK-ST		30/70/1	
d_5PMMA^{syn}/SAN/MEK-ST	30/70/0		30/70/5
Grafted-PMMA 6.1 MEK-ST/SAN		30/70/2	30/70/5
Grafted-d_8PMMA 17.3 MEK-ST/SAN			30/70/5
PMMA/SCPE^{65}/MEK-ST	50/50/0	50/50/1	50/50/5
d_5PMMA^{syn}/SCPE^{63}/MEK-ST	50/50/0	50/50/1	50/50/10
d_5PMMA^{iso}/SCPE^{63}/MEK-ST	56/44/0	56/44/10	

Notation: $d_{\#}$ = number of deuterium atoms, syn = syndiotactic, iso = isotactic, SCPE$^{\#\#}$ = percentage chlorinated. Unless otherwise stated, the PMMA samples are atactic. Polymer blend compositions are given in weight fractions.

3.2.8 Preparation of silica suspensions

Fumed silica was added into ethylene glycol in portions, with the suspension stirred mechanically and then sonicated in an ultrasonic bath for 10 minutes after each addition of silica until the desired concentration was reached. The suspensions were then sonicated for 12 hours. 10 wt% and 20 wt% suspensions of two types of fumed silica, Cab H5 and A300, were prepared for rheological measurements.

Fumed silica particles were also added into distilled water in portions, with the suspension stirred mechanically and then sonicated in an ultrasonic bath for 10 minutes after each addition of silica until the desired concentration was reached. The suspensions were then sonicated for 12 hours. 10 wt% and 20 wt% suspensions of two types of fumed silica, Cab H5 and A300, were prepared in concentrations of 0.1, 1 and 10 wt% for dynamic light scattering measurements.

3.3 Characterisation techniques

3.3.1 Differential Scanning Calorimetry (DSC)

Thermal analysis of the samples was carried out by using a Thermal Analysis (TA) DSC 2010. The samples of roughly 10 mg were heated in hermetically sealed aluminium pans. The glass transition temperature was measured by heating in the DSC

at 10 ^{o}C/min from 20 ^{o}C to 200 ^{o}C, under nitrogen flow, and measuring the excess heat flow needed to heat the sample at a constant rate compared to the empty reference pan.

3.3.2 Enthalpy Relaxation Measurements

Enthalpy relaxation experiments were carried out on a Perkin-Elmer Pyris 1 DSC on a single sample in the range 10 to 12 mg with nitrogen as the purge gas. A heating rate of 20 ^{o}C/min and a cooling rate of 40 ^{o}C/min were employed throughout. Indium and zinc were used for temperature calibration and the data were evaluated with respect to sapphire as the heat capacity (C_p) standard. The Cowie-Ferguson model was used to analyse the data collected (Section 5.2.3).

3.3.3 Elemental Analysis

Elemental analysis was used to obtain silica content. The analysis was carried out with an Exeter CE 440 Elemental Analyser on dried samples. The silica content was calculated as follows:

$$silica\ wt\% = 1 - \frac{\%C_{experimental}}{\%C_{theoretical\ pure\ polymer}} * 100\% \quad \textbf{(3.1)}$$

3.3.4 Thermal Gravimetric Analysis (TGA)

Thermogravimetric analyses were carried out on two instruments: a Dupont Instruments 951 Thermal Analyzer and a Linseis TGA PT1600. Approximately 15-25 mg of sample was heated under a flow of dry nitrogen at a heating rate of 10 °C/min over a temperature range of 40 – 600 °C. The weight loss of the polymer sample was recorded as a function of temperature to determine the polymer and silica content.

3.3.5 Dynamic Light Scattering (DLS)

3.3.5.1 Mini-emulsions

The size of the droplets formed in mini-emulsions were measured by dynamic light scattering (DLS) on a Malvern Zetasizer Nano ZS analyser at 25 ^{o}C. Miniemulsions with and without silica particles were prepared using the method in Section 3.2.3, until the step where the mini emulsion is formed using sonication. A 1 mL sample was

immediately removed from the miniemulsion to measure the initial size of the droplets. At regular intervals the size of the droplets were measured to monitor the stability of the emulsion.

3.3.5.2 Silica Suspensions

The size and zeta potential of the fumed silica particles and colloidal Ludox particles in aqueous solution at various concentrations were measured by dynamic light scattering using a Malvern Zetasizer Nano ZS analyser at 25 ^{o}C. The size of MEK-ST particles was measured at two different concentrations.

3.3.5.3 PS-fullerene stars

Dynamic light scattering experiments on PS-fullerene stars were performed on a Zetasizer Nano ZS at Napier University. Solutions of the stars and the corresponding linear PS chains in toluene and cyclohexane at various concentrations were measured at 20 ^{o}C and 35 ^{o}C respectively. Due to the small particle size (3 – 10 nm), the minimum concentration was limited to 0.1 wt%. The maximum concentration measured (2.5 wt%) was limited primarily by amount of sample available for measurements, as the overlap concentrations are higher than 5 wt% for both stars.

3.3.5.4 PMMA-silica nanocomposites

PMMA-silica samples were measured in toluene and MEK at 20 ^{o}C on a Zetasizer Nano ZS at Napier University. The small size of the unimer particles (10 – 20 nm) and the lack of solubility meant the solutions were measured at relatively large concentrations (>1 wt%). Solutions were run before and after filtering through 200 nm hydrophilic filters to remove larger aggregates.

3.3.6 Small Angle Neutron Scattering (SANS)

3.3.6.1 Sample Preparation

SANS measurements on polymer-silica samples were carried out in solution. The majority of samples were dissolved in deuterated and non-deuterated solvents for contrast matching measurements (Section 2.3.5). Both grafted and dispersed nanocomposites were prepared in solution, containing either aggregated (Cab H5) or

colloidal (MEK-ST) silica. One PMMA-silica sample was also measured at different concentrations to examine the behaviour of the grafted polymer chains in the dilute and semi-dilute regions.

Table 3.4: Dispersed and pure polymer samples measured by SANS on LOQ.

Polymer	M_w /g mol^{-1}	Silica type	Silica wt%	Solvent	Sln Wt %
PS	100,000	-	-	d_8-toluene	0.50
PS	100,000	MEK-ST	15.6	MEK	4.88
PS	100,000	Cab H5	15.0	d_8-toluene	5.00
PBA	99,000	-	-	d_8-toluene	4.74
PBA	99,000	Cab H5	15.2	d_8-toluene	4.74
PMMA	113,000	-	-	50/50 h/d tol	10.3
PMMA	113,000	Cab H5	14.9	d_8-toluene	5.02

Table 3.5: Grafted polymer-silica samples measured by SANS on LOQ.

Polymer	M_w /g mol^{-1}	Silica type	Silica wt%	Solvent	Wt % in Sln
PS	-	MEK-ST	4.9	h-toluene	13.0
PS[a]	36,500	MEK-ST	9.3	h-toluene	19.3
PS[a]	68,000	Cab H5	16.5	h-toluene	16.9
				50/50 h/d tol	10.7
PS	-	MEK-ST	4.9	-	-
d_8-PS	-	MEK-ST	11.8	-	-
d_8-PS	-	Cab H5	18.1	-	-
PBA[b]	110,000	MEK-ST	13.4	h-toluene	9.37
PBA[b]	113,000	Cab H5	3.9	h-toluene	9.64
PBA[b]	148,500	Cab H5	24.4	-	-
PMMA[a]	31,900	Cab H5	9.2	h-toluene	9.63
PMMA[a]	37,800	MEK-ST	6.1	50/50 h/d tol	0.21
				50/50 h/d tol	0.54
				50/50 h/d tol	0.98
				50/50 h/d tol	2.52
				50/50 h/d tol	5.07
				50/50 h/d tol	10.3

[a] = sample synthesised by Dr. Moussa Khlifa, [b] = sample synthesised by Gavin Ross

Pure polymers of similar molecular weight were also measured for comparison with the grafted and dispersed nanocomposites. Some of the less soluble samples were also measured as solids and prepared by wrapping in aluminium foil and taping in front of the neutron beam sample holder. The details of the polymer-silica samples measured (silica content, solvent used etc.) are in Table 3.4 and Table 3.5.

PS arms and then PS-fullerene stars were prepared at ORNL according to a procedure they published in the literature[56]. The stars produced by this method have a distribution of number of arms; the fractions were subsequently separated and purified, and the stars with an average of 5.8 arms were provided for analysis. The details of the PS-fullerene star samples and the corresponding linear PS chains measured are given in Table 3.6 and Table 3.7 respectively.

The stars were then dissolved in various solvents (toluene, benzene, chloroform) to study the dynamics in varying polymer/solvent compatible systems (i.e. good and theta solvents). Hydrogenated and deuterated solvents were also used to create contrast matching conditions. The concentrations of the solutions ranged from the very dilute (0.5 wt%) to the concentrated regime (30 wt%).

Table 3.6: PS-fullerene star sample information

Name	HPS or DPS	M_w arm /g mol^{-1}	M_w star /g mol^{-1}
2k HStar	H	2000	12320
16k HStar	H	16000	93520
2k DStar	D	2000	12320
18k DStar	D	18000	105120

Table 3.7: Linear PS sample information

Name	HPS or DPS	M_w /g mol^{-1}
2k HPS	H	2000
16k HPS	H	16000
105k HPS	H	105500

Polymer blend samples investigated by SANS were hot pressed into circular discs using a metal mould with a 13 mm diameter and 1 mm thickness. The samples were required to be this precise size, as they had to be the exact volume of the sample holder used in order to minimise volume loss effects. When the sample is heated above

the glass transition temperature of the polymers, voids can form in the polymer disc within the sample holder which affects the scattering results.

3.3.6.2 SANS measurements

Polymer-silica sample solutions were measured on the spectrometer LOQ. A series of experiments on PS-fullerene stars were carried out on three small-angle neutron scattering diffractometers - LOQ (ISIS), SANS-II (PSI) and D22 (ILL). Using three different instruments gives a wide *Q* range to measure the samples. The details and schematics of the instruments used are given in Section 2.5.2. The D22 measurements were carried out by Prof Bucknall and Dr Cabral prior to the start of the project, and the SANS-II data were collected by Prof Bucknall and Dr Arrighi. Both data reduction and data analysis was carried out during this project from raw data.

D22 and SANS-II are fixed wavelength instruments, with the wavelength and thus *Q* range depending on the distance between the sample and detector. The distances used for the D22 data are 1.5, 5.6 and 17.6 m, and 1.2, 4 and 6 m for SANS-II. After overlapping the data, this gives an experimental *Q* range of 0.004 to 0.6 Å and 0.003 to 0.26 Å for D22 and SANS-II respectively.

The phase separation of deuterated PMMA/SAN and PMMA/SCPE blends with and without silica (Table 3.3) were analysed in a series of experiments using the SANS2D instrument at ISIS. The samples were measured at a temperature range around the estimated phase separation temperature of the two blends: between 135 ^{o}C and 165 ^{o}C for PMMA/SCPE blends and 120 to 180 ^{o}C for PMMA/SAN blends.

For data analysis, the raw data from all experiments on LOQ and SANS2D was subjected to standard treatment in MANTID: corrected for background scattering from the empty cell/solvent, scaled by direct beam, transmission and sample volume and finally divided by monitor counts to obtain the scattering intensity in absolute units. The data from D22 and SANS-II was reduced using the program GRASP according to standard procedures. The partial data curves for the different distances measured on each instrument are then overlapped using Excel to create a full data curve for analysis.

3.3.7 Small-Angle X-Ray Scattering (SAXS)

Preliminary SAXS measurements on various grafted and dispersed PS-silica samples were carried out by David Bucknall at the Advanced Photon Source (APS) at Argonne

National Lab (ANL) on the beamline 12-ID-C near the end of this project. The beam was run at an energy of 12 keV and a wavelength of 1.0332 Å. The samples were run in 1 mm path length quartz cells. The data was collected on a 2D MAR CCD SAXS camera and azimuthally averaged to the 1D I(Q) data using the in-house software.

3.3.8 Rheology

3.3.8.1 PBA-silica nanocomposites

Rheological measurements on poly(butyl acrylate)-silica samples in the melt were carried out on a Malvern Bohlin Gemini HR Nano equipped with a cone and plate geometry with a 20 mm diameter and 1° angle, using a gap size of 0.15 mm. Viscosity was measured in viscometry mode using a shear rate range of 0.2 - 100 s^{-1} at temperatures between 0 and 100 °C at 10 °C increments. Complex, elastic and viscous moduli were measured in oscillation frequency sweep experiments. Frequency sweeps were carried out from a frequency of 0.1 to 100 Hz at temperatures ranging between 20 and 80 °C, under constant stress conditions. Using time-temperature superposition, master curves were created from this data at a reference temperature of 50 °C.

Two different samples of poly(butyl acrylate) were used in rheological measurements, one below the molecular weight of entanglement, M_e = 28,000 g mol^{-1},[247] and one above. The low molecular weight PBA sample was prepared by an ERASMUS student, Annika Nebel, by adapting a literature procedure for ATRP of PBA[248]. The samples were then purified by passing over an alumina column and reprecipitation in methanol or methanol-water. The properties of the two samples are listed in Table 3.8.

Table 3.8: Properties of poly(butyl acrylate) used for rheology measurements

Sample	Sample name	Source	M_w /g mol^{-1}	M_n /g mol^{-1}
Poly(n-butyl acrylate)	H-PBA	Sigma-Aldrich	99,000	-
Poly(n-butyl acrylate)	L-PBA	Synthesised	9,000	~5,000

3.3.8.2 Polystyrene-fullerene stars

The viscosity of polystyrene-fullerene nanocomposites were measured in solution on two rheometers with two different geometries: (1) a Malvern Bohlin Gemini HR Nano

equipped with a cone and plate geometry with a 20 mm diameter and 1° angle, using a gap size of 0.15 mm for concentrated solutions and (2) a TA instrument AR-G2 at Napier University equipped with a double wall concentric cylinder geometry using a gap size of 2 mm for dilute solution measurements. The viscosity was measured against increasing shear rate; 0.01 to 10 s^{-1} was used for the cone and plate geometry measurements and 0.5 to 500 s^{-1} for the double wall geometry measurements.

3.3.9 Quasielastic Neutron Scattering (QENS)

3.3.9.1 QENS on PBA-silica samples

The QENS data on PBA-silica were collected previously by Natalie Grima[30]. QENS measurements were carried out on two instruments, (1) IN16 (Institut Laue-Langevin, France) and (2) IRIS (ISIS, Rutherford Appleton Laboratory, UK).

The measurements taken on the high flux cold neutron backscattering spectrometer IN16 were carried out in the temperature range of 1.8 to 573 K. The energy range covered in the experiment was –13 to 13 μeV, and the *Q* range varied from 0.2 to 1.9 $Å^{-1}$ with a resolution in energy of 1 μeV. The raw data was collected and treated according to the normal procedure (i.e. subtraction of empty cell, corrections for self-adsorption and detector efficiency), and then imported into Microsoft Excel.

QENS measurements on the high resolution back-scattering spectrometer IRIS were carried out in the temperature range 23 to 383 K. QENS data were collected using the PG002 analyzer, giving energy resolutions of 15 μeV for IRIS. The energy range covered in the experiment was –0.2 to 1.2 meV and the *Q* range varied from 0.5 to 1.8 $Å^{-1}$. A slab cell was used in all measurements giving a sample thickness of ca. 0.2 mm. This leads to a transmission of ca. 0.9 which ensures that multiple scattering effects are kept to a minimum.

The dynamic incoherent structure factor, S(Q,ω), was computed from the time-of-flight data, after subtracting the contribution of the empty cell and correcting for absorption, using standard software available at ISIS. The dynamic structure factor, S(Q,ω), was transformed into the time domain intermediate scattering function, I(Q,t) using Excel.

3.3.9.2 QENS on PS-fullerene stars

The QENS data on PS-fullerenes was collected by Dr Arrighi and Prof Bucknall during the course of this project. Elastic window scans were carried out on the backscattering spectrometer IN16B using a temperature range of 1.8 to 573 K. The energy range covered in the experiment was –13 to 13 μeV and the *Q* range varied from 0.2 to 1.9 $Å^{-1}$ with a resolution in energy of 1μeV. The raw data was collected, treated according to the normal procedure and then imported into Microsoft Excel for analysis.

QENS measurements were carried out on the same instrument in the temperature range 440 to 500 K. QENS data were collected using the Si(111) IN16 analyser, giving energy resolutions of 0.85 μeV. The energy range covered in the experiment was –31 to 31 μeV and the *Q* range varied from 0.1 to 1.8 $Å^{-1}$.

3.3.10 Microscopy

3.3.10.1 Spin/solvent casting of polymer blends

The phase separation of polymer blends was analysed using two microscopy techniques: Optical Reflection Microscopy (ORM) and Atomic-Force Microscopy (AFM). Both techniques require thin films of the blends to be cast onto appropriate substrates.

The blend samples for AFM measurements were spin cast from 1 wt% solutions in MEK onto silicon wafers. The silicon wafers were cut into 10 mm by 10 mm segments then washed thoroughly with MEK and dried with compressed air before being placed in a Nanoscan PSD Pro Series Ultraviolet Ozone cleaner to eliminate any organic material remaining on the substrate. Due to the low boiling point and high vapour pressure of MEK, the substrates and solutions were then placed in sealed containers into the fridge to cool before casting. The samples were dropped onto the substrate while it was spinning at 3000 rpm and then spun for 90 s to achieve uniform thin films with minimal surface defects. The resulting films had thicknesses between 80 and 120 nm.[248]

For optical microscopy measurements, thicker films were made by solvent casting 2 wt% solutions in MEK onto silicon wafers. Eight drops of the solution were dropped onto silica wafers (10 mm x 10 mm) which were placed in a closed petri dish along with an open vial of MEK. The extra solvent and covering was used to slow the rate of evaporation of solvent from the samples to create homogeneous films.

Once the films were spin or solvent cast onto the substrates, the films were air-dried for 24 hours, then placed into the vacuum oven at 100 ^{o}C to dry for a further 24 hours.

3.3.10.2 Optical Reflection Microscopy (ORM)

Time resolved in situ optical reflection microscopy was carried out using a Linkam hot stage THMS600 on an Olympus BX41M-LED microscope, using an Allied Vision Technologies camera to record images. The samples were heated to 120 ^{o}C at a ramp rate of 20 ^{o}C and then held for 5 minutes to equilibrate and remove any trapped glassy state portions in the thin films before heating to 300 ^{o}C at a rate of 3 ^{o}C/min. Images were taken at regular intervals or when the sample showed significant changes.

3.3.10.3 Atomic Force Microscopy (AFM)

The surface phase morphologies of polymer blends were characterised by tapping-mode atomic force microscopy (TM-AFM). The TM-AFM measurements were carried out at ambient temperature in air using an Innova AFM and probe. The height and phase images were recorded simultaneously.

Chapter 4. Structural study of polystyrene-fullerene stars

4.1 Introduction

The addition of nanoparticles to polymers has been shown to improve mechanical and thermal properties. Studying the effect of fillers on the structure of polymer chains is crucial in explaining the reinforcement effects seen in the macroscopic properties. Recently, SANS experiments have been used to study the changes in structure of entangled polymers and polymer nanocomposites where the chains have been grafted to the surface of a filler material[23, 121].

There is particular interest in star polymer nanocomposites containing a fullerene core, as grafting polymer chains to the surface of the fullerene overcomes their incompatibility[249]. Star polymers are also ideal systems for modelling the behaviour of branched systems due to the control over the number and molecular weight of the arms. The development of controlled polymerisation grafting techniques have allowed for the synthesis of well-defined polymer nanocomposites which are ideal for structural analysis. These systems are typically analysed in comparison to pure polymer stars, using the theory for branched star polymers and corresponding calculated R_g values.

There are few thorough neutron scattering studies in the literature on the structure of grafted polymer-fullerene stars. Picot *et al.*[123] studied 6 arm polystyrene-fullerene stars and found that polymer conformation is unaffected by grafting i.e. the nanocomposites behave like pure polystyrene stars. Prior DLS measurements on polymer-fullerene stars have also shown this behaviour[55]. However Lebedev *et al.* used the Guinier approximation to calculate radius of gyration (R_g) values[124, 206] and found that the arms are in a stretched conformation with higher R_g values than calculated for pure polymer stars. They also observed the presence of a dense polymer shell around the fullerene core.

In this work, the conformational behaviour of well-defined polystyrene-fullerene stars in solution was measured by DLS and SANS under good and theta solvent conditions. The stars were measured at a range of concentrations to study the structural behaviour in the dilute and the semi-dilute regions. Two molecular weights were chosen, one below and one above the molecular weight of entanglement of polystyrene. The details of the PS-C60 stars and corresponding linear PS arms studied are given in Section 3.3.6.1. Firstly, the method of incoherent background subtraction and the models used for the data analysis are outlined. The results of the data analysis are then

divided into the sections based on the solvent system used. Finally, the hydrodynamic radius measurements are given to compliment the results from the various SANS experiments. The SANS data presented in this chapter were analysed using a combination of Microsoft Excel and SasView[214], a Small-Angle Scattering analysis program containing many of the form factors used to analyse the data.

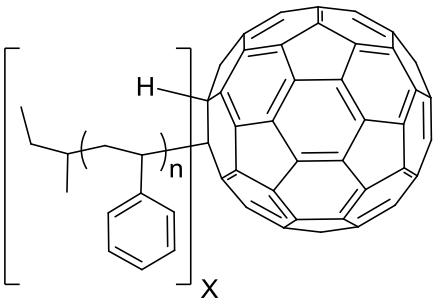

Figure 4.1: Chemical structure of PS-fullerene stars studied in the following chapter.

4.1 Background subtraction

Background scattering intensity resulting from incoherent scattering in the sample must be subtracted from the sample intensity in order to carry out quantitative analysis. The various methods detailed for incoherent background subtraction in Section 2.3.2 have been applied to the lowest measured concentrations (0.005 - 0.02 g ml^{-1}) of hydrogenated polystyrene measured on LOQ and SANS-II to find the appropriate background subtraction method. In all samples, the solvent has been subtracted by the programs used to reduce the data (MANTID/GRASP), as detailed earlier. Different molecular weights of polystyrene have also been compared. The molecular weight of the polymer should have no effect on the incoherent background scattering at the same concentration (g ml^{-1}) as there is the same number of protons in the sample. Thus, all polystyrene samples should have similar background scattering values.

Initially, the samples were fitted to the Debye model, described in Section 2.3.3, without a background. The fit for the lowest molecular weight and the highest molecular are shown in Figure 4.2. Although the Debye model without additional background describes the 2k HPS sample well, it is clear in the 105k HPS sample that there is additional background scattering that needs to be subtracted. Due to molecular weight having no effect on the incoherent scattering of a polymer at the same concentration, the lower molecular weight sample must also have additional background that must be subtracted.

Figure 4.2 shows that the scattered intensity does not reach a plateau at the highest *Q* value for the LOQ experiments of these samples, and this is a common occurrence in the other samples measured. This means that estimating the incoherent scattering from the scattered intensity at high scattering angles would significantly overestimate the background scattering and thus cannot be used consistently for the LOQ data.

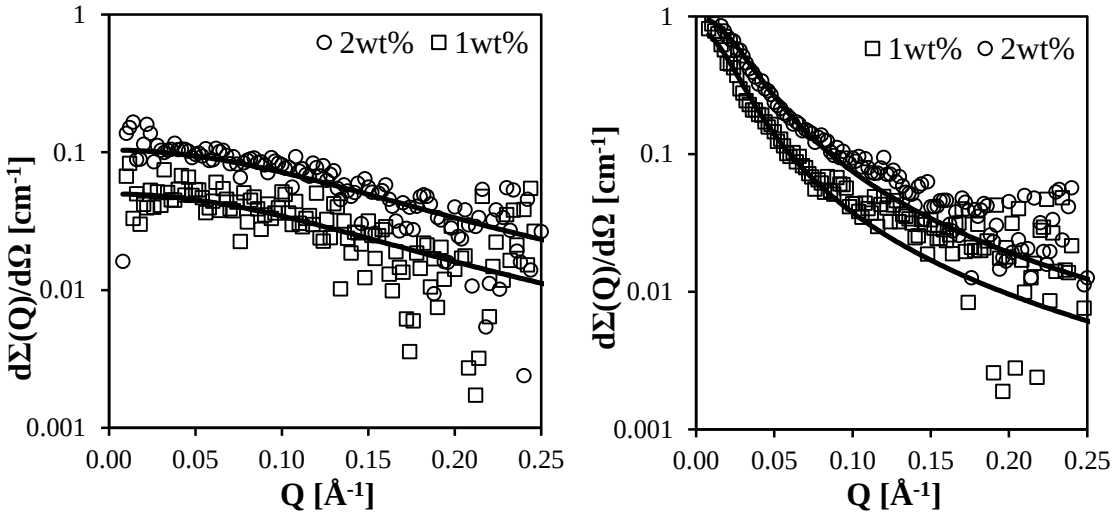

Figure 4.2: Debye Model fitted without a background for (a) 2k HPS and (b) 105k HPS in benzene.

The second method used was letting the fitting program determine the level of incoherent background for all three PS samples in dilute conditions and the results are listed in Table 4.1. This method gives very different results for all three polystyrene samples measured, with no background fitted at low molecular weight and a large background fitted at high molecular weight. The flat scattering of the lower molecular weight samples does not allow for accurate calculation of the incoherent background. Therefore, the value calculated for 105k HPS would be used for all samples. This method allows for an estimation of the level of background present, but is not reliable enough to use for quantitative analysis.

For LOQ data, the final possible method is to calculate the background level from a linear combination of the incoherent scattering intensity of the pure polymer in bulk using Equation (2.52). The incoherent background scattering is estimated from a volume fraction weighted hydrogenated polystyrene sample measured. Figure 4.3 shows the raw data and the calculated incoherent background for two polystyrene samples at varying volume fractions of hydrogenous chains and the average value for the

incoherent background scattering is listed in Table 4.1. Overall, the linear combination method provides good background subtraction for all three molecular weight samples at concentrations ranging from dilute to semi-dilute. This method will be used for all PS and PS-C60 data collected on LOQ presented in this thesis.

Table 4.1: Background calculated for LOQ HPS data by the various subtraction methods.

Sample	c /g ml^{-1}	$I_{inc}^{(a)}$ /cm^{-1}	$I_{inc}^{(b)}$ /cm^{-1}
PS 2k	0.009	0.0000	0.0066
	0.019	0.0000	0.0145
PS 16k	0.010	0.0063	0.0074
	0.019	0.0110	0.0140
PS 105k	0.010	0.0147	0.0072
	0.018	0.0208	0.0139

(a): Calculated with least squares analysis in Excel.

(b): Calculated from incoherent scattering of the pure H component from a previously measured solid PS sample in the melt using Equation 2.52.

While the transmission method cannot be used on the LOQ data, it can be applied to the SANS-II data and then compared to the method used for LOQ data. Using Equations 2.51 and 2.52, the background values were calculated and tabulated in Table 4.2 along with the values calculated using the linear combination method.

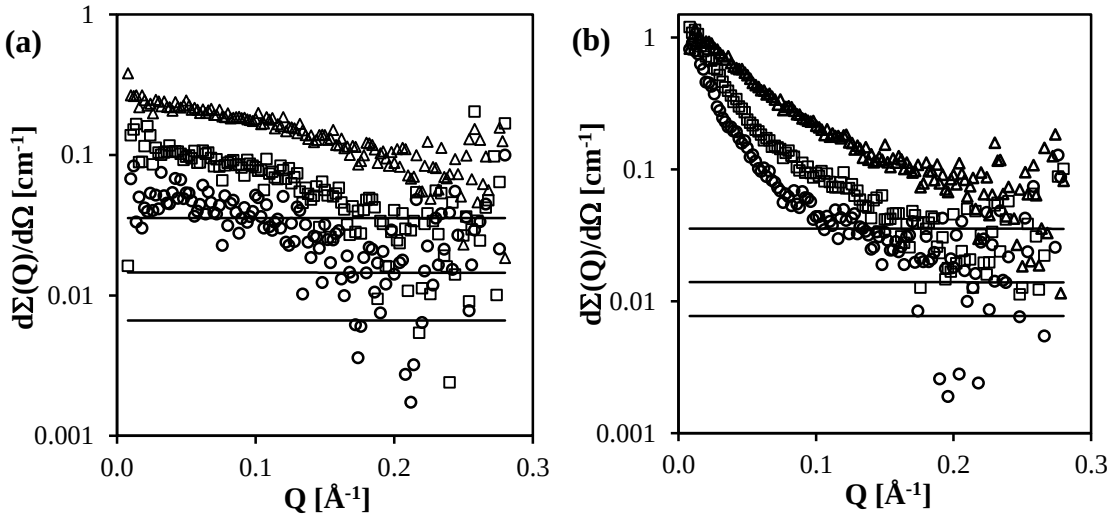

Figure 4.3: Raw data from LOQ (symbols) and calculated background using Equation 2.52 (solid line) for (a) HPS 2k and (b) HPS 105k in benzene at various volume fractions 0.008 and 0.009 (), 0.018 and 0.018 (□), 0.044 and 0.045 (Δ).

Table 4.2: Incoherent background calculated for D22 data of hydrogenated polystyrene stars

Sample	c /g ml^{-1}	$I_{inc}^{(a)}$ /cm^{-1}	$I_{inc}^{(b)}$ /cm^{-1}	$I_{inc}^{(c)}$ /cm^{-1}
hPS 2k	0.005	0.0449	0.0424	0.0357
	0.010	0.0738	0.0747	0.0648
hPS 16k	0.002	0.0183	0.0178	0.0149
	0.005	0.0450	0.0423	0.0359

(a): Average value of total scattering intensity at the *Q* range 0.5 – 0.6 Å^{-1}.
(b): Calculated from measured transmissions using Equation 2.51.
(c): Calculated from incoherent scattering of the pure H component using Equation 2.52.

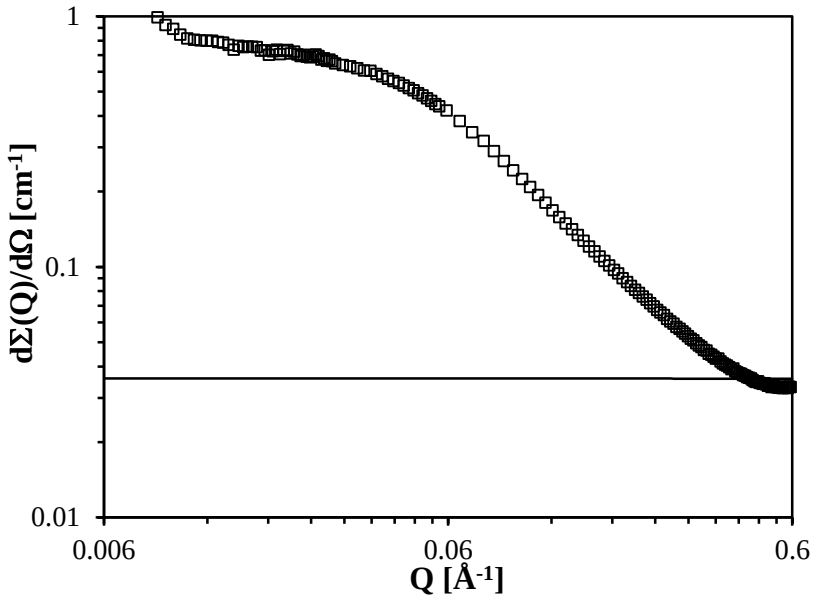

Figure 4.4: D22 data of 5 wt% PS in toluene solution showing the average calculated background from both the transmission and linear combination volume fraction method. The incoherent background scattering is overestimated, leading to a background higher than scattered intensity.

The values for all methods are comparable. For analysis of the D22 and SANS-II data an average of the values obtained using Equations 2.51 and 2.52 will be used for the incoherent background for dilute solutions. At higher concentrations, however, the incoherent background is overestimated, even using the linear recombination method that is used for the LOQ data (Figure 4.4). To correct this, the background will be adjusted using a concentration dependent coefficient fitted using least squares analysis.

4.2 Models for polymer and polymer-nanocomposite analysis

For analysis of the linear polymer chains, the excluded volume model was first considered (Equation (2.56)). This model was tested on a linear sample, and it showed that the polymer is described as a Gaussian chain (ν = 0.5, m = 2) and thus the model

simplified to the Debye model (Equation (2.54)). The standard Gaussian polymer chain form factor using the Debye formula[200] was therefore used for fitting the variation in scattered intensity.

For polymer solutions in the semi-dilute regime, the Debye model is no longer appropriate. Therefore, the semi-dilute data for linear polymer samples were analysed using an Ornstein-Zernike (OZ) equation[250] containing a Porod contribution:

$$I(q) = \frac{A}{Q^n} + \frac{C}{1 + (Q\xi)^m} \tag{4.1}$$

where the first term describes the Porod scattering from clusters and the second term is a Lorentzian function for the scattering from the polymer chains. This model is called the CorrLength model in SasView[250].

In the case of the PS-fullerenes nanoparticles, the structures are assumed to be well-defined 6 arm stars with a fullerene core. Thus, the polymer star model described in chapter 2 is a good starting point for analysis. The typical model used to fit the structure of the PS-fullerene stars is the Gaussian star form factor[215] (Equation (2.58)) described by the Benoit function (See Section 2.3.3).

To test the validity of the star model for the PS-fullerene samples, Equation (2.58) was applied to LOQ data of both the hydrogenous stars with the core contrast matched to the solvent and deuterated stars where the core has a different SLD to the chains and the solvent. In the hydrogenated samples, the star model is expected to fit well, as the core scattering should have no effect on the form factor and this is shown in Figure 4.5. However, in the deuterated samples the star model fails to describe the data, especially at high *Q*. Initially this may look like an additional background that needs to be subtracted; however both the incoherent scattering from the solvent and the coherent scattering from the deuterated chains have already been subtracted. This suggests that the core scattering is part of the form factor, especially at high *Q*. Thus, the star model is only applicable when the core is not seen due to contrast matching with the solvent.

A more complex model is therefore required for the PS-fullerene stars, one that takes into account the scattering from the fullerene core. In the literature, a core-star model form factor has been calculated for spheres with Gaussian chains attached[123]:

$$P(Q)_{c-star} = \frac{1}{\left(\Delta\rho_{sph} + f\Delta\rho_a\right)^2}\left\{\Delta\rho_{sph}{}^2 F_{sph}{}^2(Q) + \Delta\rho_a{}^2\left[fP_a(Q) + f(f-1)P_{aa}(Q)\right] + 2f\Delta\rho_{sph}\Delta\rho_a P_{sa}(Q)\right\} \tag{4.2}$$

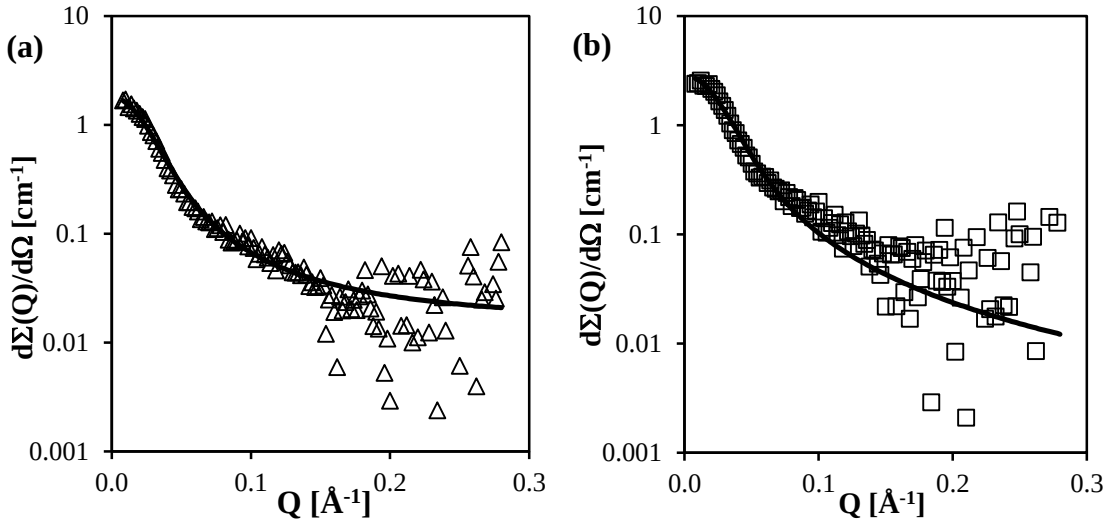

Figure 4.5: Star model fits (solid line) of (a) 16k HStar (Δ) and (b) 18k DStar (□) (2 wt% solutions in benzene).

where $\Delta\rho_a$ is the excess in scattering density of the arm and $\Delta\rho_s$ is the excess in scattering density of the spherical core. $F_{sph}(Q)$ is the scattering amplitude of a hard sphere[200]:

$$F_{sph}(Q) = \frac{9}{(qR_{sph})^6}\left(\sin(QR_{sph}) - QR_{sph}\cos(QR_{sph})\right)^2 \quad \textbf{(4.3)}$$

$P_a(Q)$ is the normalised intra-molecular form factor of the arms using the standard Debye formula (Equation (2.54)), where the radius of gyration is of a single arm. $P_{aa}(Q)$ is the normalised inter-molecular form factor[123]:

$$P_{aa}(Q) = \left(\frac{\sin(QR_a)}{QR_a}\right)^2\left(\frac{\left(1-\exp^{-Q^2R_a^2}\right)}{Q^2R_a^2}\right)^2 \quad \textbf{(4.4)}$$

and $P_{sa}(Q)$ is the form factor from cross-correlations between the sphere and the arms:

$$P_{sa}(q) = F_{sph}(Q)\left(\frac{\left(1-\exp^{-q^2R_a^2}\right)}{q^2R_a^2}\right)\left(\frac{\sin(qR_{sph})}{qR_{sph}}\right) \quad \textbf{(4.5)}$$

The different components of the core-star model are plotted in Figure 4.6 to show how the sphere affects the form factor fit of the PS-fullerene stars in 18k DStar and 16k HStar respectively. In the 16k HStar sample, the matching solvent and core SLDs mean that the scattering seen from the fullerene core is negligible. Although there are still sphere-star correlations, the star form factor is a factor of ~10^3 higher than these correlations and thus they also have little effect on the overall fit. For the 18k DStar sample, it is clear that the additional sphere form factor has a higher scattering intensity at high Q than the PS chains and changes the overall shape of the form factor.

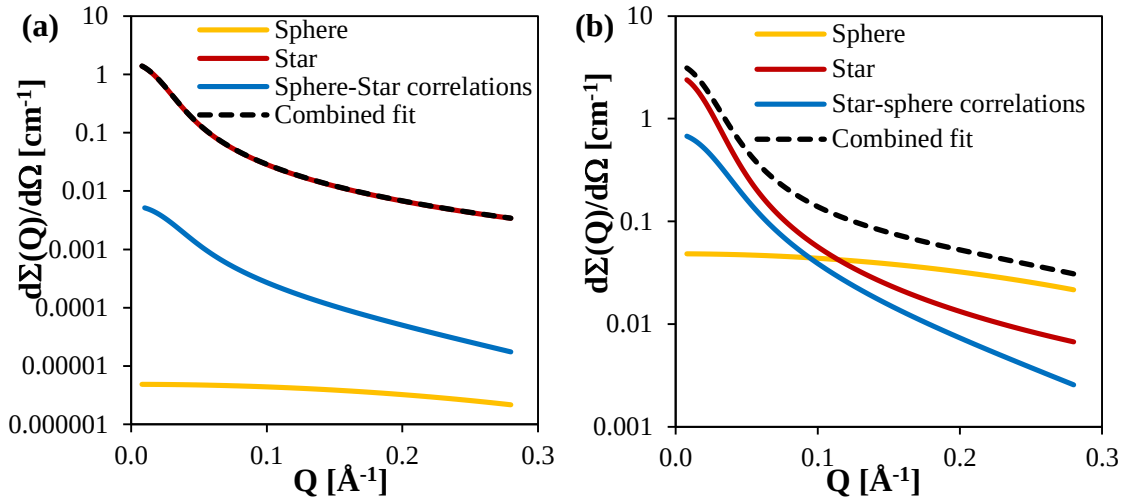

Figure 4.6: Components of the core-star model (Equation (4.2)) for (a) a core contrast matched 16k star sample (b) a non-contrast matching 16k star sample including scattering from the 5Å core.

As with the star model, the core-star model was then applied to LOQ data of both the hydrogenous and deuterated stars (Figure 4.7). The core-star model fits both the HStar data, where the core-star model is reduced to the star model, and the DStar data over the whole *Q* range of the experiment. The core-star model was then applied to all dilute SANS data for PS-fullerene stars. The results of this model analysis are reported later in this chapter.

One of the limitations of the star and core-star models is that these do not take into account excluded volume effects. Alternative, more complex methods of analysing scattering data are therefore required.

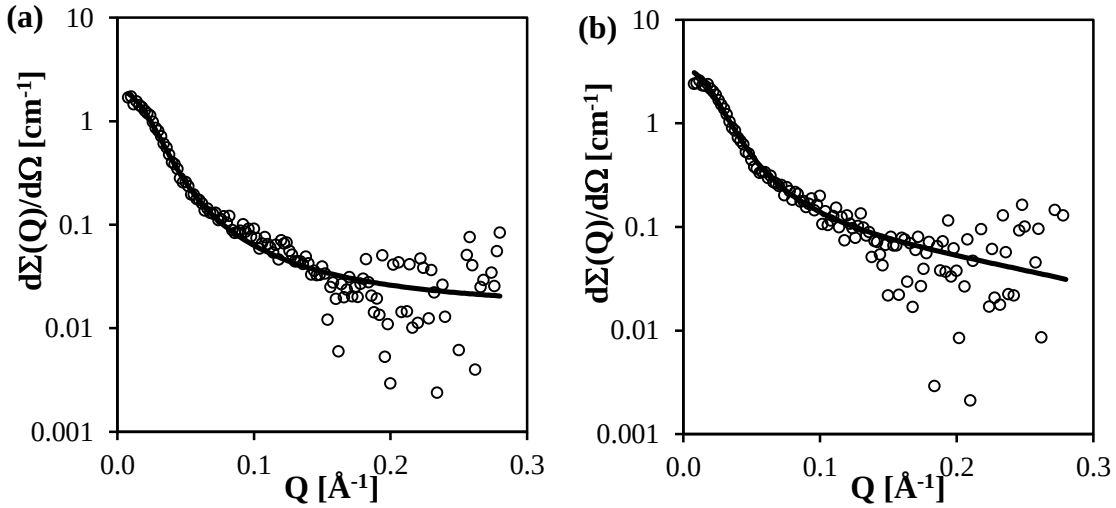

Figure 4.7: Core-star model fits (solid line) of (a) 16k HStar (Δ) and (b) 18k DStar (□) data (2 wt% solutions in benzene).

Daoud and Cotton[251] suggested a theoretical scaling approach where the star is considered to have three regions (Figure 4.8). The first is a dense core where the chains are close-packed. In PS-fullerene stars, the soft core is replaced by a hard fullerene core. Then, as the distance from the core increases, the chain conformation is considered a concentrated solution of blobs of size $\xi(r)$. As the distance increases further, the conformation is of a semi-dilute solution of blobs. The scaling regimes are defined by three characteristic lengths: The radius of gyration of the star R_{star}, blob size $\xi(r)$ and monomer size, σ.

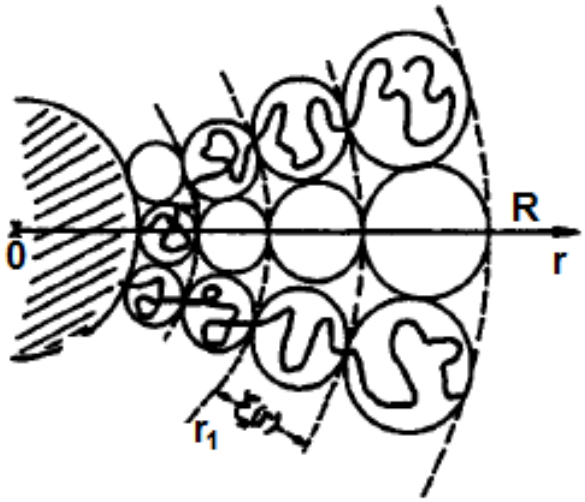

Figure 4.8: Representation of the Daoud-Cotton model showing various regions within an individual polymer star[251].

The Daoud-Cotton model also allows for prediction of the form factor of a polymer star with excluded volume effects by determining the Q dependences at various points in the curve and the point of onset of the asymptotic range. The first region is the typical Guinier regime ($QR_g < 1$), characterised by a flat plateau. The intermediate range ($1 < QR_g < f^{1/2}$) has a Q^{-3} dependence for Gaussian statistics. The asymptotic regime occurs at $QR_g > f^{1/2}$, and shows a Q^{-2} dependence in Gaussian chains. The origin of the values presented here are given in more detail in the appropriate reference[251].

A similar model from Marques *et al.*[252] predicts slightly different values for the Q dependences and the onset of the asymptotic regime, using the characteristic power laws for the form factor. After the Guinier regime, the intermediate region has a $Q^{-10/3}$ dependence and the asymptotic regime starts at $QR_g \sim f^{2/5}$ with a $Q^{-5/3}$ dependence for swollen polymer chains.

4.3 Analysis of linear polymer chains

Figure 4.9 shows examples of 2k and 16k HPS data overlapping on two different instruments, one in dilute and one in semi-dilute conditions. This is a trend seen on all instruments, all PS samples and all concentrations. Therefore, there is no need to analyse the same concentrations on different instruments. The analysis on PS chains presented within this thesis will be a mixture of the LOQ, D22 and SANS-II data, depending on the concentrations and solvent conditions (i.e. good or θ solvent) measured on each instrument.

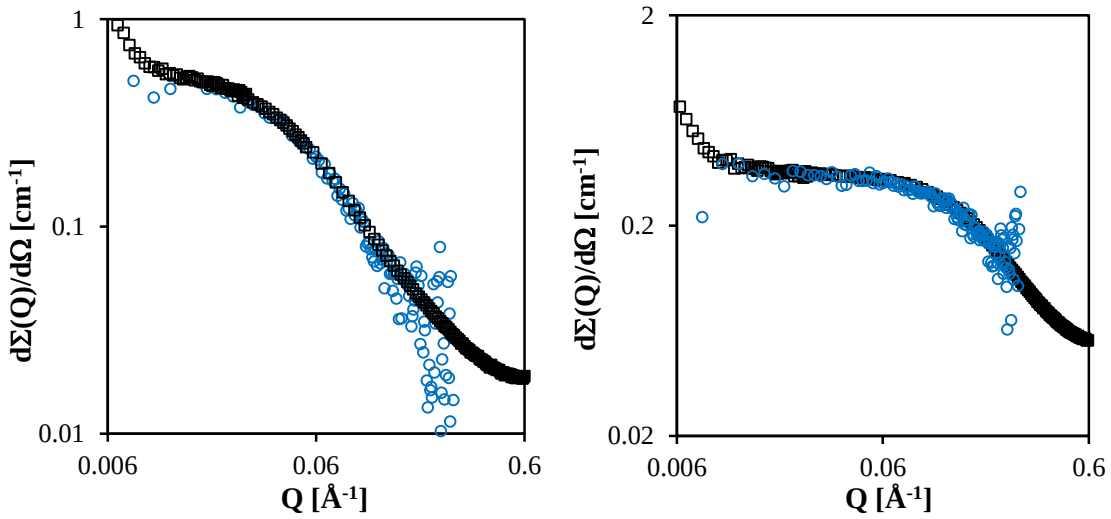

Figure 4.9: Example comparison of LOQ (○) and D22 data (□) of (a) 16k HPS at 2 wt% in a good solvent and (b) 2k HPS at 10 wt% in a good solvent.

On LOQ, the linear HPS samples were measured in benzene solution at various concentrations ranging from 0.01 g ml^{-1} to 0.2 g ml^{-1}. On D22, the concentration range was extended further, from 0.005 g ml^{-1} to 0.3 g ml^{-1}. This range covers the dilute and semi-dilute regions of concentration; therefore it is important to know the overlap concentration. The overlap concentration can be calculated using the following Equation:

$$c^* = \frac{3M_w}{4\pi N_A R_g^3} \tag{4.6}$$

where N_A is Avogadro's constant. Experimentally, the radius of gyration of linear polystyrene in benzene has been found to obey the following relationship[253]:

$$R_g[nm] = 1.21 \times 10^{-2} M_w^{0.595} [g\ mol^{-1}] \tag{4.7}$$

An almost identical relationship has been seen in toluene:

$$R_g[nm] = 1.20 \times 10^{-2} M_w^{0.595} [g\ mol^{-1}] \quad \textbf{(4.8)}$$

However, in cyclohexane (a theta solvent), the relationship is[253]:

$$R_g[nm] = 2.42 \times 10^{-2} M_w^{0.512} [g\ mol^{-1}] \quad \textbf{(4.9)}$$

where M_w is the molecular weight of the polymer. Equation (4.7) has been used to calculate the expected radius of gyration in dilute benzene solutions, which is then compared to the experimental results. The calculated R_g and c^* values for our linear PS chains in benzene are shown in Table 4.3.

The Debye model was used to fit all the linear PS in dilute solution data. An example of the Debye fits for dilute solution behaviour is shown in Figure 4.10 for the 16k HPS sample. The radius of gyration values extracted from the Debye model fit for samples below the critical overlap concentration are shown in Table 4.4.

Table 4.3. Overlap concentration and radius of gyration values calculated using Equations (4.6) and (4.7) for various molecular weights of PS in benzene.

M_w /g mol^{-1}	R_g /Å	c* (g ml^{-1})
2000	11.1	0.573
16000	38.4	0.112
105500	117.9	0.025

Table 4.4: Radius of gyration results for linear PS in benzene.

Sample	c /g ml^{-1}	R_g /Å
PS 2k	0.009	12.1 ± 0.9
	0.019	11.9 ± 0.8
	0.047	11.4 ± 0.7
	0.087	10.6 ± 1.0
	0.158	9.0 ± 1.1
PS 16k	0.010	36.6 ± 2.4
	0.019	32.7 ± 1.5
	0.045	25.1 ± 0.8
	0.091	18.3 ± 0.8
PS 105k	0.010	71.4 ± 4.3
	0.018	59.0 ± 3.0

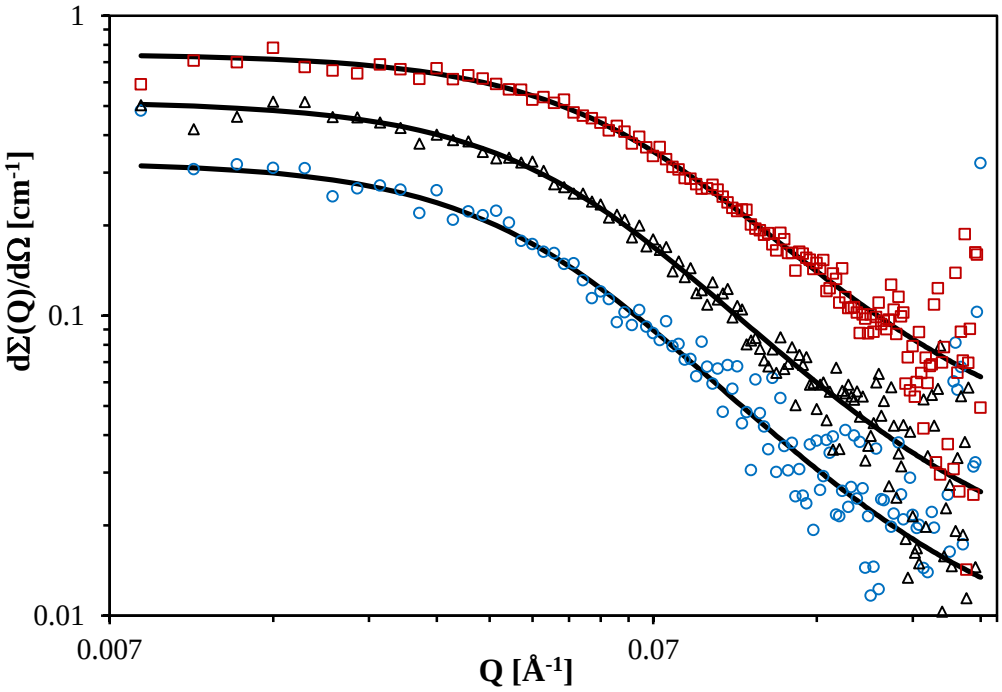

Figure 4.10: Debye model fits for 16k HPS in benzene at various concentrations: 1 wt% (○), 2 wt% (Δ) and 5 wt% (□).

The results show that the Debye model fits the linear polymer data well up to the overlap concentration in all samples. Beyond the overlap concentration, a different model is needed as semi-dilute solutions are characterised by a correlation length, ξ, rather than a radius of gyration. The Ornstein-Zernike form in Equation (4.1) was used to model the semi-dilute solutions of linear PS chains (Figure 4.11).

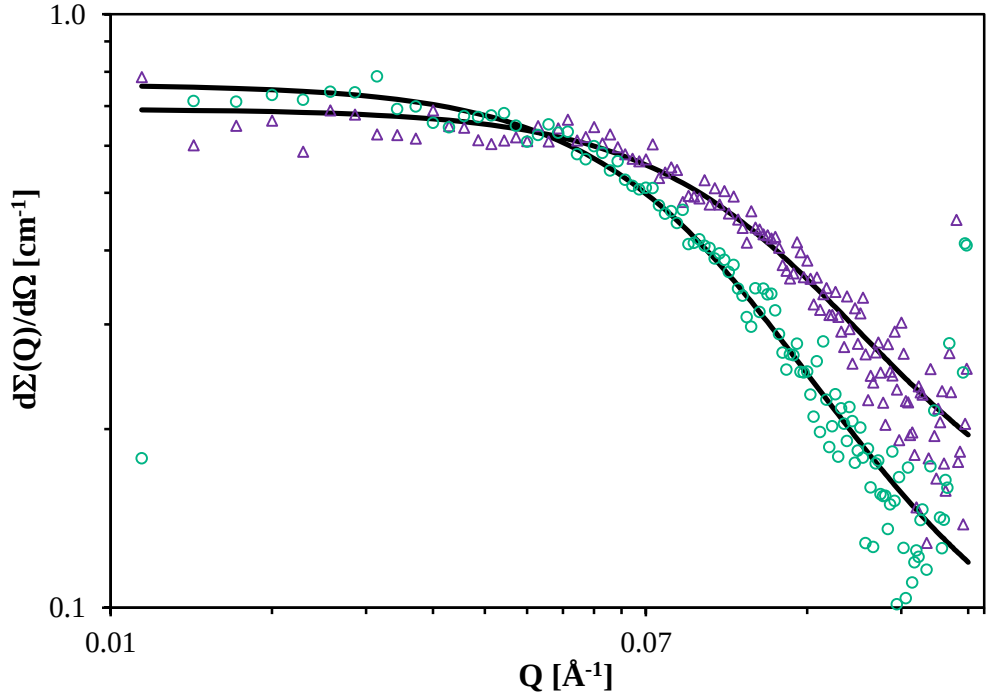

Figure 4.11: Model fits for 16k HPS in benzene at concentrations (○) 10 wt% and (Δ) 20 wt%.

The calculated correlation length values for the semi-dilute solutions of the linear polystyrenes are listed in Table 4.5. The concentration dependence of the correlation length is predicted by scaling theory as $\xi \propto c^{-v/(3v-1)}$. Using v = 0.588 for PS in a good solvent, this means that theoretically $\xi \propto c^{-0.77}$. The exponent measured here from the PS 105k data gives an exponent value of -0.772, also showing excellent agreement with the existing literature[53]. The correlation length has been shown in the literature[254] to follow the power law below:

$$\xi\,[\mathrm{nm}] = 0.27 \pm 0.1\; c\;[g/ml]^{-0.72\pm0.01} \qquad \textbf{(4.10)}$$

A wider scaling including the different molecular weights of the PS chains measured is found[255]:

$$\frac{\xi}{\mathrm{R}_g} = \left(1 + \beta \frac{c}{c^*}\right)^{\alpha} \qquad \textbf{(4.11)}$$

The structural characterisation and modelling of the linear polystyrene chain arms shows good agreement with literature values, showing the background scattering and data analysis methods used are accurate and thus suitable for analysing the PS-fullerene stars.

Table 4.5: Correlation length values for semi-dilute PS solutions in benzene.

Sample	c /g ml^{-1}	ξ/Å	m	n	A	C	error
PS 16k	0.091	10.7	2.48	1.05	7.7x10^{-4}	0.63	± 5%
	0.156	7.29	2.30	1.07	7.0x10^{-5}	0.65	± 5%
PS 105k	0.047	20.3	2.49	1.07	7.7x10^{-4}	0.87	± 3%
	0.081	13.0	2.49	1.07	1.2x10^{-3}	0.73	± 3%
	0.164	7.72	2.49	1.05	1.1x10^{-4}	0.64	± 4%

4.4 Analysis of PS-fullerene star solutions

Measurements on PS-fullerene stars have been carried out in good solvents and in theta solvents on LOQ (benzene and toluene), D22 (toluene) and SANS-II (cyclohexane). The scattering length densities (SLDs) of the components of the two types of samples and the solvents were calculated using Equation (4.12) and are listed in Table 4.6.

$$\rho_b = \frac{\Sigma b_i \rho N_A}{m_o} \qquad \textbf{(4.12)}$$

Table 4.6: Scattering length parameters for sample components and solvents.

Sample	b_{coh} /fm	m_o /g mol^{-1}	ρ /g cm^{-3}	SLD /10^{-10}cm^{-2}
hPS	23.24	104.2	1.04	1.41
d_8PS	106.6	112.2	1.13	6.46
C60	398.8	720.6	1.65	5.50
h-benzene	17.43	78.11	0.88	1.18
h-cyclohexane	-5.02	84.16	0.78	0.28
d_6-benzene	79.96	84.15	0.95	5.43
d_{12}-cyclohexane	119.9	96.23	0.89	6.70
d_8-toluene	99.96	100.2	0.94	5.66

Pure polymer stars have been studied extensively in the literature. The expected radius of gyration of a star polymer in a good solvent can be calculated from the following equation[256]:

$$R_{star} = 0.0756\, M_{star}^{0.6} \quad \textbf{(4.13)}$$

and the expected radius of gyration in a theta solvent is calculated by:

$$R_{star} = 0.183\, M_{star}^{0.5} \quad \textbf{(4.14)}$$

Across all the experiments, PS-fullerene solutions were measured at concentrations from 0.005 to 0.2 g ml^{-1} to cover both the dilute and semi-dilute regions. The overlap concentration for a typical polymer star can be calculated using the following equation:

$$c^* = \frac{3M_{star}}{4\pi N_A R_{star}^3} \quad \textbf{(4.15)}$$

The expected R_g and c^* values for the stars in good and theta solvent conditions are given in Table 4.7.

Table 4.7. Radius of gyration and overlap concentration values calculated from theory.

	Good solvent			Theta Solvent		
Sample	**R_{star} /Å**	**R_a /Å**	**c***	**R_{star} /Å**	**R_a /Å**	**c***
2k HStar	21.5	13.2	0.48	20.6	12.6	0.57
16k HStar	72.6	44.5	0.09	56.9	34.9	0.21
2k DStar	21.9	13.4	0.48	20.6	12.6	0.57
18k DStar	79.5	48.7	0.09	60.3	37.0	0.20

4.4.1 PS-fullerene stars in cyclohexane (SANS-II)

On the SANS-II instrument, the PS-fullerene stars were measured in a theta solvent (cyclohexane). For stars in cyclohexane, the Benoit star model and the core-star model should fit the data, as excluded volume effects can be ignored in theta solvents at the theta temperature[67].

The Kratky plots from the SANS-II data on PS-fullerenes in cyclohexane (Figure 4.12 and Figure 4.13) show the characteristic maximum before falling to the asymptotic plateau. The Kratky plot also shows that the core-star model is in good agreement with the experimental data, modelling both the peak and the plateau. The Benoit model for star polymers is therefore appropriate for dilute solutions of star polymers in Θ solvents, and seems to be a good fit for the PS-fullerene star data.

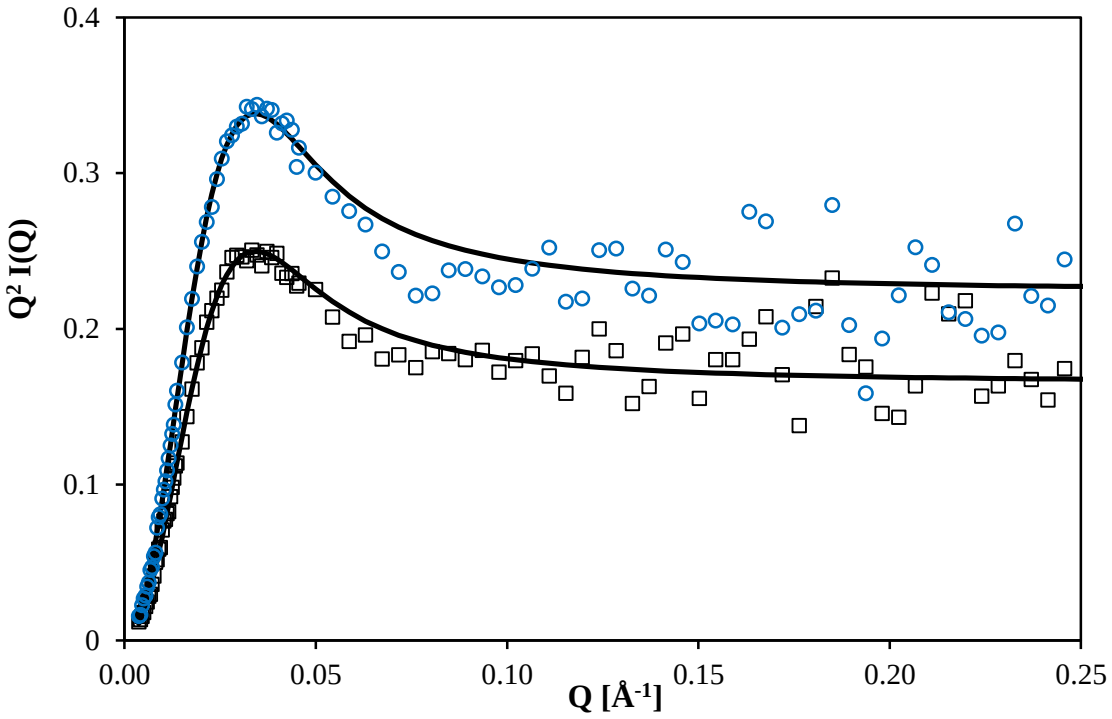

Figure 4.12: Kratky plot of 18k DStar in cyclohexane measured on SANS-II at 30 ºC (○) and 40 ºC (□) with the calculated curve from the core-star model (Equation (4.2)).

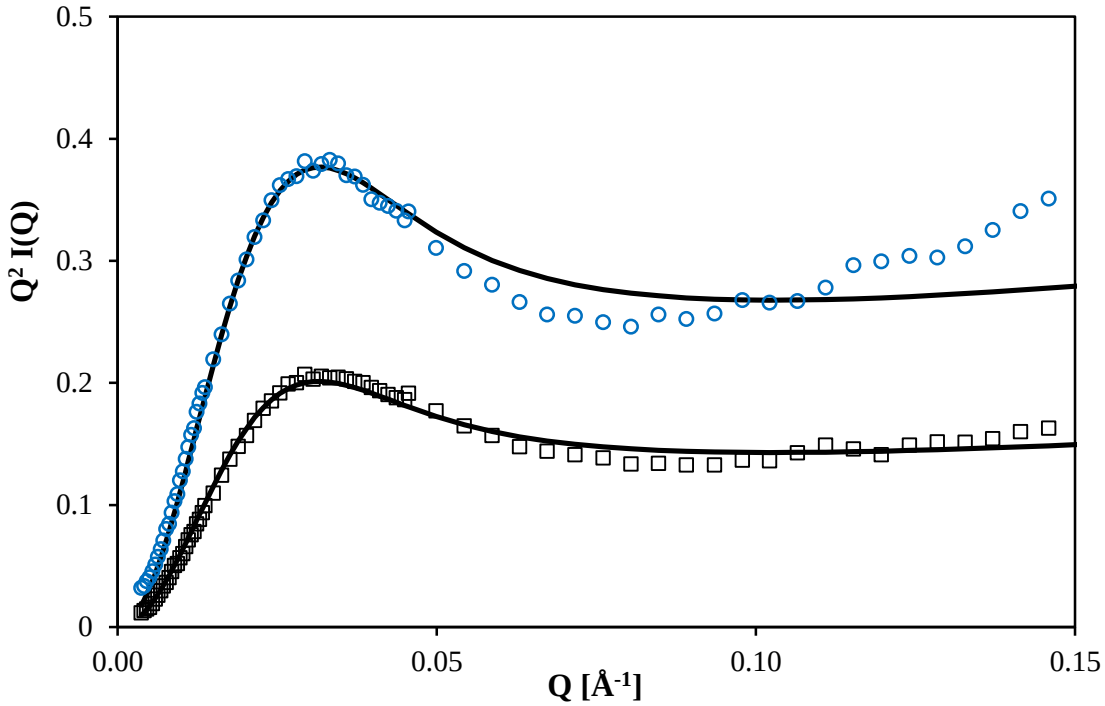

Figure 4.13: Kratky plot of 16k HStar in d-cyclohexane at 25 ºC, 1 wt% (□) and 2 wt% (○) in solution with the calculated curve from the core-star model.

The core-star model was applied to all the data obtained from the SANS-II experiments. The samples were measured at various temperatures (25 to 50 ºC) as well as concentrations (all in the dilute regime, 0.5 to 2 wt%). Qualitatively, it can be seen in the 16k HStar sample at 25 ºC (Figure 4.14) that there are slight excluded volume effects in the intermediate to high *Q* range that are not present in the solutions at 40 ºC (Figure 4.15). The literature θ temperature for the polystyrene-fullerene system is 35 ºC,[257] thus when measured at 25 ºC, the temperature of the system is sufficiently far away from the theta temperature that small excluded volume effects are present, causing deviations from the predicted star model behaviour. Effects in the intensity values are also seen, as *I*(0) generally increases when the temperature is farther from the theta temperature (Table 4.8). A virial coefficient may be required to model this effect.

However, in general the core-star model fits the 16k HStar and 2k HStar data (Figure 4.16) well, especially close to the predicted theta temperature. The core-star model also fits the DStar samples in h-cyclohexane, as shown in Figure 4.17 for 18k DStar. The core-star fits for the other samples at various temperatures are shown in Appendix A.

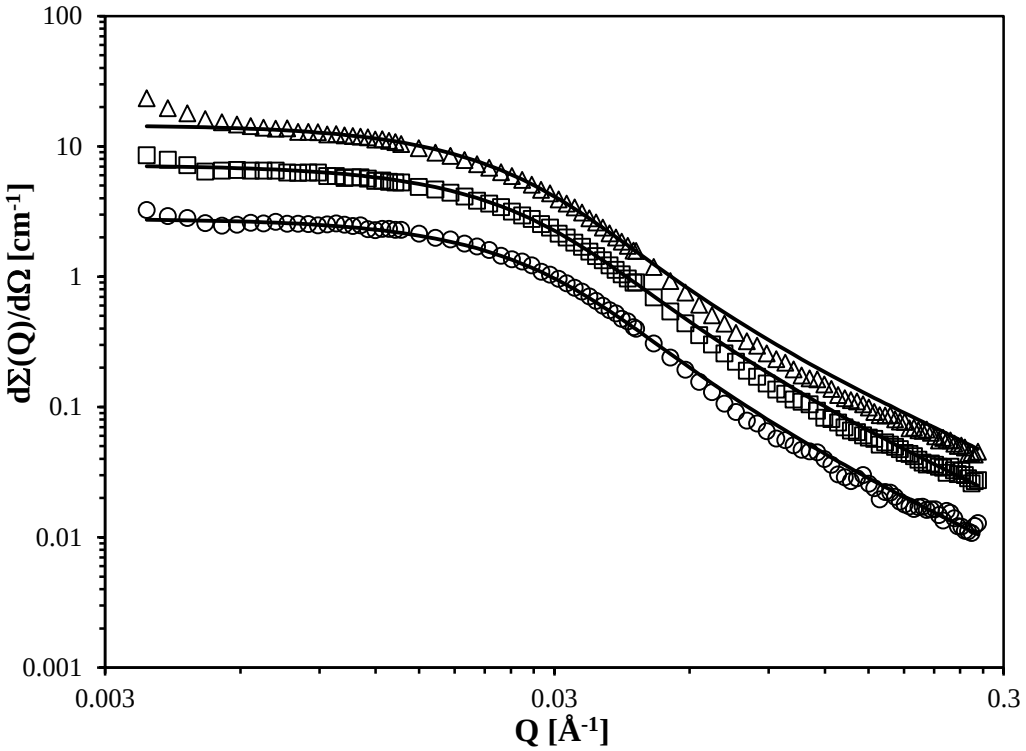

Figure 4.14: Core-star model fits on a log-log scale for 16k HStar data at 25 ºC and 0.5 wt% (○), 1 wt% (□) and 2 wt% (Δ) concentration in d-cyclohexane solution

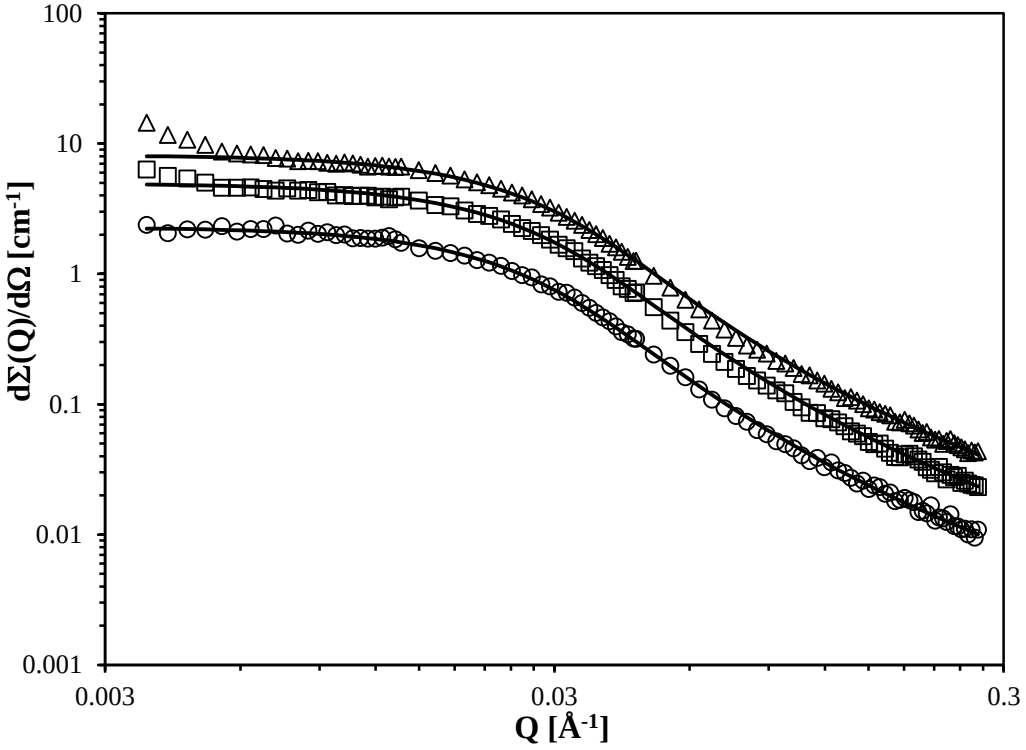

Figure 4.15: Core-star model fits on a log-log scale for 16k HStar data at 40 ºC and 0.5 wt% (○), 1 wt% (□) and 2 wt% (Δ) concentration in d-cyclohexane solution

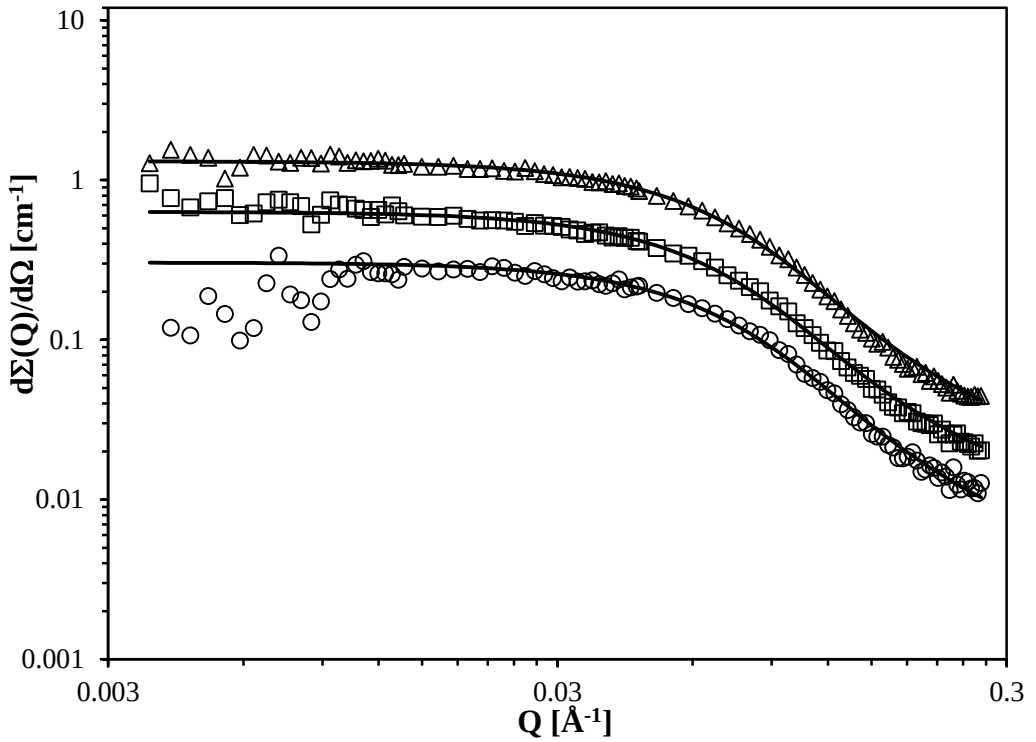

Figure 4.16: Core-star model fits on a log-log scale for 2k HStar data at 40 ºC and 0.5 wt% (○), 1 wt% (□) and 2 wt% (Δ) concentration in d-cyclohexane solution

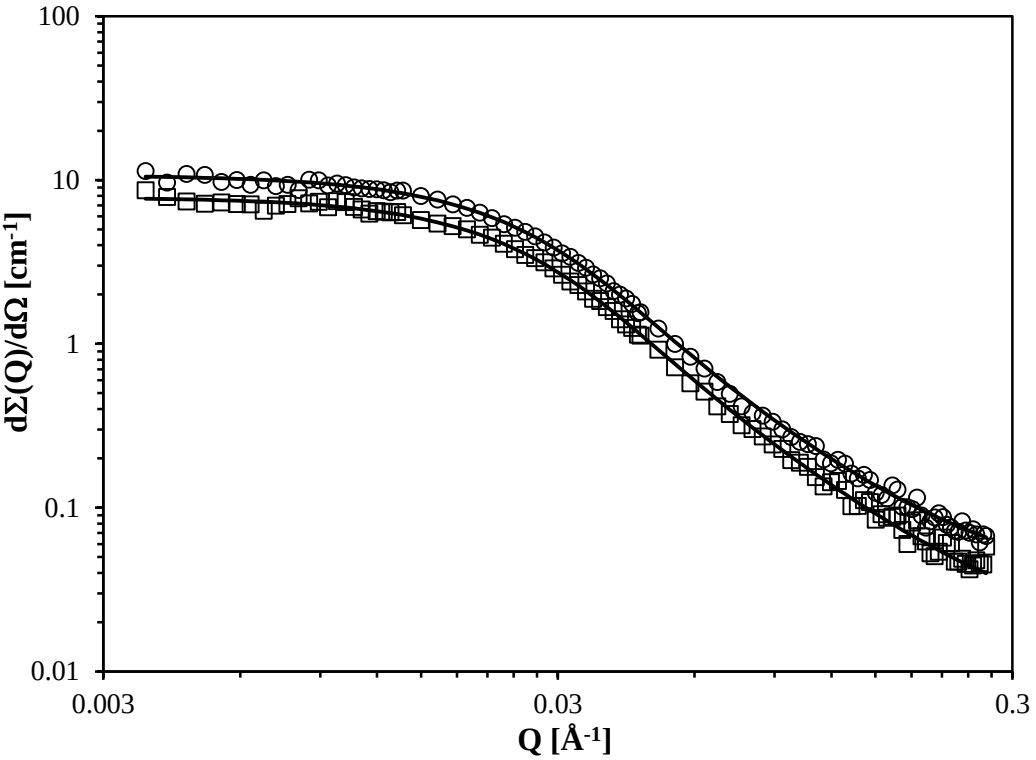

Figure 4.17: Core-star model fits on a log-log scale for 18k DStar in cyclohexane at 30 ºC (○) and 40 ºC (□) with the calculated curve from the core-star model.

The fitting parameters obtained from the core-star model are listed in Table 4.8. The radius of gyration results at the temperature nearest the theta temperature (40 ^{o}C) are plotted in Figure 4.18. It is clear that the radius of gyration values for both star samples are larger than the calculated values for pure star polymers in theta solvents.

Table 4.8: Core-Star model fitting parameters for PS-fullerene stars in cyclohexane.

Sample	Temperature /^{o}C	c /g ml^{-1}	Core-Star model		
			R_{star} /Å	R_a /Å	I(0)
2k HStar	30	0.005	23.3 ± 1.2	14.3 ± 0.7	0.53
		0.010	24.0 ± 0.8	14.7 ± 0.5	0.94
		0.021	23.9 ± 0.7	14.6 ± 0.4	1.41
	40	0.005	23.0 ± 1.6	14.1 ± 1.0	0.30
		0.010	**24.5 ± 1.0**	15.0 ± 0.6	0.63
		0.021	23.9 ± 0.7	14.6 ± 0.4	1.30
	50	0.010	23.8 ± 0.9	14.6 ± 0.5	0.81
		0.021	24.3 ± 0.8	14.9 ± 0.5	1.41
16k HStar	25	0.005	63.4 ± 2.4	38.8 ± 1.5	2.78
		0.012	67.1 ± 1.5	41.1 ± 0.9	7.18
		0.020	70.6 ± 1.3	43.2 ± 0.8	14.6
	40	0.005	65.3 ± 2.8	40.0 ± 1.7	2.27
		0.012	**62.9 ± 1.7**	38.5 ± 1.0	4.93
		0.020	60.8 ± 1.3	37.3 ± 0.8	8.14
	50	0.005	63.9 ± 2.9	39.2 ± 1.8	1.97
		0.012	61.3 ± 1.4	37.6 ± 0.8	5.28
		0.020	58.1 ± 1.3	35.6 ± 0.8	6.89
2k DStar	30	0.012	22.4 ± 0.5	13.7 ± 0.4	1.74
	40	0.012	**22.4 ± 0.6**	13.7 ± 0.4	1.25
18k DStar	30	0.011	64.7 ± 0.9	39.6 ± 0.5	10.7
	40	0.011	**64.6 ± 0.9**	39.6 ± 0.6	7.84

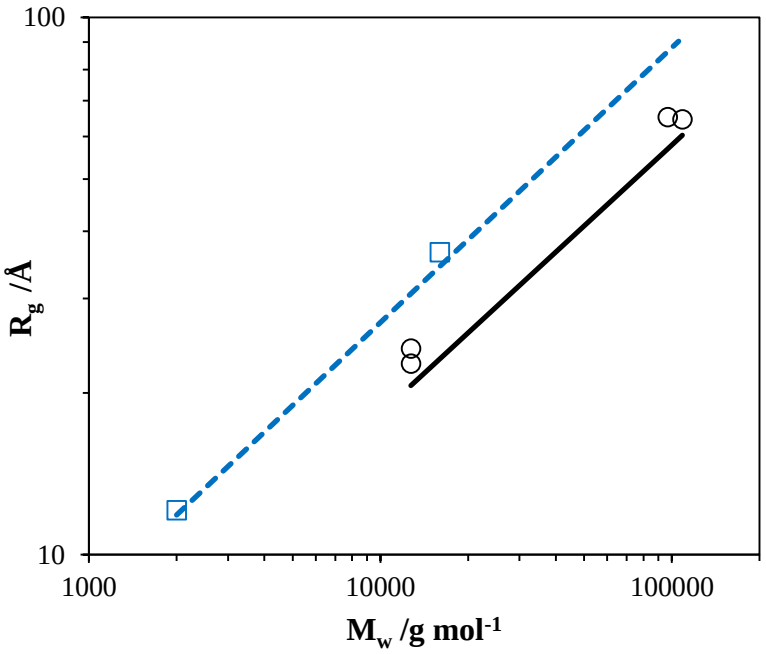

Figure 4.18: Experimental and calculated radius of gyration results for linear (□) and PS-fullerene stars (○) at 1 wt% and 40ºC in cyclohexane (see bolded R_{star} data in Table 4.8). The lines show the calculated R_g values using Equations (4.9) and (4.14) for linear (—) and star polymers (---) respectively.

4.4.2 PS-fullerene stars in benzene (LOQ)

PS-fullerene samples were measured under two contrast conditions: 1) non-contrast matching conditions to see the scattering from the chains and the fullerene core and 2) contrast matching the solvent with the core to see only the polymer scattering (see Section 2.3.5). The hydrogenated samples were dissolved in deuterated benzene and toluene and the deuterated PS samples were dissolved in hydrogenated benzene. Using Table 4.6 we can see that the SLD of the fullerene core is similar to the SLD of d_6-benzene and d_8-toluene. This means that in these hydrogenated samples, we should only see the scattering contribution from the PS chains, whereas in the deuterated samples we would see both the core and the chains in the scattering intensity. HPS-fullerene (HStar) solutions in d_6-benzene were measured at concentrations from 0.01 to 0.2 g ml^{-1}. The d_8PS-fullerene (DStar) samples in benzene were measured in the dilute region: 0.01 and 0.02 g ml^{-1}.

The data were fitted using the core-star model, which collapses to the star model for the contrast matched HStar samples. The PS-fullerene star experimental data were plotted in a double logarithm scale to determine the *Q* dependence of the different regions of the curve (Figure 4.19 and Figure 4.20). The calculated curves from the star and core-star model are also shown.

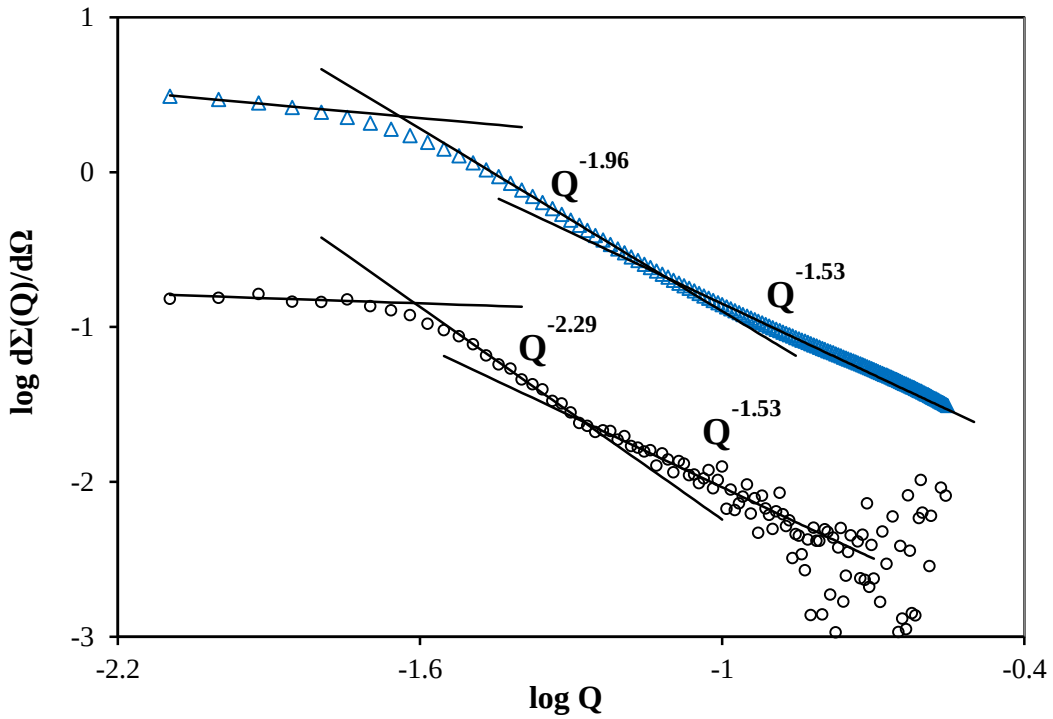

Figure 4.19: Scattered intensity on a log-log scale for 18k DStar in benzene (○) at 2 wt% in solution and the calculated core-star model fit(Δ). The solid lines show the experimental slopes and *Q* dependences for the identifiable regions of the scattered intensity.

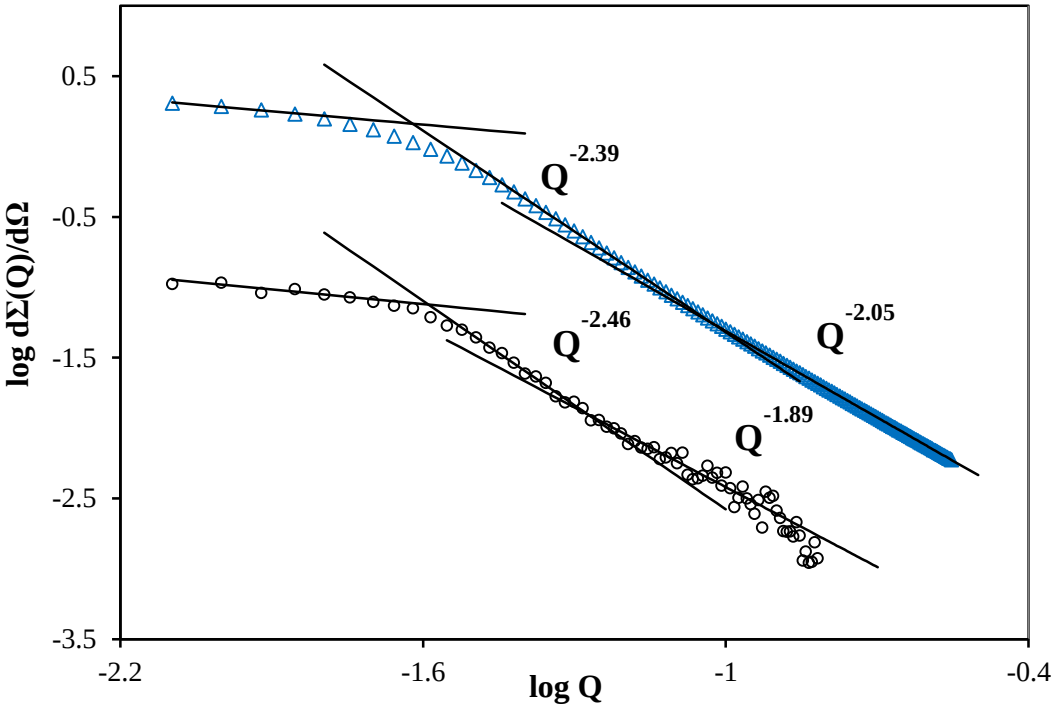

Figure 4.20: Scattered intensity on a log-log scale for 16k HStar in benzene (○) at 2 wt% in solution and the calculated core-star model fit(Δ). The solid lines show the experimental slopes and *Q* dependences for the identifiable regions of the scattered intensity.

The Kratky plot of Gaussian linear polymers reaches a plateau at high *Q* (Figure 4.21), whereas star polymer Kratky plots show a peak at intermediate *Q* values before decreasing towards the asymptotic value and reaching a plateau (Figure 4.22). Kratky plots of the experimental and calculated data were produced for PS-fullerene stars and corresponding linear chains in benzene. The calculated curves are the representation of the Debye model for linear polystyrene and the star or core-star model for PS-fullerene samples. In the LOQ data, there is a weak maximum, more clearly seen when comparing the stars to the linear polymer equivalent (Figure 4.23). The Kratky plots for the 105k HPS and 2k HStar samples are shown in Appendix A.

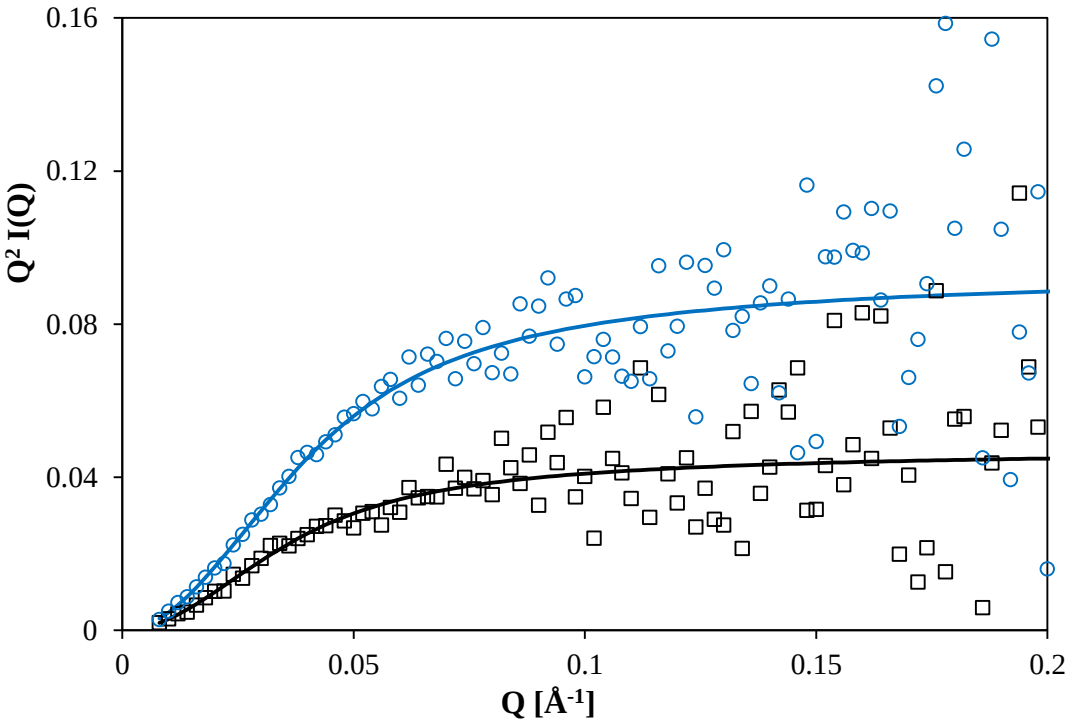

Figure 4.21: Kratky plot for the linear 16k HPS sample measured on LOQ at 1 wt% (□) and 2 wt% (○) in benzene, with calculated lines from the Debye model.

The calculated fit from the star and core-star model shows reasonable agreement with the experimental data for dilute solutions PS-fullerene stars, however there is a great deal of noise, which may be obscuring structural features of the samples in a good solvent.

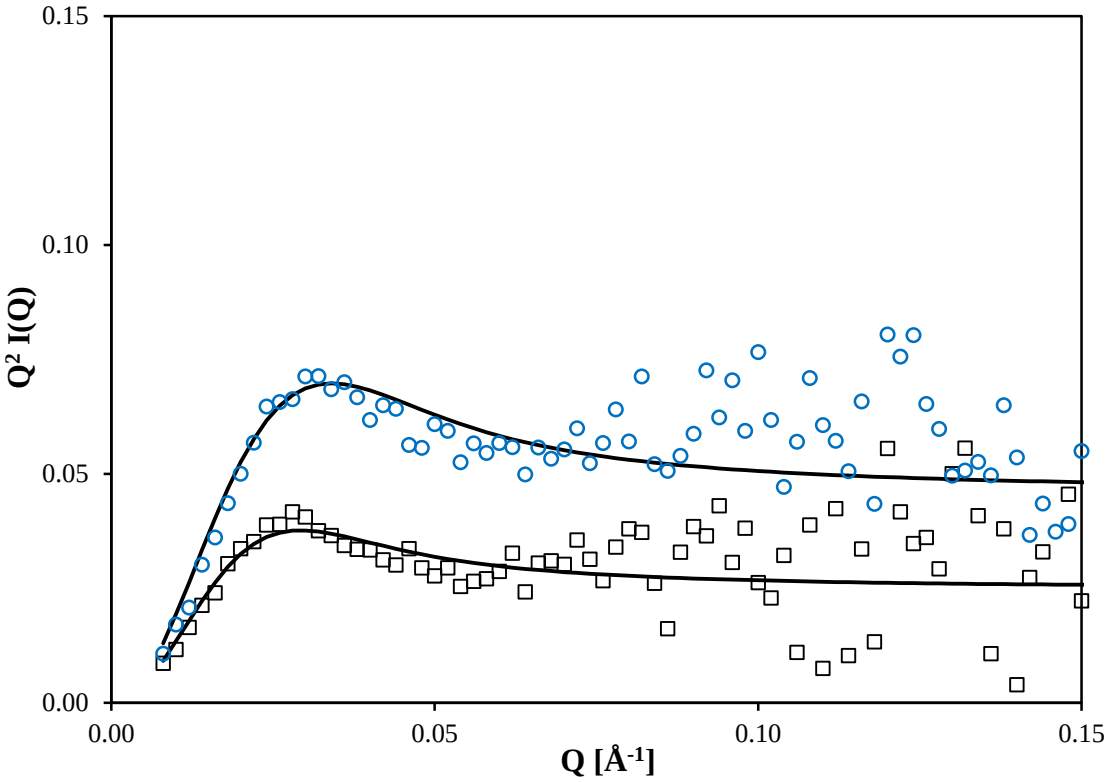

Figure 4.22: Kratky plot for 16k HStar sample measured on LOQ at 1 wt% (□) and 2 wt% (○) in benzene along with calculated lines from the star model.

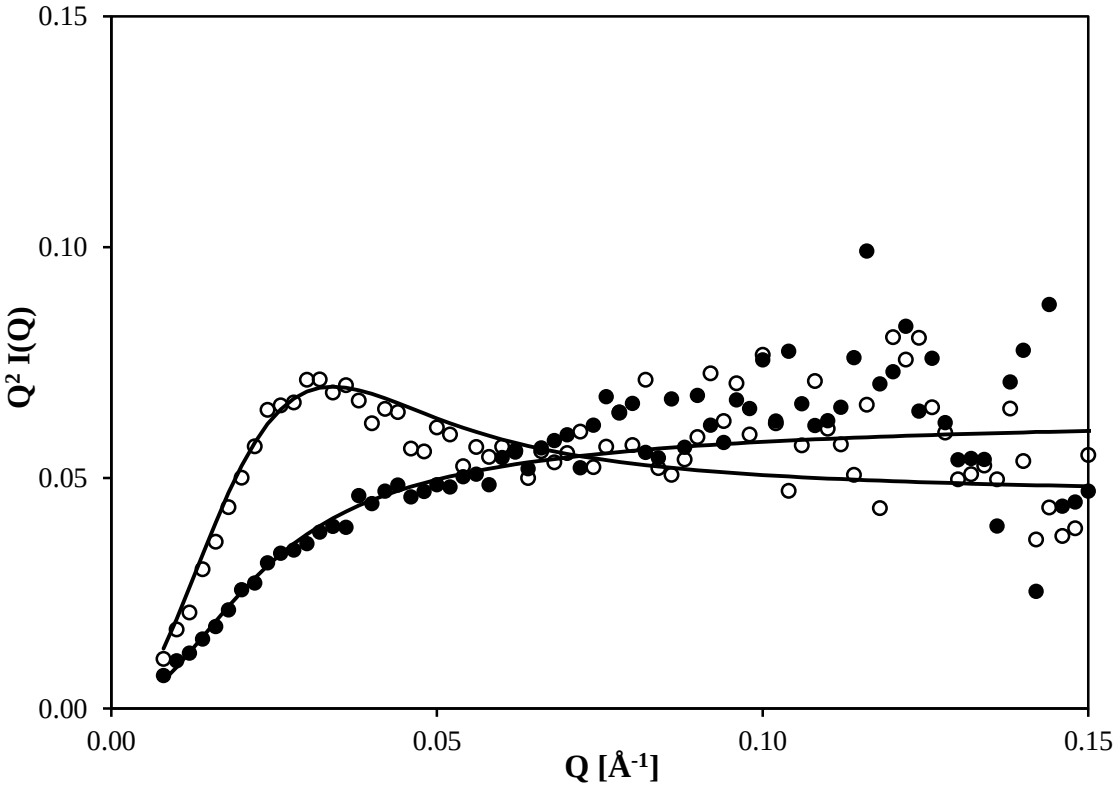

Figure 4.23: Comparison Kratky plot for linear 16k HStar (○) and 105 HPS (●) at 1 wt% in benzene along with calculated lines from the Debye and core-star model respectively.

In the core-star model, the core size is fixed at 5Å, as C60 is a monodisperse sphere with a fixed radius. This means the variables in the core-star model are the same as for the star model; R_{star} and scale/$I(0)$. The core-star model was fitted to the scattering intensity for all the PS-C60 stars at various concentrations, until the model fails to describe the data. The fits of the HStar samples are shown in Figure 4.24 and Figure 4.25, the DStar samples in Figure 4.26 and Figure 4.27. The resulting parameters from the model fitting are listed in Table 4.9. The core-star model should fit well below the overlap concentration; however even for the 2k HStar sample, the model fit is only accurate up to 2 wt%. At 5 wt% the fit is much poorer and at 10 wt% solution the model fails to describe the data entirely (Figure 4.24), showing that chains are starting to overlap even at low concentrations. From the calculated overlap concentrations in Table 4.7, c^* for this sample is 48 wt%, therefore for these stars, dilute conditions only occur at concentrations far below the calculated overlap concentration.

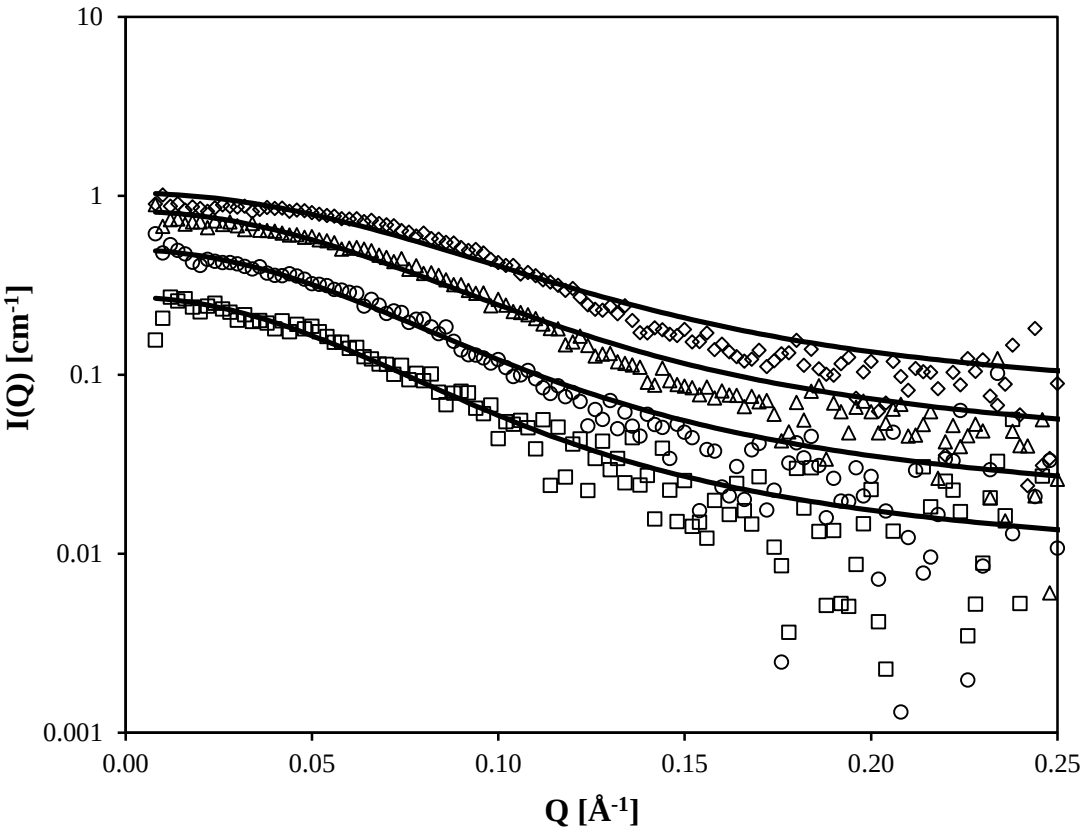

Figure 4.24: Core-star model fits for 2k HStar data at 1 wt% (□), 2 wt% (○), 5 wt% (Δ) and 10 wt% (◊) concentration in d-benzene solution.

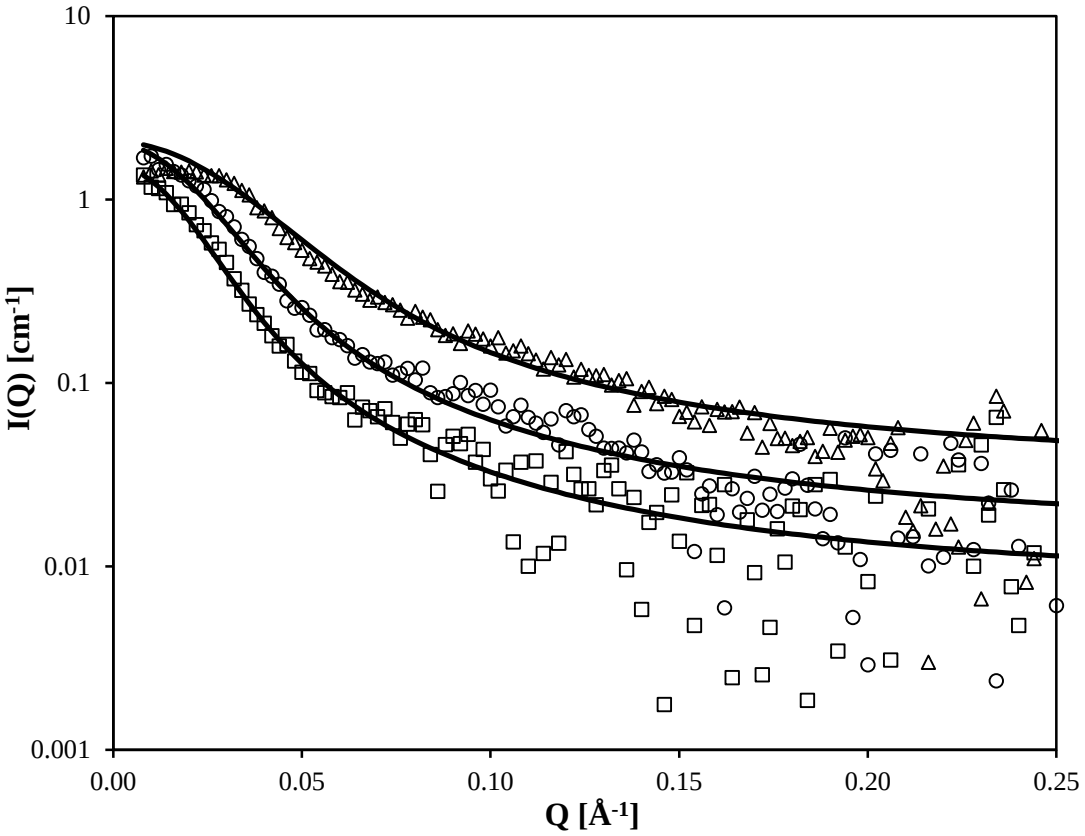

Figure 4.25: Core-star model fits for 16k HStar data at 1 wt% (□), 2 wt% (○) and 5 wt% (Δ) concentration in d-benzene solution.

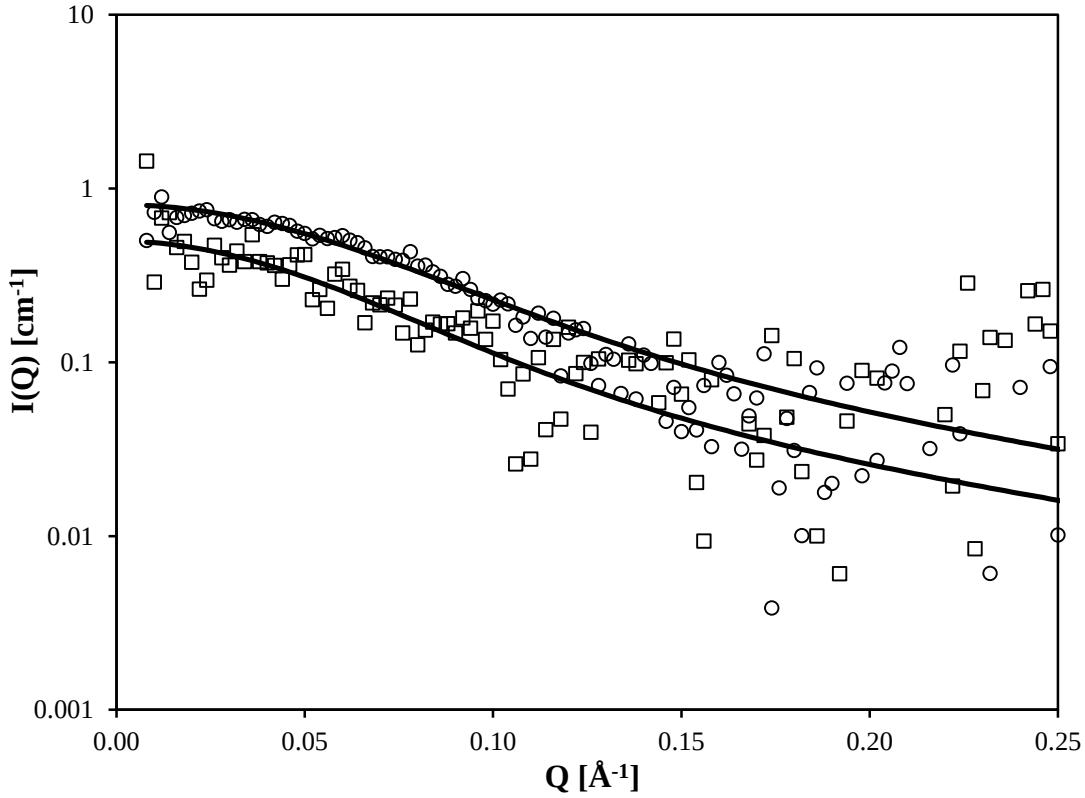

Figure 4.26: Core-star model fits for 2k DStar data at 1 wt% (□) and 2 wt% (○) concentration in h-benzene solution.

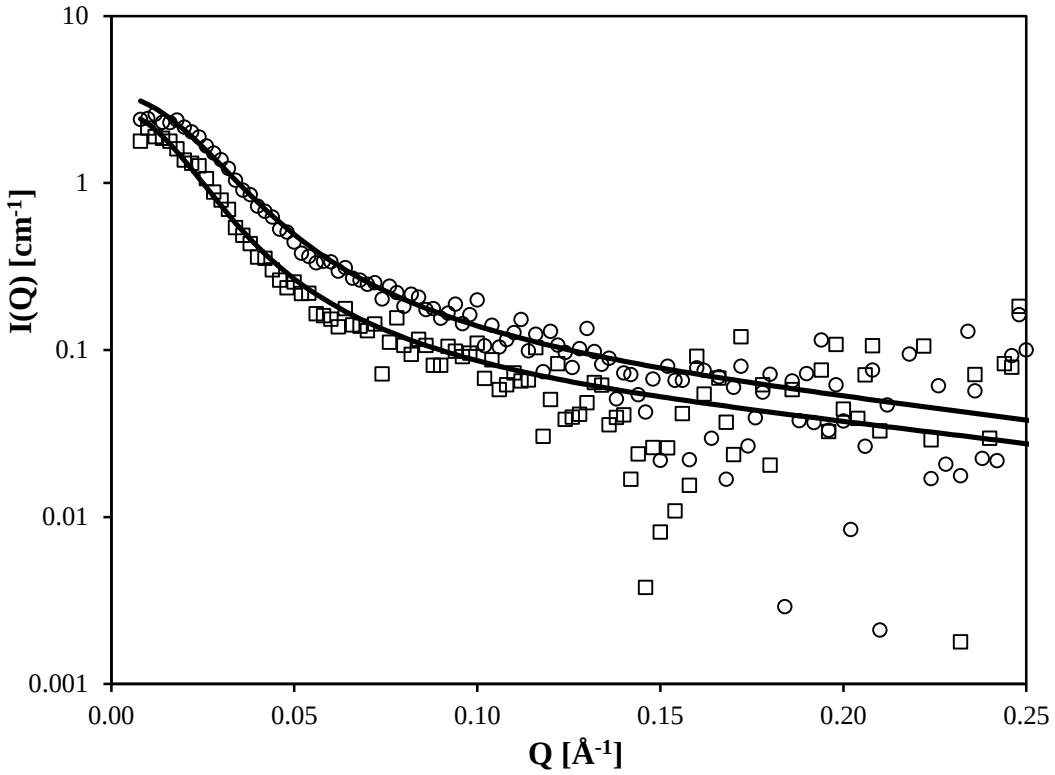

Figure 4.27: Core-star model fits for 18k DStar data at 1 wt% (□) and 2 wt% (○) concentration in h-benzene solution.

Table 4.9: Core-star model fitting parameters for PS-fullerene stars in benzene.

Sample	Instrument	c /g ml^{-1}	Core-Star model		
			R_{star} /Å	R_a /Å	I(0)
2k HStar	LOQ	0.010	25.4 ± 1.7	15.5 ± 1.0	0.26
		0.021	24.0 ± 1.0	14.7 ± 0.6	0.48
		0.048	21.6 ± 0.6	13.2 ± 0.4	0.79
16k HStar	LOQ	0.010	75.7 ± 3.0	46.3 ± 1.8	1.52
		0.020	63.5 ± 2.1	38.9 ± 1.3	2.00
2k DStar	LOQ	0.010	25.9 ± 1.3	15.9 ± 0.8	0.50
		0.018	23.0 ± 0.7	14.1 ± 0.4	0.81
18k DStar	LOQ	0.009	81.9 ± 2.1	50.1 ± 1.3	2.74
		0.019	66.7 ± 2.0	40.9 ± 1.2	3.36

The experimental radius of gyration values calculated for linear polystyrene and the PS-fullerene stars at the lowest concentration in benzene were plotted against the calculated values (Figure 4.28). This graph shows that the linear polystyrene arms and the high molecular weight PS-fullerene stars have radius of gyration values following

the expected trend. However, the lowest molecular weight stars deviates from this trend, as both the hydrogenated and deuterated stars have a higher R_g value than expected. This contradicts the results from the literature that have stated that polystyrene-fullerene stars have the same R_g values as pure polymer stars[55, 123], but is consistent with the results from Lebedev *et al.* on similar polymer-fullerene systems[206].

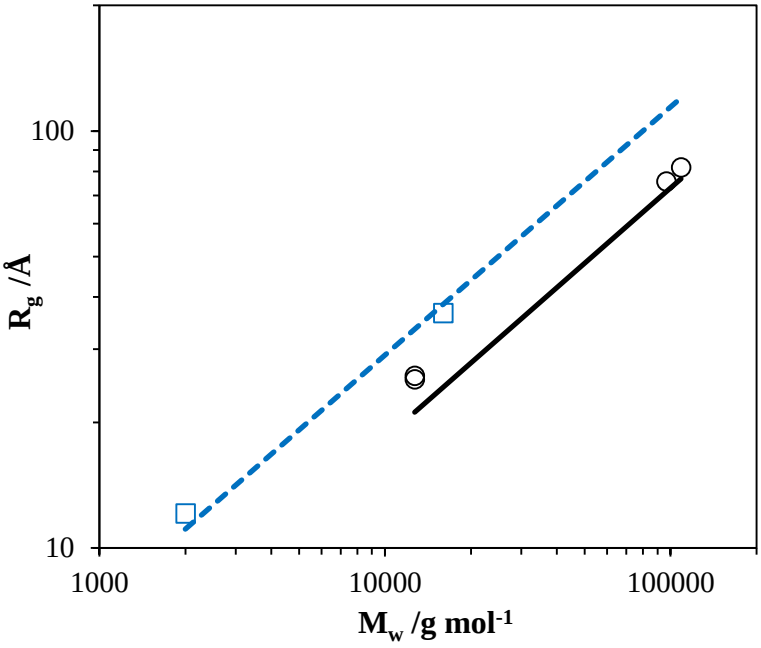

Figure 4.28: Experimental and calculated radius of gyration results for linear (□) and PS-fullerene stars (○) at 1 wt% in benzene. The lines show the calculated R_g values using Equations (4.7) and (4.13) for linear and star polymers respectively.

In dilute solution, the scattered intensity shows the form factor of individual stars. When the concentration is increased into the semi-dilute region, the polymer chain arms overlap and interpenetrate with each other. In typical polymer stars, the Daoud-Cotton model states that when the outer arms are interpenetrated, this leads to two regions of different structure within the solution[251]. A schematic representation of the Daoud-Cotton model for semi-dilute solutions is shown in Figure 4.29. Around the core, the polymer chains still exhibit single star behaviour as seen in dilute solutions. Beyond an effective radius, χ, where the chains are interpenetrated the star structure is no longer distinguishable and thus the distribution is comparable to a semi-dilute solution of linear polymer chains. However, the determination of the effective radius is non-trivial. This approach has been used to describe semi-dilute solutions of PS-fullerene stars in the

literature, by contrast matching the labelling the overlapped potions of the chains and then contrast matching with the solvent[123].

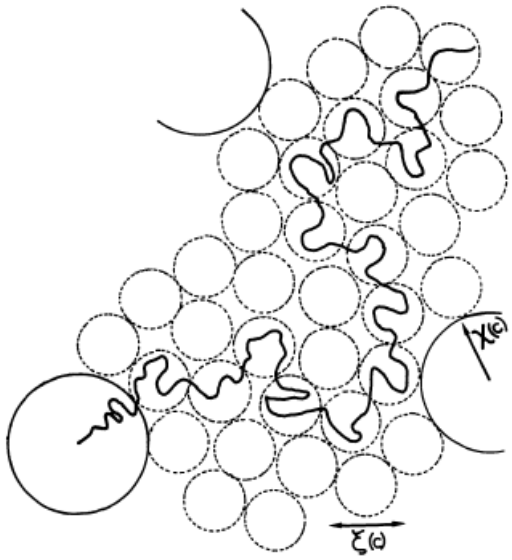

Figure 4.29: Schematic representation of the Daoud-Cotton model for the behaviour of star polymers in semi-dilute solution.

Concentrated solutions of polymer stars have shown a liquid peak in the structure factor at the reciprocal distance corresponding to star-star distances[252]. This peak represents liquid-like order of spheres, but is generally only seen in stars with large numbers of arms (>12), although a shallow peak has been seen in polyisoprene stars with 8 arms[258].

Due to concentrated solutions of pure star polymers being comparable to concentrated solutions of linear chains, a comparison of Ornstein-Zernike fits (Equation (4.1)) of 16k HStar and 105k HPS at 20 wt% is shown in Figure 4.30 and the Kratky plot shown in Figure 4.31. Both plots show that the scattering of the PS-C60 star is similar to the linear polymer but deviates at low and intermediate *Q* due to the presence of a very shallow peak, which cannot be modelled using the OZ model without changing the Guinier exponent in Equation (4.1). According to the Daoud-Cotton model, this could be due to the presence of scattering intensity from around the core of the individual stars, or a shallow version of the liquid-like ordering peak seen in other stars. Therefore, PS-C60 stars also behave structurally like pure polymer stars in semi-dilute solution.

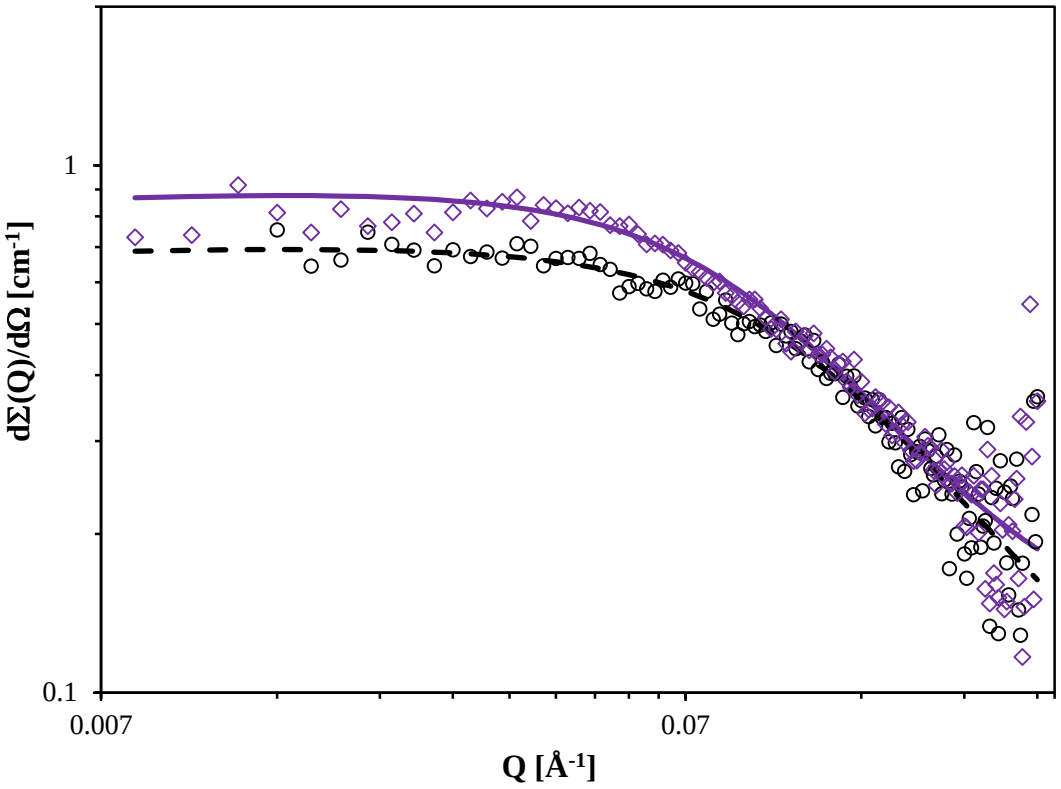

Figure 4.30: Scattered intensity on a log-log scale for 20 wt% solutions of 16k HStar (◊) and 105k HPS (○) in benzene. The lines show the fit of the Ornstein-Zernike model (Equation (4.1)).

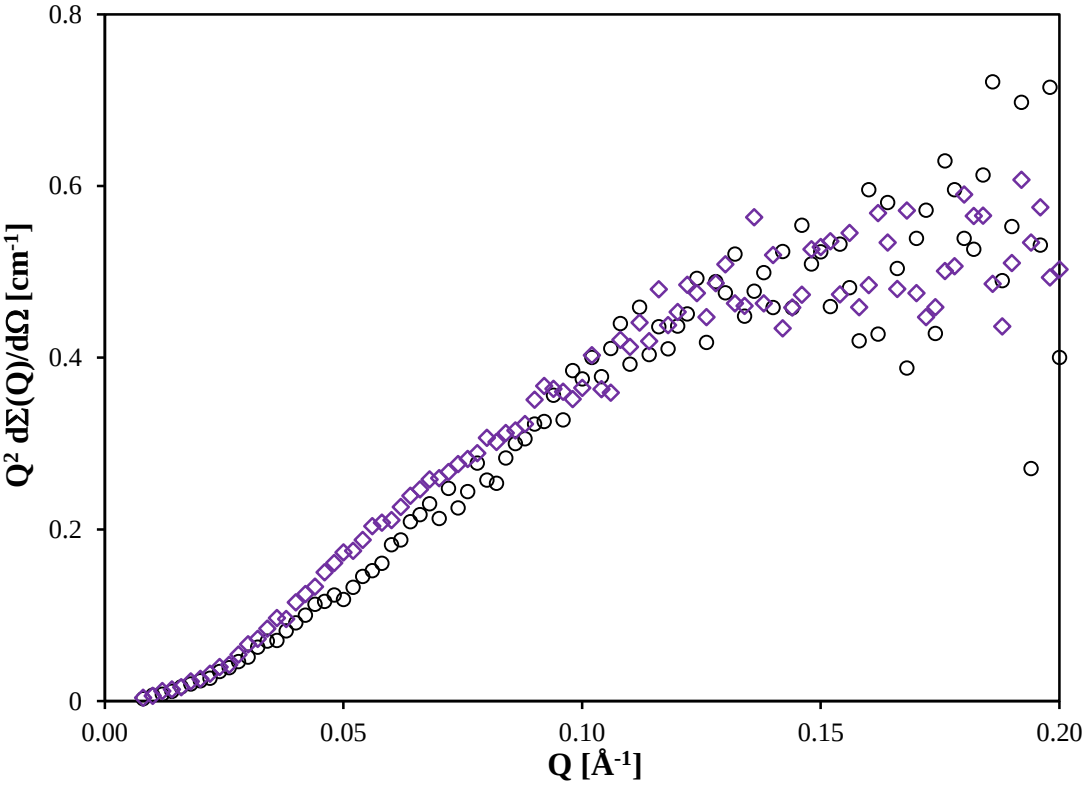

Figure 4.31: Kratky plot comparison for the 20 w% benzene solutions of 16k HStar (◊) and 105k HPS (○) samples.

4.4.3 PS-fullerene stars in toluene (D22)

Following the results from the PS-C60 stars in benzene solution on LOQ, the core-star model was applied to the data of the PS-fullerene stars in toluene collected on D22. However, the model fails to describe the data in the intermediate Q range, as shown clearly by the log-log plot (Figure 4.32). Specifically, the core-star model does not (1) describe the change in slope that occurs at $Q \sim 0.05$ A^{-1} and (2) account for excluded volume effects on the scattered intensity of the polymer stars under good solvent conditions.

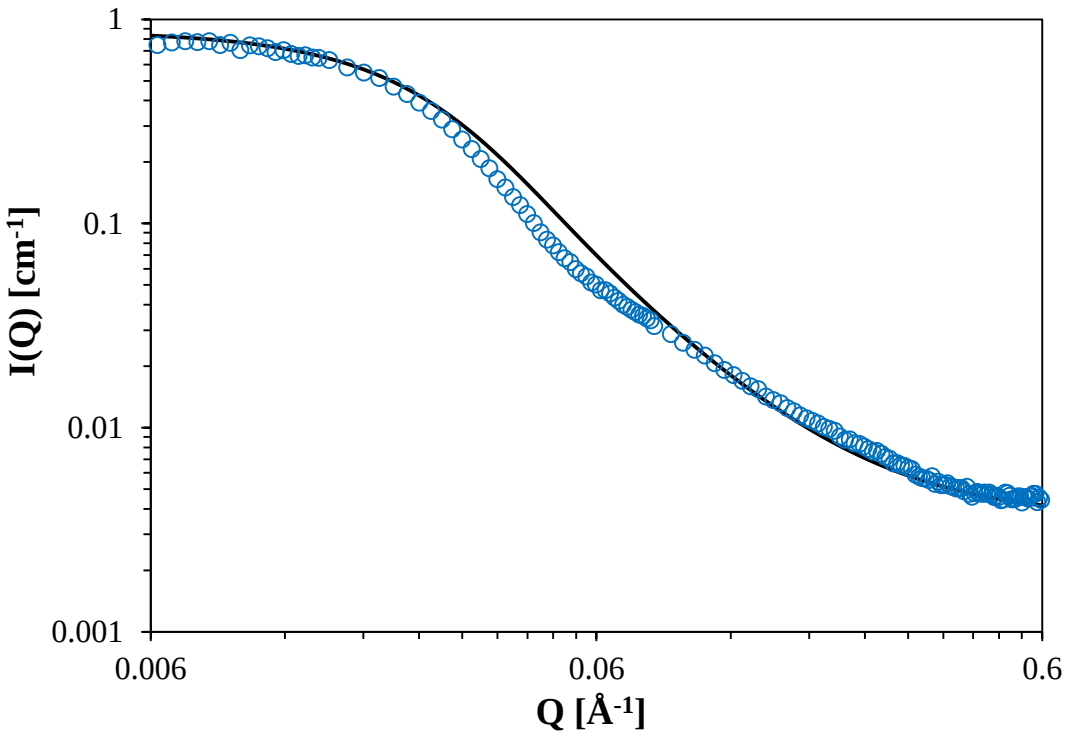

Figure 4.32: Core-star model (Equation (4.5)) applied to 16k HStar measured on D22 at 2 wt% in toluene. The fit is poor in the intermediate region ($0.02 < Q < 0.1$ Å^{-1}).

The raw data in the Kratky plot for the D22 data of PS-fullerene stars in toluene (Figure 4.33) shows the same peak at $Q \sim 0.1$ Å^{-1} that was observed in the LOQ data for PS-fullerene stars in benzene, confirming the star-like nature of the PS-fullerene hybrid particles. However, the model fit (solid line) in the plot fails to accurately describe the peak and the intermediate Q range of the experimental data. Thus, while the LOQ data appears to show reasonable agreement with these models, the star models are not appropriate for the D22 data.

The Benoit star model and the Pedersen core-star model do not describe the two-step decay we see in polymer stars in good solvent conditions. This deviation from the norm has been attributed to excluded volume effects[259]. Therefore, there is a need for another method of analysis for dilute solutions of stars in good solvents.

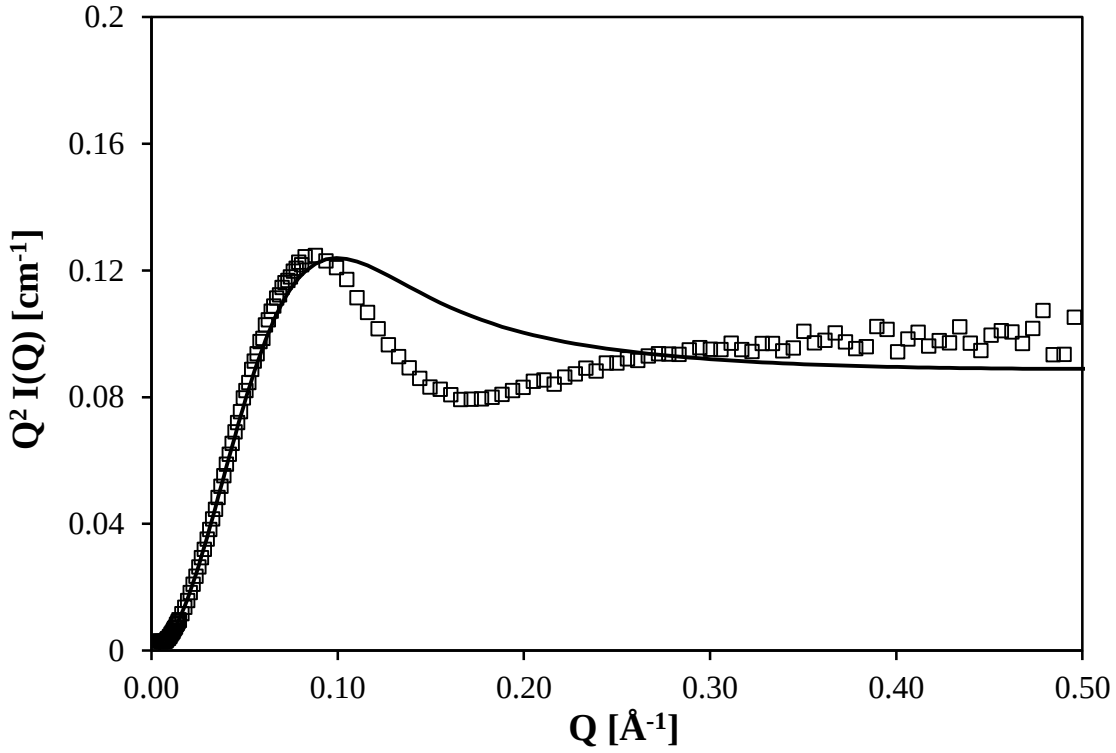

Figure 4.33: Kratky plot for 2k HStar sample collected on D22 at 2 wt% in toluene (symbols) along with calculated fit from the core-star model (line).

Scaling analysis was performed on the 2k and 16k HStar sample (Figure 4.34 and Figure 4.35), by normalising the scattered intensity to obtain the form factor. The results are compared with predicted results from the Daoud-Cotton model[251] and characteristic power law representations[252] of a star polymer which are outlined at the end of Section 4.2.2. The graphs show that the onset of the asymptotic regime occurs at higher values than those predicted by the Daoud-Cotton model ($f^{1/2}$) or the characteristic power law ($f^{2/5}$). The Q dependence of the initial slope is also lower than expected (predicted values of 3 for Daoud-Cotton model Gaussian chains and 10/3 for chains with excluded volume effects); however the final slope is approximately 5/3 as predicted for isolated swollen polymer chains with excluded volume behaviour.

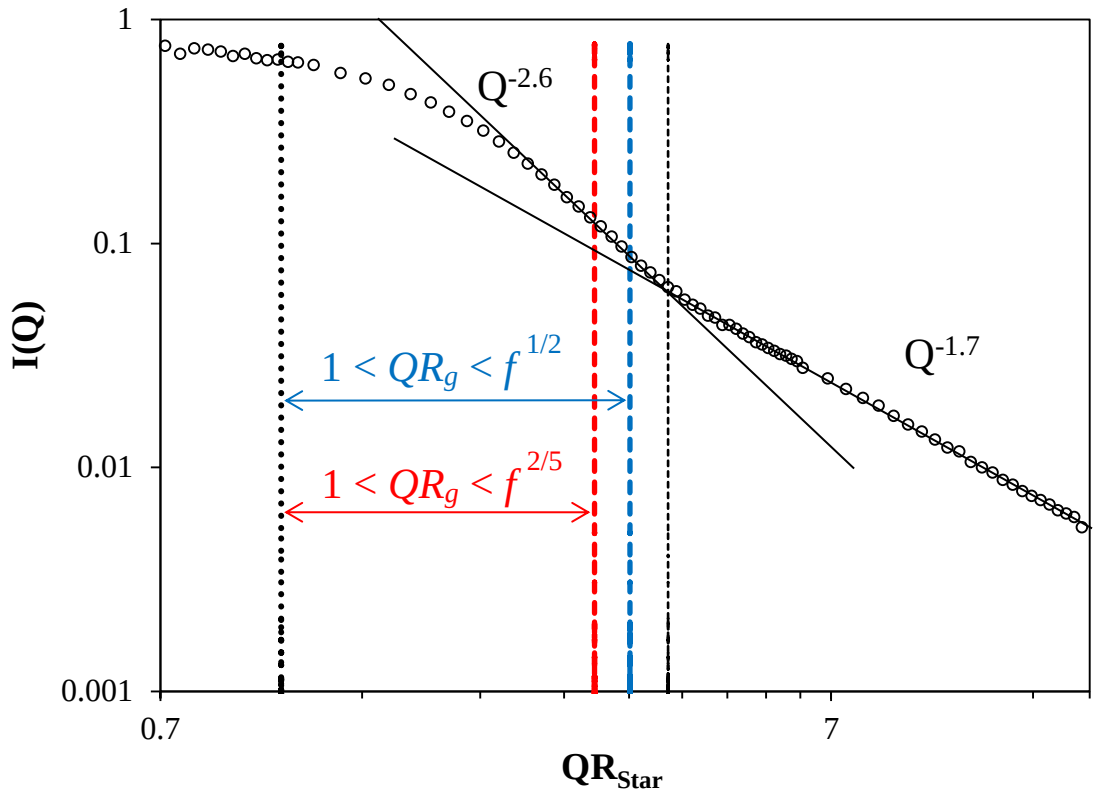

Figure 4.34: Scaling analysis of the form factor of the 16k HStar sample 0.5 wt% in d_8-benzene solution (○). The characteristic regions predicted by the Daoud-Cotton model (blue) and power law behaviour (red) are shown alongside the experimental regimes (black).

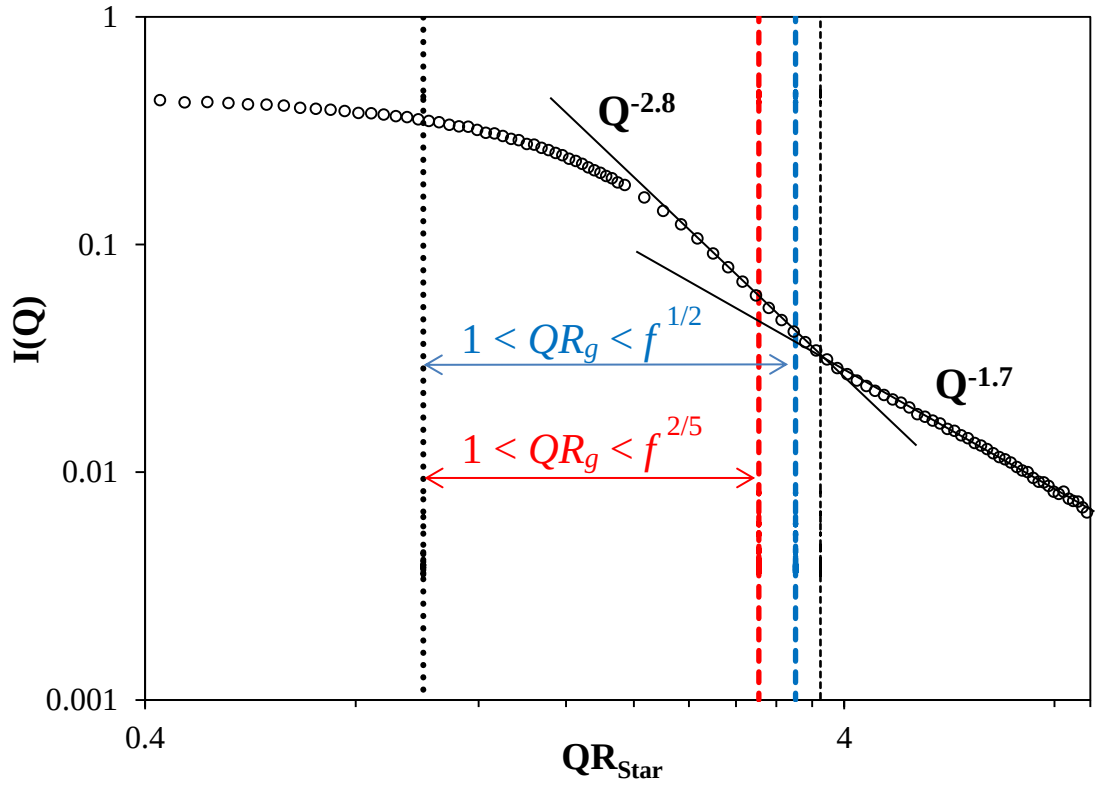

Figure 4.35: Scaling analysis of the form factor of the 2k HStar sample 2 wt% in d_8-benzene solution (○). The characteristic regions predicted by the Daoud-Cotton model (blue) and power law behaviour (red) are shown alongside the experimental regimes (black).

The onset of the asymptotic regime is higher than predicted in both of the polymer-fullerene stars measured, which has been previously attributed to a densification of chains around the fullerene core[123]. There has been evidence of chain stretching close to the core in other polymer-fullerene samples[260], which has been seen in polymer stars when chains are closely linked to a well-defined boundary[261]. The region around the core is therefore likely to be a close packed region of stretched chains due to the very sharp boundary of the C60 core. In the stars with longer arms, the effect of the region of stretched chains on the scattered intensity is lessened by the much larger scattering contribution arising from the parts of the polymer chains further away from the core. The relative size of the stretched part of the chain to the rest of the chain is much higher in the smaller star (2k) compared to the larger star (16k), therefore the effect of grafting to the core on the radius of gyration is more prominent in the 2k HStar and DStar samples.

A combination of Guinier and Zimm plots were used to estimate the radius of gyration of the D22 data for PS-C60 stars instead of the core-star model fit used for the LOQ data. The two plots are valid in the limit of $R_gQ < \sim 2$ for both 2k and 16k HStar samples, using the calculated value for R_g. A combination of the two methods is required for analysis of the D22 data, as the Guinier analysis can underestimate the chain dimensions and the Zimm plot tends to overestimate the radius of gyration values, especially in larger polymeric stars[215]. The slopes of the Guinier and Zimm plots give the radius of gyration of the entire star, from which the radius of gyration of the arm can be calculated using Equation (2.60). The Guinier plots of the two star samples at various concentrations are shown in Figure 4.36, and the Zimm plots are shown in Figure 4.37 and Figure 4.38 and the resulting radius of gyration values are listed in Table 4.10.

Table 4.10: Radius of gyration results calculated from Guinier and Zimm plots

	Calculated values		**Guinier plot**		**Zimm plot**	
Sample	**R_{star} /Å**	**R_a /Å**	**R_{star} /Å**	**R_a /Å**	**R_{star} /Å**	**R_a /Å**
2k HStar	21.5	13.2	23.1 ± 0.5	14.2 ± 0.3	27.8 ± 0.6	17.1 ± 0.4
16k HStar	72.6	44.5	71.7 ± 1.1	44.0 ± 0.7	86.0 ± 3.2	52.8 ± 2.0

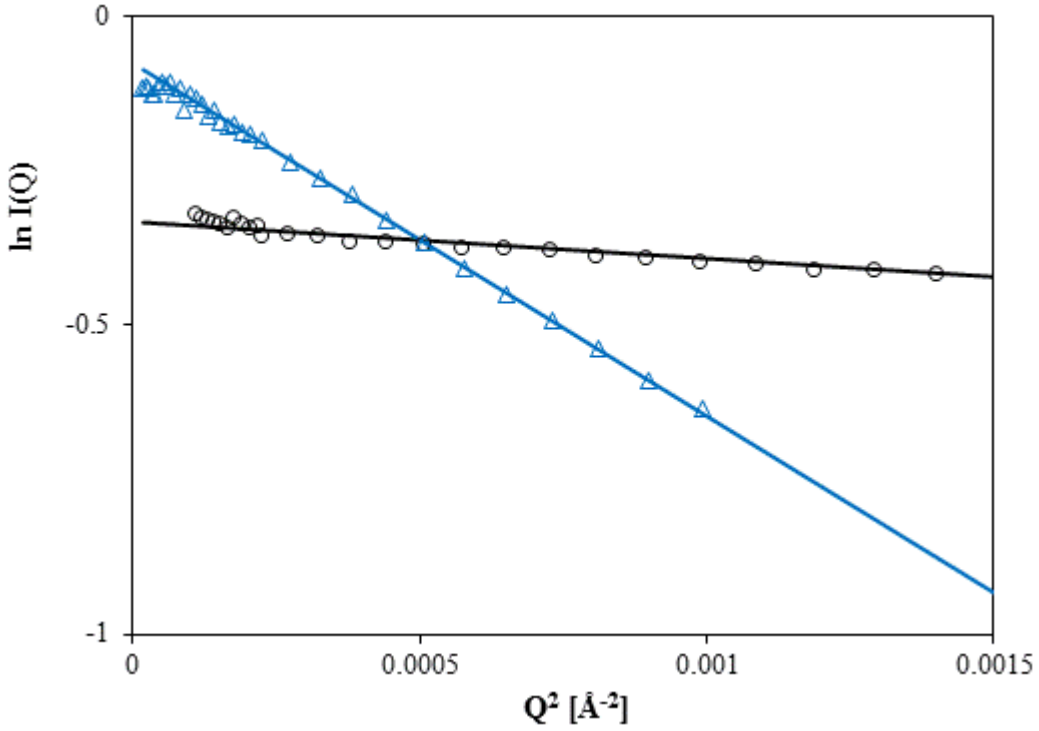

Figure 4.36: Guinier plots of 2k HStar measured on D22 at 2 wt% (○) and 16k HStar (Δ) at 0.5 wt% in toluene. The slope of the solid line gives the radius of gyration.

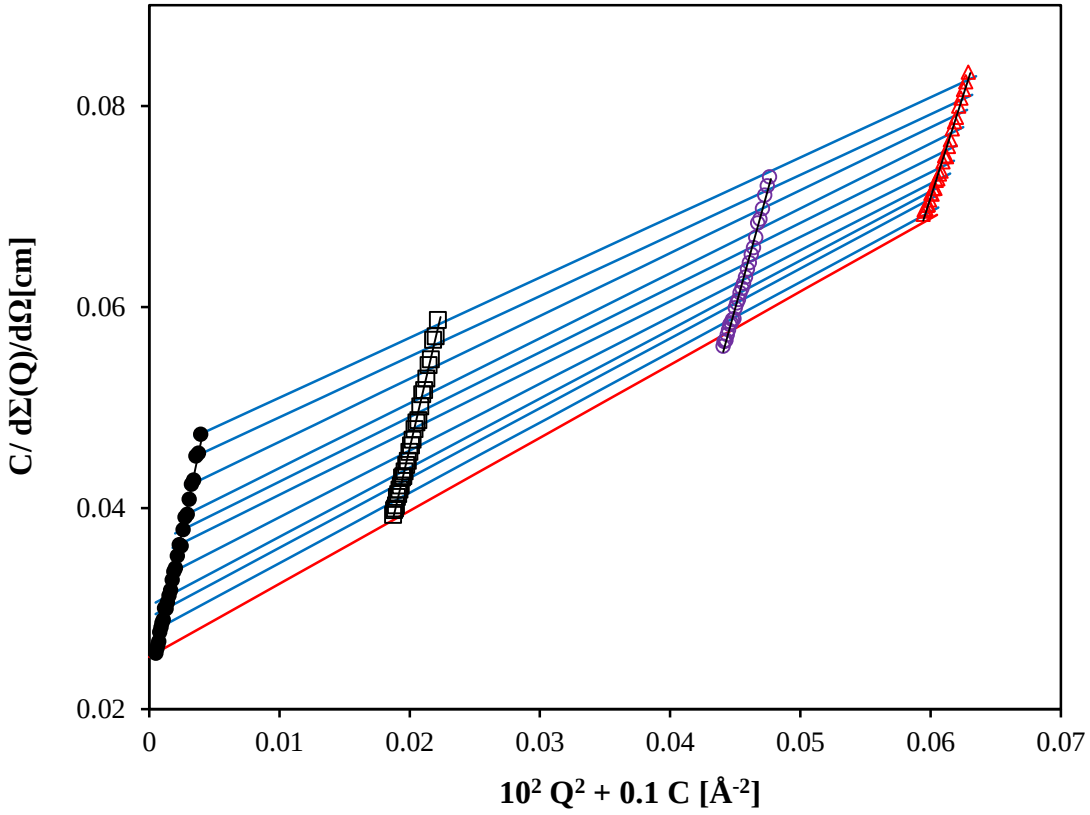

Figure 4.37: Zimm plot of 2k HStar at 2 wt% (□), 5 wt% (○) and 7 wt% (Δ). The filled symbols show the extrapolated C = 0 values.

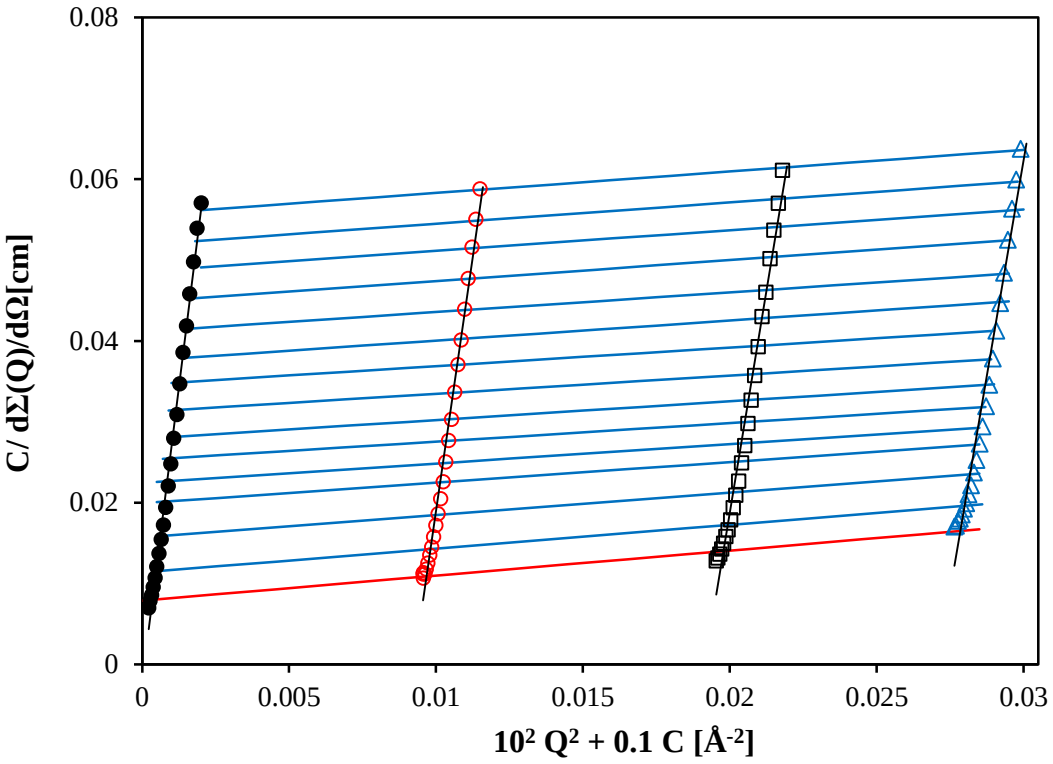

Figure 4.38: Zimm plot of 16k HStar at 1 wt% (○), 2 wt% (□) and 3 wt% (Δ). The filled symbols show the extrapolated C = 0 values.

The Guinier plot gives a larger value of R_g than predicted for the 2k HStar sample, and a value within experimental error for the 16k HStar. As mentioned previously, Guinier plots tend to underestimate the radius of gyration in polymer stars with narrow PDIs and with large R_g values (typically >100 Å depending on the Q range), as the scattering is not completely linear in plots of $I(Q)^{-1}$ against Q^2 in the Guinier region[262]. Using the calculated curve for a PS-C60 star from the core-star model, a series of calculated Guinier plots were made, showing that the Guinier plot starts to deviate from linearity when R_g > 40 Å (Appendix A). The larger star has an expected R_g larger than this value, and therefore the Guinier plot becomes less reliable for calculating an accurate R_g. Guinier analysis of the 2k HStar value is likely more accurate than the analysis of the larger 16k HStar sample due to the smaller size.

The Zimm plots give values much larger than calculated or obtained by Guinier analysis. The Zimm plots in this case are likely overestimating the radius of gyration in both stars, especially in the larger PS-C60 star sample. At higher concentrations, the data deviates from the plotted Zimm lines (Appendix A), leading to unreliable Zimm results. As such, only the lowest 3 concentrations were suitable for making the Zimm plot. In order to accurately calculate R_g from a Zimm plot, the extrapolated values must

be precise. The error for this Zimm plot is relatively large (~4%) due to the low number of concentrations and slight deviations from linearity in the experimental data.

There is consistent evidence of an increase in radius of gyration of the PS-C60 stars compared to that of the equivalent pure polymer star. When these results are combined with the core-star model results from the same stars in dilute benzene solution, we conclude that the PS-C60 stars are slightly larger than predicted for pure polymer stars of the same molecular weight in good solvents.

4.5 Hydrodynamic radius

The hydrodynamic radius of PS-fullerene stars in solution was measured by Dynamic light scattering (DLS). DLS is a technique used to measure the size and zeta potential of particles and molecules in dilute solution. The size is determined by measuring Brownian motion of the particles and converting this information into size by using the Stokes-Einstein equation[263]:

$$D_h = \frac{k_B T}{3\pi\eta D_t} \tag{4.16}$$

where D_h is the hydrodynamic diameter, D_t is the translational diffusion coefficient, k_B is Boltzmann's constant, T is the temperature and η is viscosity. The hydrodynamic diameter is automatically calculated by the DLS instrument software.

Zeta potential is a measure of the charge of a particle, and gives information on the stability of the colloidal system, as a larger charge increases the repulsive forces between individual particles. The Zetasizer nano instrument used in this project calculates zeta potential by determining the electrophoretic mobility by using an electrophoresis experiment. The software then applies the Henry equation to the data:

$$U_E = \frac{2\varepsilon\zeta\, f(\kappa a)}{3\eta} \tag{4.17}$$

where U_E is electrophoretic mobility, ζ is the zeta potential, ε is the dielectric constant and $f(\kappa a)$ is Henry's function, usually approximated to 1.5 (Smoluchowski approximation) or 1.0 (Huckel approximation)[264].

PS-fullerene star systems and corresponding linear chains were measured by DLS in a good solvent, toluene, and a theta solvent, cyclohexane, at concentrations between 0.25 – 2.5 wt % to find the hydrodynamic radius (Table 4.11). The ratio of

hydrodynamic radius to radius of gyration, R_h/R_g, was also calculated, using the experimental values for the polymers and stars extracted from SANS measurements in both solvents. The expected hydrodynamic radius of linear polystyrene in cyclohexane can be calculated from the following relationship[253]:

$$R_h = 2.15 \times 10^{-2} M^{0.502} \quad \textbf{(4.18)}$$

and the hydrodynamic radius of linear polystyrene in toluene is given by:

$$R_h = 1.06 \times 10^{-2} M^{0.575} \quad \textbf{(4.19)}$$

The hydrodynamic radius of polymer stars has previously been shown to be lower than that of linear polymer chains and is inversely proportional to the number of arms, *f*. [265-267] The ratio R_h/R_g is also different for branched polymers. For linear polymers, R_h/R_g is approximately 0.73 – 0.8.[268] However, R_h/R_g for star polymers in good solvents is dependent on f, with a value of 1.24 for 18 arms, and 1.28 for 32 arms[269], approaching the value for hard spheres (1.29). The ratio is proportional to *f*, as a 3 arm polystyrene star[265] had an R_h/R_g of ~0.85 and a computational model for a 5 arm star has a ratio of 0.97.[270] Literature DLS measurements on less well-defined PS-C60 stars in the literature showed R_h and ratio values similar to that of pure polymer stars[55].

The hydrodynamic radius results for linear polymers are close to the calculated values (within 1 – 2 Å) and generally show the characteristic R_h/R_g value of ~0.8. The PS-fullerene stars generally show hydrodynamic radius values similar to or slightly larger than those calculated for the pure PS chains of the same total molecular weight, seemingly in contradiction to the literature on pure polymer stars. However, the values of the ratio R_h/R_g in toluene range from 0.97 to 1.09, which is consistent with star branched polymers with a low number of arms and previous literature on polymer-fullerene stars. Thus, the hydrodynamic radius results are consistent with the SANS experiments and radius of gyration results as they show that the PS-fullerene systems are larger than pure polymer stars but have the similar structural behaviour in solution.

Table 4.11: DLS results for linear PS and PS-Fullerene stars in toluene and cyclohexane.

	Toluene				Cyclohexane			
Sample	**Conc. wt%**	**Calc linear R_h / Å**	**R_h /Å**	**R_h/R_g**	**Conc. wt%**	**Calc linear R_h / Å**	**R_h / Å**	**R_h/R_g**
2k HPS	2.50	9.4	10.7	0.82	0.10	9.8	9.6	-
					1.30		11.3	
16k HPS	1.00	27.7	29.4	0.80	1.30	27.7	30.7	-
	2.50		29.4					
105k HPS	1.00	81.8	79.4	0.90	1.30	71.3	83.3	-
	2.50		89.1					
2k HStar	0.25	23.5	29.4	1.09	1.30	23.6	29.5	1.21
	1.00		28.3					
	2.50		28.8					
2k DStar	0.25	23.5	27.4	1.06	-	-	-	-
	1.00		27.8					
	2.50		25.4					
16k HStar	0.25	76.1	83.9	1.05	1.30	67.0	83.7	1.25
	1.00		72.5					
	2.50		79.2					
18k DStar	0.25	81.5	79.0	0.97	1.30	71.1	73.5	1.14
	1.00		75.8					

4.6 Conclusions

A series of small-angle neutron scattering experiments on LOQ, D22 and SANS-II were carried out on grafted 6 arm PS-fullerene stars and linear polymer samples of molecular weight matching the arms and the total molecular weight of the PS-fullerene stars. The core-star model was applied to all PS-fullerene systems and it was found to fit well data for the hydrogenated and deuterated PS-fullerene stars in cyclohexane and benzene. However, in toluene, excluded volume effects preclude the use of the star models, thus a scaling approach was used to describe the data and the Guinier and Zimm methods used to calculate the radius of gyration.

In both theta and good solvents, the PS-C60 stars show a significantly larger radius of gyration than calculated for model stars, and this increase is most significant in the 2k HStar and DStar samples. This is a result of the chains being tethered to a hard core with a sharp well-defined boundary, with dense region of extended chains around the core. Further away from the core, the chains behave as normal swollen chains as predicted by the Daoud-Cotton model[251] for polymer stars. Attaching polystyrene chains to fullerenes, thus preventing fullerene aggregation seen in dispersed nanocomposites[53], has a small effect on the overall structure behaviour of the chains in samples with high molecular weight arms, but the size of the smaller stars are greatly affected by this stretching of chains around the fullerene core.

This was confirmed by the hydrodynamic radius measurements using DLS. The hydrodynamic radius values were consistently larger than the calculated values for linear polymer chains, whereas pure polymer stars have lower R_h values than equivalent linear chains. However, the ratio of R_g/R_h was close to 1.0, as predicted for polymer stars with a low number of arms. Therefore, PS-C60 stars are structurally similar to polymer stars, however there is a region of stretched chains around the fullerene core that leads to larger values of R_g and R_h than predicted by the current models for pure polymer stars.

Chapter 5. Structural study of polymer-silica nanocomposites

5.1 Introduction

PS-fullerene stars with well-defined arms can be considered as model systems for structural analysis. Systems that more closely resemble the type of grafted nanocomposites that could be used in commercial applications are polymers grafted to colloidal or fumed silica. Silica is commonly used as filler in polymers and plastics in coatings[57], resin encapsulants for electronics and other applications. While there are many papers using SANS to study the effect of dispersing fillers on a polymer matrix[122], there are far fewer studies on the effect of grafting chains[121] and even fewer on comparing the two types of nanocomposites.

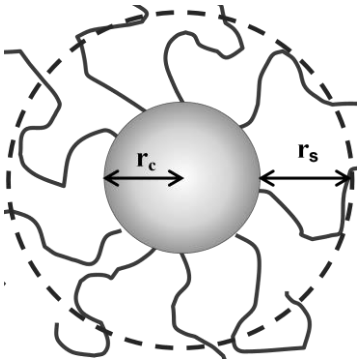

Figure 5.1: Graphical representation of a core-shell structure where r_c is the core radius and r_s is the shell radius.

The simple core-shell model is usually used as a starting point for analysing SANS data on grafted nanoparticles; however a more complex model may be required to describe the form factor of polymer nanocomposites that do not have well-defined structures. Whilst a study on absorbed layer nanocomposites used this core-shell model to accurately model the data[271], another neutron scattering study on a similar grafted system has shown that the simple core-shell model (Figure 5.1) is often insufficient to describe the structure of these systems[121].

Grafted polymer-silica nanocomposites (PMMA, PBA and PS, with fumed and colloidal silica) have been synthesised using controlled radical polymerisation and investigated using DLS, SANS and Small-Angle X-ray Scattering (SAXS). The samples were measured primarily in toluene and MEK solution, and the results compared to those obtained from pure polymers and dispersed polymer-silica nanocomposites.

5.2 Background subtraction

The polymer-silica hybrid particles in solution were measured on the LOQ instrument. As stated previously, this is a variable wavelength instrument and thus the transmission methods for background subtraction cannot be used. For the subtraction of the incoherent background scattering, the method using a linear combination of the scattered intensity of the pure hydrogenated and deuterated components (Equation (2.52)) was applied. Similarly to the PS-fullerene samples in Chapter 4, the background is overestimated at high concentrations and therefore adjusted using a concentration dependent coefficient fitted using least squares analysis.

5.3 Models for polymer analysis

Bare colloidal silica nanoparticles in solution were analysed using the form factor for a monodisperse spherical particle that has a uniform scattering length density[272]. The form factor equation used in SasView is shown below:

$$I(Q) = \frac{scale}{V_{sph}}\left[\frac{3V_{sph}(\Delta\rho)[\sin(QR_{sph}) - QR_{sph}\ \cos(QR_{sph})}{(QR_{sph})^3}\right]^2 + bkg \qquad \textbf{(5.1)}$$

where I(Q) is the form factor, scale is the volume fraction, V_{sph} is the volume of the sphere, $\Delta\rho$ is the difference in scattering length density (SLD) of the sphere and the solvent, R_{sph} is the radius of the sphere, and bkg is the background. The equation is then adjusted for some degree of polydispersity in the size of the spheres using a lognormal function.

Due to the aggregated structure, fumed silica was analysed using a modified Ornstein-Zernike function, known as the MassSurfaceFractal model in SasView[273]:

$$I(Q) = scale\ \times\left\{[1 + (Q^2a)]^{\frac{D_2}{2}} \times [1 + (Q^2b)]^{6-D_s-D_m)/2}\right\}^{-1} + bkg \qquad \textbf{(5.2)}$$

where *a* is:

$$a = \frac{{R_g}^2}{\left(\frac{3D_m}{2}\right)} \qquad \textbf{(5.3)}$$

and *b* is given by:

$$b = \frac{{r_g}^2}{\left[\frac{-3(D_s + D_m - 6)}{2}\right]} \qquad \textbf{(5.4)}$$

where R_g is the radius of gyration of the aggregates, r_g is the radius of gyration of the primary particles, D_m is the mass fractal dimension and D_s is the surface fractal dimension of the primary particles.

Pure polymers were analysed using the Debye model (Equation (2.54)) and the Corrlength model (Equation (4.1)). However, the choice of structural model for the polymer-silica samples is substantially more complex. DLS results (Appendix A), TEM results collected by Dr. Khlifa[31] and some literature studies on similar systems[274] suggested that the first step is the core-shell model[272]:

$$P(q) = \frac{scale}{V_s}\left[\frac{3V_c(\rho_c - \rho_{solv})[\sin(qR_c) - qR_c\cos(qR_c)}{(qR_c)^3} + \frac{3V_s(\rho_s - \rho_{solv})[\sin(qR_s) - qR_{sh}\cos(qR_s)}{(qR_s)^3}\right]^2 + bkg \quad \textbf{(5.5)}$$

where *scale* is a scale factor, V_c is the core volume, V_s is the shell volume, r_c is the radius of the core, r_s is the radius of the shell, ρ_c is the SLD of the core, ρ_s is the SLD of the shell and ρ_{solv} is the SLD of the solvent.

5.4 Silica nanoparticles

5.4.1 Hydrodynamic radius and zeta potential

Previous mechanical measurements carried out on polymers containing the two types of fumed silica (H5 and A300) showed different mechanical reinforcement behaviour[31]. These particles are nominally the same size and have the same surface characteristics, so this difference in behaviour in a polymer matrix is unexpected. The two types of fumed silica could also potentially affect the structure and dynamics differently, thus DLS and rheology measurements (presented in Chapter 6) were carried out to characterise the particle size, zeta potential and behaviour in solution.

Dynamic light scattering measurements were carried out on aqueous suspensions of the two types of fumed silica (H5 and A300) to calculate the zeta (ζ) -potential and particle size (Table 5.1). For both types of silica, at low concentrations the average aggregate hydrodynamic radius is approximately 100 nm or 0.1 microns. This corresponds to a radius of gyration of ~160 nm (using the ratio R_h/R_g = 0.72 for aggregated silica from the literature[275]), which is consistent with the manufacturer's specifications of an aggregate length of 0.2-0.3 microns. At higher concentrations (~10

wt %), both silica samples show signs of slightly bigger aggregates being formed, especially the H5 sample. However, neither show signs of the flocculation required to form a gel at up to 10 wt%.

At 20 wt% in solution, the point where the H5 silica suspension displays gelation behaviour in rheological measurements (Section 6.2.2.1), the concentration is too high to be measured accurately by DLS. Nonetheless, there is some evidence of larger aggregates (~300 nm) forming in the 10 wt% suspensions that could lead to gelation at even higher concentrations.

Table 5.1: Aggregate size and zeta potential of fumed silica

H5			A300		
wt% silica	**R_h /nm**	**ζ-potential /mV**	**wt% silica**	**R_h /nm**	**ζ-potential /mV**
0.1	115.1	-33.3	0.1	108.6	-40.6
1.0	104.9	-34.8	1.0	101.7	-26.6
10.0	276.1	-29.4	10.0	208.0	-21.9

Zeta potential results for both types of silica suspensions in distilled water are consistent with literature values for fumed silica at neutral pHs.[276] However, although the decreasing zeta potential of A300 particle suspensions suggests it is less stable than H5 suspensions, the H5 shows larger sized aggregates at higher concentration.

The size of colloidal silica particles was also measured to determine the dispersion and confirm the size of these particles (Table 5.2). The zeta potential of the bare Ludox particles was also measured and listed below. The results confirm the particles are well dispersed and values are consistent with the manufacturer's diameter (10-15 nm). The zeta potential of Ludox particles is similar to the aggregated silica.

Table 5.2: Size and zeta potential of colloidal silica

Ludox-AM			MEK-ST	
wt% silica	**R_h /nm**	**ζ-potential /mV**	**wt% silica**	**R_h /nm**
2.5	8.3	-	10.0	7.8
5.0	7.4	-40.1	40.0	11.0
10.0	6.2	-29.4		
30.0	4.4	-25.3		

Additionally, the zeta potential of the bare particles was compared to that of initiator-silica particles to confirm the presence of bound initiator on the particle's surface. The zeta potential of the particles will change as the hydroxyl groups are replaced by other molecules, and the nature of the change will depend on the groups present in the initiator molecule. Other techniques used, such as elemental analysis, confirm only that there is initiator present, not that it is covalently attached to the silica surface. The zeta potential of the silica particles decreased from approximately -30 to -10 when ATRP initiators were bound to the surface of the particles. This large decrease of zeta potential is typical of silica that has been surface-modified with amine groups, thus showing that the initiator has been successfully bound to the surface of the silica.

5.4.2 Radius of gyration

Using the SasView program, the sphere model was applied to various concentrations of colloidal MEK-ST particles in solution, ranging from 0.5 to 40 wt%, adding a log-normal function to account for polydispersity of the radius. The fit of the sphere model for 4 wt% silica is shown in Figure 5.2 and the parameters listed in Table 5.3.

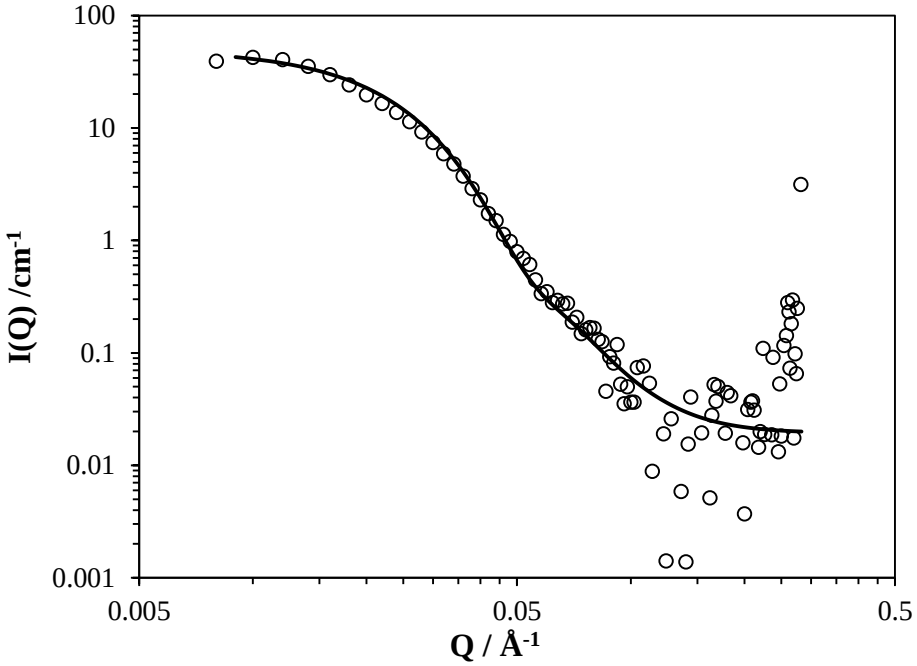

Figure 5.2: SANS data of 4 wt% MEK-ST in MEK. The solid line shows the sphere model fit.

Table 5.3: Fitting parameters for the sphere model fit of 4 wt% MEK-ST silica in MEK.

Background /cm^{-1}	0.017 ± 0.004
Scale/Volume fraction	0.016 ± 0.001
Core Radius /Å	69.5 ± 0.4
SLD of solvent /x10^{-6} Å^{-2}	0.17 ± 0.01
SLD of sphere / x10^{-6} Å^{-2}	3.41 ± 0.12
PD of radius	0.25 ± 0.01

The results confirm that the bare MEK-ST particles are spheres with a diameter of approximately 14 nm and a slight polydispersity (~0.25) which is consistent with the manufacturer's specifications.

The fumed silica H5 was measured in toluene solution. The *Q* dependence of the regions is shown in the log-log plot (Figure 5.3). The scattered intensity from fractal structures such as fumed silica displays two distinct breaks in the log-log representation, corresponding to r_g of the primary silica particles and R_g of the aggregates. The *Q* dependences on the log-log scale for scattering function of fumed H5 silica is similar to other fumed silica reported in the literature[277]. The MassSurfaceFractical model was then used successfully to describe the fumed silica data (Figure 5.4 and Table 5.4). The surface and mass fractal dimensions are consistent with fumed silica modelled in the literature[273].

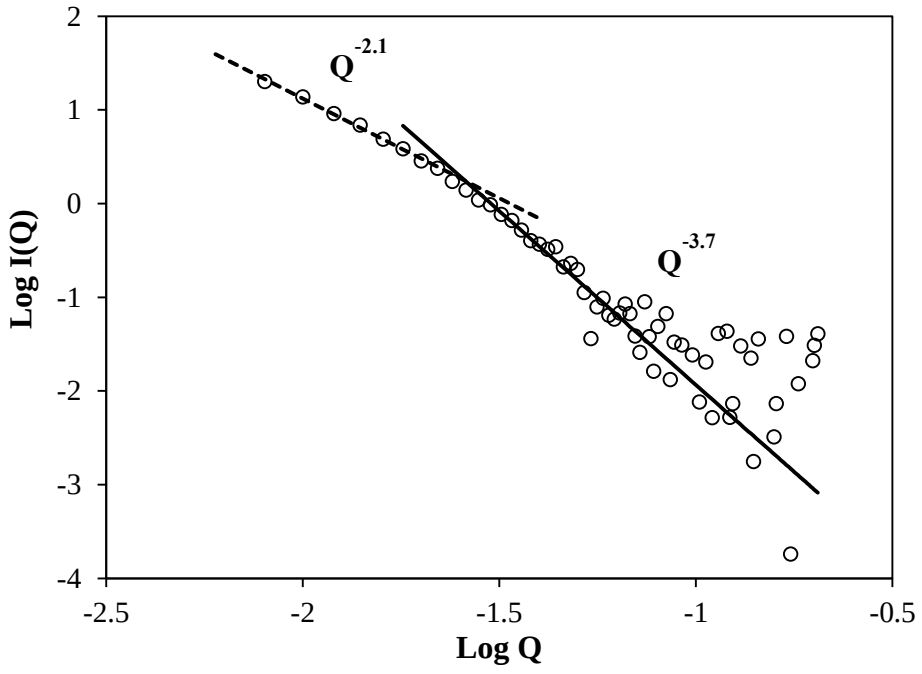

Figure 5.3: Scattered intensity on a log-log scale for fumed silica H5 in toluene solution. The lines show the slopes for the two distinct regions present in the fractal scattering.

Table 5.4: Fitting parameters for H5 silica using the MassSurfaceFractal model.

Background /cm^{-1}	0.01 ± 0.001
D_m	2.17 ± 0.09
D_s	1.54 ± 0.12
R_g (cluster) /Å	1508 ± 28
r_g (primary particle) /Å	40.5 ± 1.2
scale	2092 ± 50

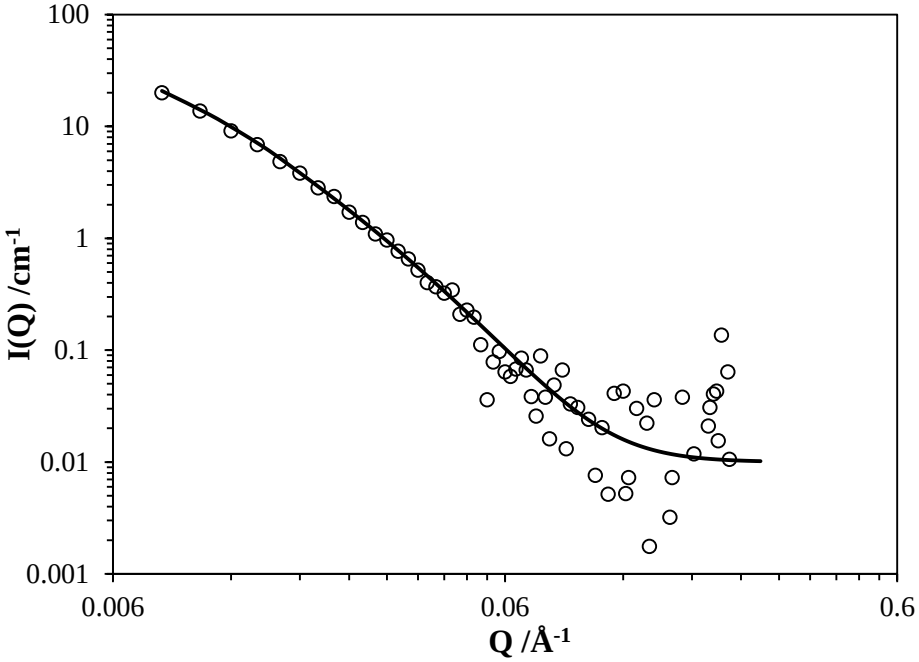

Figure 5.4: MassSurfaceFractal model fit for H5 particles in toluene solution.

5.4.3 Contrast Matching Point

In order to carry out contrast matching experiments, the scattering length density of the solvent must be the same as the silica or the polymer component. The contrast match point for fumed silica was determined by a series of experiments on dispersed H5 particles in mixtures of h-toluene and d-toluene. The contrast match point is the point where the scattered intensity falls to 0 (Figure 5.5).

The contrast match point determination measurements confirm that the scattering length density of the silica is approximately 3.41×10^{-6} Å^{-2}, which corresponds to a 56/44 H/D-toluene mixture. Due to time and solvent constraints, the colloidal silica particle contrast match point was not measured, but assumed to be the same value as the fumed silica as this is also the value used for MEK-ST particles in the literature.

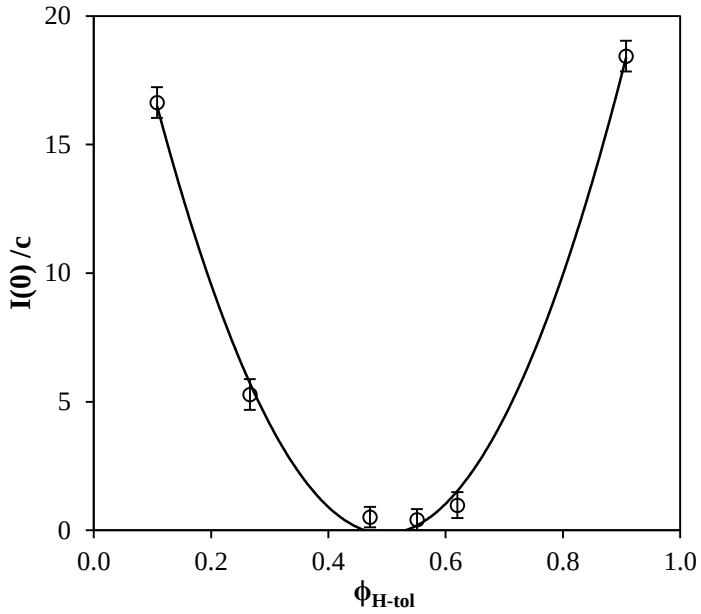

Figure 5.5: Contrast match point determination for fumed silica particles by plotting the intensity of the scattering curve at 0 divided by the concentration against the volume fraction of H-toluene in the H-toluene/D-toluene mixture.

5.5 Polymer-silica solutions

PMMA, PBA and PS-silica samples, both grafted and dispersed, were measured in solution under contrast matching conditions. The scattering length parameters for the various samples and solvents measured in this project are shown in Table 5.5.

Table 5.5: Scattering length parameters for polymer-silica components and solvents

Sample	b_{coh} /fm	m_o /g mol^{-1}	ρ /g cm^{-3}	SLD /10^{-10}cm^{-2}
PMMA	14.91	100.1	1.18	1.06
PS	23.24	104.2	1.04	1.41
PBA	13.24	128.2	1.09	0.68
Silica	-	-	0.17	3.41
Methyl ethyl ketone	2.460	72.11	0.81	0.17
h-toluene	16.59	92.14	0.87	0.94
d_8-toluene	99.96	100.2	0.94	5.66
50/50 h/d-toluene	-	-	-	3.30

5.5.1 Colloidal silica nanocomposites

PMMA, PS and PBA chains grafted and dispersed with MEK-ST particles were measured under contrast and non-contrast matching conditions. A qualitative comparison of the scattered intensity from dispersed and grafted polystyrene nanocomposites under non-contrast matching conditions shows that the scattered intensity from the two types of hybrid particles is very similar (Figure 5.6).

The core-shell model (Equation (5.5)) was applied to the data collected on grafted-PMMA 2.9 MEK-ST at 5 wt% in MEK solution. The initial results from fitting the model with fixed SLD values gave a core radius of 5 nm and a shell radius of ~2 nm (Figure 5.7). This contradicts our core size value calculated from bare silica NPs and the overall size of 7 nm is not consistent with the results obtained from DLS measurements, which showed spherical particles between 15-20 nm. When the core size was fixed at 7 nm, the shell radius calculated was ≤ 0, an unphysical result. Therefore, the core-shell model is not an appropriate model for these samples.

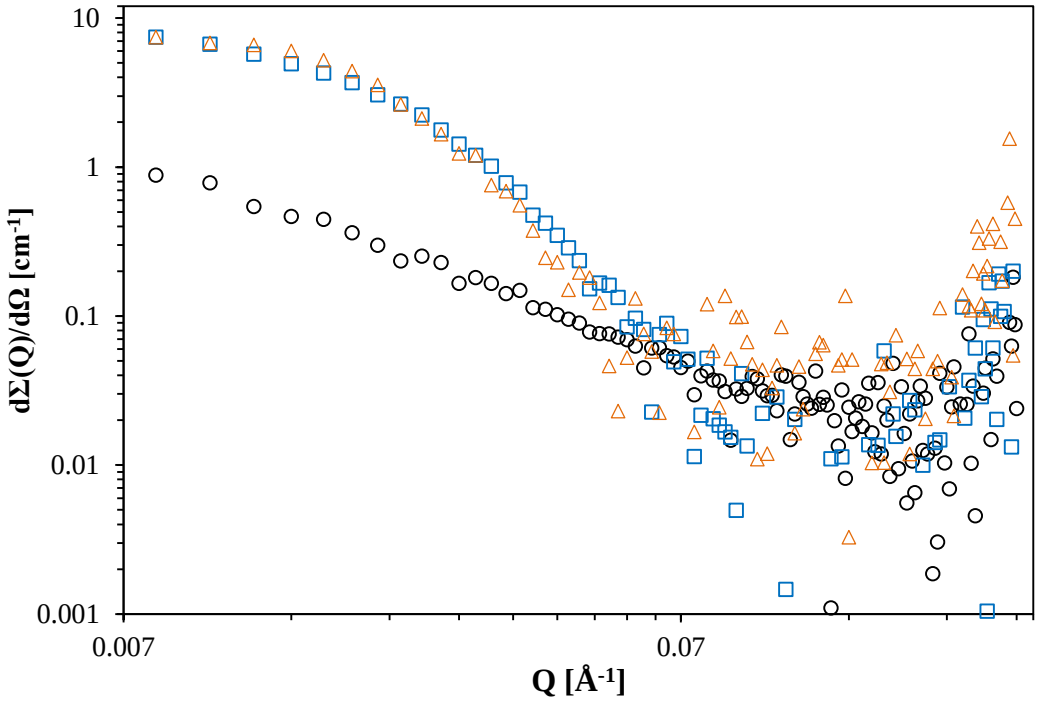

Figure 5.6: Qualitative comparison of 5 wt% solutions in d-toluene of pure PS (○), grafted-PS 4.9 MEK-ST (Δ) and dispersed-PS 6.1 MEK-ST (□).

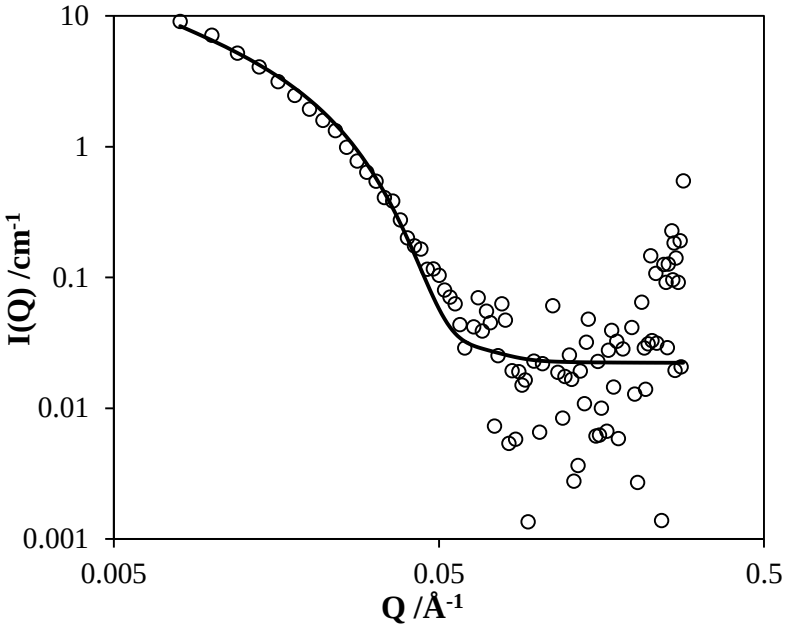

Figure 5.7: Core-shell model fitting of grafted-PMMA 2.9 MEK-ST collected on LOQ at 5 wt% in MEK. The solid line shows the fit of the curve using the core-shell model (Equation (5.5)).

Due to the samples being measured primarily between 5 – 10 wt%, the particles may be aggregated into clusters which would affect the form factor. Therefore, the data was also modelled using the fractal core-shell model that describes aggregates of core-shell particles. However, as with the core shell mode, unphysical results of negative shell thicknesses were obtained with this model. Therefore, the core-shell model is insufficient in describing the structure of our PMMA-silica samples. This result corroborates data reported in the literature, where the core-shell model failed to describe other nanocomposites[278].

Fits using the core-star model used for PS-fullerene samples was also attempted; however it was also a poor fit to the data and gave unphysical results of shells with a thickness of over 100 nm. This is likely due to the fact that the polymer-silica samples were not in the dilute regime, especially considering that only the most dilute PS-fullerene samples could be modelled using the core-star model (<2 wt%). Other effects, such as excluded volume and interpenetrating polymer chains, affect the use of the core-star model.

Therefore, a model including the silica scattering was not applied to the polymer-silica data. Instead, the silica contribution will be subtracted, either by contrast matching in the experiment or subtracting the contribution in Excel, and the polymer chains analysed using the models in Section 2.3.3.

Contrast matching experiments on PMMA chains grafted to MEK-ST silica at loadings from 3 wt% to 18 wt% were carried out to evaluate the effect of silica on the polymer chain scattering. After subtraction of the incoherent background, the results from PMMA chains grafted to MEK-ST silica particles were qualitatively compared to pure PMMA chains (Figure 5.8 and Figure 5.9). The scattered intensity is very similar to pure PMMA for all grafted samples, regardless of the silica loading (3 wt % to 18 wt %). There are slight deviations at low Q values ($Q < 0.016$ Å^{-1}) in the grafted sample containing 3 wt% silica, which could be due to differences in the molecular weights of the samples. Overall, however, we conclude that grafting PMMA chains from colloidal silica does not change their structural behaviour, even at high loadings.

Using this result that polymer chain scattering is largely unaffected by the presence of silica, the scattered intensity from polymer-MEK-ST nanocomposites under non-contrast matching conditions was modelled using a combination of a sphere model for colloidal silica nanoparticles and a Debye model for the polymer chains. The components are plotted for a contrast matched polystyrene sample (Figure 5.10) and this provided a good fit of the data. In the samples with higher loadings of silica, a significant contribution from polymer-silica correlations is also present, similar to the core-star model used for polystyrene-fullerene stars.

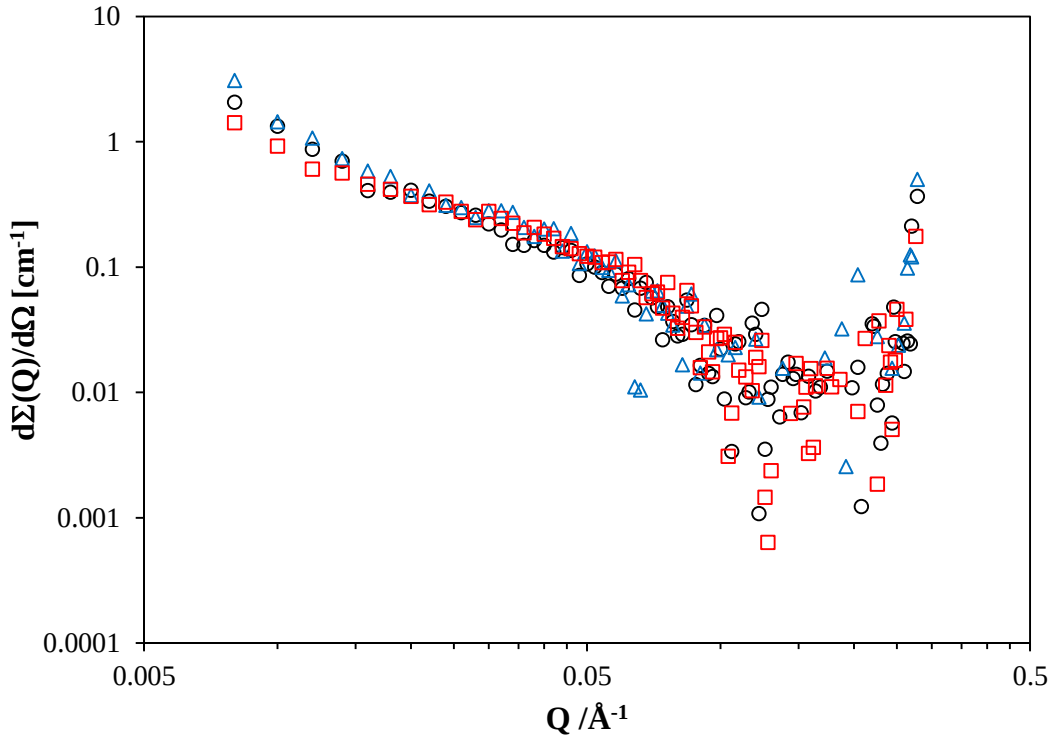

Figure 5.8: Scattered intensity on a log-log scale of 5 wt% solutions in 50/50 h/d-toluene for pure PMMA (○), grafted-PMMA 2.9 wt% MEK-ST (□) and grafted-PMMA 6.1 wt% MEK-ST (Δ).

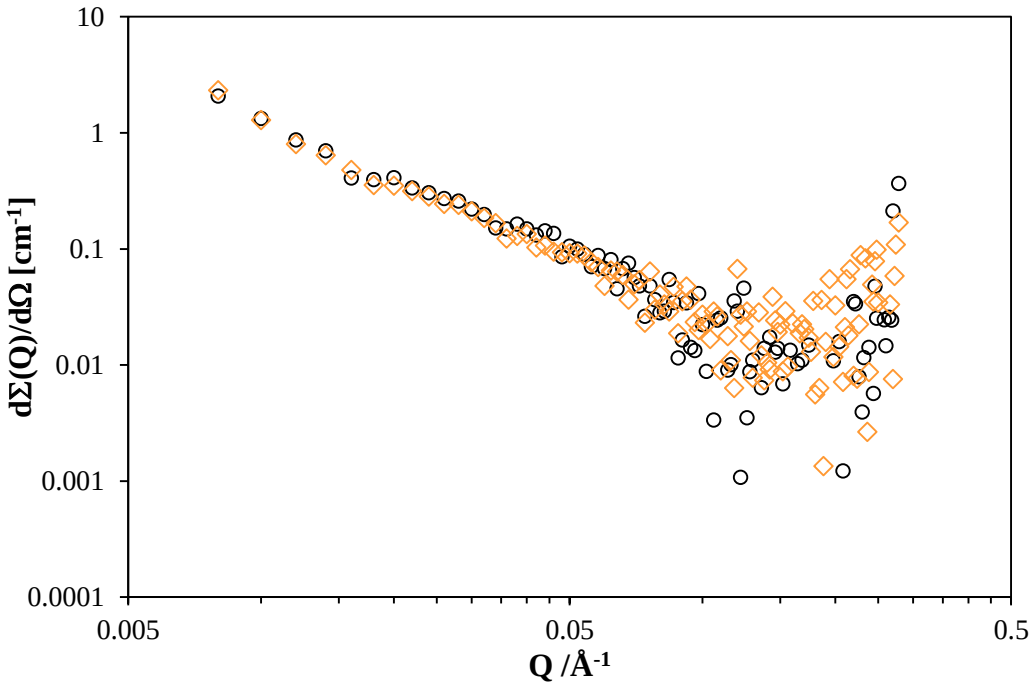

Figure 5.9: Scattered intensity on a log-log scale of 5 wt% solutions in 50/50 h/d-toluene for pure PMMA (○) and grafted-PMMA 18 wt% MEK-ST (◊).

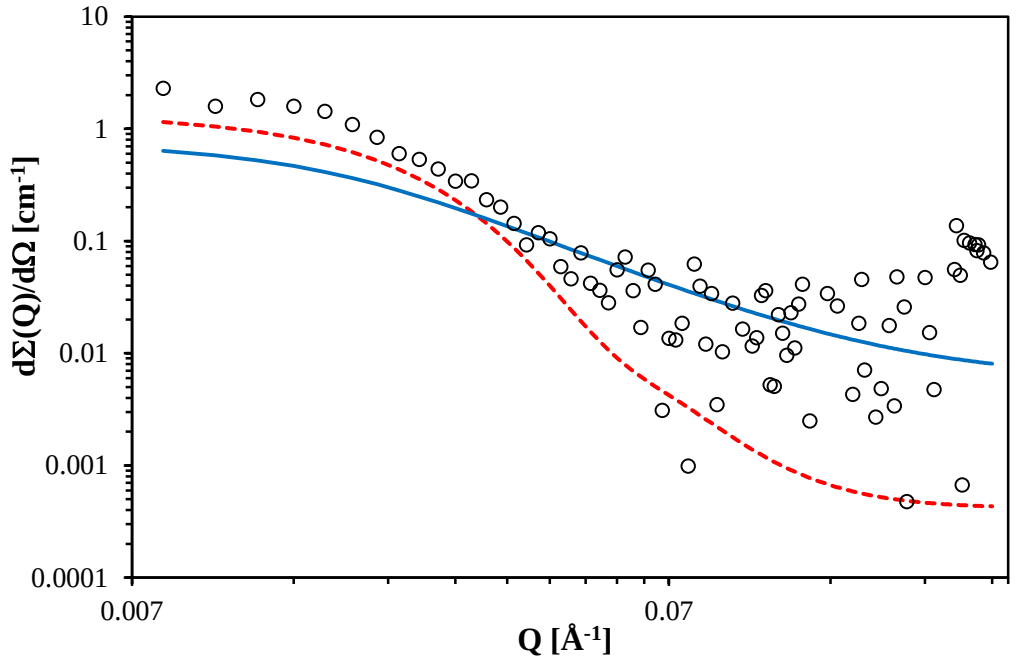

Figure 5.10: Contribution to the scattered intensity in a non-contrast matched grafted-PS 4.9 wt% MEK-ST sample: experimental data (○) and calculation using the sphere (- - -) and the Debye model (—).

Grafted and dispersed polystyrene-silica nanocomposites were measured in deuterated toluene and the scattering from the silica subtracted using a volume fraction

weighted bare silica scattering curve (Figure 5.11). The results show that the polystyrene chains are not affected by addition of silica, either by dispersion or by grafting the chains to the surface of the silica. This result is consistent with the results from the PMMA samples and the literature, as unperturbed structural behaviour has been observed in the literature for polystyrene-colloidal silica dispersions[118]. Gaussian chain behaviour has also been observed in hydrogenated polystyrene grafted to Ludox silica nanoparticles by Chevigny *et al.*[121], however they found that deuterated polystyrene grafted to silica was better modelled with a core-shell like structure.

Models used for linear polymer chains were applied to the contrast matched data. The Debye model only reliably fits the PS data at these concentrations, and the R_g values obtained are listed in Table 5.6. The PMMA and PBA samples were modelled using the Ornstein-Zernike Equation (4.1) for semi-dilute polymer chains and the values for the correlation length are listed in Table 5.7. Examples of the fits are shown in Figure 5.12. Samples not listed in the table were too poor to accurately model beyond qualitative comparisons with pure polymers. The results show that the grafted chains are of similar sizes to the pure polymers, as expected from the qualitative analysis, and corroborate the recent general trend in the literature that colloidal fillers do not affect chain conformation[114, 122].

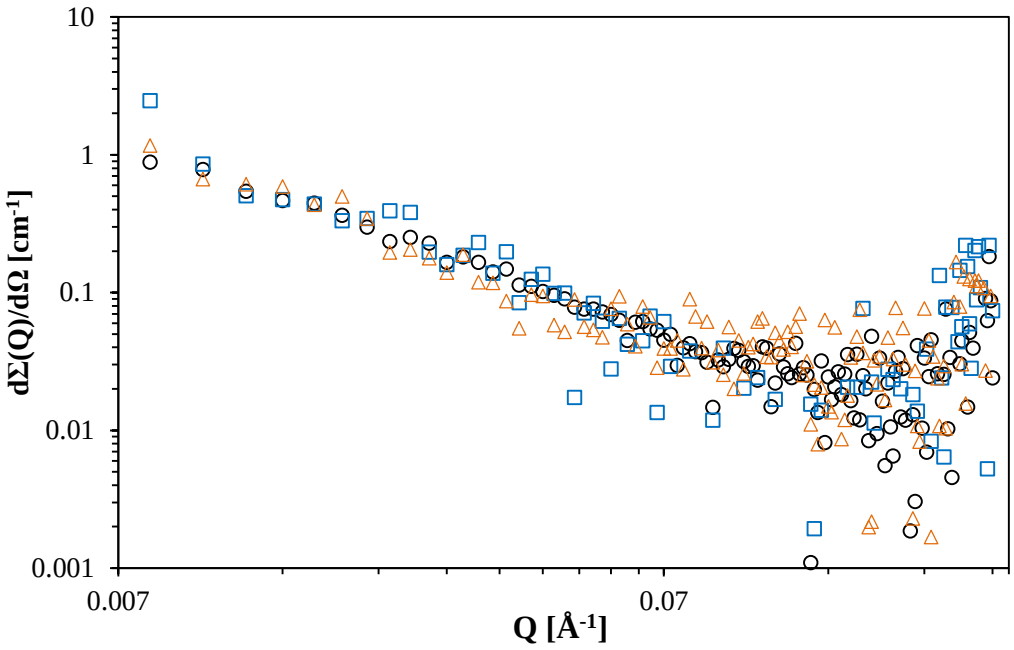

Figure 5.11: Scattered intensity on a log-log scale of 5 wt% solutions in D-toluene for pure PS (○), grafted-PS 4.9 wt% MEK-ST (Δ) and dispersed-PS 6.1 wt% MEK-ST (□), after subtraction of the silica scattering.

Table 5.6: SANS parameters obtained from Debye model fits of PS and PS-silica samples.

Sample	Solvent	M_w /g mol^{-1}	c /g ml^{-1}	R_g /Å	I(0)
PS	d-toluene	100,000	0.048	108.6	0.809
dispersed-PS 6.1 MEK-ST	MEK	100,000	0.049	106.7	1.044

Table 5.7: SANS parameters obtained from Ornstein-Zernike (Equation (4.1)) fits of polymer-colloidal silica nanocomposites.

Sample	Solvent	M_w /g mol^{-1}	c /g ml^{-1}	ξ /Å
PMMA	50/50 h/d-tol	100,000	0.051	17.8 ± 0.8
grafted-PMMA 6.1	50/50 h/d-tol	37,800	0.052	18.3 ± 0.9
MEK-ST			0.101	12.3 ± 0.6
grafted-PMMA 2.9	50/50 h/d-tol	-	0.047	18.5 ± 0.7
MEK-ST			0.097	12.7 ± 0.5
PBA	d-toluene	99,000	0.047	29.0 ±

Notation: ##.# = wt % of silica measured by elemental analysis

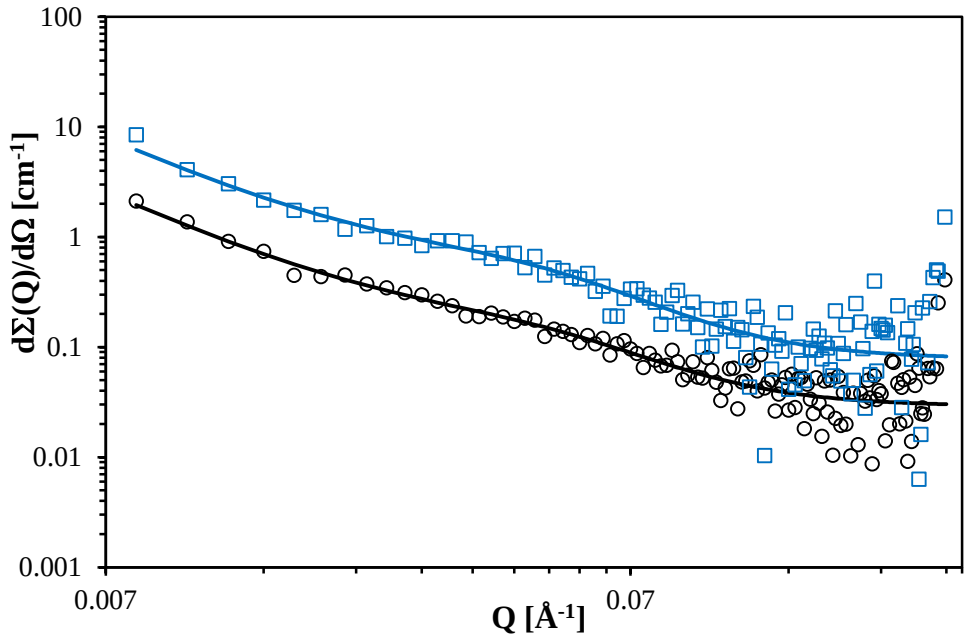

Figure 5.12: Example of Ornstein-Zernike fits of pure PMMA (○) and grafted-PMMA 6.1 MEK-ST (□) measured on LOQ at 5 wt% in 50/50 h/d-toluene solution.

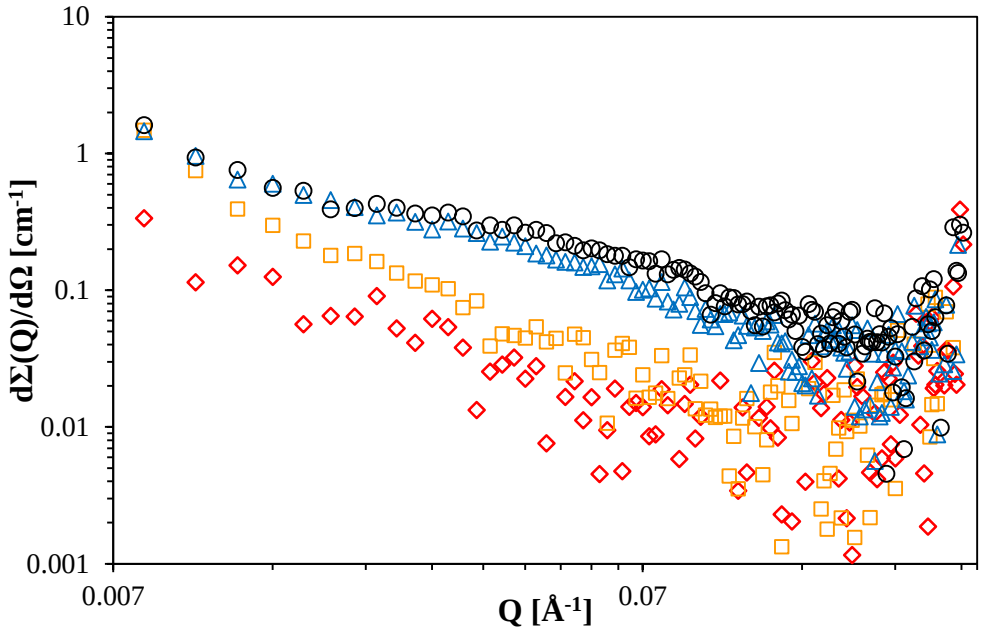

Figure 5.13: Scattered intensity on a log-log scale for grafted-PMMA 2.9 MEK-ST at 0.5 wt% (◊), 1 wt% (□), 5 wt% (Δ) and 10 wt% (○) in 50/50 h/d-toluene solution.

The grafted PMMA samples were measured at concentrations ranging from 0.5 to 10 wt%. However, as shown in Figure 5.13, dilute solutions are difficult to analyse due to the low scattering intensity (<0.1 at low Q) and high level of noise in the measurements. Therefore only the higher concentration solutions could be accurately modelled. In order to improve dilute solution measurements, deuterated grafted polymers are required for measurements.

5.5.2 Fumed silica nanocomposites

Fumed silica has been shown in the literature to have larger effects on the mechanical and thermal properties of polymers than colloidal silica. Therefore, although colloidal silica has no effect on polymer conformation, fumed silica may be expected to show different results. A qualitative comparison of dispersed and grafted PBA and PS-fumed silica hybrid particles in Figure 5.14 shows similarity, as already noted for the colloidal silica samples. However, both the PBA and PS grafted nanocomposites display an increase in scattered intensity at low *Q* (most prominent in the PS samples), which is typically indicative of larger agglomerates within the sample.

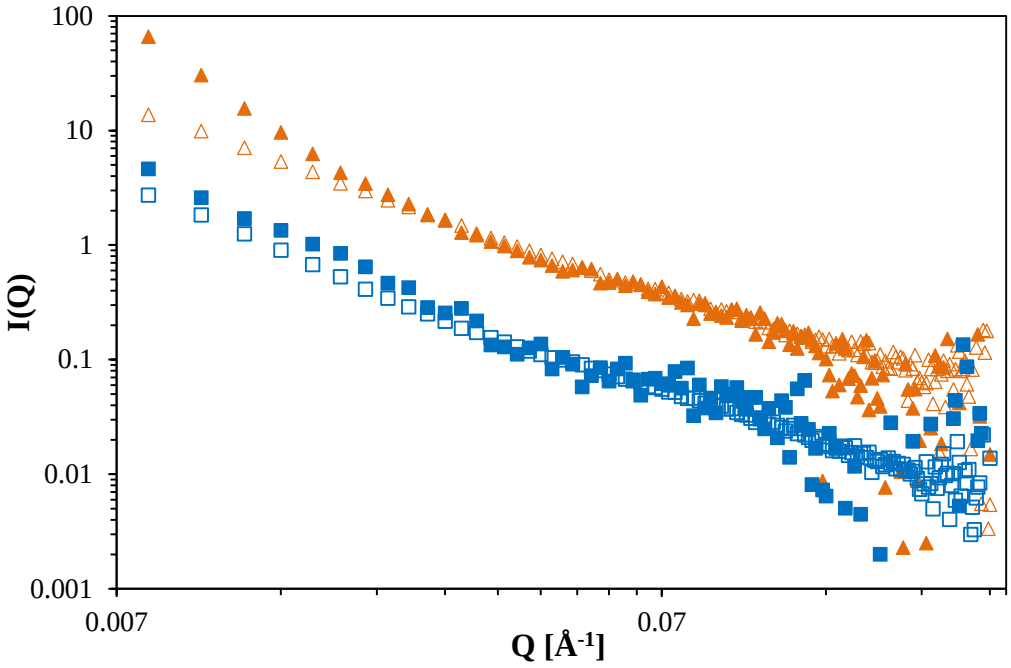

Figure 5.14: Qualitative comparison of grafted-PS 16.5 H5 (▲), dispersed-PS 15.0 H5 (△), grafted-PBA 3.9 H5 (■) and dispersed-PBA 15.2 H5 (□) 5 wt% solutions in D-toluene. The PBA curves have been shifted vertically using a shift factor for clarity.

The most unusual sample is the grafted-PMMA 9.2 H5 sample (Figure 5.15), which shows very similar scattering behaviour to the grafted PMMA-MEK-ST sample, in contradiction to the other samples containing fumed silica. This result, combined with the DLS data (Appendix A) and the TEM results from a previous student[31], shows that the structure of the aggregated silica can be broken down into its primary particles during the polymerisation process and the resulting nanocomposite is similar to the samples grafted to colloidal silica sample. Therefore it is crucial to control the polymerisation conditions to keep the fractal structure of the silica present in the grafted PS and PBA samples.

Samples of grafted PBA-silica and grafted PS-silica with fumed silica nanoparticles were measured under contrast matching conditions (Figure 5.16). The scattered intensity is similar to that of the pure polymer; however there is a small decrease in the intensity at intermediate values, and potential evidence of aggregation in the samples as the scattered intensity increases at the low *Q* values measured.

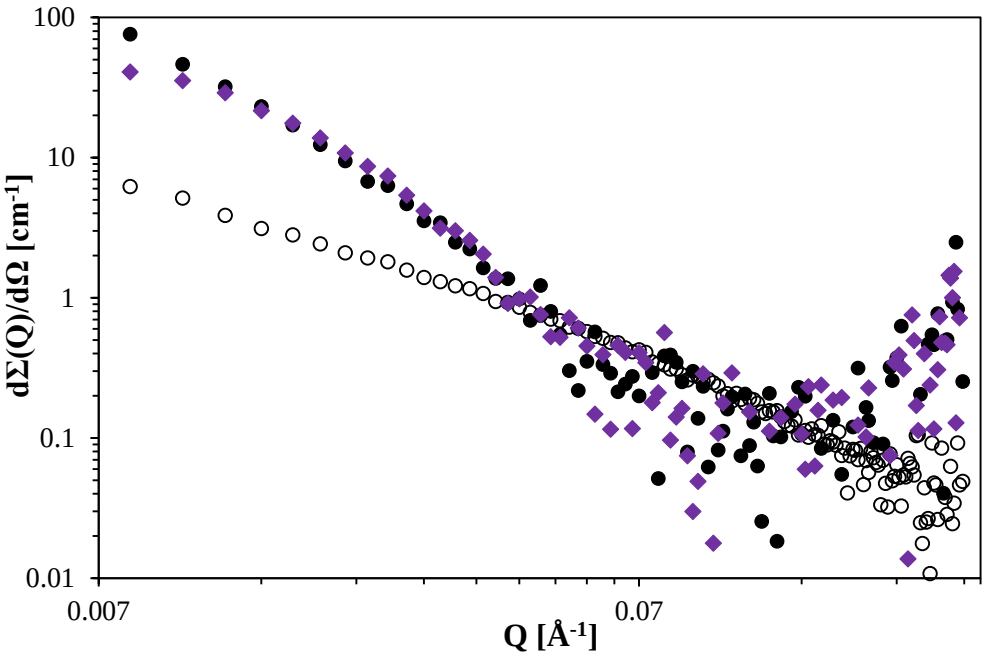

Figure 5.15: Qualitative comparison of 5 wt% solutions in d-toluene of grafted-PMMA 9.2 H5 (●), dispersed-PMMA 14.9 H5 (○) and grafted-PMMA 6.1 MEK-ST (♦).

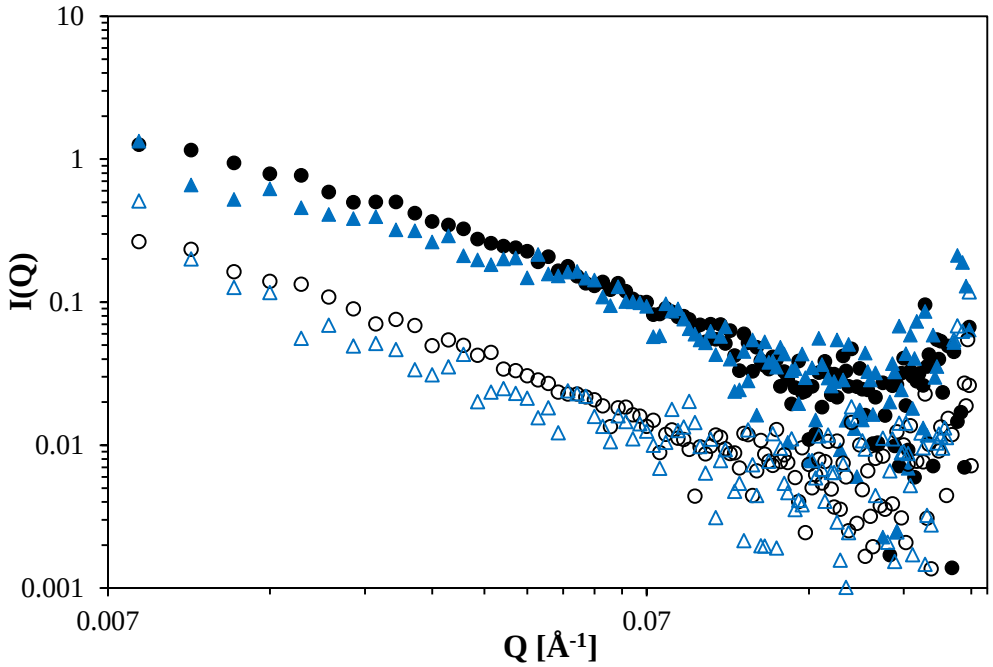

Figure 5.16: Scattered intensity on a log-log scale of 10 wt% solutions in 50/50 h/d toluene for pure PS (○), pure PBA (●), grafted-PS 16.5 H5 (△) and grafted-PBA 3.9 H5 (▲)under contrast matching conditions. The PBA curves have been shifted vertically using a shift factor for clarity.

When the data are modelled using the Debye equation for linear polymer chains (shown for polystyrene in Figure 5.17), the experimental radius of gyration is close to the calculated value (Table 5.8). The molecular weight of the grafted sample is lower than that of the pure polymer measured, resulting in the slightly different shape of the scattered intensity at intermediate *Q* values.

Table 5.8: SANS parameters obtained from contrast matched polymer-fumed silica nanocomposites (Figure 5.16).

Sample	M_w /g mol^{-1}	c /g ml^{-1}	Calc. R_g /Å	R_g /Å	I(0)
grafted-PBA 3.9 H5	113,000	0.096	70.7*	66.5	0.917
grafted-PS 16.5 H5	68,000	0.107	90.8	92.4	0.575

***R_g value calculated according to Equation (4.8)**

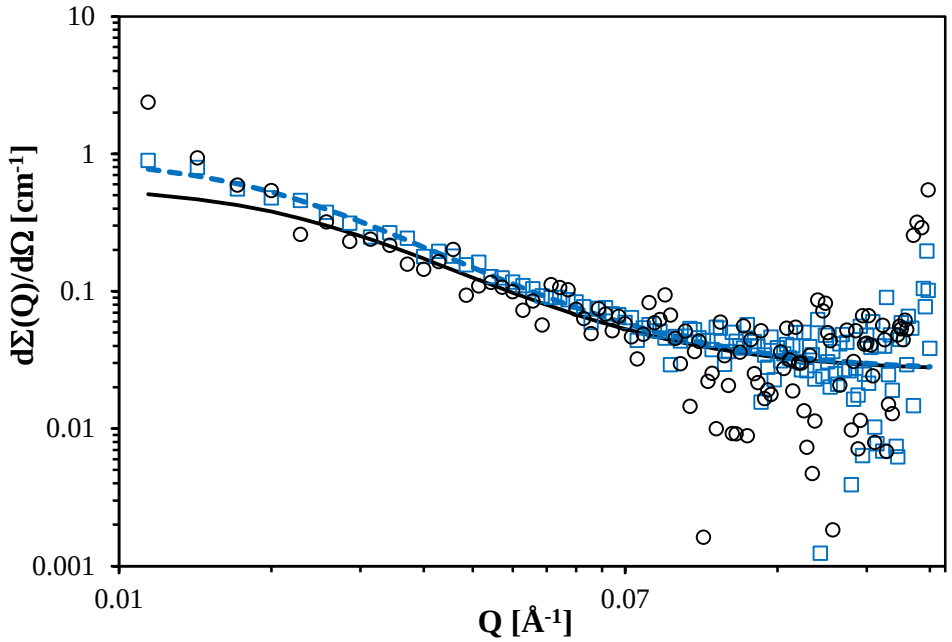

Figure 5.17: Debye model fits (lines) of pure PS (□) and grafted-PS 16.5 H5 (○) 10 wt% solutions in 50/50 h/d-toluene solution.

However, there is clearly additional scattered intensity at low *Q* (< 0.015 Å) that is not modelled by the Debye equation (Figure 5.17). In the literature, this has often been attributed to unwanted silica contributions that are still present despite contrast matching conditions[122, 271]. The cause of this has been attributed to selective absorption of hydrogenated/deuterated chains on the surface of the nanoparticles, voids around the silica particles caused by inhomogeneous mixing[118] or, most recently, a thin shell of polymer chains with reduced mobility around the particle surface causing "mismatches" with the H/D-ratio used in the local environment[114]. The only plausible explanation for these grafted samples is a mismatch caused by a polymer shell around the nanoparticles, as the grafted chains could potentially be considered a shell with possible reduced mobility at the surface. However, there is also potential aggregation in the grafted samples, detected by the earlier DLS measurements, which may cause an increase in scattered intensity in the low *Q* range.

The samples containing fumed silica were also measured under non-contrast matching conditions. An attempt to model the data in a similar method to the samples containing colloidal silica: using a combination of the model for the polymer chains and the model for the silica. The first step was subtracting the silica model, i.e. the MassSurfaceFractal model for fractal objects, to determine the polymer chain scattering model. However, both the dispersed and the grafted PBA samples (Figure 5.18 and Figure 5.19 respectively) show considerable increased scattered intensity in the low Q region with a $\sim Q^{-2}$ dependence, even after the scattering of the silica has been subtracted. Since the contrast matched samples indicate that polymer chains themselves are only slightly perturbed by the presence of fumed silica, the additional scattering most likely arises from the silica particles. The low Q region is dominated by large scale structure, therefore the additional scattering could be due to the formation of agglomerates of the silica nanoparticles or polymer-silica hybrid particles in the grafted sample, either through particle agglomeration or bridging polymer chains. Particle aggregation is commonly seen as a sharp increase in scattered intensity in the low Q region.

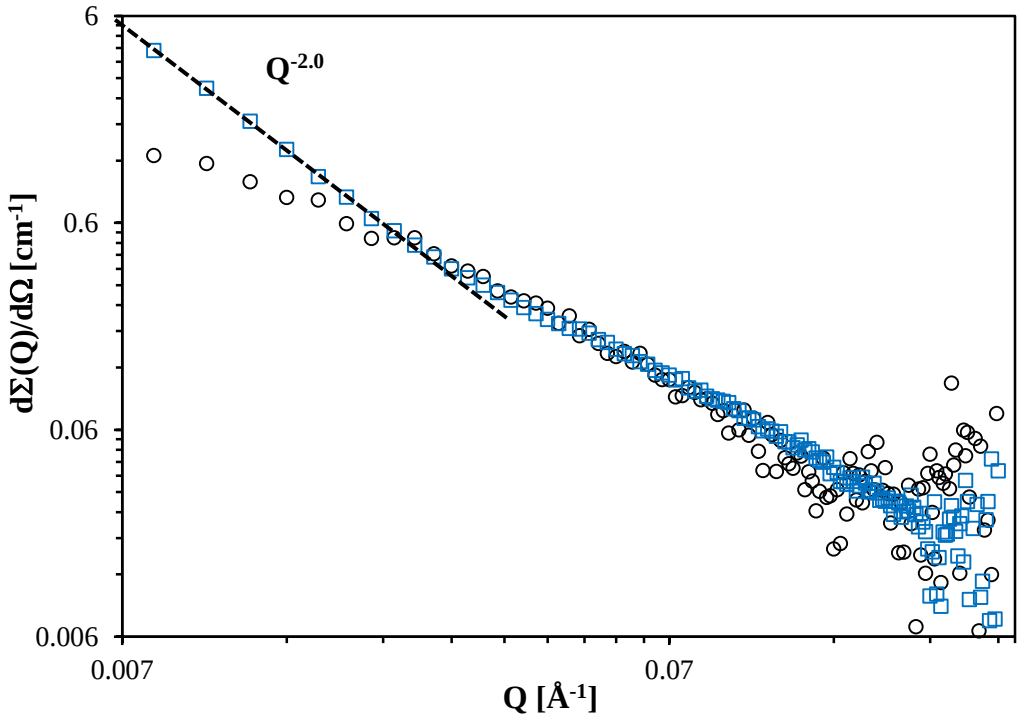

Figure 5.18: Comparison of pure PBA chains (○) to dispersed-PBA 15.2 H5 (□) 5 wt% solutions in d_8-toluene where the fractal model for the silica contribution has been subtracted.

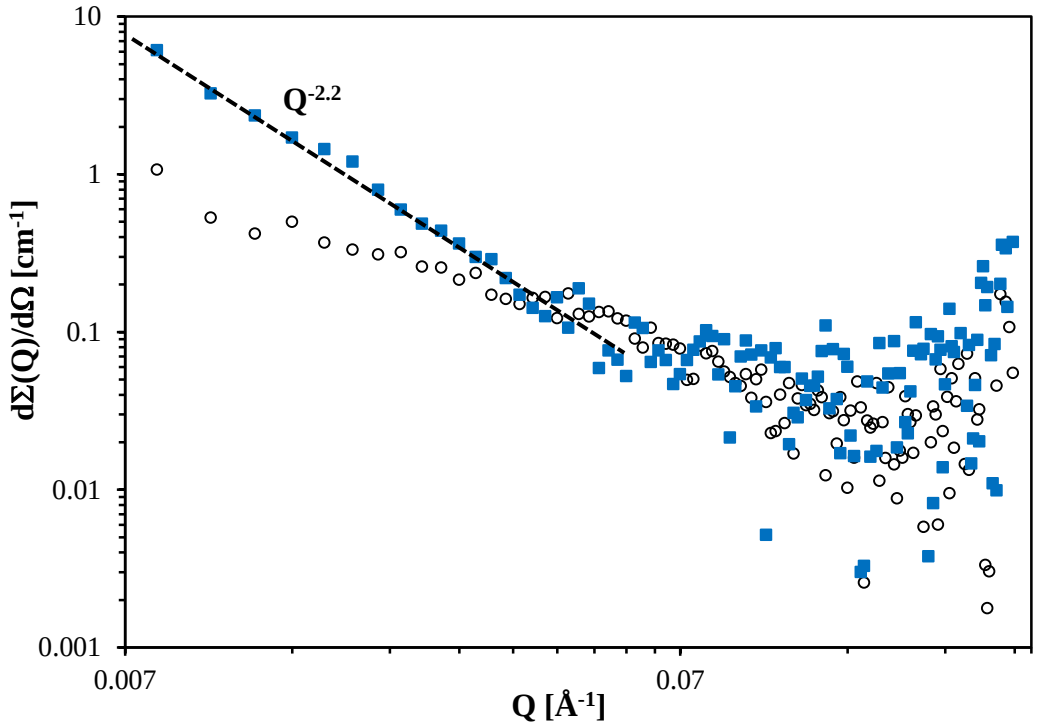

Figure 5.19: Comparison of contrast matched grafted-PBA 3.9 H5 (○) to grafted-PBA 3.9 H5 (■) 5 wt% solutions in d_8-toluene where the fractal model for the silica contribution has been subtracted.

Although aggregation is the common explanation for this increase in scattering at low *Q*, the range of the scattering extends into the intermediate range for the grafted sample (Q = 0.04 Å^{-1}). Therefore, another potential explanation is scattering intensity arising from polymer-silica interactions and correlations that are not modelled using a simple linear combination of models. Polymer-filler correlations can be also masked when contrast matching the solvent to one of the two components (see the core-star model in Section 4.2), and thus may only be present in the non-contrast matched scattering.

Other models were attempted to try to fit the data, such as the fractal core shell model, however there is no simple model for chains grafted or physisorbed onto fumed silica. Guinier and Zimm plot analysis cannot be carried out due to aggregation causing a large increase of scattered intensity in the low *Q* region. Contrast matching experiments that match the polymer chains to the solvent are required to examine the structure of the silica in the nanocomposites and determine whether the model requires the fractal model for silica to be adapted or whether it is polymer-nanoparticle correlations that need to be modelled.

5.6 Polymer-silica solids

5.6.1 Small-Angle X-Ray Scattering (SAXS)

SAXS measurements were performed on a range of dispersed and grafted PS-silica samples at APS (ANL). The averaged SAXS curves are shown in Figure 5.20. The PS samples grafted to aggregated silica show the same fractal behaviour as the fumed silica. The grafted-PS MEK-ST samples, however, show a peak at intermediate *Q* values. The SAXS data of the various silica and polystyrene-silica samples were first analysed using a Lorentz correction by plotting I(Q) Q^2 against *Q* (Figure 5.21). This shows more clearly the appearance of a peak in the grafted samples with colloidal silica.

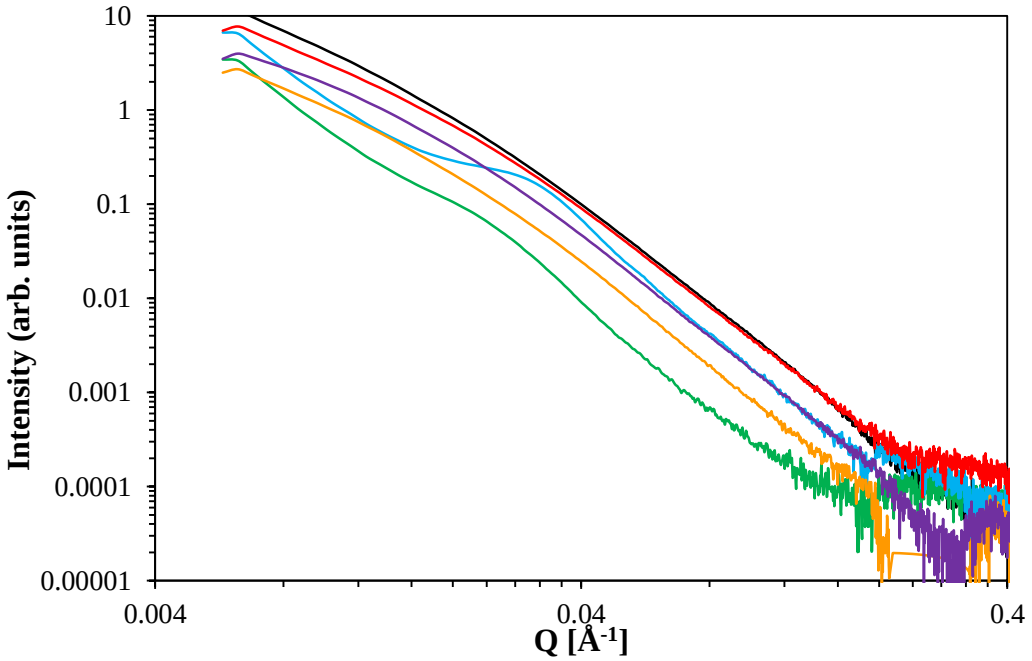

Figure 5.20: SAXS intensity profile of A300 silica particles (black), dispersed-PS 20 H5 (red), grafted-PS 25 A300 (purple), grafted-PS 17.1 MEK-ST (blue), grafted-PS 16.5 H5 (orange) and grafted-PS 9.3 MEK-ST (green). The curves have been shifted vertically using shift factors for clarity.

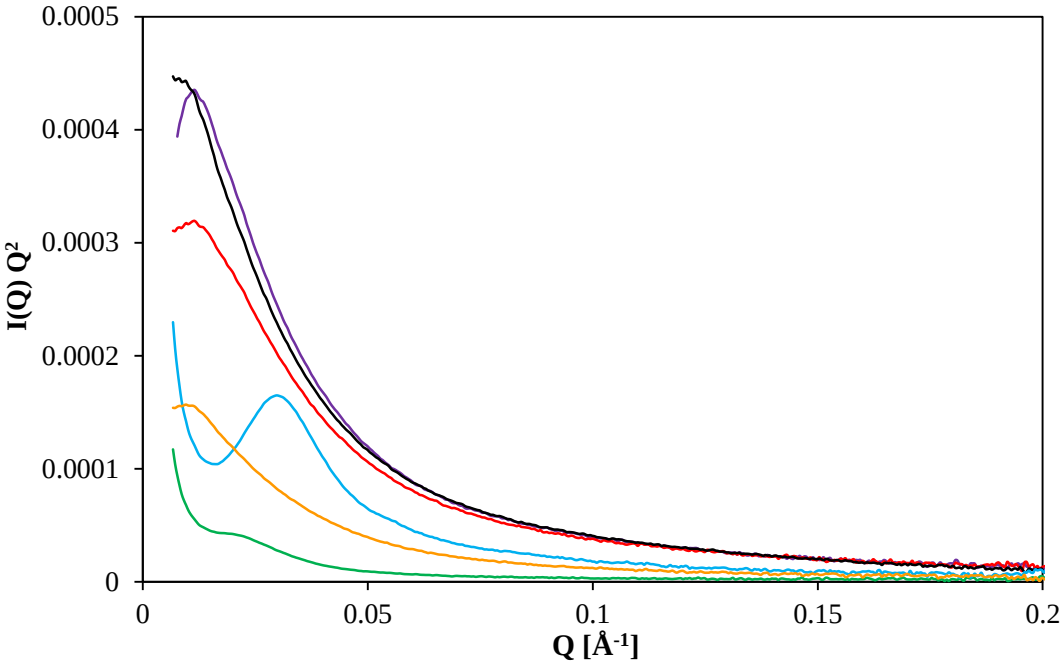

Figure 5.21: Lorentz-corrected SAXS intensity profile of A300 silica particles (black), dispersed-PS 20 H5 (red), grafted-PS 25 A300 (purple), grafted-PS 17.1 MEK-ST (blue), grafted-PS 16.5 H5 (orange) and grafted-PS 9.3 MEK-ST (green).

The appearance of this peak at Q = 0.023 Å^{-1} and 0.029 Å^{-1} (for grafted-PS 9.3 MEK-ST and grafted-PS 17.1 MEK-ST respectively) is consistent with the results from Janes *et al.* on dispersed poly(methyl acrylate) (PMA) nanocomposites with MEK-ST silica that show a peak at Q = 0.035 Å^{-1} at high loadings of silica (vol fraction of silica = 0.19 to 0.51)[279]. This peak was attributed to interparticle correlations arising from strong repulsive interactions at high loadings. The group fitted the PMA-silica SAXS data using the Beaucage model[280]:

$$I(Q) = \sum_{i=1}^{N} G_i exp\left(\frac{-q^2 {R_{g,i}}^2}{3}\right) + \frac{B_i\left[erf\left(\frac{qR_{g,i}}{\sqrt{6}}\right)\right]^{3P_i}}{q^{P_i}} + bkg \qquad \textbf{(5.6)}$$

where P_i is the Porod power law, G_i and B_i are Guinier and Porod scaling factors and N is the number of independent structural levels. The term [erf($(qR_{g,i})/\sqrt{6}$)] provides a smooth transition between the Guinier and the Porod regions. The Beaucage model is an empirical model that has been used to approximate the scattering from many types of materials, from random coils to fractal clusters[281]. Janes *et al.* used a Porod exponent of 4 but did not report the remainder of the fitting parameter values, as they state that agglomerates in the nanocomposites could only be partially characterised by the Beaucage model.

Holt *et al.* ran SAXS experiments on dispersions of poly(2-vinylpyridine) (PVP) with colloidal silica and the resulting data were interpreted with a linear combination of the Beaucage and the core-shell model[282]. The scattering function obtained was similar to that obtained from a core-shell structure, however the interfacial bound layer was found to be non-uniform with a broad interface with the matrix. Thus a Beaucage component was required to account for the effect of non-uniformity of density of the shell on the scattered intensity. However, as expected from the SANS analysis reported in previous section, the SAXS data of PS-silica samples cannot be modelled using the core-shell model.

The Beaucage model was therefore applied to the nanocomposites containing colloidal silica, using the SasView program. A two level (n = 2) Beaucage model is required due to the presence of agglomerates in the low *Q* region and formation of the peak in intermediate *Q* range. The fitted curves are shown in Figure 5.22 and the parameters listed in Table 5.9. The peak in the scattering function causes a poorer fit in the sample containing a higher amount of silica.

Table 5.9: Fitting parameters from the Beaucage model on SAXS data of PS-silica samples

Sample	$G_{i\,1}$	$G_{i\,2}$	$B_{i\,1}$	$B_{i\,2}$	P_i	$R_{g\,1}$/Å	$R_{g\,2}$/Å
grafted-PS 9.3 MEK-ST	405	283	1.69×10^{-5}	5.22×10^{-5}	3.8	192.8	2860
grafted-PS 17.1 MEK-ST	361	100	1.77×10^{-5}	4.51×10^{-6}	3.8	132.3	2100

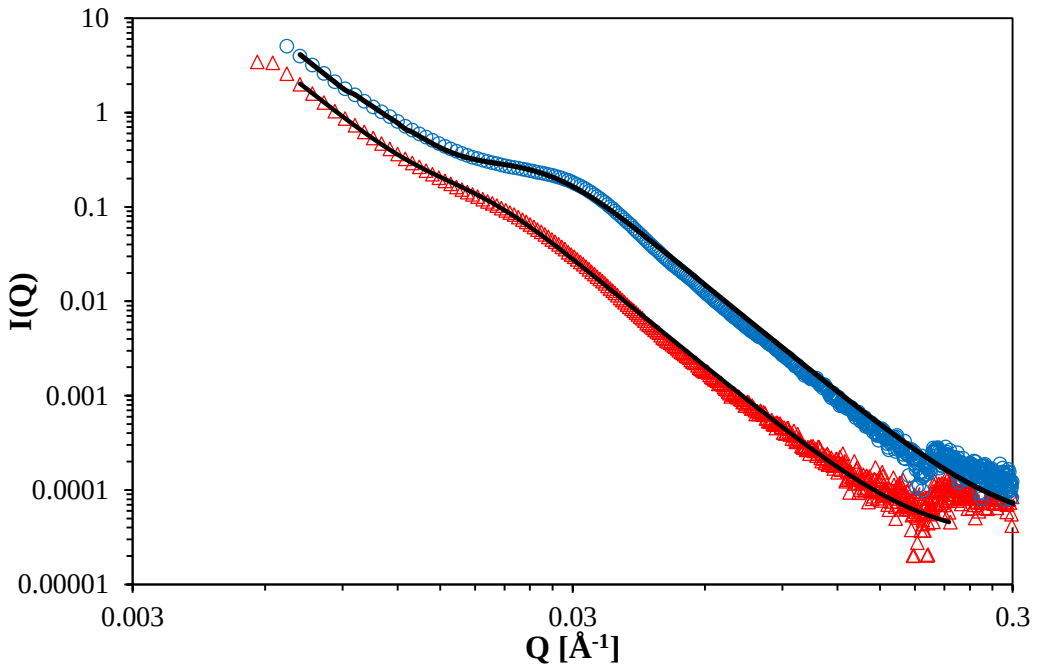

Figure 5.22: Beaucage model fitting of the SAXS data for grafted-PS 17.1 MEK-ST (○), and grafted-PS 9.3 MEK-ST (Δ). The fitting parameters are listed in Table 5.9.

The calculated radius of gyration values of approximately 13-19 nm (unimer) and 200-300 nm (aggregates) are consistent with the DLS results. The samples were also fitted using the single level Beaucage model by ignoring the low Q region, giving similar R_g values of 18 and 14 nm for grafted-PS 9.3 MEK-ST and grafted-PS 17.1 MEK-ST samples, respectively. However, there is a large degree of uncertainty in the obtained R_g value. This is due to the large number of variables and the correlation between variables that is not taken into account when varied independently. Additionally, the Beaucage model has recently come under scrutiny in the literature, as letting the Guinier and Porod scale factors vary independently can cause artifacts in the resulting scattering function[283]. The Beaucage model was found to be accurate for Porod exponents in the range $5/3 < P_i < 3$, which is below the Porod exponent of these samples ($P_i = 3.8$).

The nanocomposites containing fumed silica show the same scattering behaviour as the bare fumed silica particles, regardless of whether the sample is grafted or dispersed (Figure 5.23). The bare fumed particles are plotted on a log-log scale (Figure 5.24), showing the same behaviour as the SANS spectra of H5 particles (Section 5.4.2). As with the H5 data, the fumed silica SAXS data can be successfully fitted using the MassSurfaceFractal model in SasView (See Appendix A). The double logarithmic plot of PS grafted from A300 (Figure 5.24) shows that the grafted sample has a similar scattered intensity to the bare fumed silica.

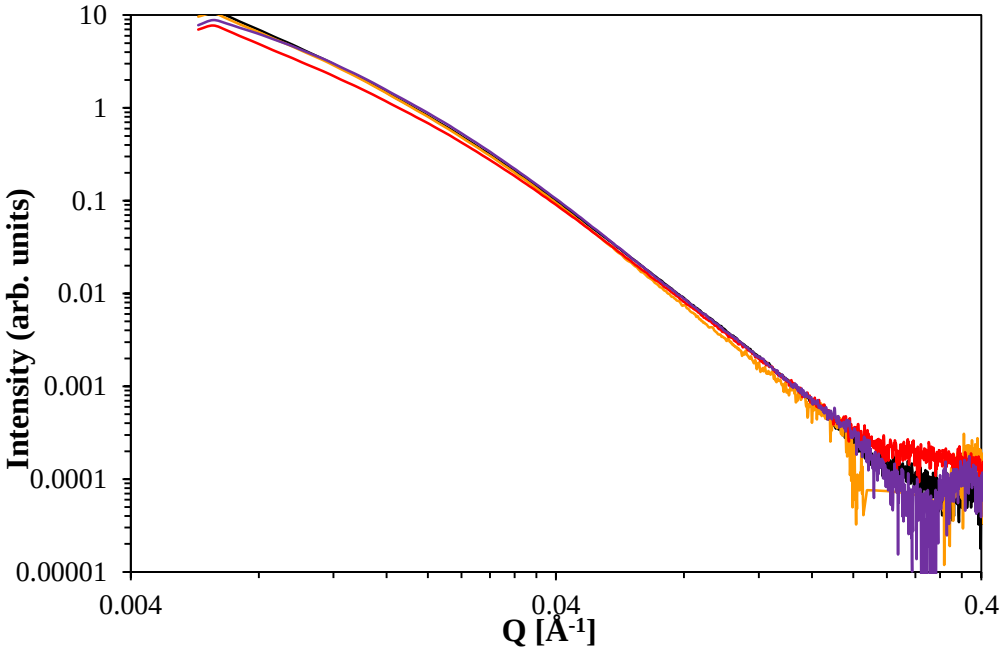

Figure 5.23: SAXS data of fumed silica and PS-fumed silica nanocomposites: A300 silica particles (black), dispersed-PS 20 H5 (red), grafted-PS 25 A300 (purple) and grafted-PS 16.5 H5 (orange). The curves have been shifted vertically to show the similarity between all the samples.

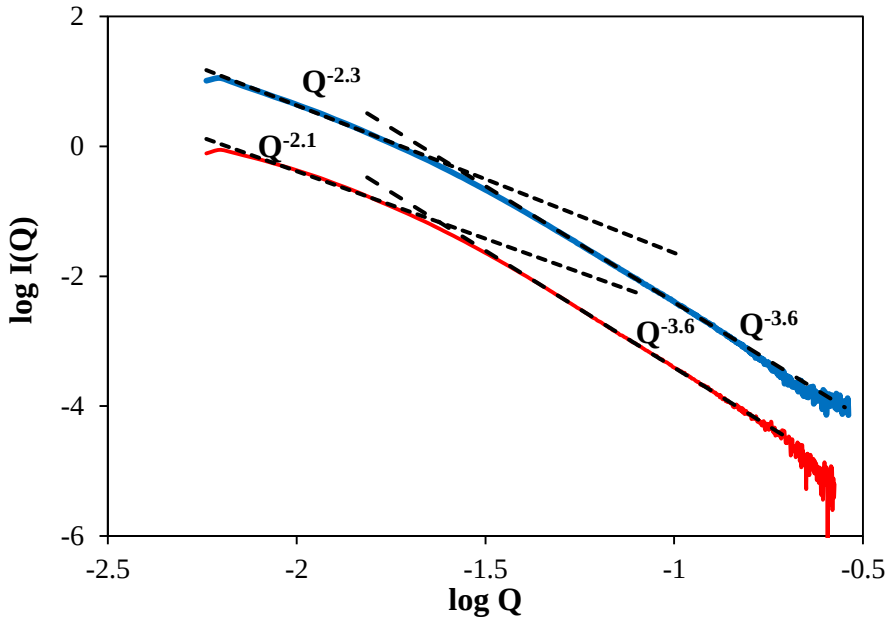

Figure 5.24: SAXS data on a log-log scale for fumed silica A300 (blue) and grafted-PS 25 A300 (red). The straight lines show the slopes for the two distinct regions present in the fractal scattering. The curves have been shifted vertically for clarity.

Botti *et al.* performed SAXS and SANS experiments on polyisoprene samples containing precipitated silica to characterise the filler structure in the nanocomposite[284]. An adapted Beaucage model for fractal clusters was used, showing that the aggregated silica structure within a polymer matrix can be described by a one-component model, and can subsequently be subtracted with a suitable weighting from the SANS scattering of the polymer nanocomposite. The scattering from the chains was then fit to the Debye model, showing that the chains are not significantly perturbed by the presence of the aggregated filler. However, in these PS samples the remaining scattered intensity after subtraction of the silica contribution for the PS-silica samples measured cannot be modelled with the Debye model (Appendix A), as seen in the solution behaviour results. Further experiments are required to fully understand the structural behaviour of polymer-silica solids.

5.6.2 Small-Angle Neutron Scattering (SANS)

A few SANS measurements on solid PS grafted samples were carried out on LOQ. The SANS data show good agreement with the results from the SAXS experiments: the colloidal silica nanocomposites exhibit a peak at similar intermediate *Q* values between 0.02 to 0.04 $Å^{-1}$ (Figure 5.25), whereas the SANS curves of fumed silica samples show

a a fractal structure similar to that of the bare silica particles (Figure 5.26). Therefore, as with the SAXS data, further analysis and measurements are required on these samples.

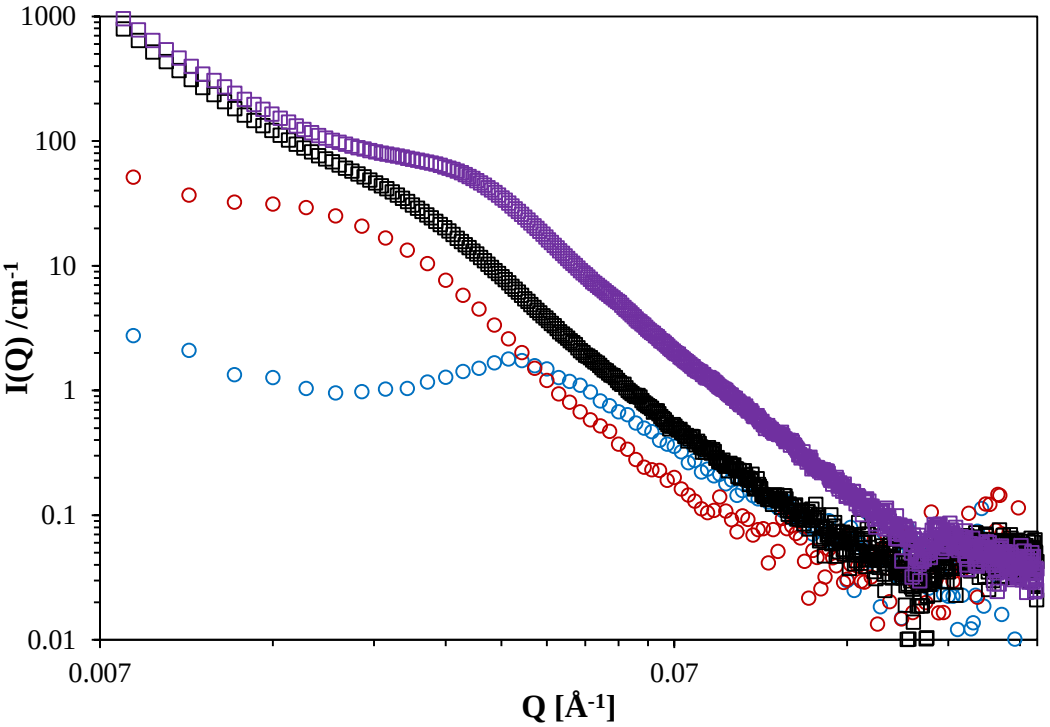

Figure 5.25: Comparison of SAXS and SANS data for colloidal silica samples. SANS data of grafted-PS 11.9 MEK-ST (○) and grafted-PS 4.9 MEK-ST (○), SAXS data on grafted-PS 17.1 MEK-ST (□) and grafted-PS 9.3 MEK-ST (□)).

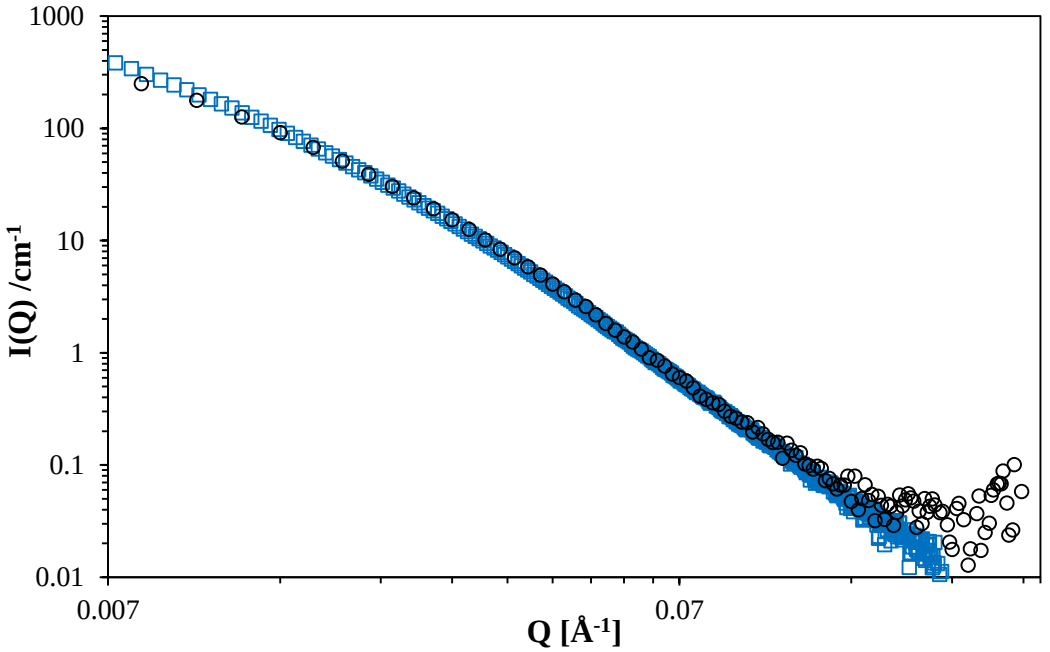

Figure 5.26: Comparison of SAXS and SANS data for fumed silica samples: SAXS data of grafted-PS 16.5 H5 (□) and SANS data of grafted-d_8PS 18.1 H5(○). The curves have been shifted vertically to show the identical structural behaviour.

A grafted d_8-PMMA MEK-ST nanocomposite was measured at various temperatures on the SANS2D instrument at ISIS (Figure 5.27). The scattering is similar to the PS-silica samples containing colloidal MEK-ST silica. Beaucage model fitting of the curve gives a unimer R_g value of 16 nm, close to the values obtained from DLS measurements, however the model fails to fit the data at intermediate to high Q values.

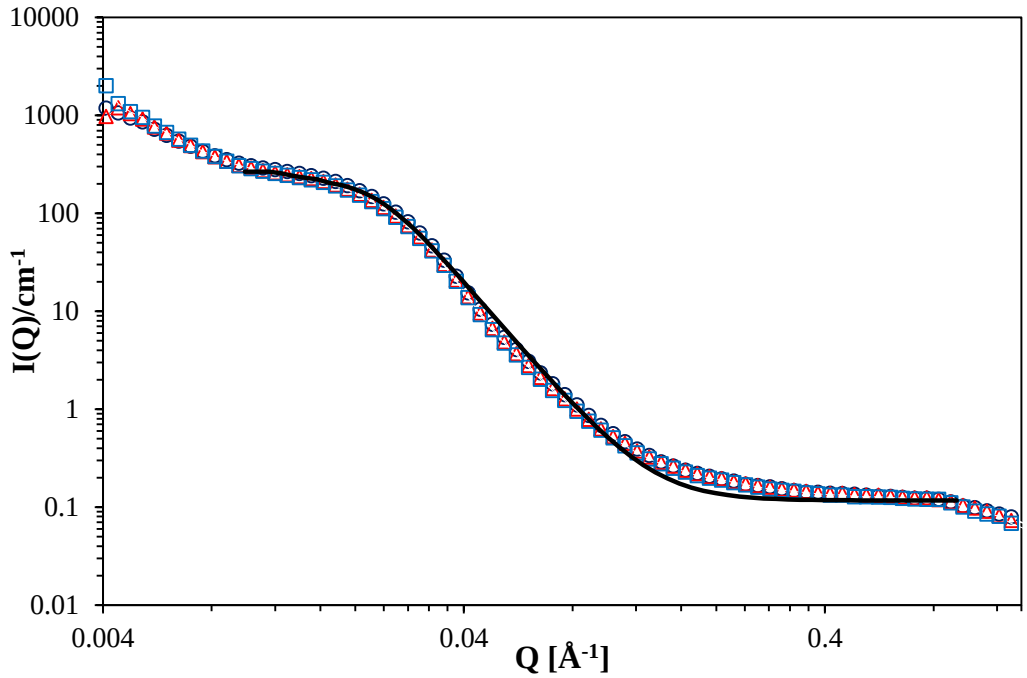

Figure 5.27: Scattered intensity of grafted-d_8PMMA 17.3 MEK-ST at 25 ºC (○), 100 ºC (Δ) and 120 ºC (□). The solid lines show the Beaucage model fits.

5.7 Conclusions

In the polymer-silica samples, grafting high molecular weight PMMA chains from colloidal silica particles (approx. 7 nm diameter) has no effect on the PMMA structural behaviour in solution; the grafted samples behave similarly to the pure polymer. The core-shell model, which has been used previously in the literature to model data of similar nanocomposites[285], does not fit our data; instead the chains behave as normal Gaussian polymer chains. This has been shown in several grafted PMMA samples in Section 5.5.1, regardless of silica loading and despite the presence of covalent bonding between the polymer chains and the filler. This result is consistent with a recent trend in the literature that has shown that nanoparticles do not affect the structure of polymer chains[119, 121].

Both dispersed and grafted polymer samples containing colloidal silica nanoparticles can be modelled using a linear combination of the sphere model (for

silica) and the Debye/Ornstein-Zernike models (for the polymer chains). The results confirmed that the size of the polymer chains was unchanged upon addition of colloidal silica nanoparticles. This result, combined with the PS-fullerene analysis from Chapter 4, shows that grafting polymers to or from the surface of small, spherical nanoparticle fillers has little effect on the structure of polymer chains.

However, the structure of polymer nanocomposites is more complex when fumed silica is used as the filler. Contrast matching measurements show that the polymer chains are slightly perturbed by the presence of the silica but still largely follow Gaussian statistics and linear polymer behaviour. The additional scattering at low Q is either some residual silica scattering, despite being under contrast matching conditions, or some aggregation of the polymer-silica particles that is seen in the chain scattering. When the scattering from both components is present, the different polymers show slightly different behaviour. In PS samples, the scattering from the dispersed nanocomposite can be accounted for entirely by a combination of the fractal silica scattering and the scattering from the pure PS sample. In the grafted sample, there is significant additional scattering in the low Q region. However, in PBA nanocomposites, both the dispersed and grafted samples show this increase in scattered intensity at low Q values. The two possible explanations for this are the formation of nanoparticle or polymer-nanoparticle agglomerates or strong polymer-particle interactions that are not accounted for using a linear combination of models.

Preliminary SAXS and SANS measurements on primarily polystyrene-silica nanocomposites in the bulk were also carried out. The two types of measurements show good agreement with each other and show similar structural behaviour to PMA-silica samples in the literature[279]. An attempt to fit the data using the Beaucage model was made and the R_g values obtained were consistent with the DLS analysis; however the error for the R_g value is very large. Further measurements and analysis of the SAXS and SANS data is required for full understanding of the structural behaviour of polymer-silica nanocomposites in the bulk.

Chapter 6. Dynamics and Rheology of Polymer Nanocomposites

6.1 Introduction

The addition of fillers to a polymer can improve various properties of the polymer matrix. The origin of these reinforcement effects arises from changes in the structure and the dynamics of the polymer chains. In this chapter, the focus is on the effect of dispersing and grafting fillers on the chain dynamics and the effect this has on macroscopic properties of the polymer matrix such as rheology and physical ageing.

The effect of fillers on the local chain dynamics of polymers is a relatively new area of research with few studies in the literature (see Section 1.5.2). Various explanations have been proposed to explain changes in dynamics in the presence of nanoparticles. Due to polymer-particle interactions, theoretically the chain mobility near the surface of the particles would be greatly reduced which creates a interfacial layer of static chains around the particles[286]. This is known as the 'bound layer' and has a significant effect on the overall dynamics, the mechanical and thermal properties of the polymer matrix. However, other groups have observed changes in chain dynamics that cannot be explained by the presence of an immobile layer[132].

The addition of nanoparticles can also have significant effects on the rheological properties of polymer nanocomposites. This is another recent area of interest, especially for commercial purposes, as the rheology of materials is important in industrial applications. Viscoelastic behaviour affects the processing of the materials in the melt, therefore an increase in the viscosity can lead to lower processability. The effects of fillers on viscoelastic properties has been the subject of many studies in the literature (see Section 1.5.5), however the effects are complex and depend on many different variables such as the size, shape and aggregation of the fillers[172], polymer-particle interactions etc.

The segmental motion of polymer chains is also directly related to the rate of physical ageing. If nanoparticles affect the local dynamics of the polymer chains, a corresponding change in ageing would be expected. The effect of fillers on physical ageing of polymers is a relatively recent area of research that is of particular interest for applications of polymer nanocomposites. As physical ageing of materials leads to a loss of thermal and mechanical properties over time, the use of cheap fillers to reduce the rate of ageing would give a longer shelf life and reduce the rate of deterioration of the material. However, the exact effect of fillers on ageing and the mechanisms behind it

are still under debate in the literature[157], and the effect of grafting chains over dispersing nanoparticles in the polymer matrix has been little explored.

In this chapter, the dynamics of two systems were investigated:

1. Polymer-silica nanocomposites (grafted and dispersed). The local chain dynamics were investigated by glass transition, elastic window scans (EWS) and quasi-elastic neutron scattering (QENS) measurements. Rheological measurements were used to measure the dynamic modulii and viscosity in the melt, and enthalpy relaxation experiments quantified the physical ageing of the nanocomposites. The results are compared to pure polymers to determine the effect of dispersing fillers and grafting onto fillers on the microscopic and macroscopic dynamics of the polymer chains.
2. Grafted PS-fullerene star systems. The chain dynamics were analysed by glass transition measurements, EWS and QENS measurements. Rheological measurements on the viscosity of dilute and concentrated solutions were carried out to compare the macroscopic dynamics to linear polystyrene chains.

6.2 Polymer-silica nanocomposites

Some of the measurements presented in this Section were collected prior to the start of this project. QENS measurements at ISIS and ILL and glass transition measurements on PBA-silica samples were carried out by Natalie Grima[30], but the data had not been analysed prior to this project. The analysis of the QENS data was completed during the course of this project.

The choice of polymer-silica nanocomposite for various measurements is closely related to the properties of the polymers. QENS and rheological measurements were carried out on PBA-silica samples because PBA has a low glass transition temperature (-49 ^{o}C), allowing for neutron measurements at relatively low temperatures and for rheological measurements in the melt at temperatures between -5 and 100 ^{o}C, which is the limit of the rheometer. However, physical ageing experiments require controlled cooling below the glass transition temperature, which was not possible for PBA with the limitations of the water cooling system on the Pyris 1 DSC instrument. Due to this, physical ageing experiments were carried out on PS-silica and SAN-silica samples used for mechanical measurements previously[31].

6.2.1 Local chain dynamics

6.2.1.1 Glass Transition Temperature

DSC measurements were carried out on a variety of polymer-silica nanocomposite systems, both dispersed and grafted, to evaluate the effect of silica on the T_g of the polymer matrix. Due to the local dynamics of PBA-silica samples being studied further in QENS and rheological experiments, the T_g of pure PBA and PBA-silica samples are presented separately to the other polymers.

Selected dispersed and grafted PBA-silica nanocomposites of similar silica content are shown in Figure 6.1 for comparison. The results for all PBA nanocomposites (Table 6.1) show that there is a slight decrease in T_g (1-2 ^{o}C) when the silica is dispersed and a slight increase in T_g (1-2 ^{o}C) when the PBA chains are grafted to the silica. Although the difference in T_g is small, a change in T_g of 1 – 2 ^{o}C has been shown to be significant in other polymer nanocomposites, such as polystyrene-fullerenes[148, 287]. Carrot *et al.*[288] reported an increased T_g when PBA is grafted to silica nanoparticles and suggested this was due to reduced chain mobility.

Table 6.1: Glass Transition measurements for PBA and PBA-silica nanocomposites.

Polymer/Nanocomposite	T_g /^{o}C	ΔC_p /Jg^{-1}^{o}C^{-1}
Pure PBA	-48	0.36
dispersed-PBA 3.4 H5	-49	0.35
dispersed-PBA 13.8 H5*	-50	0.32
dispersed-PBA 20.0 H5	-49	0.27
dispersed-PBA 30.1 H5	-49	0.26
dispersed-PBA 40.0 H5	-48	0.23
grafted-PBA 5.0 H5	-46	0.34
grafted-PBA 13.8 H5*	-47	0.33
dispersed-PBA 2.1 A300	-48	0.36
dispersed-PBA 13.7 A300*	-49	0.34
grafted-PBA 13.7 A300*	-46	0.33
Error	± 1	± 0.02

Notation: ##.# = wt % of silica measured by elemental analysis. Samples labelled with * were synthesised by Natalie Grima.

Fragiadakis *et al.*[127] found that while there was little change in the position of T_g with increasing silica content, the heat capacity of the transition decreased after

normalising to the polymer content in poly(dimethyl siloxane) (PDMS)-silica nanocomposites. They also reported a double structure shape in the glass transition, which together with the C_p results suggested the presence of an interfacial layer of polymer chains with reduced mobility at the silica surface. However, in our results we see no evidence of a double step in the glass transition (Figure 6.1). The change in heat capacity can also be entirely accounted for by subtracting the unseen contribution from silica (Figure 6.2). This suggests that all chains, including those potentially immobilised, participate in the glass transition.

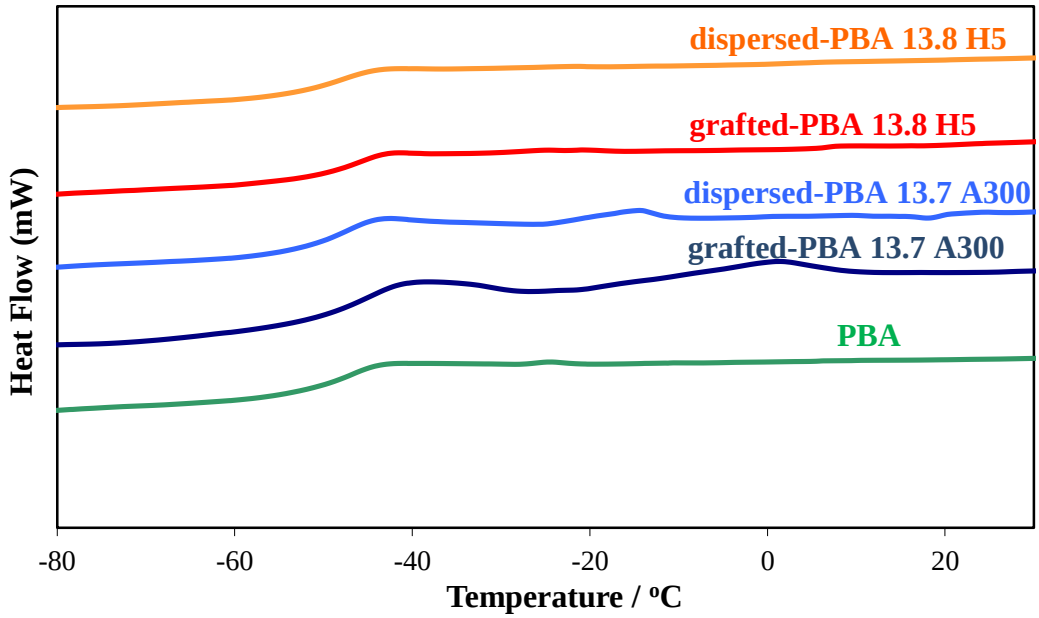

Figure 6.1: DSC traces of pure PBA and PBA-silica nanocomposites, shifted vertically for clarity.

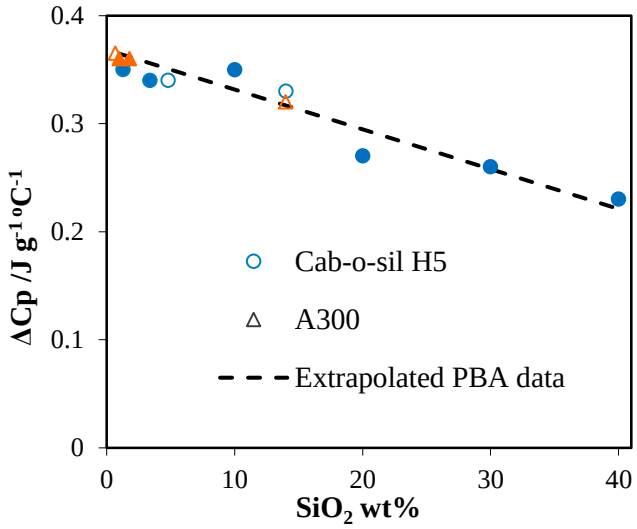

Figure 6.2: Change in heat capacity at the glass transition for PBA grafted to H5 (○) and PBA grafted to A300 (Δ). The filled symbols show dispersed silica samples and the unfilled symbols denote grafted samples. The dashed line shows the extrapolated change in PBA heat capacity considering the fraction of PBA only.

Table 6.2: T_g of PMMA-silica, PS-silica and SAN-silica nanocomposites.

Polymer/Nanocomposite	T_g / °C	M_w (g mol^{-1})
PS	102.3	100,000
dispersed-PS 10 MEK-ST	102.0	100,000
grafted-PS 14 H5*	112.2	26,000
grafted-PS 14 MEK-ST*	109.3	83,000
SAN	105.9	165,000
dispersed-SAN 20 H5	105.7	165,000
grafted-SAN 17 H5	109.1	140,000
grafted-SAN 17 MEK-ST	110.6	139,000
PMMA	118.0	64,000
dispersed-PMMA 20 MEK-ST*	118.6	64,000
dispersed-PMMA 20 H5*	116.5	64,000
grafted-PMMA 20 MEK-ST*	122.9	31,000
grafted-PMMA 22 H5*	128.3	30,000
Error	± 1.0	± 1000

Notation:## = wt % of silica measured by elemental analysis. Samples labelled with * were synthesised by Dr. Moussa Khlifa.

The glass transition temperature of PMMA-silica, PS-silica and SAN-silica nanocomposites was also measured. The results are listed in Table 6.2, alongside M_w values determined by GPC by Dr. Moussa Khlifa before the start of this project[31]. Dispersing silica has either no significant effect or results in a slight decrease (~2 °C) in the T_g of the polymer in all systems measured and is consistent with the PBA-silica results. However, the grafted nanocomposites show a significant increase in T_g compared to the pure polymers. In PMMA and PS, aggregated silica has the greatest effect on the thermal properties, showing an increase of ~10 °C in both of these polymers. Grafting SAN from aggregated silica also increases the T_g (106 °C to 109 °C), however in this case the colloidal silica sample has a higher T_g than the fumed silica nanocomposite (111 °C).

The reported literature on the effect of silica on the thermal properties on PMMA systems show mixed results. Several groups reported a significant increase in T_g for PMMA-silica nanocomposites compared to the pure polymer[146]. Other studies found that grafting to silica particles has no effect on the glass transition temperature of PMMA[158, 289, 290]. This had previously been attributed to the silica having little to no effect on the segmental motion of the polymer chains in highly dispersed samples, especially colloidal nanoparticles[156], which does not appear to be the case with our

grafted samples. Grafted polymers have stronger bonding interactions with the filler than simply dispersing the silica nanoparticles. Although we might expect a bound layer in the nanocomposite samples, there is no evidence of a double-step glass transition that would arise from the presence of a glassy region around the silica nanoparticles. The increased T_g indicates that there may be a significant decrease in chain mobility in grafted polymer nanocomposites.

6.2.1.2 Elastic Window Scans (IN16)

Elastic window scan (EWS) measurements allow us to follow polymer dynamics occurring faster than the resolution of the neutron scattering instrument. The neutron scattered intensity is integrated within a narrow energy interval around the elastic peak, which gives us the decrease in elastic intensity as a function of temperature and momentum transfer, Q. Figure 6.3 shows the temperature dependence of the elastic intensity for the pure PBA sample, which has been normalised at T=0.

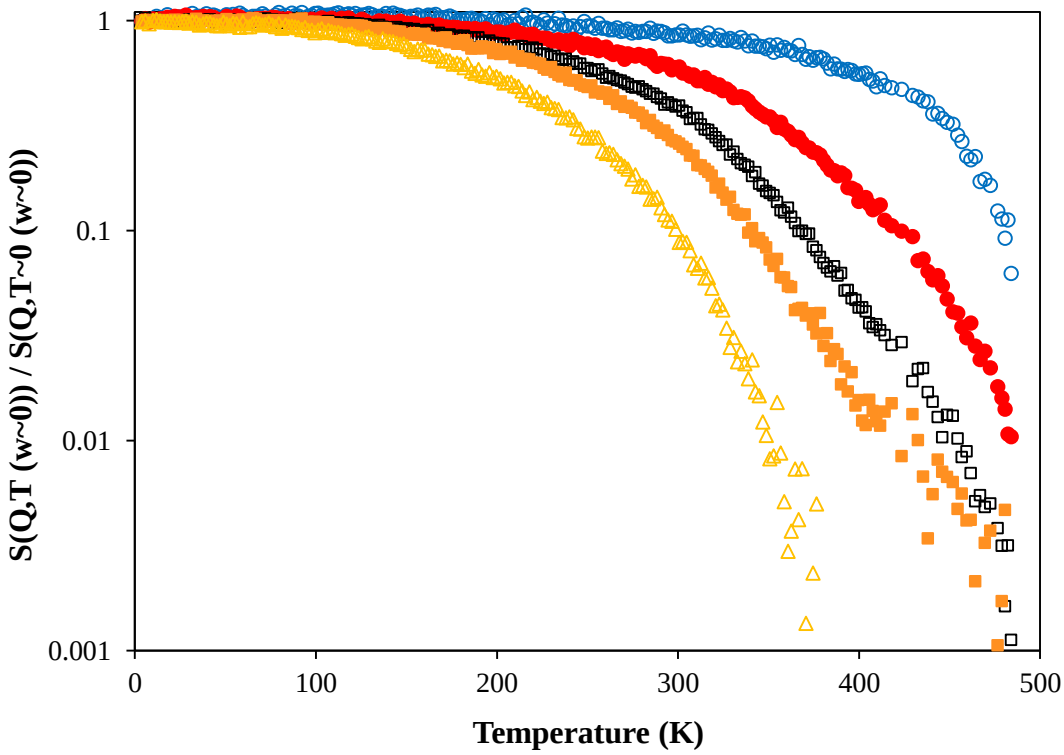

Figure 6.3: Temperature dependence of normalised elastic window scan data for pure PBA at: 0.292 Å^{-1} (○), 0.544 Å^{-1} (●), 0.863 Å^{-1} (□), 1.157 Å^{-1} (■) and 1.809 Å^{-1} (Δ).

The decrease of the elastic intensity is continuous across the temperature range measured. This shows that at high resolution there is no obvious separation between

side group and segmental dynamics. This is due to the fact that poly(butyl acrylate) has relatively large side groups (6 carbon atom long chains), thus the side group motions and back bone segmental dynamics are difficult to distinguish from each other. The same general dynamic behaviour is also seen in the grafted PBA-silica sample (grafted-PBA 13.7 A300) (Figure 6.4).

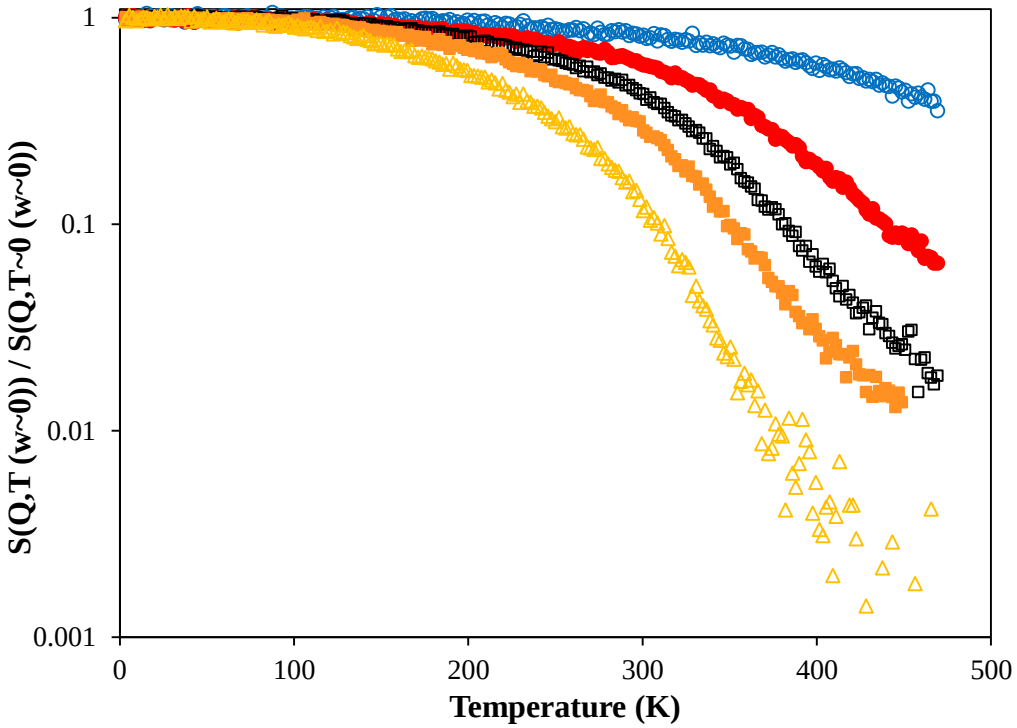

Figure 6.4: Temperature dependence of normalised elastic window scan data for grafted-PBA 13.7 A300 at: 0.292 Å^{-1} (○), 0.544 Å^{-1} (●), 0.863 Å^{-1} (□), 1.157 Å^{-1} (■) and 1.809 Å^{-1} (△).

The elastic window scan data can be used to compare the pure polymer and the PBA grafted sample. As shown in Figure 6.5, after subtracting the empty cell and scattering contribution from the silica particles, grafting has no effect on the polymer motion below the glass transition temperature. However, above the glass transition temperature we clearly observe a slowing down of segmental dynamics for the grafted PBA compared to the pure polymer at all Q values measured. This is also evidenced by the larger values of the mean square displacement for pure PBA. The mean square displacement $\langle u^2 \rangle$ is determined from the temperature dependence of the normalised elastic intensity:

$$\frac{S(Q,\omega \approx 0,T)}{S(Q,\omega \approx 0,T=0)} \propto e^{-\frac{\langle u^2 \rangle Q^2}{3}} \qquad \textbf{(6.1)}$$

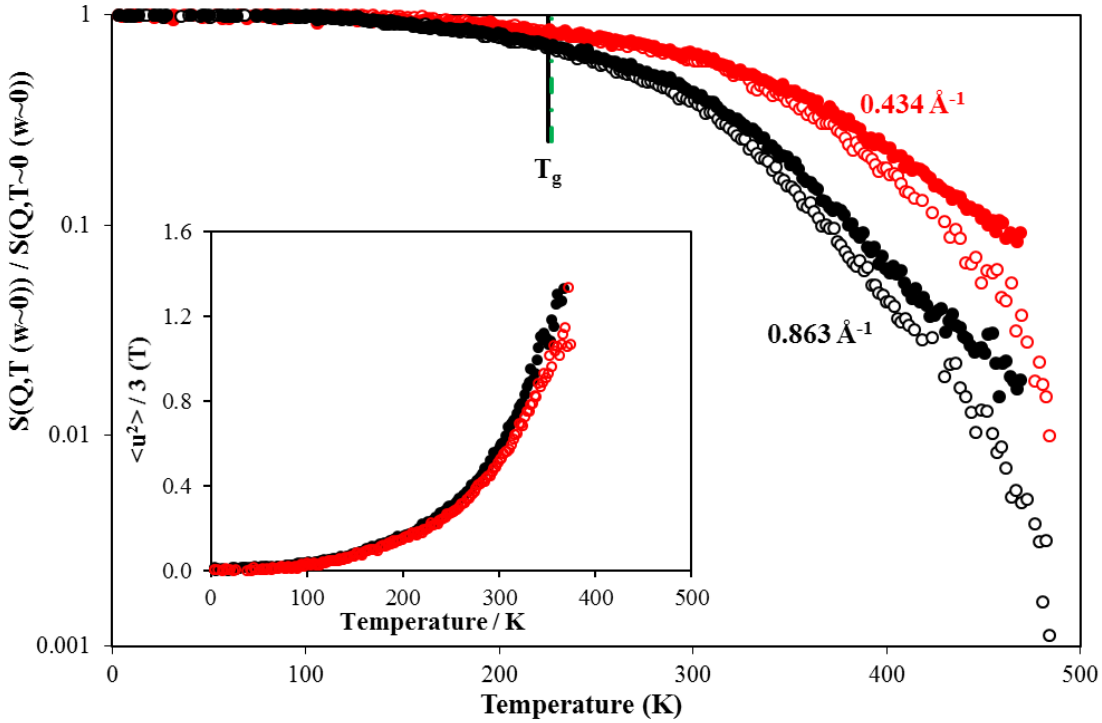

Figure 6.5: Elastic window scan data for PBA (○) and grafted-PBA 13.7 A300 (●) after subtracting the contribution from the empty cell (PBA) or the empty cell plus silica contribution (grafted PBA). Inset: Mean square displacement, $\langle u^2 \rangle/3$, versus temperature for PBA (○) and PBA-grafted (●).

6.2.1.3 Quasi Elastic Neutron Scattering (IRIS)

The dynamic incoherent structure factors of pure PBA, silica-grafted PBA (grafted-PBA 13.7 A300) and silica-dispersed PBA (dispersed-PBA 13.7 A300) measured at 173 K and Q = 1.58 Å^{-1} are shown in Figure 6.6 and compared to the resolution (in this case given by the silica-grafted PBA sample at 173 K), after subtraction of the empty cell contribution and correcting for adsorption. These correspond to low temperature data, below the polymer glass transition (T_g = 224 K). As expected, a broad but relatively small quasielastic contribution arising from side chain motion is evident when comparing the three samples with the resolution, at all Q values.

The dynamic incoherent structure factor results also show that the S(Q,ω) data of the pure PBA and both PBA-silica nanocomposites are very similar below the glass transition temperature (Figure 6.6 for Q = 1.58 Å^{-1}), and this is seen at all Q values. This confirms that (a) molecular motion at this temperature is unaffected by either dispersed or grafted silica nanoparticles and (b) the scattering from the nanoparticles is negligible in comparison to the polymer contribution at low temperatures. No additional elastic contribution is observed due to the addition of nanoparticles.

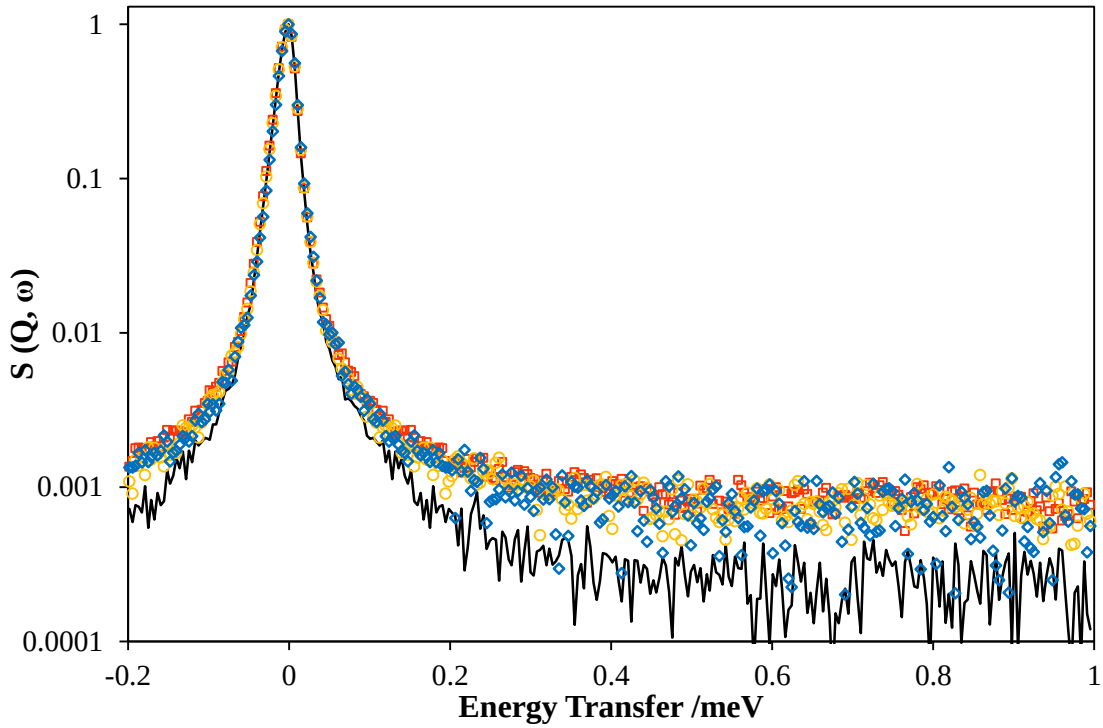

Figure 6.6: Dynamic incoherent structure factor as a function of energy transfer for : PBA (□), grafted-PBA 13.7 A300 (○) and dispersed-PBA 13.7 A300 (◊) at 173 K and Q = 1.58 Å^{-1}. The empty cell background has been subtracted and the data corrected for adsorption.

The first finding is not a surprising result, based on previous measurements carried out on PDMS/silica composites where the methyl group rotational motion was found to be unaffected by the presence of silica nanoparticles[129]. Similarly, we expected that any local motions in PBA (i.e. side group rotations) would not be affected by the presence of the nanoparticles below the polymer glass transition. Therefore, covalent bonding to the nanoparticles does not affect the local dynamics of the side chains. The second finding confirms that the incoherent scattering cross-section, σ_{inc}, of the particles, considered as $(SiO_2)_n$, is small compared to σ_{inc} of PBA: 0.004 versus 963 barns. One should note, however, that the silica particles contain a very small amount of OH groups on their surface (SiO_2 content > 99.8% for A300) and therefore a small contribution to the scattering may arise due to the hydrogens "fixed" on the filler surface.

Different behaviour is observed at temperatures above the glass transition, where clear differences between grafted, dispersed and unfilled PBA are seen at all temperatures (303, 343 and 383 K) and Q values. This is shown in Figure 6.7 for Q = 1.58 Å^{-1} and T = 383 K. Qualitatively, the dynamic changes at higher temperature appear to affect the quasielastic broadening only, with little evidence for an increased elastic contribution due to immobile chains in either nanocomposite.

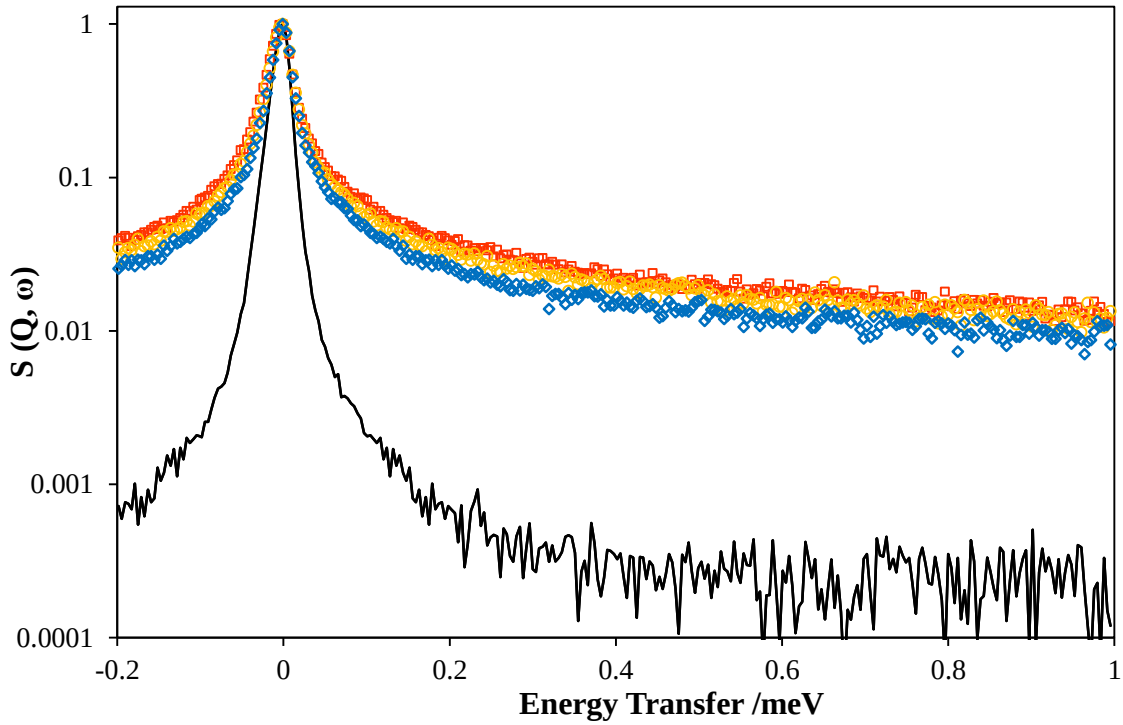

Figure 6.7: Dynamic incoherent structure factor as a function of energy transfer for : PBA (□), grafted-PBA 13.7 A300 (○) and dispersed-PBA 13.7 A300 (◊) at 383 K and *Q* = 1.58 Å^{-1}. The empty cell background has been subtracted and the data corrected for adsorption.

In order to simplify the analysis, the experimental data were Fourier Transformed using Excel and divided by the resolution to obtain the intermediate scattering function I(Q,t). This allows us to more easily compare the different samples measured and obtain information on the *Q* and temperature dependence of the molecular motions. The I(Q,t) functions of the pure polymer and the grafted-PBA nanocomposite at 383 K and various *Q* values are shown in Figure 6.8 and Figure 6.9, respectively.

The different dynamic behaviour of the polymer nanocomposite samples compared to the pure polymer is even more evident in the comparison plot of I(Q,t) against time curves (Figure 6.10) of pure PBA, silica-grafted PBA and silica-dispersed PBA at three *Q* values (0.57, 1.14 and 1.84 Å^{-1}). The I(Q,t) decays qualitatively show that the PBA chains move faster than the PBA-grafted one, a result that is consistently observed at all *Q* values and the three temperatures investigated. However, an unusual result is that the PBA-grafted chains move faster than the PBA-dispersed chains at equal weight fraction of silica nanoparticles. It would normally be expected that grafting the chains to silica would have slower chain dynamics, as covalent bonding is a stronger polymer-particle interaction than adsorption.

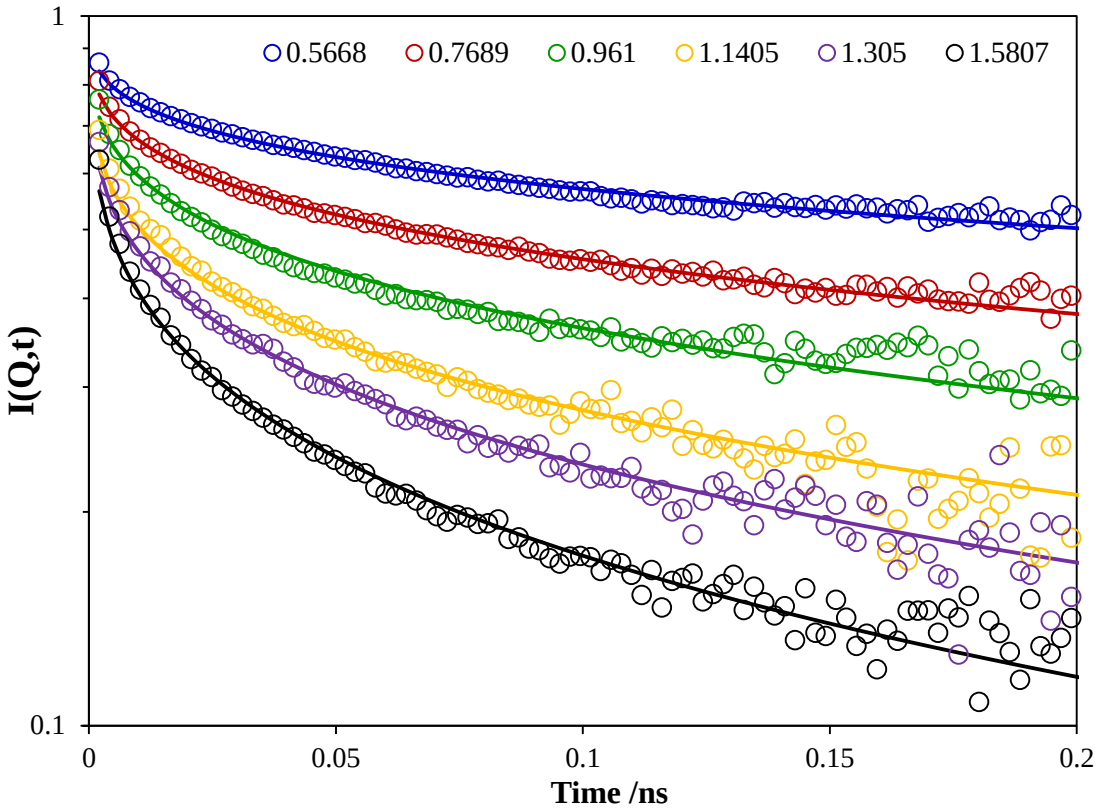

Figure 6.8: Intermediate scattering functions of pure PBA at 383 K and several *Q* values, as indicated. The solid lines are fits to Equation (6.2).

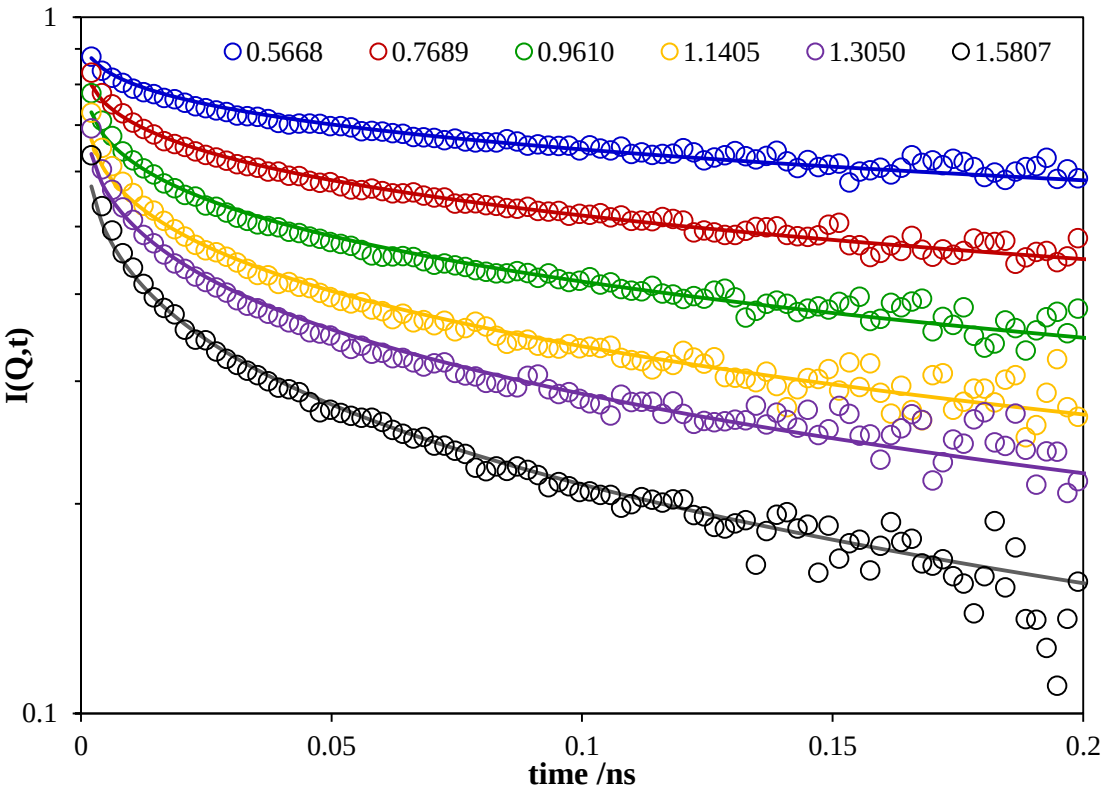

Figure 6.9: Intermediate scattering functions of grafted-PBA 13.7 A300 at 383 K and several *Q* values, as indicated. The solid lines are fits to Equation(6.3).

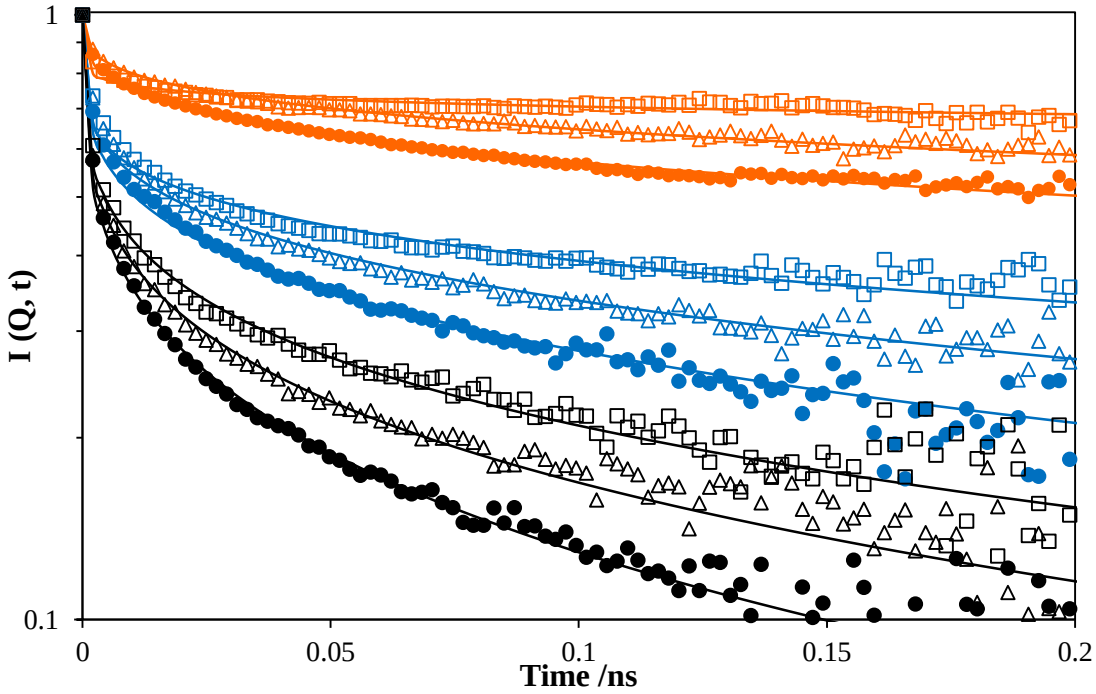

Figure 6.10: Intermediate scattering functions of PBA (●), grafted-PBA 13.7 A300 (Δ) and dispersed-PBA 13.7 A300 (□) at 383 K and several *Q* values, 0.5668 Å^{-1} (orange), 1.1405 Å^{-1} (blue) and 1.8358 Å^{-1} (black). The lines indicate fits to the experimental data using Equation (6.2).

The I(Q,t) data sets of the pure PBA sample were fitted to the following the stretched exponential KWW function (Equation 2.94):

$$I(Q,t) = C(Q)exp\left(-\left(\frac{t}{\tau_{eff}Q^{-n}}\right)^{\beta}\right) \quad \textbf{(6.2)}$$

where $C(Q)$ is a parameter accounting for those motions that are too fast to be detected on the IRIS spectrometer (but are causing a decay of the I(Q,t) data at short times). The other parameters are: the stretched exponent, β, characterising the relaxation time distribution, and the characteristic time of the motion, τ_{eff}, whose Q dependence is expressed by the Q^{-n} term. The I(Q,t) functions at various Q values can be fitted either simultaneously or individually. Values of the fitting parameters are given in Table 6.3 for the three different temperatures for the three samples measured.

Table 6.3: KWW fitting parameters obtained from the time domain analysis of the pure PBA intermediate scattering function.

Temperature (K)	β	*n*	τ_{eff} (ns)	τ_c (ns)
303	0.27	3.7	0.396	6.80
343	0.28	3.8	0.170	2.40
383	0.29	3.7	0.081	0.82

For the PBA-silica nanocomposite samples, a variation on the above equation was initially fitted. As discussed in the introduction, NMR and other dynamic studies on various polymer nanocomposites have suggested the existence of an immobile or, in the case of dispersed nanocomposites, an adsorbed layer due to polymer-particle interactions[291, 292]. This layer would appear as an elastic component in the I(Q,t) function. Therefore, the nanocomposite data was fitted with the assumption of bimodal dynamics, i.e. a model consisting of fast and slow chains. The slow portion of the chains is modelled with an elastic incoherent structure factor (EISF) that represents the portion of the chains seen as static within the dynamic window of the instrument. Thus the KWW function used was adjusted as follows:

$$I(Q,t) = (1 - EISF)\ exp\left(-\left(\frac{t}{\tau_{eff}Q^{-n}}\right)^{\beta}\right) + EISF \quad \textbf{(6.3)}$$

When the nanocomposite data was fitted using an additional EISF component, the value reduced to 0 in the majority of samples, and thus the nanocomposite data was well modelled without an extra elastic contribution. This suggests that there is no additional elastic component arising from a 'bound layer' in either the grafted or the dispersed PBA-silica nanocomposite, within the limit of the data. The polymer and nanocomposites were therefore all modelled using Equation (6.2), and a comparison of the I(Q,t) data and fits are shown in Figure 6.10. The fitted KWW parameters for the two PBA-silica nanocomposites are given in Table 6.4 and Table 6.5 for the three temperatures measured. The lack of indication of bimodal dynamics suggests that the reduced molecular motion seen in this particular polymer nanocomposite may not be due to the presence of an immobile layer of chains at the nanoparticle surface.

The stretched exponent, β, which characterises the relaxation time distribution, shows no apparent temperature dependence in all three samples investigated. The average value of β varies slightly from 0.26 to 0.29, with the dispersed sample showing the broadest distribution, though the values are all within experimental error and so this decrease in β may not be significant. The low β value indicates considerable stretching and a broad distribution of relaxation times. This is not unexpected as the samples are unlabeled, thus the I(Q,t) decay is due to the overlap of different motions. In the literature, a β value of 0.36 for pure PBA was obtained from dielectric relaxation measurements[83]. Considering the polymer structure, we expect a considerable contribution from the alkyl side chain motion with a smaller component from the backbone dynamics.

Table 6.4: KWW fitting parameters obtained from the time domain analysis of the grafted-PBA 13.7 A300 nanocomposite intermediate scattering function.

Temperature (K)	β	*n*	τ_{eff} (ns)	τ_c (ns)
303	0.26	4.2	0.91	18.64
343	0.27	4.2	0.33	5.40
383	0.27	4.1	0.14	2.10

Table 6.5: KWW fitting parameters obtained from the time domain analysis of the dispersed-PBA 13.7 A300 nanocomposite intermediate scattering function.

Temperature (K)	β	*n*	τ_{eff} (ns)	τ_c (ns)
303	0.26	4.7	2.84	59.24
343	0.25	4.6	0.68	18.03
383	0.26	4.5	0.25	5.14

The characteristic time varies with Q^{-n} with *n* ca. ~3.7 in pure PBA to values of ca. ~4.6 for PBA with dispersed silica nanoparticles. The *Q* dependence is approaching $Q^{-2/\beta}$ for homogeneous dynamics[293] (= ~6.7-7.4), confirming the more diffusive nature of the dynamic process. More studies are needed to be able to interpret this change in *Q* dependence, as it is likely a result of various microscopic motions which require a higher temperature range at higher resolution to interpret.

Within the narrow temperature range investigated, the correlation times τ_c were calculated from the following equation and listed in Tables 6.3, 6.4 and 6.5:

$$\tau_c = \tau \frac{\Gamma\left(\frac{1}{\beta}\right)}{\beta} \quad \textbf{(6.4)}$$

The correlation times calculated for each sample follow Arrhenius behaviour (Equation 2.82) across the small temperature range measured (Figure 6.11), with calculated activation energies of 28 kJ mol^{-1} for the dispersed sample, 27 kJ mol^{-1} for the grafted sample and 25 kJ mol^{-1} for PBA. The higher activation energy values for the polymer nanocomposites compared to the pure polymer corroborates the significant decrease in molecular motion. Additionally, the nanocomposite sample with dispersed silica has the highest activation energy value and the slowest dynamics.

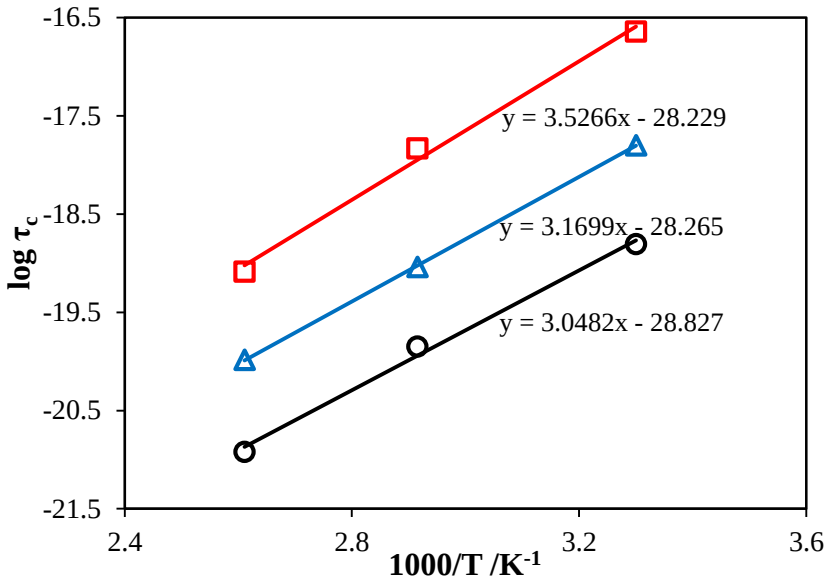

Figure 6.11: Temperature dependence of the correlation times for PBA (O, black), grafted PBA-A300 (Δ, blue) and dispersed PBA-A300 (□, red). The solid lines indicate straight line fits using the Arrhenius law (Equation (2.75)).

Another advantage of analysing the intermediate scattering function rather than the incoherent dynamic structure factor is that information on the temperature dependence of the molecular motions can be more easily obtained by using the Time-Temperature Superposition (TTS) principle. The TTS principle states that the function of a measured dynamic property (e.g. dynamic modulus, viscoelastic behaviour) at a specific temperature is similar to the shape of the functions of the adjacent temperatures[294]. Therefore, measurements on samples taken at different temperatures can be horizontally shifted using a shift factor along the time or frequency axis to create a master curve which can then be analysed using a suitable model. For amorphous polymers, the shift factors for the alpha relaxation are expressed by the William-Landel-Ferry (WLF) Equation (1.12).

TTS cannot be applied in cases where more than one relaxation process with different temperature dependences occurs[295], as often encountered in immiscible polymer blends. However, TTS has been used successfully on polymer nanocomposites in the literature[129]. Master curves of the PBA and PBA-silica nanocomposites were constructed by overlapping the data collected at 303, 343 and 383 K (Figure 6.12).

The pure PBA and PBA-silica data was initially shifted using literature values (C_1 = 8 and C_2 = 13) obtained from dielectric and NMR measurements[84], then adjusted on ad hoc basis to obtain the best horizontal shifts. The intermediate scattering functions of PBA, grafted and dispersed nanocomposites all obey TTS and good quality master

curves were created. The shift factor values used are listed in Table 6.6 and shown in Figure 6.13. Pure PBA and grafted-PBA 13.7 A300 have similar shift factor values to each other and to the literature, showing the expected temperature dependence. However, dispersed-PBA 13.7 A300 has significantly lower shift factor values, showing a change in the temperature dependence of the dynamics. These lower shift factors arise from higher C_1 and C_2 values than the literature values, which therefore leads to a lower fractional free volume according to Equation (1.16).

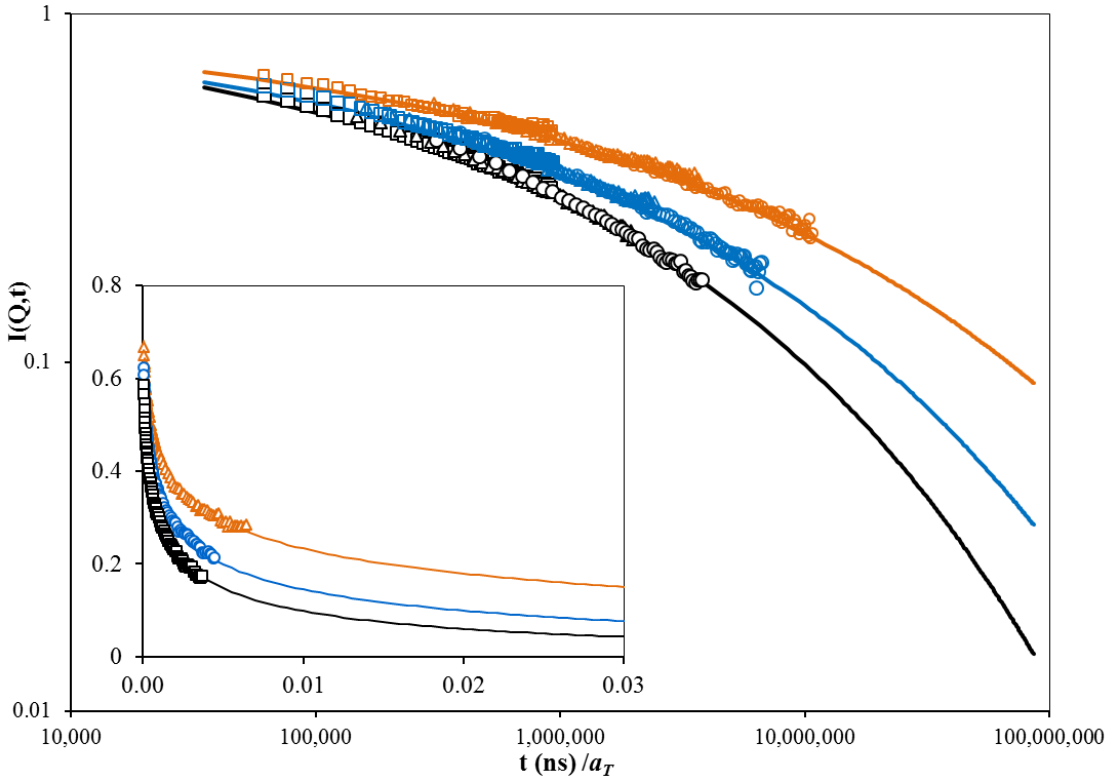

Figure 6.12: Fourier transformed QENS spectra for unfilled PBA (black), grafted-PBA 13.7 A300 (blue) and dispersed-PBA 13.7 A300 (orange) at Q = 1.58 Å^{-1} in a log scale. The data was collected at 303 (○), 343 (Δ) and 383 K (□) and shifted according to the William-Landel-Ferry (WLF) temperature dependence for the relaxation times using the T_g of PBA (224 K) as the reference temperature. The inset shows unfilled PBA (□, black), grafted-PBA (○, blue) and dispersed-PBA (Δ, orange) on a non-log scale. The lines represent the KWW function (Equation (6.2)) fits of the data.

Table 6.6: Horizontal shift factors for PBA and PBA nanocomposites data, shifted with T_0 = 303 K

Sample	log α_T		
	30 °C	70 °C	110 °C
Literature (WLF)	-6.87	-7.21	-7.4
PBA	-6.87	-7.25	-7.57
grafted-PBA 13.7 A300	-6.87	-7.21	-7.53
dispersed-PBA 13.7 A300	-6.87	-7.47	-7.84

Notation: ##.# = wt % of silica measured by elemental analysis.

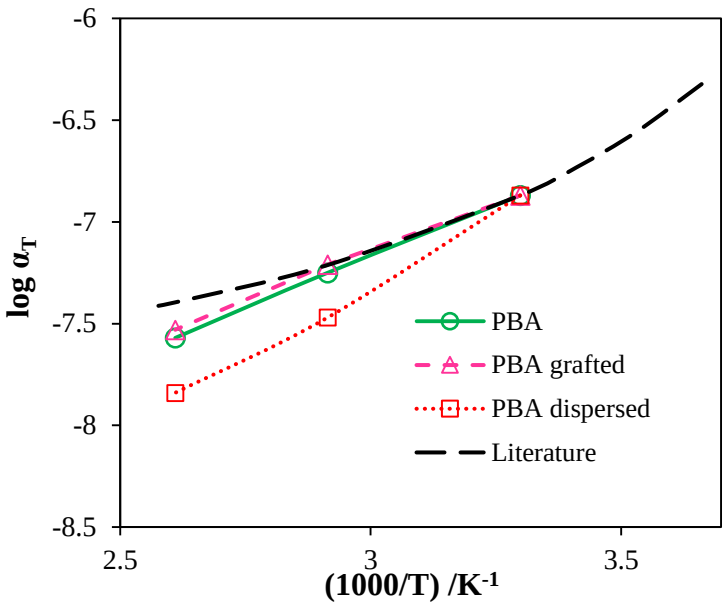

Figure 6.13: WLF shift factors for PBA(□), grafted-PBA 13.7 A300 (○) and dispersed-PBA 13.7 A300 (Δ) compared to literature values calculated from NMR measurements by Gaborieau *et al.*[84]

The KWW function was applied to the PBA and PBA-silica nanocomposite master curves and the resulting parameters are shown in Table 6.7. The parameters are consistent with the previous KWW analysis, and shows that the dispersed sample has the most pronounced difference in chain dynamics compared to the pure PBA sample, with the highest *Q* dependence and characteristic time values.

Table 6.7: KWW fitting parameters obtained from the TTS analysis of the PBA and PBA nanocomposite samples

Sample	β	*n*	τ_{eff} (ns)	τ_c (ns)
PBA	0.28	3.5	0.025	0.32
grafted-PBA 13.7 A300	0.26	4.2	0.060	1.24
dispersed-PBA 13.7 A300	0.24	5.1	0.237	6.87

Notation: ##.# = wt % of silica measured by elemental analysis

The QENS analysis presented here shows that nanoparticles slow down segmental dynamics in the poly(butyl acrylate) matrix, with dispersing the nanoparticles in the polymer resulting in a larger effect on dynamics than grafting the chains to the filler. We have also shown that this may not be due to an immobile layer at the silica particle surface, which has been found in other polymer-silica nanocomposites[227], as there is no evidence of an additional elastic component when comparing the two

nanocomposites to each other or to the pure polymer. However, this may require further investigation and the presence of an immobile layer cannot be ruled out.

Dielectric measurements in the literature have shown that there is segmental relaxation around the silica nanoparticles with longer relaxation times than the bulk polymer[133]. The chain segments around the silica particles may have fewer possible conformations and thus reduced molecular motion. In dispersed nanocomposites, the chains may interact with the surface of the large aggregated silica at multiple points in the chain. In the grafted nanocomposites, the chains are attached to the silica particles at one end of the chain, preventing both nanoparticle aggregation and further polymer-particle interactions. Additionally, attaching the initiator to the silica particles uses up the hydroxyl groups on the surface of the silica. Free OH groups in the dispersed samples can interact with the PBA chains and further slowing down dynamics of chains around the silica nanoparticles.

Another potential explanation for the reduced molecular motion in the dispersed polymer nanocomposite relies on the further agglomeration of fumed silica particles. A large network structure of aggregated silica particles or smaller aggregates bridged by polymer chains would restrict the free volume available for chain translation and diffusion, causing a large decrease the dynamics of the polymer chains. In their study of PMMA grafted nanoparticles in miscible and immiscible PMMA mixtures, Akcora *et al.*[132] have shown that the mean square displacement of grafted segments is affected by structural changes in particle agglomerates and discussed these effects in terms of local free volume. The TTS results support this explanation, as the change in shift factors for the dispersed sample resulted in a lower fractional free volume and thermal coefficient than either the pure or the grafted sample, although this change is relatively small.

6.2.2 Rheological behaviour

Rheological measurements carried out on silica suspensions and PBA-silica nanocomposites are presented in the following sections. The rheological properties of silica suspensions were measured in response to prior mechanical measurements that showed that two brands of fumed silica with seemingly identical size and surface area properties showed different levels of mechanical reinforcement in PS and PMMA-silica nanocomposites[296]. The rheological behaviour of silica particle suspensions is also crucial to understanding the chain dynamics and the rheological properties of PBA-silica nanocomposites.

6.2.2.1 Silica Suspensions

The rheological behaviour of hydrophilic fumed silica suspensions has been studied previously in polar solvents and shows shear thickening behaviour after a critical shear stress[297, 298]. Shear thickening in silica particle suspensions is primarily seen under two conditions: 1) there is a high concentration of particles and 2) the particles are neutral to or repel each other[297]. This is assumed to be the behaviour seen in all types of untreated, hydrophilic fumed silica. Rheological measurements were carried out on H5 and A300 hydrophilic fumed silica suspensions to examine the behaviour of the particles in dispersions. Viscosity measurements with increasing shear rate/shear stress, and frequency sweeps of the dynamic moduli of silica suspensions in ethylene glycol were measured using a cone and plate geometry.

Suspensions of 20 wt% A300 in ethylene glycol behave similarly to fumed silica-ethylene glycol 20% suspensions in the literature[298]: showing shear thinning behaviour until a critical stress upon which the dispersion becomes shear thickening (Figure 6.14). This critical stress occurs at ~50 Pa, which is consistent with literature results[298]. However, H5 silica suspensions behave differently to the A300 fumed silica suspension, as shown in Figure 6.15. At low shear rates and shear stress, the viscosity increases and the suspension shear thickens. The viscosity is very large (~100-1000 MPa) compared to that of the pure medium (~2 mPa). This causes the rheometer to have great difficulty in rotating or oscillating the cone and plate, resulting in a large amount of noise in the measurements. In the stress experiment (Figure 6.15(a)), shear thickening occurs until the stress reaches ~2000 Pa, then the suspension finally reaches a yield point and the suspension starts to shear thin with little noise in the measurements.

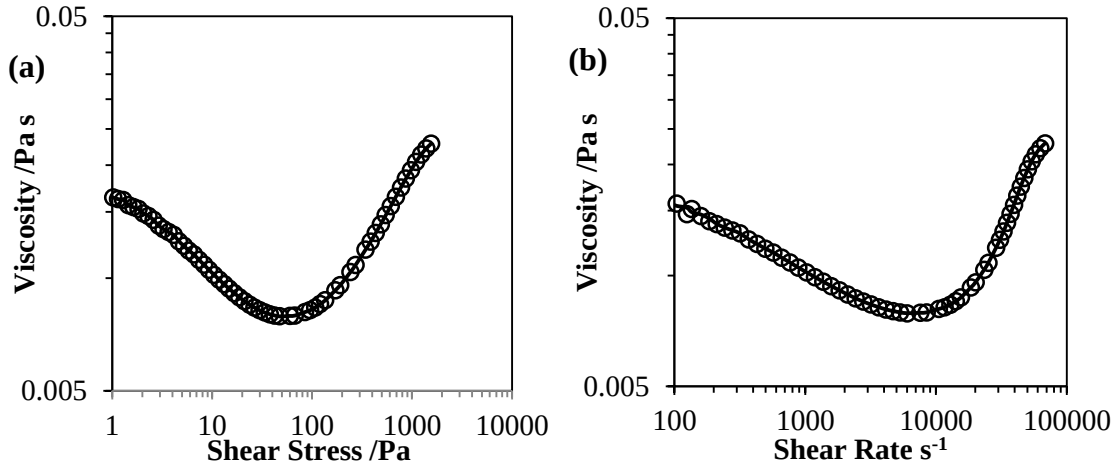

Figure 6.14: Rheological properties of A300 in ethylene glycol suspensions (a) steady shear viscosity versus shear stress and (b) steady shear viscosity versus shear rate.

In the shear rate experiment shown in Figure 6.15(b), the behaviour of the suspension at low shear rates matches the shear stress experiments, where there is shear thickening until a yield point, and then shear thinning occurs. At intermediate shear rates, the viscosity results are inherently noisy due to the solid nature of the suspension and the limitations of the rheometer. A second yield point occurs at ~20 s^{-1} and then the suspension exhibits more shear thinning behaviour until it reaches a viscosity roughly equal to the ethylene glycol medium. There is no shear thickening behaviour at high shear rate as seen in the A300 sample and other concentrated silica suspensions, suggesting that the H5 suspension is flocculated and behaving like a physical gel.

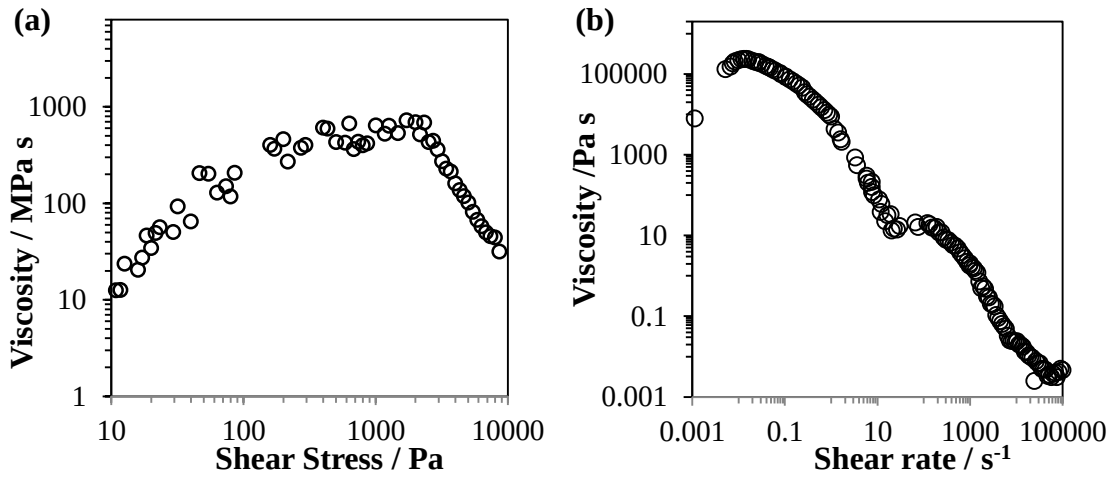

Figure 6.15: Rheological properties of H5 in ethylene glycol suspensions (a) steady shear viscosity versus shear stress and (b) steady shear viscosity versus shear rate.

In order to corroborate the viscosity results, frequency sweeps were carried out on the two suspensions. Flocculated fumed silica suspensions are expected to behave as a physical gel[299] and thus have a frequency independent elastic modulus (*G'*), whereas unflocculated silica suspensions show lower *G'* values that are frequency dependent[299].

Figure 6.16 shows the dynamic elastic modulus results for both silica suspensions. The H5 particle suspension shows a near constant elastic modulus across the entire range of frequencies, corresponding to a gel-like network structure being formed. A300 suspensions, on the other hand, exhibit a linear change of storage modulus across the frequency sweep. Therefore, a large network structure is not being formed in this concentrated suspension. In the literature, this is explained as the hydroxyl groups on the surface A300 particles showing a preference to hydrogen bonding with the ethylene glycol molecules over particle-particle interactions[297].

Although there are also hydroxyl groups on the surface of H5 particles, the gel-like structure shows that filler-filler interactions dominate. Whether matrix-filler interactions or filler-filler interactions are stronger determines the rheological behaviour of the silica particles. It is unclear why two supposedly similar silica particles have consistently different rheological behaviour at high concentrations.

The behaviour of silica particles in suspensions may explain the large decrease in dynamics of the polymer chains that cannot be attributed just to a bound layer (Section 6.2.1.3). Filler networks occur when polymer-particle interactions are weaker than the particle-particle interactions. The formation of a large network structure of gelated fumed silica particles would restrict the free volume available for segmental motion, causing a large decrease in the dynamics of the polymer chains.

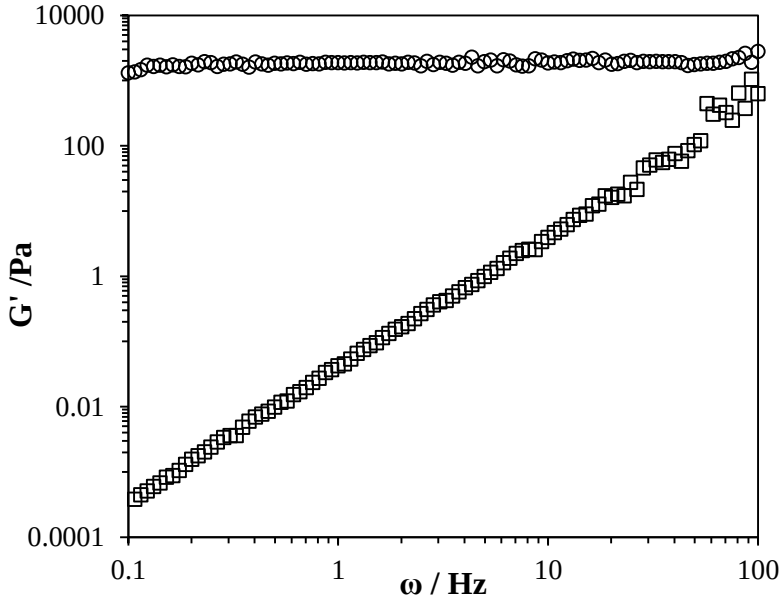

Figure 6.16: Dynamic elastic modulus (G') vs frequency (ω) for 20 wt% H5 and A300 silica suspensions in ethylene glycol.

6.2.2.2 PBA-silica nanocomposites: Viscosity

Viscosity against increasing shear rate of PBA-silica nanocomposites was measured using a cone and plate geometry at temperatures between 0 and 100 ^{o}C. Measurements were carried out primarily on dispersed nanocomposites using both colloidal silica (MEK-ST and Ludox) and fumed silica (H5 and A300). Two types of PBA were used, one above the molecular weight of entanglement, H-PBA, and one below, L-PBA (Table 3.8) in order to study entanglement effects.

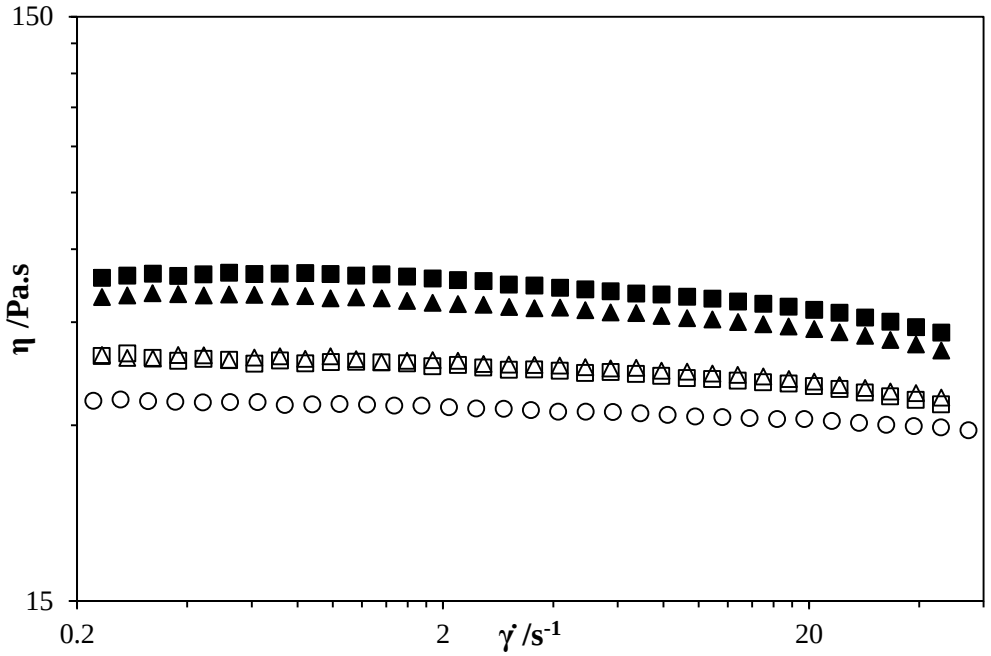

Figure 6.17: Viscosity against shear rate curves at 50 ºC for pure PBA (Mw = 99,000 g mol^{-1}) (○), dispersed-PBA 0.8 Ludox (□), dispersed-PBA 5.5 Ludox (■), dispersed-PBA 1.0 MEK-ST (Δ) and dispersed-PBA 5.2 MEK-ST (▲).

The nanocomposites containing colloidal silica show similar viscoelastic behaviour to that of the pure polymer matrix at low shear rates. This is shown in Figure 6.17 for T = 50 ºC, and is observed at all temperatures measured for both types of colloidal silica. At higher shear rates, shear thinning behaviour occurs, most clearly seen in the higher loaded samples (~ 5 wt% silica). Increased shear thinning has been seen in

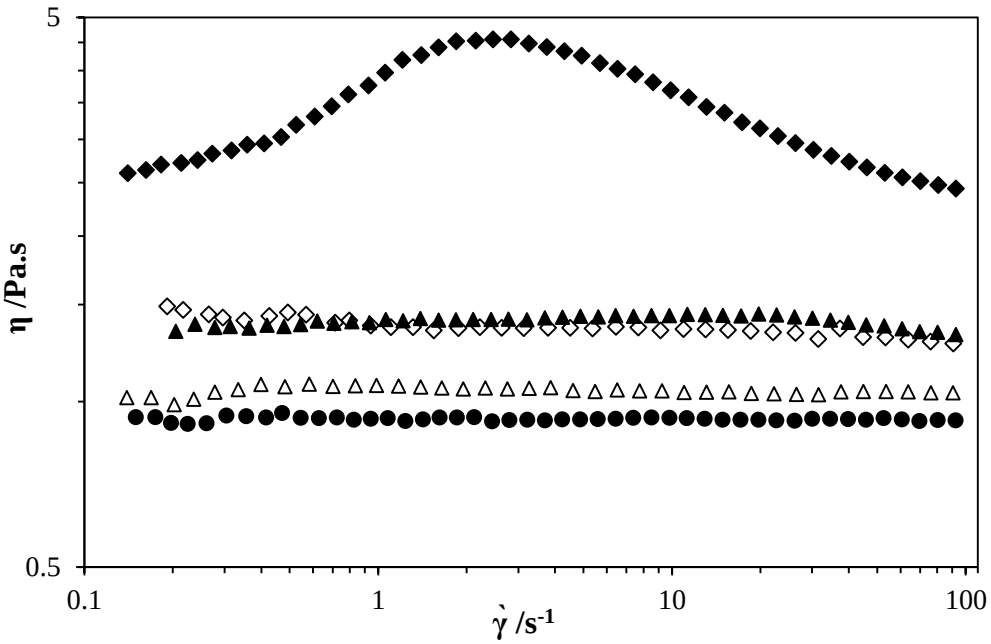

Figure 6.18: Viscosity against shear rate curves at 50 ºC for L-PBA (●), dispersed-PBA 0.9 MEK-ST (Δ), dispersed-PBA 2.7 MEK-ST (▲), dispersed-PBA 1.0 A300 (◊) and dispersed-PBA 2.5 A300 (♦).

other nanocomposites containing colloidal silica, showing a decrease in viscosity towards the value of that of the pure polymer[177, 300]. It was not possible to measure the samples at even higher shear rates to determine if the sample viscosity eventually reaches a plateau, as slippage occurs and the sample spills out from the cone and plate geometry. In the dispersed samples made using low molecular weight PBA, this shear thinning behaviour is also observed in the 2.5 wt % MEK-ST sample (Figure 6.18).

The effect of nanofillers on the viscosity of the polymer matrix is complicated. In order to quantitatively analyse the effect of nanoparticle fillers on the viscosity of the polymer matrix, an appropriate model is required. These models are similar to the ones used for modulus enhancement upon addition of silica nanoparticles. The increase in viscosity for hard spheres in a Newtonian fluid was described by Einstein with the following equation[301]:

$$\eta = \eta_f(1 + 2.5\phi) \quad \textbf{(6.5)}$$

where η is the viscosity of the suspension, η_f is the viscosity of the fluid and ϕ is the volume fraction of the filler. This equation only holds for very dilute suspensions where there are no interactions between filler particles. The particles also have to be rigid spheres or the behaviour becomes non-Newtonian[302]. The Einstein equation was then adjusted for hard spheres by Batchelor[303]:

$$\frac{\eta_0}{\eta_p} = 1 + 2.5\phi + 6.2\phi^2 \quad \textbf{(6.6)}$$

where η_0 is the viscosity of the composite, η_p is the viscosity of the polymer and therefore η_0/η_p is the relative viscosity.

The application of the adjusted Einstein expression to polymer nanocomposites has been shown to not be accurate for non-ideal nanocomposite systems[180]. Many recent studies on colloidal spherical nanoparticles dispersed in polymers have shown a decrease in viscosity compared to the pure polymer[181, 182], directly contradicting the above equations. There are many reasons for the observed deviations. Firstly, polymer matrixes are viscoelastic in nature. Secondly, if the polymer is above the critical molecular weight of entanglement (M_e) then entanglement effects can greatly affect the viscosity of the resulting nanocomposite. The observed decrease in viscosity of polymer nanocomposites is generally seen under two conditions: 1) the polymer is above the entanglement molecular weight and 2) the distance between nanoparticles is less than two times the radius of gyration (R_g) of the polymer[181].

Polymer-particle interactions are another factor that must be considered in modelling the viscoelastic behaviour of polymer nanocomposites. Zhang and Archer[304] conducted a rheological study of poly(ethylene oxide)-silica systems and found a high degree of polymer-particle interactions, forming a network structure with immobilised polymer chains on the surface of the particles and causing an increase in viscosity. Modifying the surface of the silica particles reduced the polymer-particle interactions and thus reduced the effect on the viscosity.

The addition of colloidal silica particles to the PBA matrix increases the viscosity, in line with the literature results from PEO-silica[304] and other similar samples with polymers that are highly interacting with the filler. An attempt to model the change in viscosity with the Bachelor modified Einstein equation (Figure 6.19) showed that the increase is greater than that predicted in both PBA samples. An empirical equation was proposed by Krieger and Dougherty to calculate the relative viscosity, η_r, for non-Newtonian flow in suspensions of rigid spheres[305]:

$$\eta_r = \left(1 - \frac{\phi}{\phi_m}\right)^{-[\eta]\phi_m} \quad \textbf{(6.7)}$$

where ϕ_m is the maximum packing or volume fraction and $[\eta]$ is the intrinsic viscosity. In some cases, $[\eta]$ is replaced with a shape factor, k,[306] and for monodisperse spheres $[\eta]$ = 2.5.[307] In order to account for an adsorbed layer of chains bound to the surface of the silica particles, the volume fraction of silica, ϕ, is replaced by an effective volume fraction, ϕ_{eff}, which can be estimated from the following equation:

$$\phi_{eff} = \phi(1 + \delta/\alpha)^3 \quad \textbf{(6.8)}$$

where δ is the thickness of the adsorbed polymer later and α is the radius of the nanoparticle. The Krieger-Dougherty equation has been used successfully to model polymer nanocomposites in the literature that exhibited increases in viscosity higher than those predicted by the Einstein equation[308-310].

Using 0.639 as the ideal maximum packing fraction for close packed spherical particles[311], the radius of the MEK-ST nanoparticle (7 nm) for α and setting $[\eta]$ and δ as variable parameters for least squares analysis, the Krieger-Dougherty equation was used to model the increased viscosity. The Krieger-Dougherty equation fits well with 0 values for thickness and thus no presence of a bound layer, however far too high intrinsic viscosity values are obtained: 16 and 11 for H-PBA and L-PBA respectively. It has been suggested that the $[\eta]$ is also determined by particle-particle and polymer-particle interactions, therefore strong interactions[309], leading to the large $[\eta]$ value. As

an alternative, Equation (6.6) can be adjusted using an effective volume fraction. However, this leads to small and unreliable values for volume fraction.

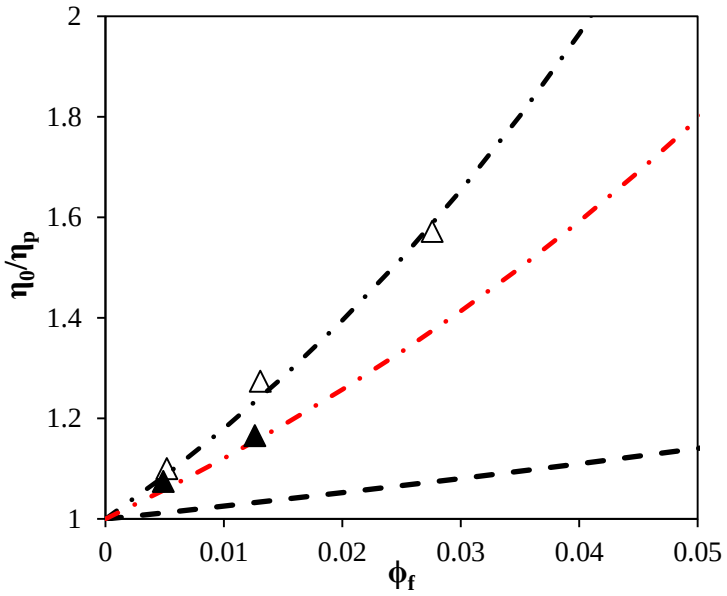

Figure 6.19: Relative viscosity of PBA-MEK-ST dispersed nanocomposites, H-PBA (Δ) and L-PBA (▲) in comparison with model calculations/fits: (– –) Equation (6.6), (– · –) Equation (6.7) using ϕ_{eff} for M_w = 99,000 g mol^{-1} sample and (– · –) Equation (6.7) using ϕ_{eff} for M_w = 9000 g mol^{-1}.

The nanocomposites containing fumed silica particles show different viscoelastic behaviour to the colloidal silica nanocomposites (Figure 6.20). The higher loading samples (~5 wt%) show shear thickening at low shear rates until reaching a maximum, and then returning to increased shear thinning behaviour. This could be due to the formation of large agglomerates of silica (as seen in the H5 sample suspension in ethylene glycol in the previous section) at higher filler volume fractions, which causes solid-like behaviour and shear thickening. At increased shear rates, these larger agglomerates are broken down and disentanglement of the chains can occur, resulting in shear thinning behaviour. This behaviour is more pronounced in the lower molecular weight PBA sample due to the lower viscosity of the medium.

From Figure 6.18 and Figure 6.21, it is clear that aggregated silica has a much greater effect on the viscosity than colloidal silica at roughly the same concentration of filler particles. This is likely due to the larger aggregate structure of the silica hindering movement of free polymer chains more than small colloidal silica particles. Attempts to model this increase to the Einstein-Bachelor and the Krieger-Dougherty equation were unsuccessful as the increase in modulus is underestimated or requires unphysical values to fit. The additional factors of the larger particle shape and the formation of a filler

network cause a larger increase than predicted, and as such require a far more complex model such as the continuum model developed by Stephanou *et al.*[312]

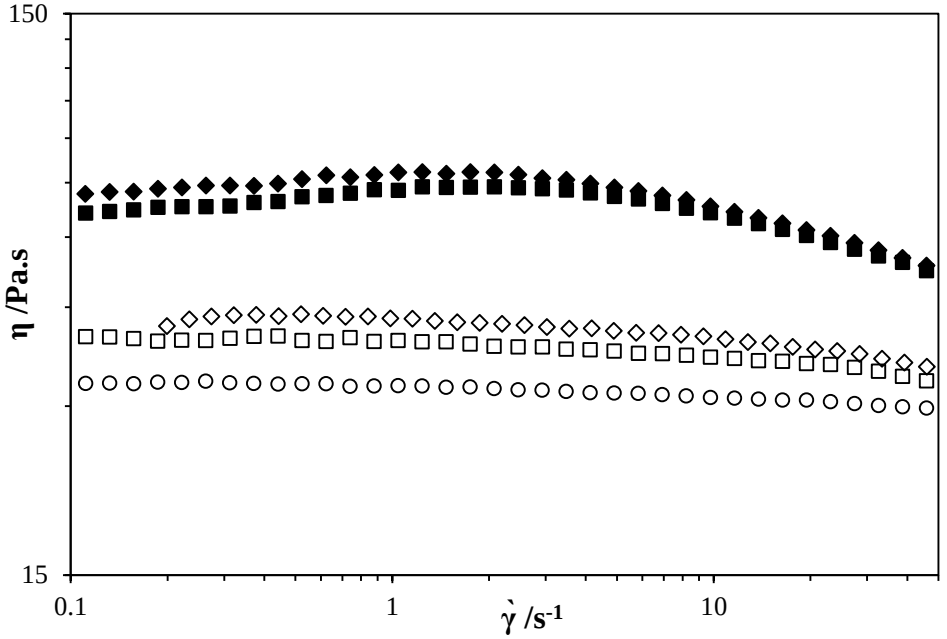

Figure 6.20: Viscosity against shear rate curves at 50 ºC for H-PBA (○), dispersed-PBA 0.8 A300 (□), dispersed-PBA 5.5 A300 (■), dispersed-PBA 1.0 H5 (◊) and dispersed-PBA 5.2 H5 (♦).

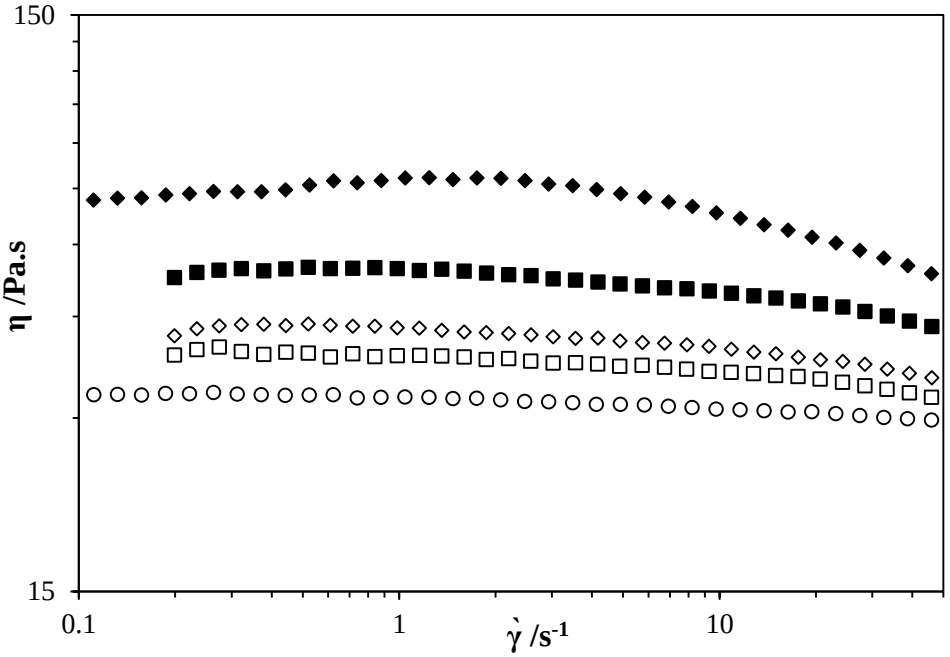

Figure 6.21: Viscosity against shear rate curves at 50 ºC for H-PBA (○), dispersed-PBA 0.8 Ludox (□), dispersed-PBA 5.5 Ludox (■), dispersed-PBA 0.9 H5 (◊) dispersed-PBA 5.1 H5 (♦).

Thus, aggregation of filler particles can have profound effects on the viscoelastic properties of the matrix, especially in regards to solid-like or gel-like behaviour. As the behaviour of aggregated silica particles in suspension can greatly differ, the effect of

aggregated fillers on the viscosity can be complex. Grafting polymer chains to the surface of the filler particles hinders particle-particle interactions and prevents the formation of a filler network.

Many of the grafted PBA-silica samples synthesised by this group show partial solid-like behaviour[31], and thus were unsuitable for rheological measurements. However, a grafted PBA-MEK-ST sample suitable for viscosity measurements was synthesised by Gavin Ross and subsequently measured during this project. The molecular weight is unknown in this sample due to not having enough remaining sample for accurate GPC measurements. Based on the synthetic method used and previous molecular weight measurements on similar samples[31], the molecular weight is estimated at $\leq$ 100,000 g mol^{-1}. The results from the shear rate experiments were therefore compared to the H-PBA samples are shown in Figure 6.22. The grafted PBA-MEK-ST sample shows a much higher increase in viscosity than the dispersed MEK-ST 5.2 wt% sample and shows significant shear thinning behaviour at low shear rates. The increase in viscosity is far beyond that of any model we have attempted to fit previously, and is possibly due to the formation of a percolated network of polymer-silica nanoparticles. However, the increased viscosity may be due to cross-links within the sample. The grafted sample shows a higher viscosity than the dispersed aggregated silica samples, but not the shear thickening behaviour present in those samples.

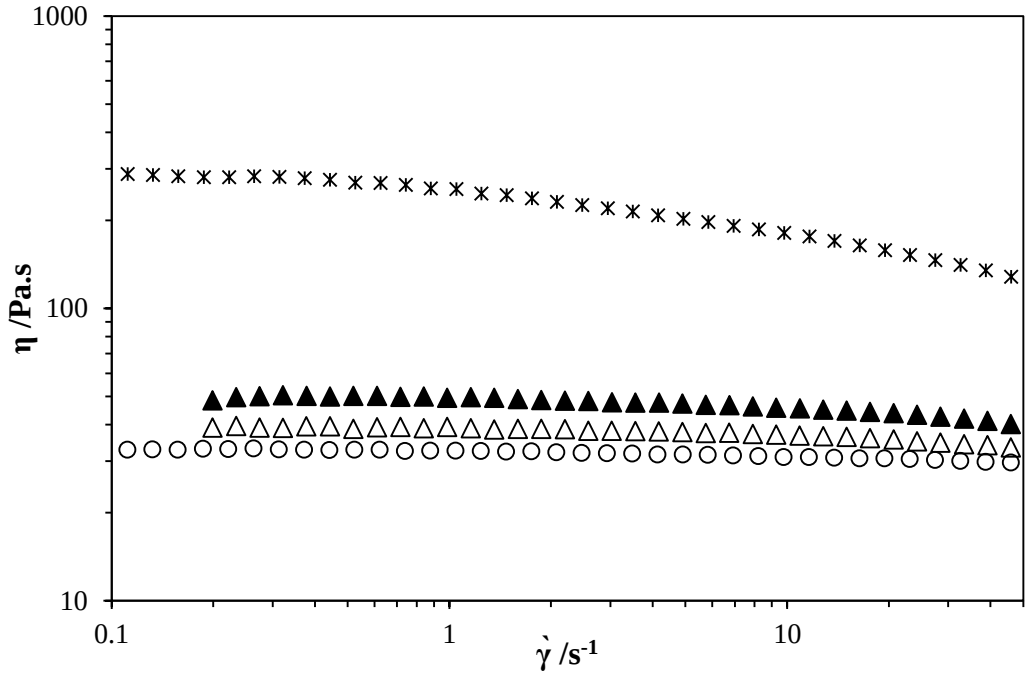

Figure 6.22: Comparison of viscosity against shear rate curves for grafted and dispersed colloidal silica nanocomposites, grafted-PBA 6.7 MEK-ST (◊), dispersed-PBA 1.0 MEK-ST (Δ) and dispersed-PBA 5.2 MEK-ST (▲), to H-PBA (○) at 50 ºC.

As the conventional models for viscosity increase have failed to describe our observations in the dispersed fumed silica samples and the grafted nanocomposite, molecular dynamics simulations or far more complex models[312] are needed to fully understand the mechanisms behind this reinforcement.

6.2.2.3 PBA-Silica nanocomposites: Dynamic Moduli

Rheological measurements can also analyse the mechanical properties and viscoelastic behaviour of the polymer nanocomposite by measuring the storage/elastic modulus, *G'*, and the loss/viscous modulus, *G''*, as a function of angular frequency. It is well known that the size, shape and dispersion of nanoparticles are important factors in reinforcement of polymer nanocomposites[166, 172]. Therefore, a comparison of different types of fillers and a comparison of grafted versus dispersed nanocomposites is key in understanding all of these effects. There are very few studies comparing the rheological behaviour of polymer nanocomposites containing different types of silica. Zhao *et al.* recently published a study that compared the effect of fumed and colloidal silica in poly(2-vinylpyridine) (PVP)[173] that showed that fumed silica has a larger effect on modulus than colloidal silica.

The dynamic moduli of PBA and PBA-silica nanocomposites were measured via frequency sweep experiments in isothermal mode. However, isothermal measurements have a limited time/frequency range and thus cannot capture the entire viscoelastic response of a polymer. By measuring frequency sweeps of the sample at various temperatures, the TTS principle can be applied (in a similar method to the QENS data in Section 6.2.1.3) which expands the frequency window and gives more information about the viscoelastic behaviour. The curves of *G'*, *G''* against frequency produced by the frequency sweep measurements can be horizontally shifted until they overlap with each other to produce a smooth master curve. Some samples also require vertical shifting in order to create this master curve[313].

While TTS has been used successfully in the literature to analyse the rheological properties of some polymer nanocomposites, such as poly(methyl methacrylate) filled with silica nanoparticles[314], other filled systems showed a failure of the TTS principle at low frequencies. Styrene-butadiene rubber containing carbon black failed to follow TTS at low frequencies without additional vertical shifting due to the filler system affecting the dynamic behaviour[167].

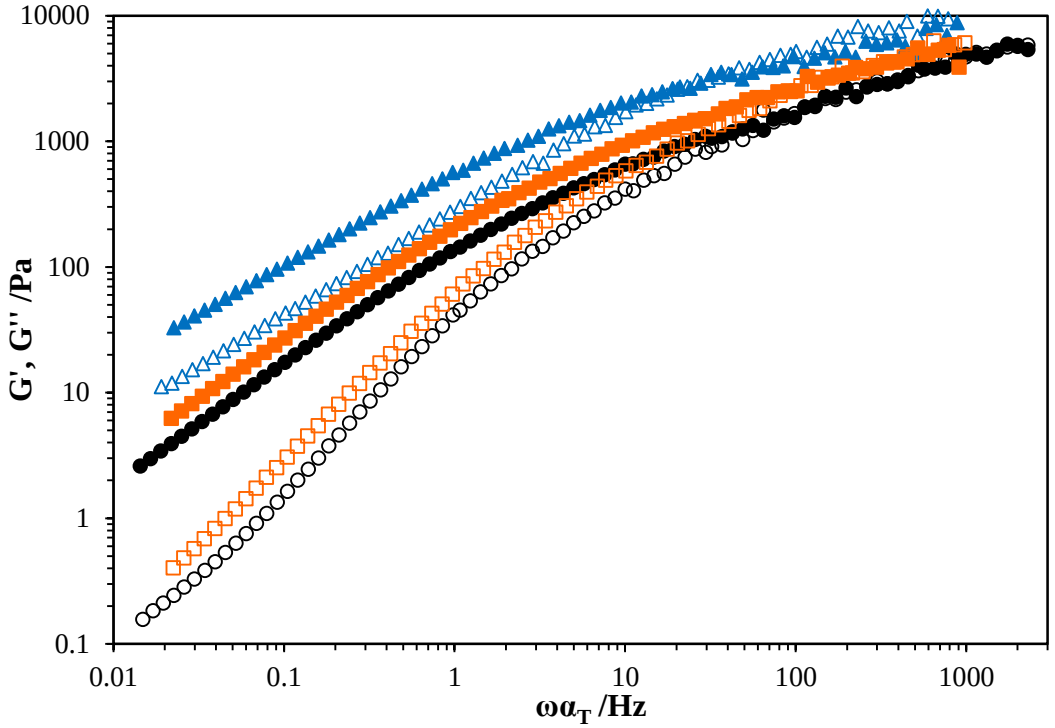

Figure 6.23: Master curves of elastic modulus G′ (empty symbols) and viscous modulus G′′ (filled symbols) for pure PBA (○), dispersed-PBA 5.2 MEK-ST (□) and grafted-PBA 6.7 MEK-ST (Δ) obtained from frequency sweep measurements (0.1 to 100 Hz) at temperatures between 0 to 100 ºC.

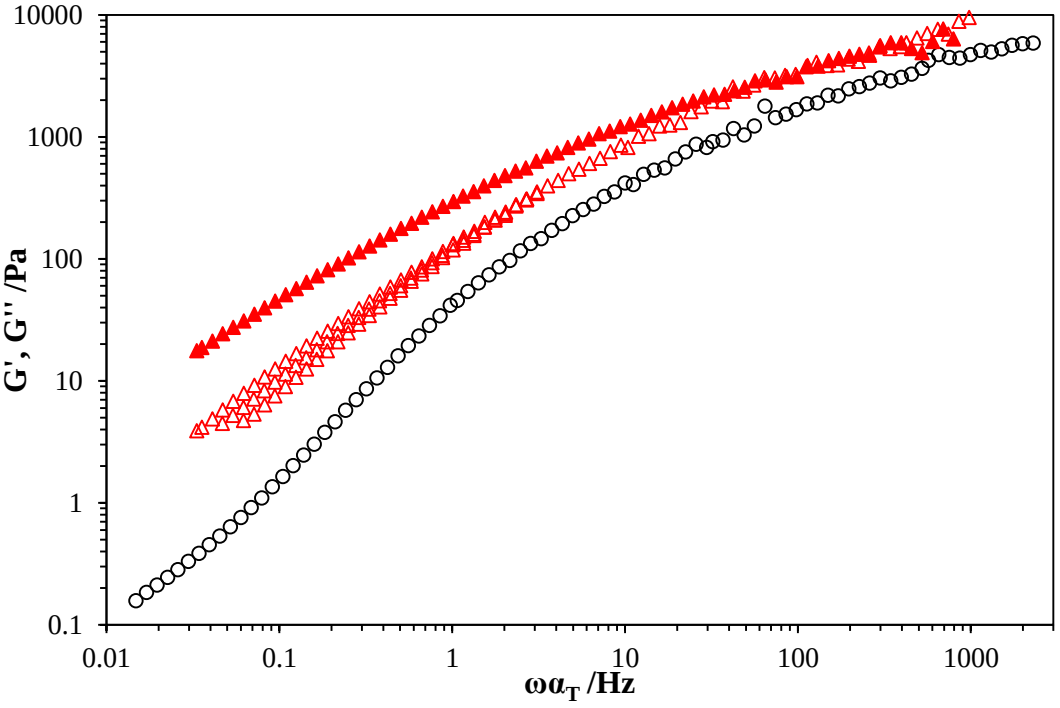

Figure 6.24: Master curves of elastic modulus G′ (empty symbols) and viscous modulus G′′ (filled symbols) for pure PBA (○) and dispersed-PBA 5.1 H5 (Δ) obtained from frequency sweep measurements (0.1 to 100 Hz) at temperatures between 0 to 100 ºC. The loss modulus of pure PBA has been removed for clarity.

Due to its commercial availability, the higher molecular weight PBA was initially used to make dispersed nanocomposites. Master curves of PBA and PBA-silica

nanocomposites were produced and then analysed using the WLF Equation (Equation 1.12)). Figure 6.23 and Figure 6.24 show comparisons of the master curves of the elastic modulus and viscous modulus (G′ and G″) for pure PBA and various nanocomposites created by shifting curves measured at 0 – 100 ^{o}C at 10 ^{o}C increments. For clarity, only one of each type of silica (colloidal or fumed) has been shown as similar rheological behaviour is seen in both colloidal samples (MEK-ST and Ludox), and in both fumed samples (H5 and A300). The horizontal shifting of curves for all the dispersed and grafted samples with colloidal silica produces smooth master curves.

The fumed silica at low loadings (1 and 2.5 wt%) also showed good overlap for both the elastic and viscous modulus with horizontal shifting alone. However, Figure 6.24 clearly shows that there is a TTS failure in the elastic modulus at low frequencies/high temperatures in the fumed silica samples at high loadings (≥ 5 wt%), as the curves no longer overlap with horizontal shifting. There is also a change in the slope in the terminal zone in the composite with fumed silica ($G' \propto f^{1.0}$) compared to the pure polymer and dispersed polymer nanocomposites ($G' \propto f^{1.5}$). This indicates changing elastic behaviour when the samples are heated in the terminal zone. This behaviour has been seen in other filled systems, and has been attributed to decreased mobility of the chains adsorbed onto the surface of the silica nanoparticles[315].

Another explanation in the literature for this type of behaviour is formation of a filler network in the polymer nanocomposite as an interpenetrating filler network dominates the mechanical properties at high temperatures because the filler network is harder than the polymer matrix[131, 167]. However, literature TEM images on similar samples showed no evidence of a percolated particle network in samples with low loadings of silica (<20 wt %)[31]. A study of fumed silica dispersed in poly(2-vinylpyridine) (PVP) found very similar behaviour to our results, with increased modulus with increasing silica content with no corresponding evidence in the TEM of a filler network[173]. It has been suggested that mechanical percolation occurs at lower filler content than structural percolation when there is strong polymer-particle interaction[316].

Whilst a similar change in slope ($G' \propto f^{0.9}$) is observed in the terminal zone in the grafted PBA-MEK-ST sample measured, the high temperature curves overlap well using horizontal shift factors with no need for additional vertical shifting. In grafted polymer nanocomposites, a percolated network of polymer-silica particles could be formed with bridging polymer chains, leading to an increased modulus and the decreased slope in the terminal zone region.

After generating the master curves and obtaining the shift factors for all temperatures, Equation (1.15) was used to obtain the values of the WLF fitting parameters C_1 and C_2, which are listed in Table 6.8. As the TTS principle for fumed silica samples fails in the low frequency region, constants have been calculated using the high frequency/low temperature region only, where there is good overlap.

The constant values calculated for PBA fall within the typical values obtained for amorphous polymers. As expected from the overall behaviour shown in the master curve, the horizontal shift values for dispersed nanocomposites containing colloidal silica are similar to the PBA values, within experimental error values. In addition to the lower increase in viscosity and modulus, these results shows that colloidal silica has a smaller effect on viscoelastic behaviour of the PBA matrix than fumed silica.

Table 6.8: WLF parameters for H-PBA and H-PBA-silica nanocomposites.

Polymer/Nanocomposite	C_1	C_2	f_o / x10^{-2} K^{-1}	a_f / x10^{-4}
Pure PBA	4.96	181.7	8.75	4.82
dispersed-PBA 1.0 MEK-ST	5.00	182.3	8.69	4.77
dispersed-PBA 2.5 MEK-ST	4.99	177.2	8.70	4.91
dispersed-PBA 5.2 MEK-ST	4.99	178.3	8.70	4.88
dispersed-PBA 0.8 Ludox	4.92	178.7	8.83	4.94
dispersed-PBA 2.7 Ludox	4.87	176.8	8.92	5.05
dispersed-PBA 5.5 Ludox	5.08	181.3	8.55	4.71
dispersed-PBA 0.9 H5	5.04	181.7	8.61	4.74
dispersed-PBA 2.5 H5	5.18	189.4	8.38	4.42
dispersed-PBA 5.1 H5	5.55	199.0	7.82	3.93
dispersed-PBA 1.0 A300	4.62	173.0	9.20	5.32
dispersed-PBA 2.6 A300	5.18	192.3	8.37	4.36
dispersed-PBA 5.3 A300	6.42	223.5	6.76	3.03
grafted-PBA 6.7 MEK-ST	4.94	181.3	8.77	4.84

Notation: ##.# = wt % of silica measured by elemental analysis

The dispersed aggregated silica samples show a significant increase in both C_1 and C_2 values as the filler loading increases. This leads to a reduction in free volume, f_0, and thermal coefficient, α_f, when fumed silica is dispersed within the PBA matrix. This result is consistent with the results obtained from the QENS data, which indicates that the decrease in free volume leads to the slowing down of chain motions and this is likely a significant factor behind the large increase in viscosity and dynamic moduli in these samples compared to the pure PBA sample.

Only the dispersed fumed silica samples exhibit different temperature dependence values from the pure PBA. This is the same temperature dependence behaviour seen in the TTS analysis of QENS measurements in Section 6.2.1.3, and thus further establishes that free volume effects are a significant factor in the dynamics of polymer chains in polymer nanocomposite systems. The formation of a filler network through bridging polymer chains could cause this significant decrease in free volume, leading to an increased viscosity, elastic and viscous modulus and therefore decreased chain mobility in the PBA-fumed silica nanocomposites. Interestingly, the grafted MEK-ST sample G' curve is similar in shape to the dispersed aggregated sample but the horizontal shift factors are identical to the pure PBA sample.

After performing TTS analysis, an attempt to model and thus quantify the increase in modulus was made. The starting point for modelling the increase in dynamic moduli is Einstein's Equation (6.5). Guth and Gold[317] modified this equation by adding a further term accounting for interactions between the filler particles. The following equation was therefore proposed for calculating the modulus enhancement, G_δ:

$$G_\delta = \frac{G_c}{G_m} = 1 + 2.5\,\phi + 14.1\,\phi^2 \qquad \textbf{(6.9)}$$

where G_c and G_m are the modulus of the composite and the polymer matrix respectively. Equation (6.9) only applies when the filler particles are spherical, non-interacting and evenly dispersed. This equation was further modified by the introduction of a shape factor parameter, f, to account for non-spherical particles[318]:

$$G_\delta = \frac{G_c}{G_m} = 1 + 0.67f\,\phi + 1.62\,f\,\phi^2 \qquad \textbf{(6.10)}$$

The modified Guth model does not account for aggregation due to particle-particle interactions or for changes in the polymer's elastic behaviour due to excluded volume of the filler and chain adsorption on the particle surface. In order to account for

a portion of the polymer matrix that is highly interacting with the filler, Medalia replaced the volume fraction of filler with an effective volume fraction, ϕ_{eff}[319, 320]:

$$G_\delta = \frac{G_c}{G_m} = 1 + 2.5\ \phi_{eff} + 14.1\ \phi_{eff}^2 \quad \textbf{(6.11)}$$

which can be experimentally determined from dibutyl phthalate (DBP) absorption measurements. Alternatively, one can account for various effects of fillers on the modulus by introducing a shift factor to convert the filler volume fraction to ϕ_{eff}. From these calculations, it is found that the increase in modulus is independent of the particle size of the filler and it is directly proportional to the loading.

A variety of other models are available to predict the increase in the elastic modulus in polymer composites containing well dispersed particles. Among these, the Halpin-Tsai equation gives a simple empirical expression which has been used extensively to model elastic modulus (primarily used for the Young's modulus, but can also be applied to shear or bulk modulus[321]). According to this model, the modulus of the composites is expressed in terms of a fitting parameter, A, that accounts for filler geometry[322]:

$$G_\delta = \frac{G_c}{G_m} = \frac{1 + A\,B\phi}{1 - B\phi} \quad \textbf{(6.12)}$$

The parameter B is given by:

$$B = \frac{\frac{G_f}{G_m} - 1}{\frac{G_f}{G_m} + A} \quad \textbf{(6.13)}$$

where G_f is the modulus of the filler particles. If G_f/G_m is much greater than 1, then B≈1 and Equation (6.12(6.14) simplifies to:

$$G_\delta = \frac{G_c}{G_m} = \frac{1 + A\ \phi}{1 - \phi} \quad \textbf{(6.14)}$$

To account for the packing fraction of the filler, ϕ_m, Nielsen modified Equation (6.12) by adding an additional term[321]:

$$G_\delta = \frac{G_c}{G_m} = \frac{1 + A\phi}{1 - BC\phi} \quad \textbf{(6.15)}$$

where *C* is defined as:

$$C = \left(1 + \frac{1 - \phi_m}{\phi_m^2}\right)\phi \qquad \textbf{(6.16)}$$

Quantitative analysis of the extent of reinforcement in non-cross-linked polymers is not straightforward. As shown in Figure 6.23 and Figure 6.24, the increase in modulus value is not constant across the frequency/temperature range measured due to filler network effects, thus identifying representative G' values is not trivial. As such, only the modulus values obtained in the high frequency region were fitted using the above models, as the increase in modulus caused by the formation of a filler network or bridging polymer chains is primarily seen in the low frequency region.

As the colloidal silicas used in these experiments are spherical in shape and are well-dispersed, the Guth-Gold equation would be expected to fit the data. While the mechanical reinforcement is much lower than that seen in the fumed silica samples, it is still significantly higher than predicted by the Guth-Gold equation (Figure 6.25). When the Medalia modified equation is used to account for chains interacting with the filler particles, the increase in modulus is still not sufficiently well modelled, suggesting that the increase is not due to fully occluded chains, which is consistent with the QENS results. Other groups studying the effect of nanoparticles on polymers have stated that the Guth-Gold equation is theoretically inaccurate and severely underestimates the modulus values[171, 316].

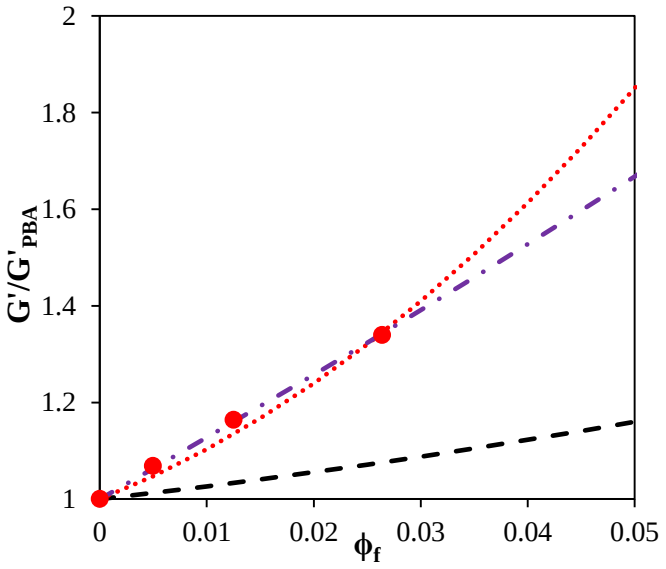

Figure 6.25: Relative elastic moduli of PBA-MEK-ST dispersed nanocomposites (●) and comparison with model calculations/fits: (– –) Equation (6.9), (– · –) Equation (6.15) and (·····) Equation (6.10).

The Nielson modified Halpin-Tsai Equation gives the best fit for the increase in modulus, with an *A* value of 11.6. This *A* value would be expected for aggregated silica geometry rather than well-dispersed colloidal silica particles, thus what the *A* value expresses in this case may not be particle size but rather polymer-particle aggregates. The exact cause of the increase in the modulus in PBA-silica nanocomposites is still unclear. The simple hydrodynamic models above are not sufficient to describe the changes in modulus observed.

Despite the published literature on the failure of the Guth equation to model polymer nanocomposites, the modified Guth-Gold Equation (6.10) has been used to model the mechanical reinforcement of polymer nanocomposites containing fumed silica even in recent studies[173, 323]. When applied to the dispersed H5 and A300 nanocomposite data (Figure 6.26), the equation fits well only with very large shape factor values (20 and 19 respectively) that are expected when the fillers are rod-like in shape rather than fractals[173]. These *f* values are similar to those obtained in the literature, which was attributed to the shape factor reflecting loosely packed clusters of aggregated particles. However, as stated previously, this equation does not take into account various factors, such as polymer-particle interaction, potential mechanical heterogeneity caused by a bound glassy layer etc., and therefore the physical significance of this large *f* value is questionable. The Nielson modified Halpin-Tsai equation was also applied to the data, using ϕ_m = 0.37 for random packing of aggregated identical spheres, but is a poor fit for the increase in modulus (Figure 6.26).

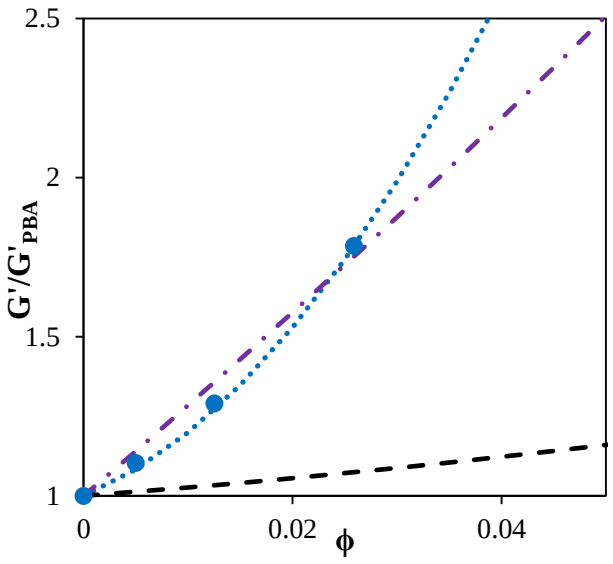

Figure 6.26: Relative elastic moduli of PBA-H5 dispersed nanocomposites (●) and comparison with model calculations/fits: (– –) Equation (6.9), (– · –) Equation (6.15) and (·····) Equation (6.10).

Finding a hydrodynamic model for the aggregated silica is more challenging due to the more complex geometry of the fractal structure. The majority of current models are limited to ideal geometries, such as spherical fillers. While there is currently no complete and rigorous model for quantitative non-ideal nanocomposites, a more complex hydrodynamic model, the Christensen-Lo model[324], has been successfully applied to small-strain modulus reinforcement in carbon black fractal fillers by Raos[171]. Computational modelling of the modulus reinforcement in polymer nanocomposites could provide more information on the origin of the phenomena.

6.2.3 Physical Ageing

6.2.3.1 Physical Ageing Theory

Enthalpy relaxation experiments are used to measure the effects of physical ageing on a polymer material. Figure 6.27(a) shows the general temperature cycles for these short-term enthalpy relaxation experiments and Figure 6.27(b) is a schematic of the DSC curves obtained and how the enthalpic change, ΔH, values are calculated from the curves. The sample is heated up to a temperature at least 50 ^{o}C above T_g (point A) in order to erase any previous thermal history. The sample is then cooled at a fixed cooling rate to the ageing temperature (point B), which is a fixed distance below T_g, where it is held for the desired ageing time. The cooling rate must be the same for all measurements as the distance of the sample from its equilibrium state depends on cooling rate. During the ageing time, a loss of enthalpy occurs (B-C) which is proportional to ageing time; the longer the ageing time, the closer to the equilibrium state (point E) the sample will reach. The sample is then quenched (point D) and then heated at a constant rate which causes the enthalpy to overrun the unaged curve proportionally to ΔH. This difference is expressed as the following equation, which is equivalent to the area (A-B):

$$\Delta H(t_a, T_a) = \int_{T\alpha}^{T\beta} [C_p(aged) - C_p(unaged)]\, dT \qquad \textbf{(6.17)}$$

where t_a is the ageing time and T_a is the ageing temperature. Accelerated ageing is carried out at temperatures close to T_g as lower temperatures increase the time scale for relaxation events and therefore the ageing process. Increasing the temperature to a few degrees lower than T_g allows for accurate measurements over a period of a few days maximum.

Several models have been proposed to analyse the experimental data collected by enthalpy relaxation experiments using differential scanning calorimetry (DSC). A potential model for predicting long term ageing is the Cowie- Ferguson (C-F) model which uses an empirical equation to model the data[325, 326]:

$$\Delta H(t_a, T_a) = \Delta H(\infty, T_a)[1 - \phi(t_a)] \quad \textbf{(6.18)}$$

This model considers $\Delta H(\infty, T_a)$ is adjustable and measured by curve fitting a $\Delta H(t_a, T_a)$ vs. log t_a plot, and $\phi(t_a)$ is defined as:

$$\phi(t_a) = exp\left\{-\left(\frac{t}{t_c}\right)^{\beta}\right\} \quad \textbf{(6.19)}$$

where t_c is a characteristic time when the polymer has aged to 63.2% of a fully aged sample[327]. The Cowie-Ferguson model predicts the time, t_a, needed to reach 99.9% of the thermodynamic equilibrium state of the polymer from short-term enthalpy relaxation experiments.

For polymer nanocomposites, enthalpy relaxation experiments measure the heat capacity of both the polymer matrix and the filler material. In order to compare the results of nanocomposites to pure polymers, the contribution to heat capacity from the silica should be subtracted and only the contribution from the dispersed or grafted chains considered. The polymer contribution can be calculated with the following equation[328]:

$$C_{p,polymer} = \frac{(C_p m) - (C_{p,silica} m_{silica})}{m_{polymer}} \quad \textbf{(6.20)}$$

where C_p, $C_{p,polymer}$ and $C_{p,silica}$ are the heat capacities of the sample, the polymer and the silica respectively, m is the total mass of the sample and $m_{polymer}$ and m_{silica} are the corresponding masses of polymer and silica. The temperature dependence of the heat capacity of amorphous silica was calculated using the following polynomial equation and literature data[329]:

$$C_p = a + bT - cT^{-2} \quad \textbf{(6.21)}$$

where a = 56.06, b = 15.42x10^{-3} and c = 14.5x10^5. This formula was used to determine the heat capacity of silica across the temperature range of the enthalpy relaxation experiments.

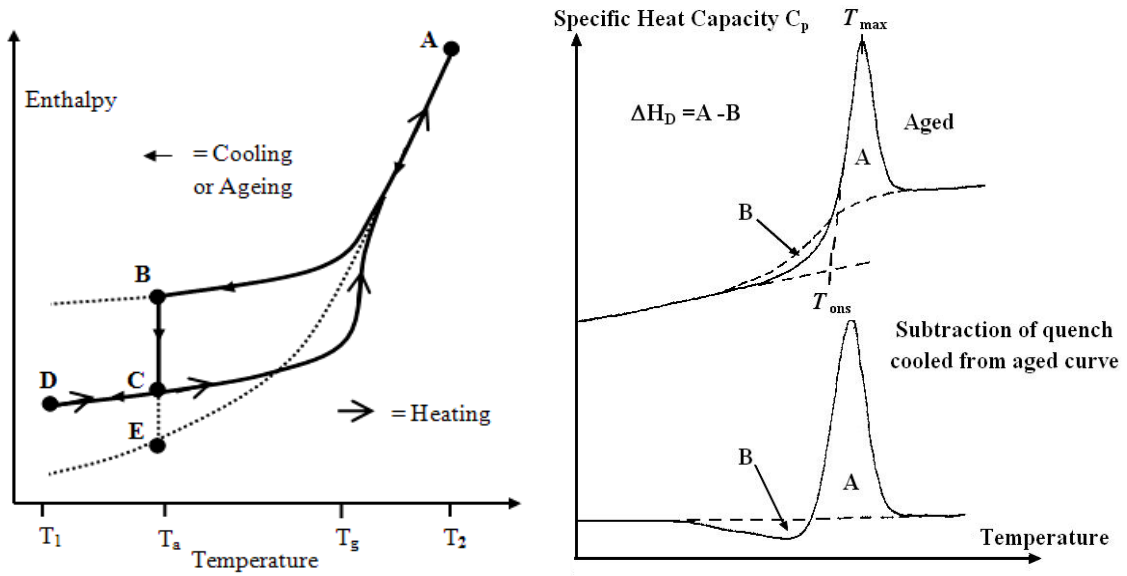

Figure 6.27: Schematic diagram of (a) cooling, aging and heating cycles for enthalpy relaxation experiments and (b) DSC for aged (solid line) and unaged (broken line) curves of a polymer[327].

6.2.3.2 PS-silica and SAN-silica nanocomposites

PS and SAN nanocomposites containing colloidal and fumed silica were measured by enthalpy relaxation experiments. Examples of the obtained aged and averaged unaged heat capacity curves for the different types of SAN samples at one ageing temperature, after subtracting the silica contribution to heat capacity, are shown in Figure 6.28. The graphs show that as the sample is aged for a longer time, the magnitude of the ageing peak increases, resulting in an increased relaxed enthalpy value. When comparing the dispersed and grafted nanocomposite samples, there is a clear decrease in relative heights and a slight broadening of the peaks where the polymer has been grafted instead of dispersed.

The ΔH values for all ageing times were calculated by integrating the area under the aged curves using a combination of Excel and the software programs developed by Dr Roderick Ferguson. The data were then analysed using the C-F model (Equation (6.18)), and the obtained fitting parameters are listed in Table 6.9 and Table 6.10. A comparison of the C-F model fitted curves for $T_g - T_a = 10$ for SAN and SAN-silica is shown in Figure 6.29, and Figure 6.30 shows PS and PS-silica nanocomposite curves. Qualitatively, the PS curves show a significant decrease in ΔH_∞ values when comparing grafted nanocomposites to the pure polymer and an increase in ΔH_∞ for the dispersed nanocomposites, whereas all SAN nanocomposite samples show an increase in ΔH_∞.

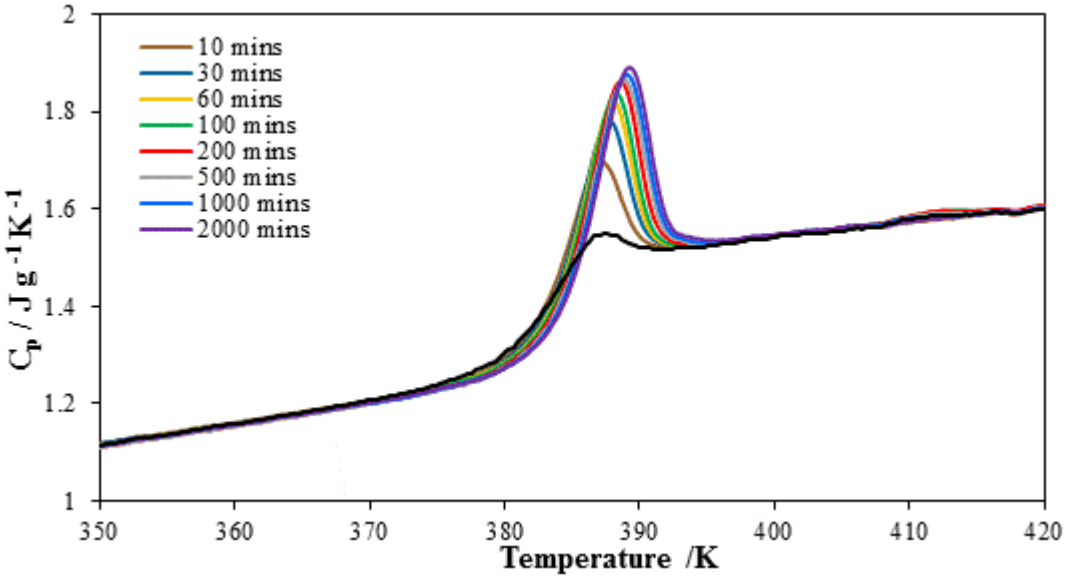

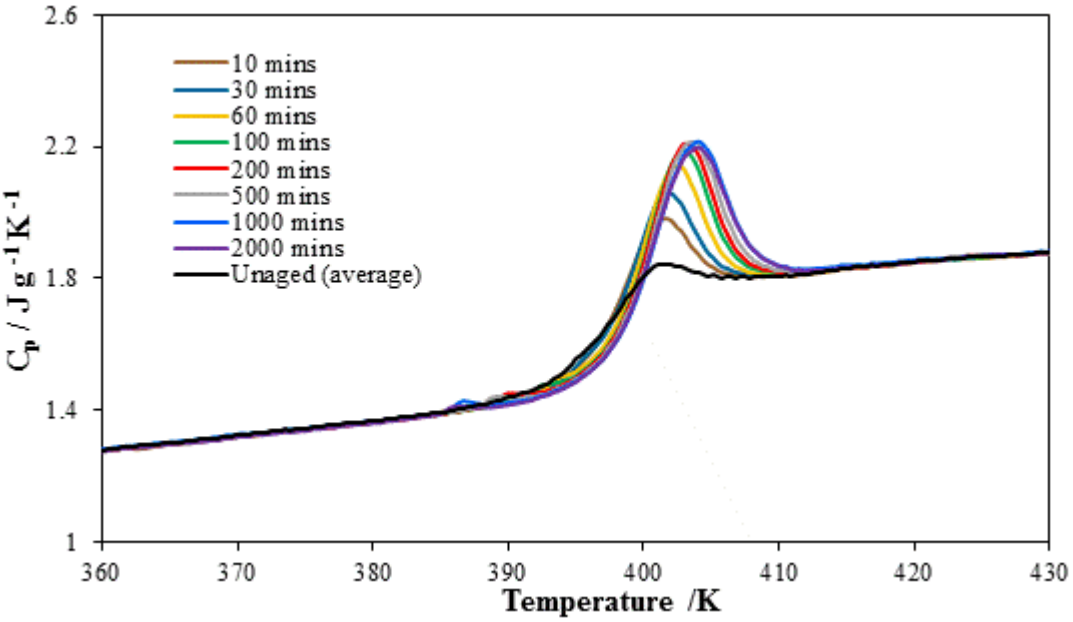

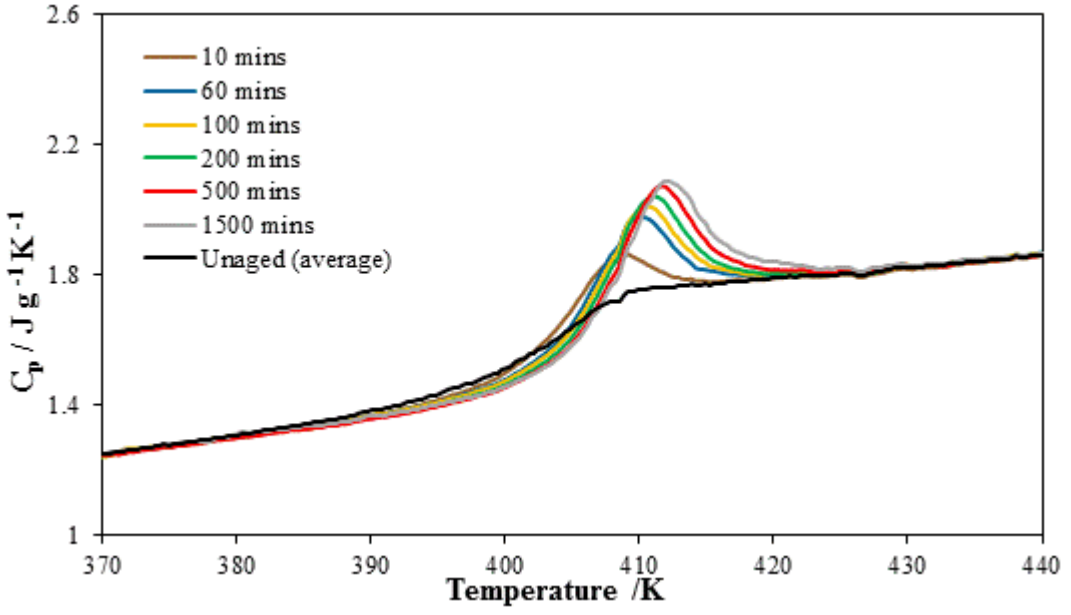

Figure 6.28: DSC thermograms showing the average unaged and aged curves for (a) SAN, (b) dispersed-SAN 20 H5 and (c) grafted-PSAN 17 H5 at $T_a = T_g - 9$.

Table 6.9: Cowie-Ferguson model fitting parameters for SAN and SAN-silica nanocomposites

Polymer/Nanocomposite	$T_g - T_a$ / K	$\Delta H_\infty(T_a)$ / J g^{-1}	Log (t_c /min)	β
SAN	14.9	2.01	2.19	0.39
	9.9	1.21	1.24	0.47
	4.9	0.58	0.48	0.43
grafted-SAN 17 H5	14.5	2.80	2.31	0.36
	9.5	1.63	1.37	0.50
	4.5	0.69	0.77	0.47
grafted-SAN 17 MEK-ST	14.6	2.80	2.28	0.36
	9.6	1.53	1.32	0.41
	4.6	0.56	0.79	0.50
dispersed-SAN 20 H5	15.1	2.40	2.16	0.38
	10.1	1.44	1.20	0.48
	5.1	0.57	0.65	0.50

Notation: ## = wt % of silica measured by elemental analysis

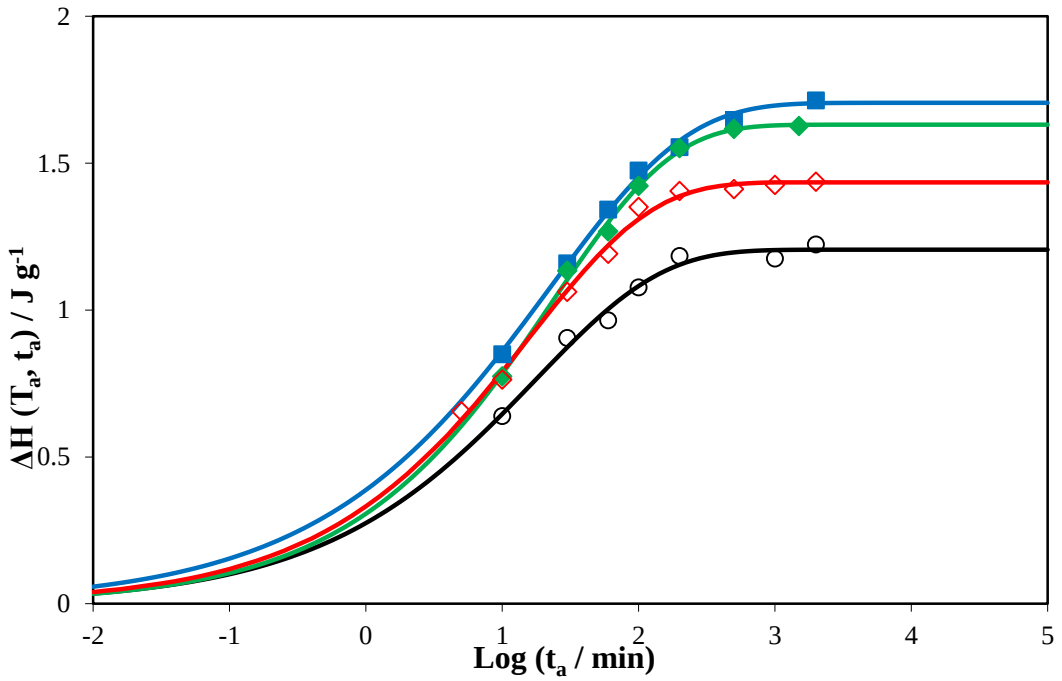

Figure 6.29: Comparison of model fitted ΔH curves at $T_a = T_g - 10$ after subtraction of silica heat capacity of SAN (○), grafted-SAN 17 MEK-ST (■), grafted-SAN 17 H5 (♦) and dispersed-SAN 20 H5 (◊). The symbols are the experimental data and the solid lines show the C-F model fits.

Table 6.10: Cowie-Ferguson model fitting parameters for PS and PS-silica nanocomposites

Polymer/Nanocomposite	$T_g - T_a$ / K	$\Delta H_\infty(T_a)$ / J g^{-1}	Log (t_c /min)	β
PS	15.3	1.80	2.016	0.38
	9.3	1.01	0.961	0.44
	5.3	0.33	0.460	0.49
dispersed-PS 10 MEK-ST	15.6	2.26	2.064	0.40
	9.6	1.22	1.123	0.48
	5.6	0.43	0.524	0.47
grafted-PS 14 H5	15.3	2.20	1.972	0.36
	9.3	0.89	0.929	0.38
	5.3	0.25	0.775	0.44
grafted-PS 14 MEK-ST	14.9	1.80	2.395	0.39
	8.9	0.71	1.043	0.42
	4.9	0.33	0.542	0.48

Notation: ## = wt % of silica measured by elemental analysis

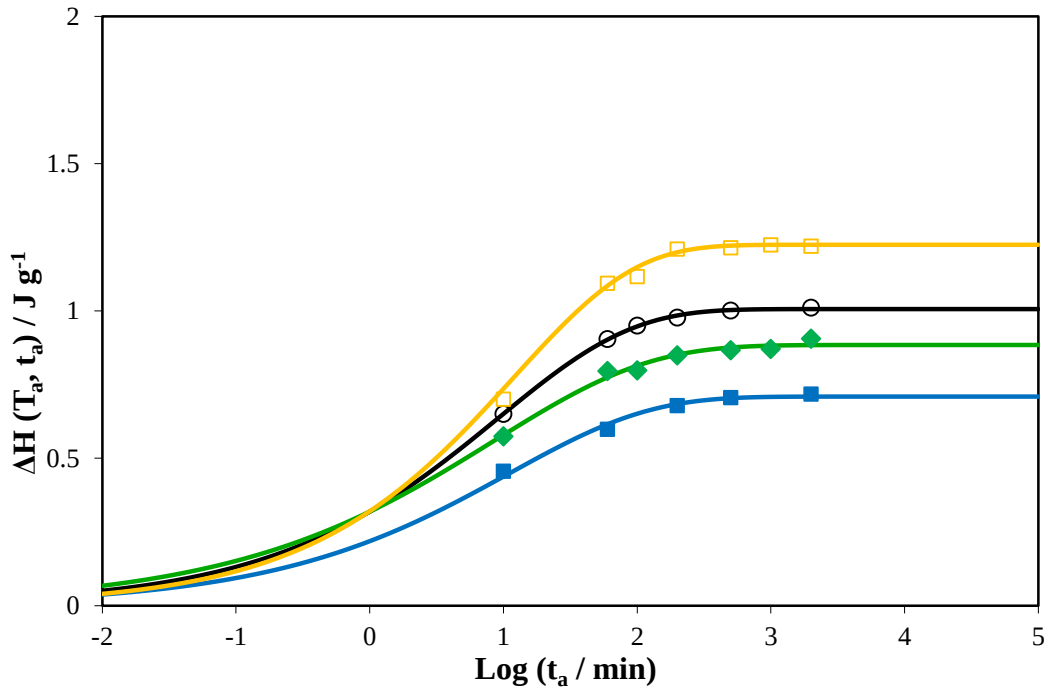

Figure 6.30: Comparison of model fitted ΔH curves at $T_a = T_g - 10$ after subtraction of silica heat capacity of PS (○), grafted-PS 14 MEK-ST (■), grafted-PS 14 H5 (♦) and dispersed-PS 10 MEK-ST (□). The symbols are the experimental data and the solid lines show the C-F model fits.

Figure 6.31 shows that, as expected, the majority of the $\Delta H_\infty (T_a)$ values for each sample increase as distance from T_g increases. However, the increase is not entirely consistent in the grafted PS samples, as the sample shows a lower ΔH_∞ than pure PS at small distances from T_g, but has a higher ΔH_∞ at $T_g - 15$. This highlights a problem with the C-F model: the inability to accurately predict ΔH_∞ where there is no clear inflection point in the data[154]. It has also been shown in previous papers that experimental

estimation of ΔH_∞ is only possible in a small temperature range below T_g.[158] Fixing some of the parameters or using trends between values is a possible solution.

The grafted SAN systems show a more consistent increase in ΔH_∞ (T_a), especially at larger distances from T_g (Figure 6.31). A possible explanation is the additional annealing of the samples in order to get a consistent T_g value for the ageing experiments, which has been shown to affect calorimetric measurements in other nanocomposites and ultra-thin films[330]. Additionally, the SAN-silica grafted samples are prepared using a different ATRP method to PS-silica nanocomposites (see Chapter 3). In SAN-silica nanocomposites there is also the possibility of strong hydrogen bonding between the hydroxyl groups on the silica surface and the acrylonitrile groups in the polymer[331]. This may account for the large difference in the ΔH_∞ (T_a) behaviour seen in the SAN samples as hydrogen bonding between the silica hydroxyl group and nitrile group in SAN is stronger and has a different geometry to the suggested hydrogen bonding between the hydroxyl units in silica and carbonyl groups in PMMA[332].

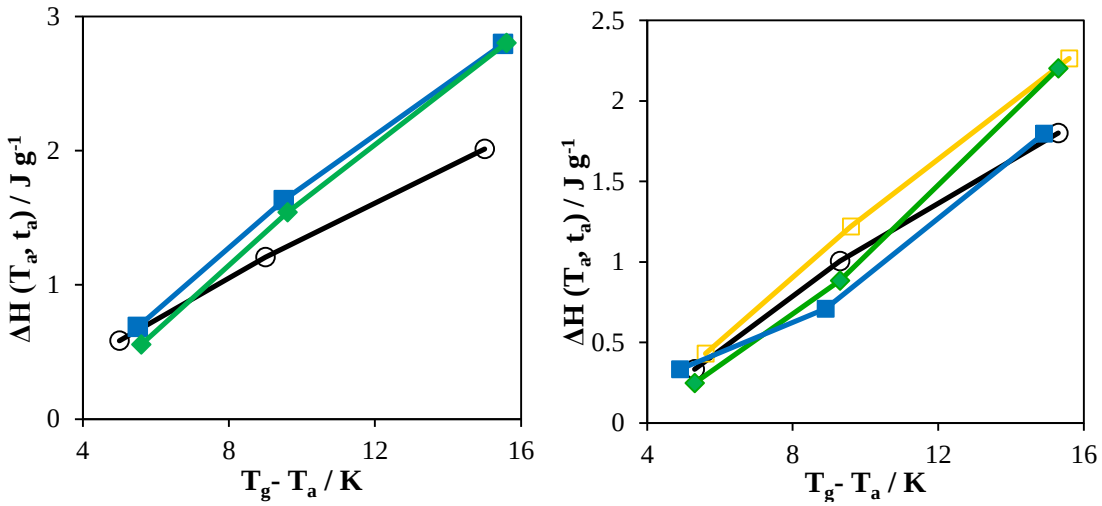

Figure 6.31: $\Delta H_\infty(T_a)$ *vs.* $T_g - T_a$ for (left) SAN (○), grafted-PS 17 MEK-ST (■) and grafted-SAN 17 H5 (♦), and (right) PS (○), grafted-PS 14 MEK-ST (■), grafted-PS 14 H5 (♦) and dispersed-PS 10 MEK-ST (□).

The β values give the distribution of relaxation times; a small value implies a larger distribution. The β values obtained range from 0.36 to 0.50, are similar between the different samples and generally increase as distance from T_g increases. However, due to interrelation of the fitting parameters, the variation of β is often not predictable[154].

Acceleration or deceleration in the polymer nanocomposites can be assessed by the log ($<t_c>$ /min) value (Figure 6.32)), which are calculated from the log (t_c /min) and the β values obtained from the C-F model and the following equation:

$$< t_c >= t_c \frac{\Gamma(1/\beta)}{\beta} \quad \textbf{(6.22)}$$

The graphs show that in the case of SAN and PS grafted nanocomposites both the colloidal and aggregated silica show a reduction in ageing rate. This correlates with the glass transition measurements of the nanocomposites that showed a significant increase in T_g when PS or SAN are grafted to the surface of silica (Section 6.2.1.1). Significant deceleration of physical ageing has been reported in polymer nanocomposites with increased T_g values due to reduced segmental motions[333, 334].

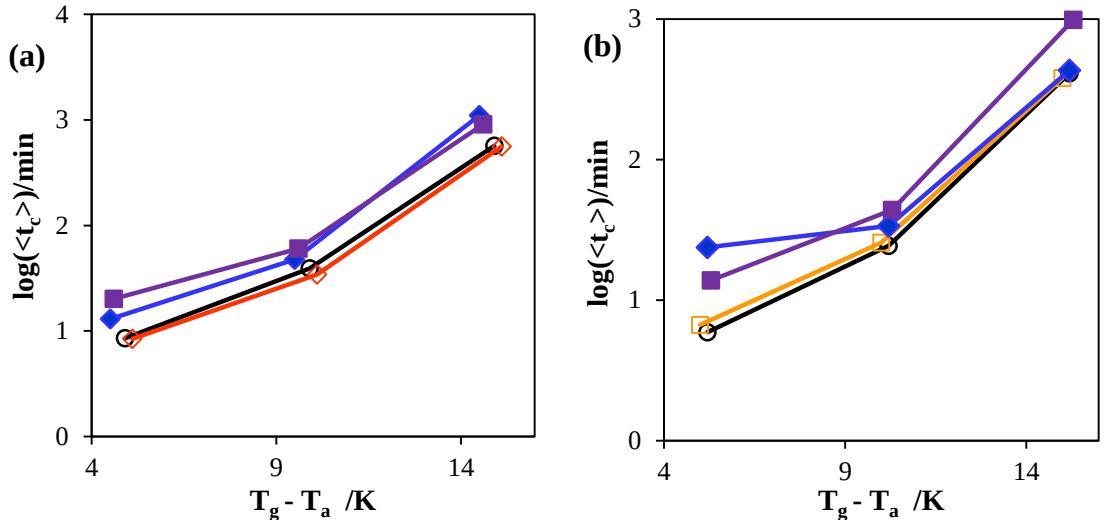

Figure 6.32: Log(<t_c>/min) *vs.* T_g - T_a for (a) SAN (○), grafted-SAN 17 MEK-ST (■), grafted-SAN 17 H5 (♦) and dispersed-SAN 20 H5 (◊), and (b) PS (○), grafted-PS 14 MEK-ST (■), grafted-PS 14 H5 (♦) and dispersed-PS 10 MEK-ST (□).

Additionally, the dispersed samples, which exhibited no change in T_g, show no significant change in physical ageing compared to the pure polymer. Rittigstein and Torkelson[335] reported a similar invariant T_g in PS upon addition of silica, due to the lack of attractive interactions between PS chains and silica filler particles. Thus in PS-silica dispersions, we would not expect any partially immobilised chains or changes in segmental dynamics and therefore no change in the physical ageing of the polymer. The results from dispersed PS-fullerene mixtures by Sanz *et al.*[148] also support the lack of physical aging in dispersed nanocomposites. Although the paper itself concludes that there is a suppression of aging in these nanocomposites, in fact this is due entirely to the increased T_g and thus increased $T_g - T_a$ value, as the samples are aged at the same absolute temperature rather than at temperatures relative to T_g. When the samples are rescaled to compare the physical ageing of the nanocomposite to the pure polymer at the same distance from T_g, the changes in physical ageing disappear.

6.3 PS-fullerene stars

6.3.1 Local chain dynamics

6.3.1.1 Glass transition temperature

The glass transition temperature (T_g) of the various PS-fullerene stars was measured by DSC and compared to linear PS chains. The results (Figure 6.33 and Table 6.11) show that the PS-fullerene stars have similar T_g values to PS chains that have the same total molecular weight as the star. Deuterated samples have a lower T_g than hydrogenated samples, which is seen in both the linear chains and the stars, most likely due to increased free volume as the mass is the same but the lengths of the chains are different.

Typically, pure polymer stars do not show total molecular weight dependent glass transitions, but rather have end-group concentration dependent glass transitions[336]. This has been attributed to the star polymers relaxing by arm retraction rather than reptation. Thus the dynamic and viscoelastic properties of pure polymer stars are determined by the length and behaviour of the individual arms, rather than the star as a whole. As the PS-fullerene stars are structurally similar to a pure polystyrene star, we might expect the same glass transition dependence behaviour. However, the PS-C60 stars studied have T_gs that are determined by the total molecular weight.

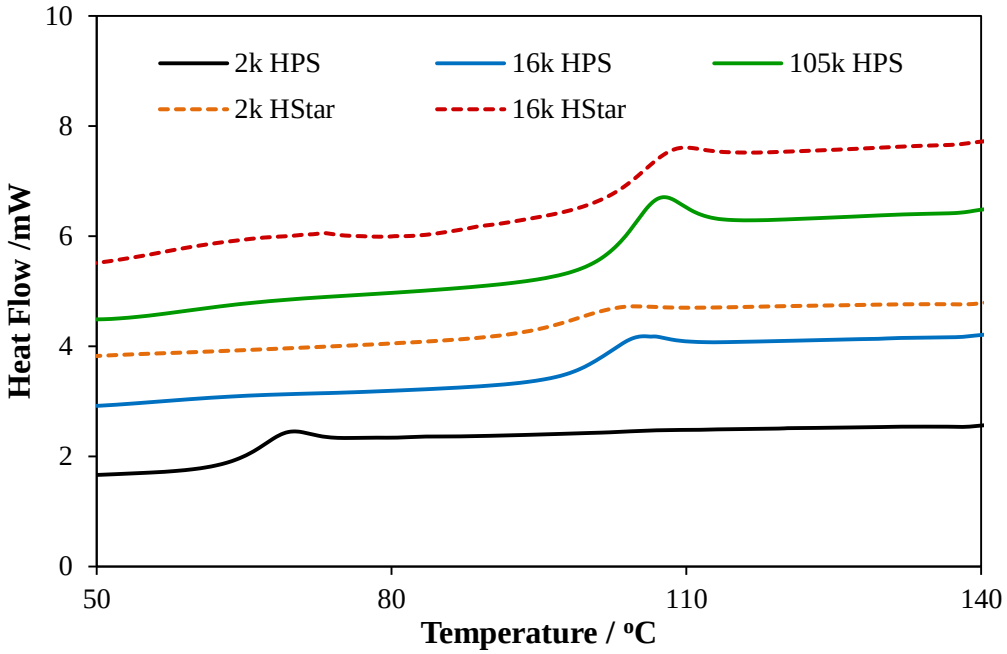

Figure 6.33: DSC traces of linear PS chains and PS-fullerene stars. The curves have been shifted vertically for clarity.

Table 6.11: Glass transition temperatures of linear PS and PS-fullerene star samples.

Sample	T_g /ºC	Onset /ºC	Endpoint /ºC	ΔC_p / J g^{-1} ºC^{-1}
2k HPS	67.2	63.6	68.0	0.310
16k HPS	102.5	97.5	103.3	0.249
105k HPS	105.0	101.0	105.4	0.250
2k DPS	63.2	59.4	63.7	0.235
2k HStar	99.3	93.0	101.7	0.268
16k HStar	106.4	102.8	108.3	0.243
2k DStar	97.8	90.8	101.1	0.232
18k DStar	100.0	94.8	101.5	0.249

Other non-typical polymer stars have shown this total molecular weight dependent behaviour. Polybutadiene stars with unentangled arms of a similar molecular weight to the lowest PS-fullerene star sample investigated here, were studied by Kisliuk *et al.*[337] These stars showed total molecular weight dependence of both T_g and segmental dynamics, however the group was unable to provide an explanation for why this contrary result to the existing literature occurred. Choi *et al.* synthesised and investigated the dynamics of poly(ε-caprolactone) stars with ultra-small arms (molecular weights of ~300 to ~700 g mol^{-1}), also finding a total molecular weight dependence for both glass transition and chain dynamics, following linear behaviour rather than typical star polymer dynamics[338]. They have attributed this to the star behaving as a whole unit in terms of Rouse segmental motion due to the low molecular weight of the arms.

In the case of PS-fullerene stars, both the star with arms above and below the molecular weight of entanglement shows this total molecular weight dependence. The difference between these grafted stars and pure polymer stars is that the arms are attached to a hard core instead of a soft tethered centre. The grafting of the arms to a hard centre may cause molecular coupling, which would result in the dynamics depending on the whole star rather than a single arm. If this is the case, we would also expect the segmental dynamics and the viscoelastic behaviour of PS-fullerene stars to also show total molecular weight dependence.

However, we also have to take into account filler effects on the glass transition. The effect of dispersing fullerenes within a polystyrene matrix has been investigated in the literature. Kropka *et al.*[130] found increased T_g values for PS, PMMA and TMPC-

fullerene nanocomposites containing up to 1 wt% filler. For dispersed PS-fullerene mixtures, Sanz *et al*. found that the addition of well-dispersed fullerenes increased the glass transition temperature up to a loading of 4 wt%, above that the T_g decreased back towards the value for pure polystyrene[148]. They also find that changes in the glass transition are highly dependent upon fullerene aggregation, as fullerenes could only be sufficient dispersed at concentrations below 1 wt% and 4 wt%. Grafting PS chains to fullerene stops aggregation of fullerenes and overcomes the polystyrene-fullerene incompatibility, leading to stable dispersions.

An increase in the glass transition was reported by Bershtein *et al*.[339] for 6-arm grafted PS-fullerene stars (M_{arm} = 5,000 g mol^{-1}, M_{star} = 30,000 g mol^{-1}) when compared to linear PS of a molecular weight equal to one arm (M_{arm} = 5,000 g mol^{-1}). They also observed a greatly broadened glass transition range (increased from ~6 ^{o}C in the linear PS sample to ~20 ^{o}C in the PS-C60 star) which is absent from our DSC measurements. Our results have shown that the T_g of the PS-fullerene star is determined by the overall molecular weight of the star, not that of the individual arm, and therefore the observed increase in T_g may actually be due to the increased molecular weight.

6.3.1.2 Elastic Window Scans and QENS (IN16B) measurements

Elastic window scan (EWS) measurements were carried out on PS-fullerene samples and linear PS chains of corresponding molecular weight. Figure 6.34 shows the temperature dependence of the elastic intensity for the 16k HStar sample, which has been normalised at T=0. Two linear decreases of the logarithmic elastic intensity is observed up to the polymer T_g. The initial decay is consistent with the Debye-Waller factor. Phenyl group motions occurring below T_g then cause a more pronounced slope up until the glass transition. The decrease in elastic intensity becomes more pronounced after the glass transition temperature.

We can use window scans to compare the PS-fullerene star to linear polystyrenes of molecular weights comparable to the size of the arms and the whole star (Figure 6.35 and Figure 6.36). The mean square displacement for all the samples was calculated according to Equation (6.1). The elastic window scans show that the PS-fullerene stars show very similar dynamics to the linear polystyrene chains that are similar to the total molecular weight of the star.

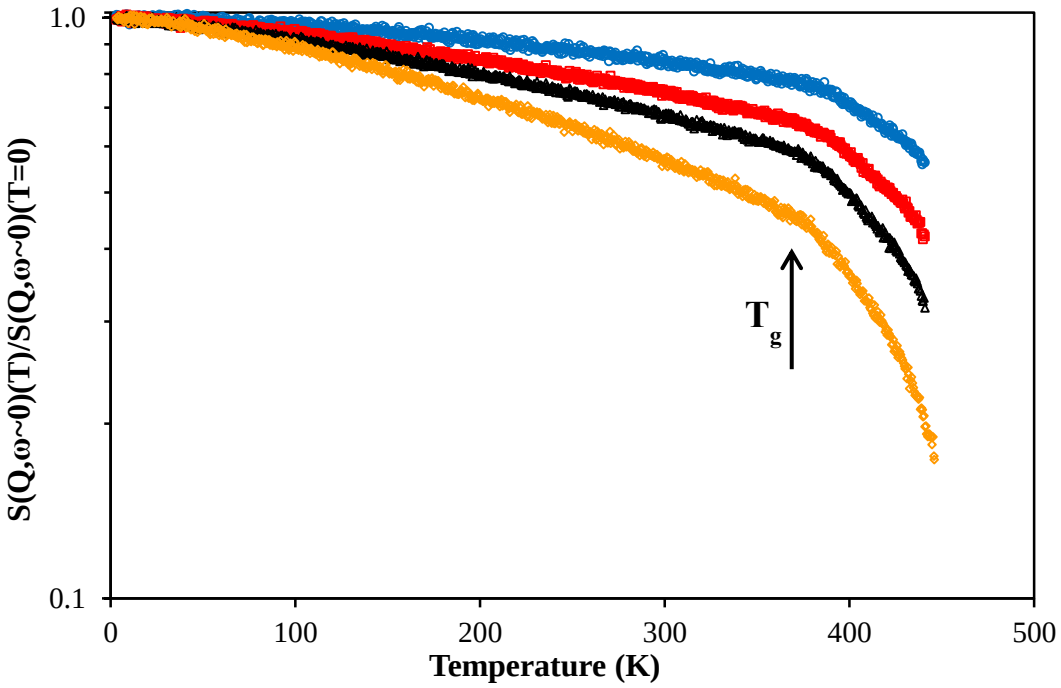

Figure 6.34: Temperature dependence of normalised elastic window scan data for 16k HStar at: 0.57 Å^{-1} (○), 0.95 Å^{-1} (□), 1.29 Å^{-1} (Δ) and 1.79 Å^{-1} (◊). The glass transition temperature of the sample is indicated on the graph with an arrow.

The literature studies on the effect of fullerenes on the dynamics of polystyrene are often contradictory. Sanz *et al.*[137] showed slightly accelerated dynamics in PS-fullerene mixtures due to a plasticisation effect of the fullerenes on the fast local dynamics of the polymer chains, with a corresponding increase in the glass transition temperature[148]. However, Kropka *et al.*[130] reported hindered segmental motion in polymer-fullerene mixtures above T = 200 K, and that the effect of fullerene on chain dynamics is limited to the nanosecond time scale. Molecular dynamics simulations also predict a slowing down of dynamics in PS-C60 mixtures as fullerenes suppress the average chain motion[340]. There are very few studies on the dynamics of grafted polymer-fullerene stars. Lebedev *et al.* reported that the presence of fullerene hinders chain diffusion on a local segmental scale[341] and that dynamic behaviour deviates from the Rouse or Zimm models. However, they do not compare the dynamic results to PS chains of the total molecular weight of the star.

Other than changing the dynamic dependence on the molecular weight, attaching the chains to fullerene has no other effect on the dynamics of the chains, unlike the results that have been reported for dispersed polymer-fullerene mixtures. It is well known that PS and fullerenes are incompatible leading to aggregation of fullerene particles, which has been shown to be an important factor in the chain dynamics of PS-fullerene mixtures[148]. The negative interactions between PS and fullerenes that are

overcome by grafting may also affect the dynamics of PS chains in dispersions but not in the grafted stars.

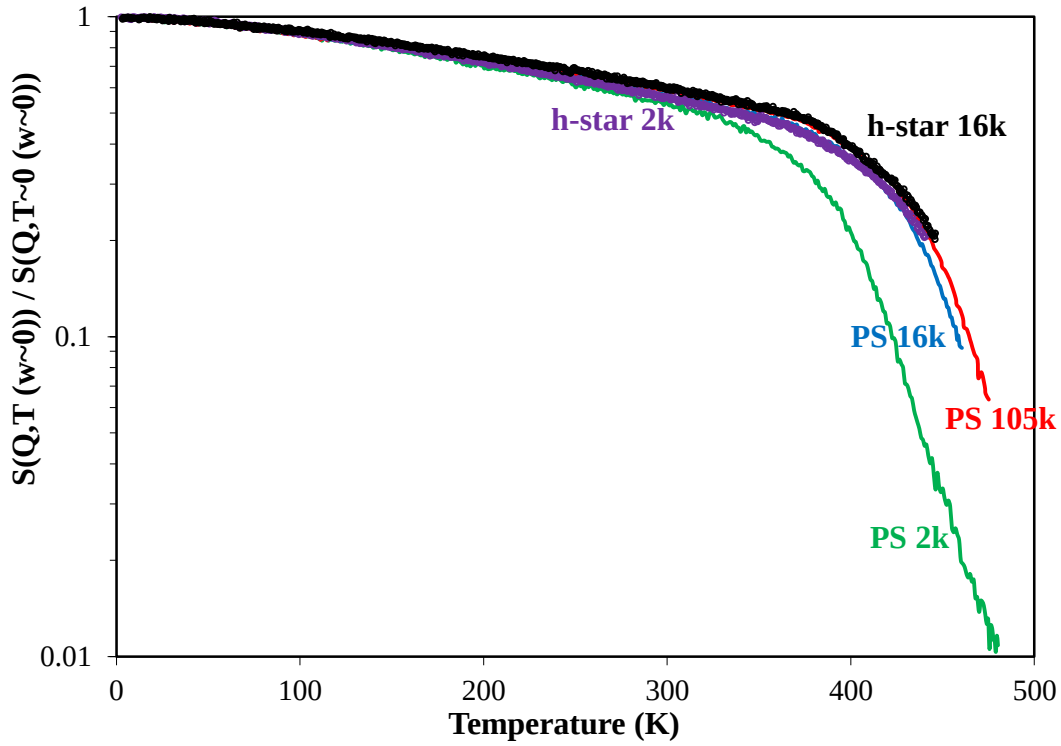

Figure 6.35: Elastic window scan (EWS) data for all PS-fullerene stars and linear polystyrene chains after subtracting the contribution from the empty cell at *Q* = 1.7Å^{-1}.

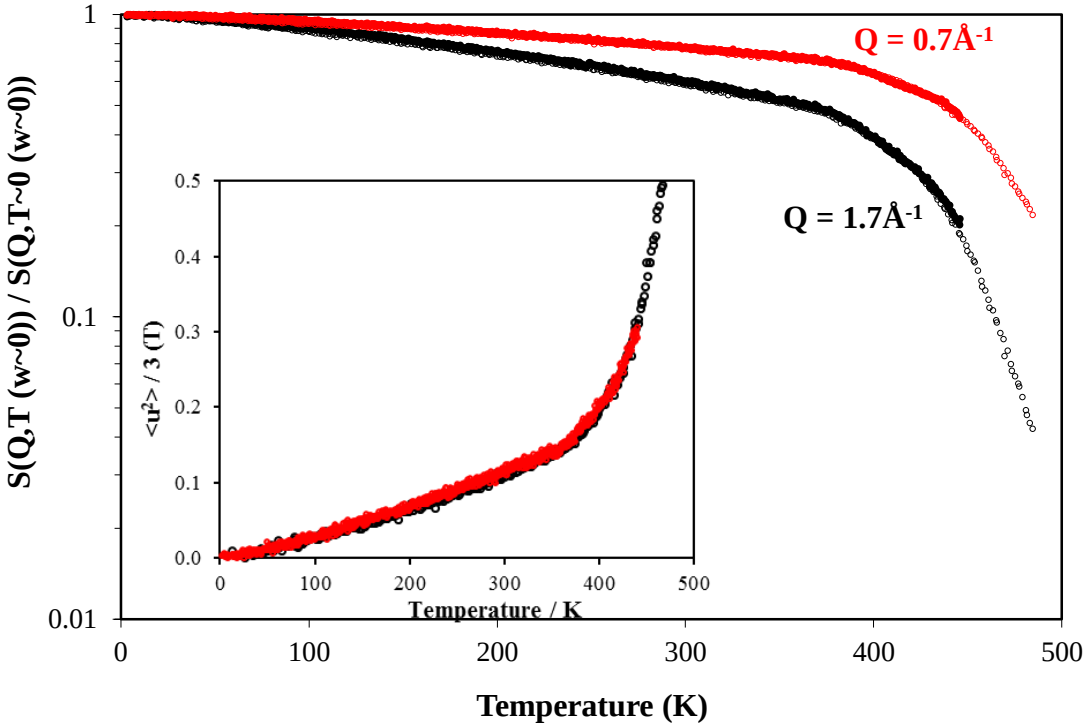

Figure 6.36: Elastic window scan (EWS) data for 16k HStar (●) and 105k HPS (○) and corresponding linear polystyrenes after subtracting the contribution from the empty cell at two different *Q* values, (black) 1.7Å^{-1} and (red) 0.7Å^{-1}. Inset: Mean square displacement, <u^2>/3, versus temperature for 16k HStar (○) and 105k HPS (●).

QENS measurements at high temperatures (460 - 500K) on IN16B were also carried out on the PS-fullerene samples and lower molecular weight linear PS chains. The dynamic incoherent structure factor shows the same results as the EWS measurements, the PS-fullerene stars have the same dynamic behaviour as the linear chains of the same total molecular weight. This is only shown for one star sample at 500 K and Q = 1.58 Å^{-1} in Figure 6.37, but is consistent across both PS-fullerene stars, all Q values and the temperature range measured.

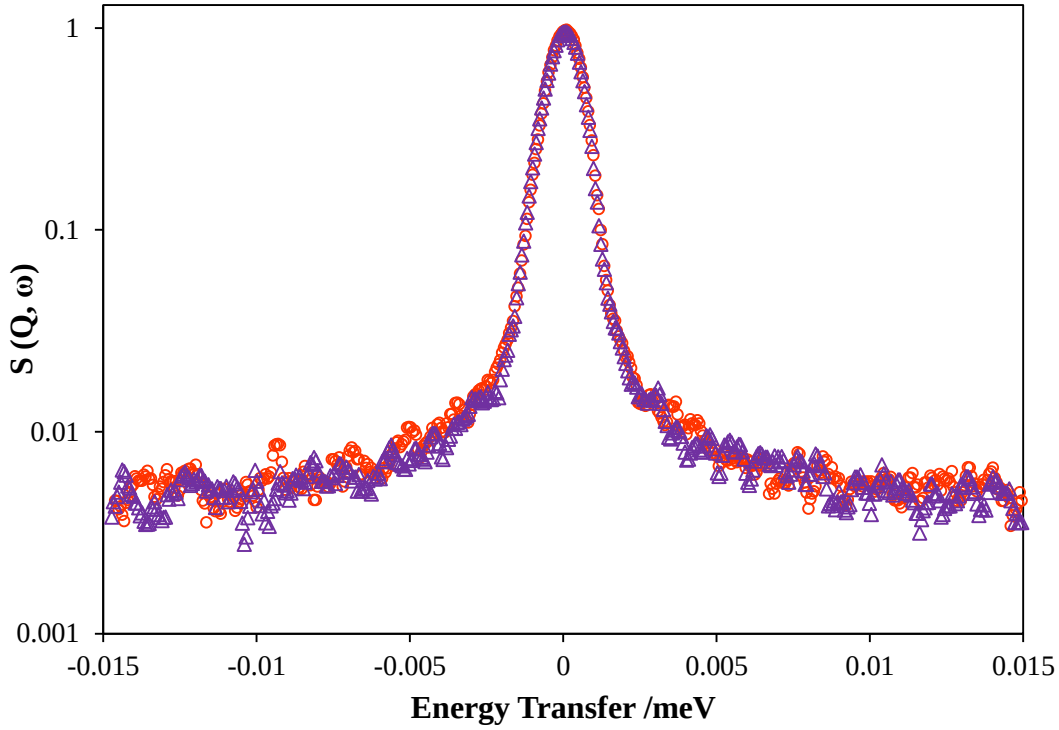

Figure 6.37: Dynamic incoherent structure factor as a function of energy transfer for : linear 16k HPS (○) and 2k HStar (Δ) at 500 K and Q = 1.58 Å^{-1}. The empty cell background has been subtracted and the data corrected for adsorption.

The EWS and QENS measurements on PS-fullerene stars and the corresponding linear polymer chains show that molecular weight has a significant effect on the dynamics of the polystyrene chains. The different molecular weight samples of linear polystyrene show different dynamic behaviour at T>100K, which is far below the T_g (Figure 6.38). Additionally, the changes in dynamic behaviour at different Q values are not consistent across the Q range measured. This shows that there is change in Q dependence with increasing molecular weight.

As discussed in Section 1.3.3, the origin of sub-T_g dynamics of polystyrene has been studied extensively, with varying conclusions. Recently, Colmenero *et al.*

attributed sub-T_g dynamics of polystyrene to phenyl ring oscillations rather than 180° ring flips[89]. Therefore, increasing the molecular weight of both the linear PS and the PS-fullerene star samples hinders both phenyl ring oscillations and segmental dynamics. This result may be the subject of future dynamics work on polystyrene chains but is not within the scope of this project.

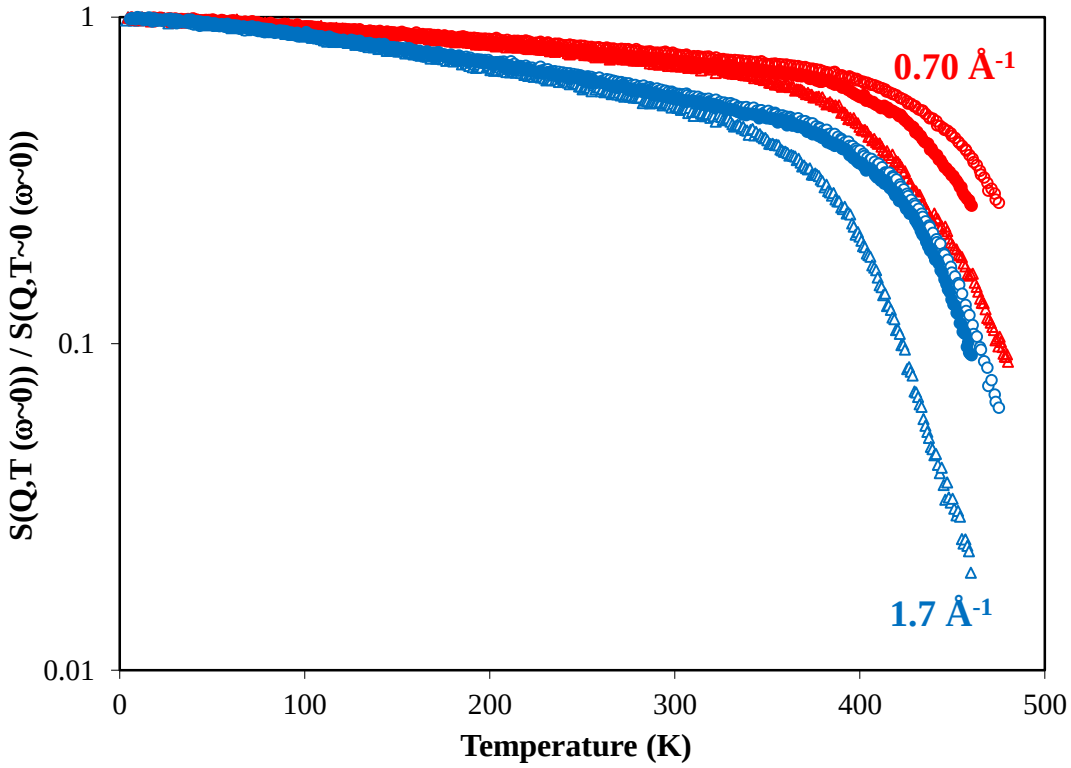

Figure 6.38: EWS data for polystyrene chains of different molecular weights (○) 105k, (●) 16k and (Δ) 2k at two different *Q* values, 0.7 Å^{-1} (red) and 1.7 Å^{-1} (blue).

6.3.2 Rheological behaviour

The previous experiments to measure local chain dynamics on PS-fullerene stars have shown that they behave differently to typical polymer stars, and instead exhibit dynamic behaviour similar to that of linear chains of the same total molecular weight. Rheological measurements on PS-fullerene stars and linear PS chains in dilute and concentrated solutions were carried out to determine if the viscoelastic behaviour, and therefore macroscopic dynamics, follows the same trend.

6.3.2.1 Dilute Solution

The rheology of PS-fullerene stars and corresponding linear PS chains 1 wt% solutions in toluene were measured on a double wall concentric cylinder geometry (Figure 6.39

and Figure 6.40 respectively). This geometry has the highest sensitivity for low viscosity polymer solutions and minimises solvent evaporation effects but requires a large sample size (minimum 12 mL).

Dilute linear polystyrene solutions are expected to act primarily as Newtonian fluids as the behaviour of the solvent dominates over the change in viscosity predicted for isolated polymer coils. At high shear rates (>100 s^{-1}), instabilities in the fluid cause non-Newtonian behaviour to occur. This was the case in all linear polystyrene samples measured at 1 wt% in toluene solution. The polystyrene-fullerene stars show the same Newtonian behaviour in the same range as the linear polystyrene corresponding to the total molecular weight of the star. However, it is well known in the literature that the viscosity of pure polymer stars depends mainly on the molecular weight of the arm rather than the whole star[342, 343].

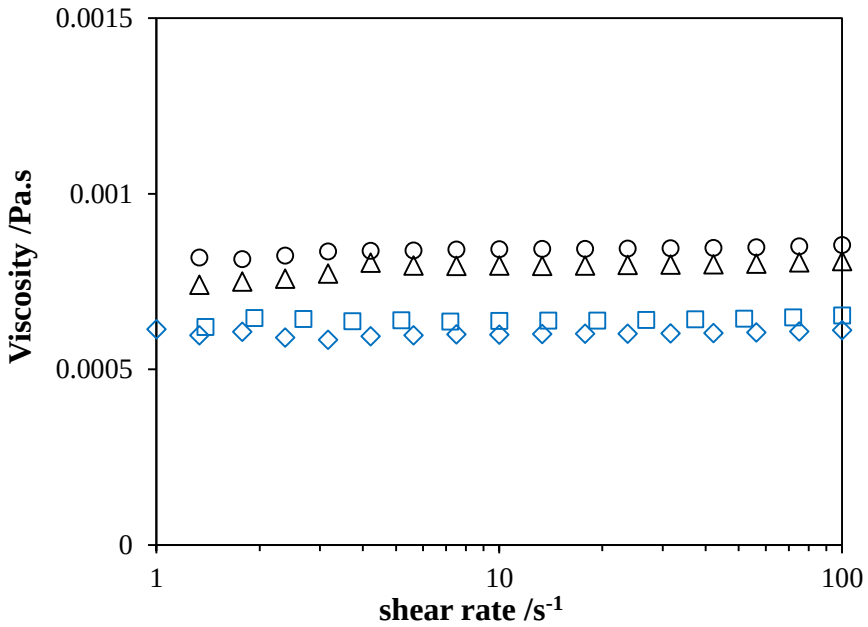

Figure 6.39: Viscosity against shear rate curves for dilute solutions (1 wt%) in toluene of 16k HPS (□), 105k HPS (○), 2k HStar (◊) and 18k DStar (Δ).

Table 6.12: Obtained η_0 values for the PS-C60 stars and linear PS 1 wt% solutions in toluene

Sample	η_0 /Pa.s
16k HPS	0.0064
105k HPS	0.0084
2k HStar	0.0059
18k DStar	0.0079

There is a slight decrease in viscosity in the star samples in 1 wt% solution compared to the pure polymer (Table 6.12). Pure polymer stars with relatively short arms measured in the literature have shown a decrease in viscosity compared to the molecular weight of the appropriate linear analogues. This is expected, as pure branched polymers have a lower radius of gyration, R_g, than linear polymers of the same molecular weight, resulting in fewer entanglements and therefore a lower viscosity[302]. Although the results in Chapter 4 showed that the R_g values of the PS-C60 stars are larger than those calculated for pure polymer stars (see Section 4.2.4 for details), the PS-C60 stars are still smaller than the equivalent linear chain (e.g. the Zimm plot obtained R_g value of 86 Å for 16k HStar in toluene is significantly smaller than the calculated R_g value of 118 Å for the equivalent linear polystyrene chain).

Therefore, the star polymers have a lower hydrodynamic volume, resulting in a reduced zero-shear viscosity, η_0 compared to linear polymers[344]. The zero-shear viscosity of linear polymers is given by the modified Mark-Houwink equation:

$$\eta_0 = K{M_w}^{\alpha} \quad \textbf{(6.23)}$$

where K and α are empirical parameters obtained from the slope and intercept of the log plot. The typical values for the α parameter depends on the molecular weight: 3.4 – 3.6 when M_w is greater than M_e, and 1 – 2.5 for M_w values less than M_e.[66] However, when the branches in branched polymers are large, i.e. far above the molecular weight of entanglement, a viscosity increase over the equivalent linear polymer chains is seen[342]. This occurs as the large branches cannot relax independently from each other due to being tethered. This results in an increase in η_0 compared to linear chains, and thus causes a change in the viscosity relationship with molecular weight: the zero-shear rate viscosity of polymer stars does not increase with a power law of the molecular weight, but rather increases exponentially[342].

In polymer stars that exhibit total molecular weight dependence of viscoelastic behaviour, such as the ultra-small arm poly(ε-capralocatone)s, this exponential power law is not observed[338]. Instead, these stars showed a linear increase with total molecular weight, as observed in unentangled linear polymers. Although there are only two molecular weight data points in our study, the change in viscosity with total molecular weight for the PS-fullerene stars in 1 wt% solution is identical to the linear PS chains measured (0.002 Pa.s), suggesting there might also be a linear dependence in PS-C60 stars. However with only two data points it is not possible to distinguish an exponential

from a linear curve. More samples with different molecular weights are required to obtain an accurate measure of the molecular weight dependence of the stars.

The higher molecular weight samples were also measured in the semi-dilute region (10 wt% solutions). The results are similar to those obtained in dilute solution: Newtonian fluid behaviour with a slight decrease in viscosity compared to the linear chain of equivalent total molecular weight.

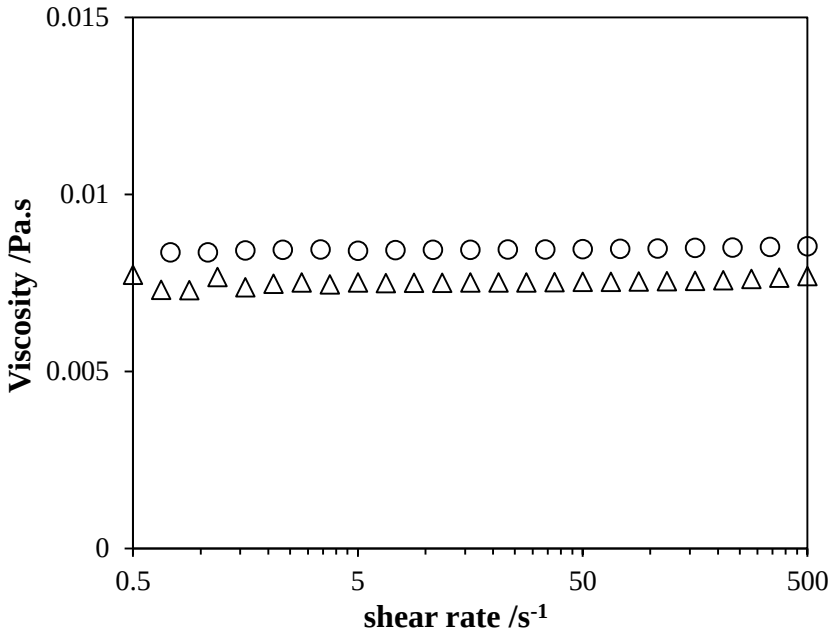

Figure 6.40: Viscosity against shear rate curves for dilute solutions (10 wt%) viscosity of 105k HPS (○) and 18k DStar (Δ).

6.3.2.2 Concentrated Solution

Concentrated solutions of PS-fullerene stars were measured on a cone and plate geometry, due to the limited amount of PS-fullerene stars available for analysis. However, measuring low viscosity solutions on a cone and plate rheometer leads to high levels of volatile solvent evaporation and results in noisy measurements. As such, only general statements on the behaviour can be made with these results.

Concentrated solutions of PS-fullerene stars show the same rheological behaviour as concentrated linear polystyrene solutions of the same total molecular weight, with decreasing viscosity with increasing shear rate until a plateau is reached at higher shear rates. The rheological behaviour of concentrated polymer solutions are dominated by polymer-polymer entanglements, leading to shear thinning behaviour.

There also appears to be no significant change in the viscosity value of the PS-fullerene chains when attached to fullerenes compared to the polymer chains close to the total molecular weight of the star. This is contradictory to what is seen in dilute solutions, where there is a small decrease in viscosity in the stars compared to the pure polymer. Due to the level of noise and potential error bars in the sample runs, it is impossible to definitively state that there is no change in viscosity due to grafting to fullerene cores. It is clear, however, that the PS-fullerene stars have the same molecular weight dependence behaviour as linear polymers.

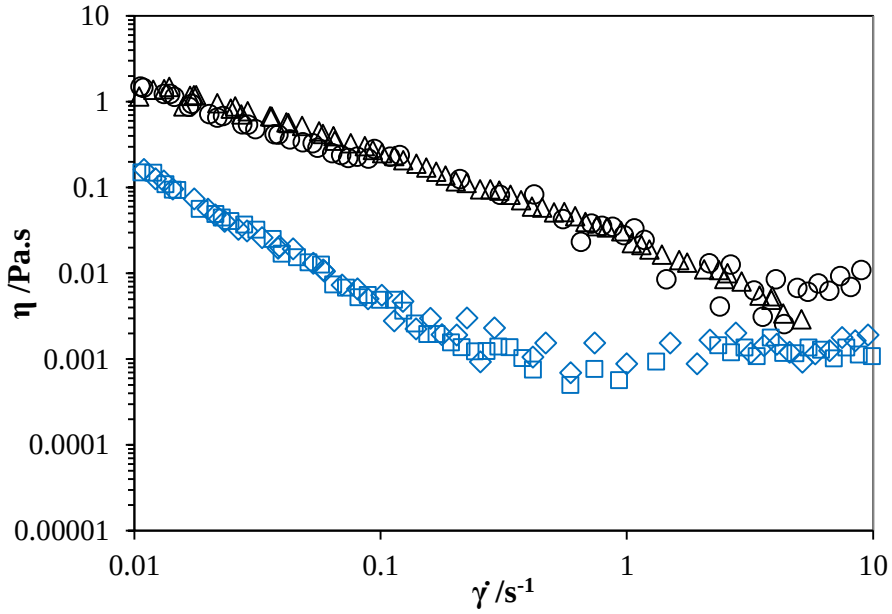

Figure 6.41: Viscosity against shear rate for concentrated (20 wt%) toluene solution for 16k HPS (□), 105k HPS (○), 2k HStar (◊) and 16k HStar (Δ).

6.4 Conclusions

6.4.1 Polymer-silica nanocomposites

The effect of silica nanoparticles on various dynamic properties of polymers was investigated by a variety of techniques. The DSC results showed that dispersing nanofillers has no significant effect on the glass transition temperature of PS, PMMA, PBA or SAN. Grafting PBA chains to the surface of silica results in a small increase in T_g. In PMMA, PS and SAN, significant increases in T_g are observed when the chains are grafted, particularly with the fumed silica. This suggests that the chain mobility is greatly decreased in the grafted samples.

DSC measurements were also used for enthalpy relaxation experiments to measure the physical ageing of polymer-silica nanocomposites. In PS and SAN-silica, the grafted samples showed a decreased ageing rate whereas the dispersed samples showed no change in ageing, which corresponds well to the glass transition measurement results. This suggests suppressed segmental motion in the grafted samples but not in the dispersed nanocomposites.

The effect of grafting and dispersing nanoparticles on the segmental motion of poly(butyl acrylate) was studied by quasi-elastic neutron scattering. Below the glass transition temperature, there is no apparent effect on motions from the presence of filler particles or by grafting polymer chains onto these particles. However, above the glass transition temperature there is a reduction of molecular motion due to grafting. This effect is even more pronounced when silica particles are dispersed into the PBA matrix. Due to our finding of little to no elastic component contribution to the change in molecular motion and lack of indication for bimodal mechanics, this effect on the molecular motion cannot be attributed purely to a fraction of slow immobile chains on the surface. This is corroborated by the lack of evidence in the glass transition temperature properties of an interfacial layer that would cause a double step transition and a drop in the heat capacity of the transition. Time-Temperature-Superposition analysis on the QENS data reveals that there is a loss of free volume in the dispersed sample compared to the pure polymer and the grafted sample, which leads to a reduction in chain mobility[132].

Rheological measurements on dispersed PBA-fumed silica samples also showed a significantly reduced free volume. This confirms that free volume effects are the likely cause of the significantly reduced chain dynamics. These samples also exhibited a reduction in the slope in the terminal zone region (from $G' \propto f^{1.5}$ to $G' \propto f^{1.0}$), which has been attributed to reduced mobility of chains around the silica nanoparticles or the formation of a percolated network. Neither a free volume increase nor a change in slope are observed in the nanocomposite samples containing colloidal silica. However, both colloidal and fumed silica greatly increase the viscosity and dynamic moduli, with fumed silica having the largest effect on the polymer matrix. The apparent increase in these two properties cannot be modelled with the conventional models, such as the Guth-Gold equation. This is due to strong polymer-particle and particle-particle interactions that greatly affect the rheological behaviour of the PBA chains.

6.4.2 Polystyrene-fullerene stars

The dynamics of PS-fullerene nanocomposites were also investigated by various techniques. The PS-fullerene stars showed unusual dynamic behaviour when compared to pure polystyrene stars. The dynamics of grafted PS-fullerene stars depend on the total molecular weight of the star, whereas the dynamic properties of typical polymer stars depend only on the molecular weight of the arm. This result was consistent across glass transition, EWS, QENS and rheological measurements. An explanation for this dynamic behaviour could be molecular coupling occurring when PS chains are grafted to fullerene; the arms of the star are dynamically identical and results in the whole star motion acting as one dynamic unit. This atypical behaviour has been seen in a small number of polymers stars with ultra-short arms in the literature[338].

There is some evidence of a decrease in absolute viscosity in the dilute solutions of PS-fullerene stars compared to linear polymers. However, the molecular weight dependence of viscosity is identical to that of linear polystyrene chains measured. Thus, grafting polymer chains to colloidal spherical fullerene particles appears to have little to no effect on either the macroscopic or microscopic dynamics of the polystyrene chains. This lack of change in the dynamics is contrary to the behaviour observed for polystyrene-fullerene dispersions in the literature, which showed either increasing[137] or decreasing[130] segmental motion upon addition of fullerenes.

Chapter 7. Preliminary structure and phase separation studies on polymer nanocomposite blends

7.1 Introduction

As detailed in Section 1.5.6, there are few systematic studies on the effects of nanofillers on polymer blends, and the results are often contradictory. Literature studies on polymer blends containing fillers have shown both increased[184] or decreased[345] phase separation temperatures compared to the pure polymer blend. Preferential segregation of the fillers into one of the polymer phases can also affect the polymer phase separation kinetics[346]. There are even fewer studies on the effect of grafting one of the polymers to the nanoparticles[195].

This chapter presents preliminary microscopy and SANS results on the effect of silica particles on two partially miscible blends: PMMA/SAN and PMMA/SCPE. The experiments are primarily on dispersed nanocomposites, with some very limited results on grafted PMMA-silica/SAN blends, as only a small amount of expensive deuterated monomer (~2 ml) required for neutron scattering measurements was available for ATRP synthesis of grafted PMMA-silica nanocomposite due to consumable funding constraints.

7.2 PMMA/SAN/silica blends

In general, studies on PMMA/SAN blends have shown increasing phase separation temperatures and improved miscibility upon addition of nanoparticles[183]. Segregation of silica nanoparticles into the PMMA phase has also been observed[191]. However, the effect of fillers on the phase behaviour of polymer blends is still not completely understood. The following sections will show the results of glass transition measurements, preliminary microscopy and SANS experiments for PMMA/SAN blends with and without silica nanoparticles.

7.2.1 Glass transition temperature measurements

Although glass transition measurements are a common method of determining miscibility in polymer blends, the glass transition temperatures of atactic PMMA and SAN have similar values (within 20 ^{o}C). Therefore, it is likely that DSC measurements will not fully resolve the glass transition of the blend to determine if there are two

overlapping transitions or a single broad transition, an effect that has been seen previously in the literature for this blend[347]. However, due to the use of different tactic forms of PMMA, which have different T_g values, and the effect of grafting on the T_g of PMMA (see Section 5.2.1.1), preliminary DSC measurements on the components and selected blends were carried out to determine if DSC is a viable technique for determining miscibility in PMMA/SAN blends containing silica nanoparticles. The results are shown in Table 7.1.

Glass transition measurements were carried out on the pure polymers and one blend before and after phase separation. However, the glass transition temperatures of all of the pure polymer components are too similar, and only a single glass transition is seen in the blend regardless of whether it is one or two phase mixture. The phase separated sample has an increased T_g and a smaller range (i.e. smaller width of the transition) compared to the initial one phase blend, whereas we would expect a broadening due to two overlapping glass transitions. Therefore it is not possible to use DSC measurements to determine miscibility of the PMMA/SAN blends. Other measurements, such as microscopy and neutron scattering, are required to determine the miscibility of PMMA/SAN blends.

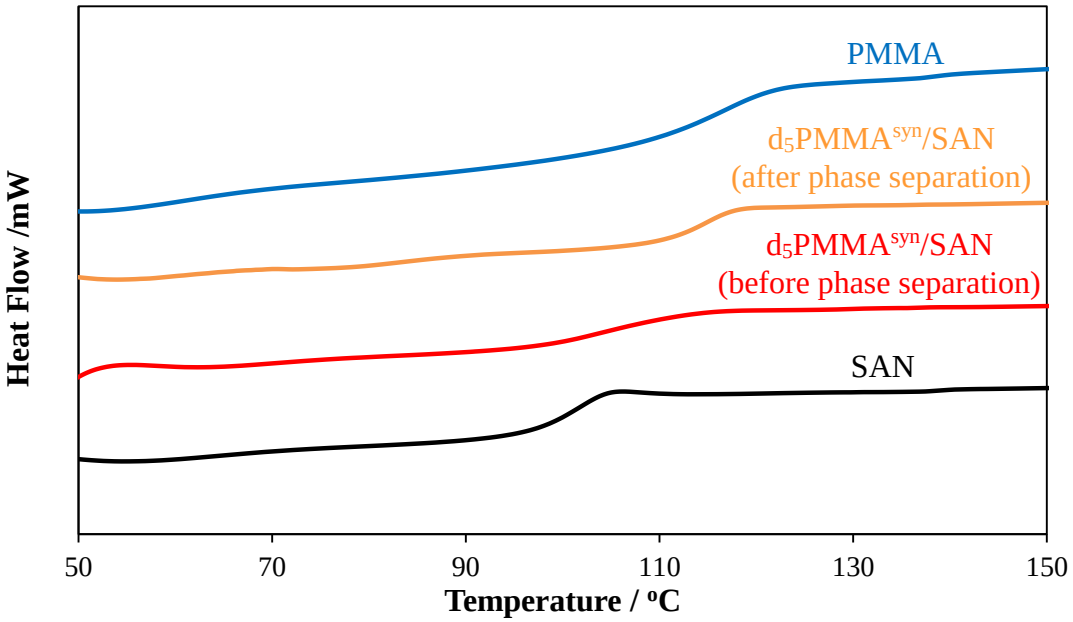

Figure 7.1: DSC traces of PMMA, SAN and the d_5PMMA^{syn}/SAN 30/70 blend before and after phase separation. The curves have been shifted vertically for clarity.

Table 7.1: Glass transition temperatures of pure polymers and blends

Polymer	M_w /g mol^{-1}	T_g /ºC	Range /ºC	ΔC_p /J g^{-1} ºC^{-1}
hPMMA	90,000	117.9	13.8	0.373
d_5PMMA^{syn} [ref [348]]	250,000	107.0	-	-
Grafted-d_8PMMA 17.3 MEK-ST	-	107.8	12.0	0.241
SAN	68,600	101.4	5.9	0.369
Grafted-d_8PMMA/SAN 30/70		99.5	8.7	0.308
d_5PMMA^{syn}/SAN 30/70		104.2	12.0	0.290
d_5PMMA^{syn}/SAN 30/70 (two phase)		112.3	7.5	0.287

Notation: ##.# = wt % of silica measured by elemental analysis, syn = syndiotactic. Unless otherwise stated, the PMMA samples are atactic.

7.2.2 Optical Microscopy measurements

Optical microscopy was used to probe the phase separation temperature of the PMMA/SAN blends with and without colloidal silica. The samples were heated at a slow, controlled rate (1 ºC/min) and observed until the blend visibly phase separated or dewetted from the substrate. Dewetting is an undesirable process where the homogeneous thin polymer film becomes unstable and breaks into small droplets on the surface of the substrate. Dewetting commonly occurs upon heating of the film, and thus may affect the observation of phase separation using optical microscopy.

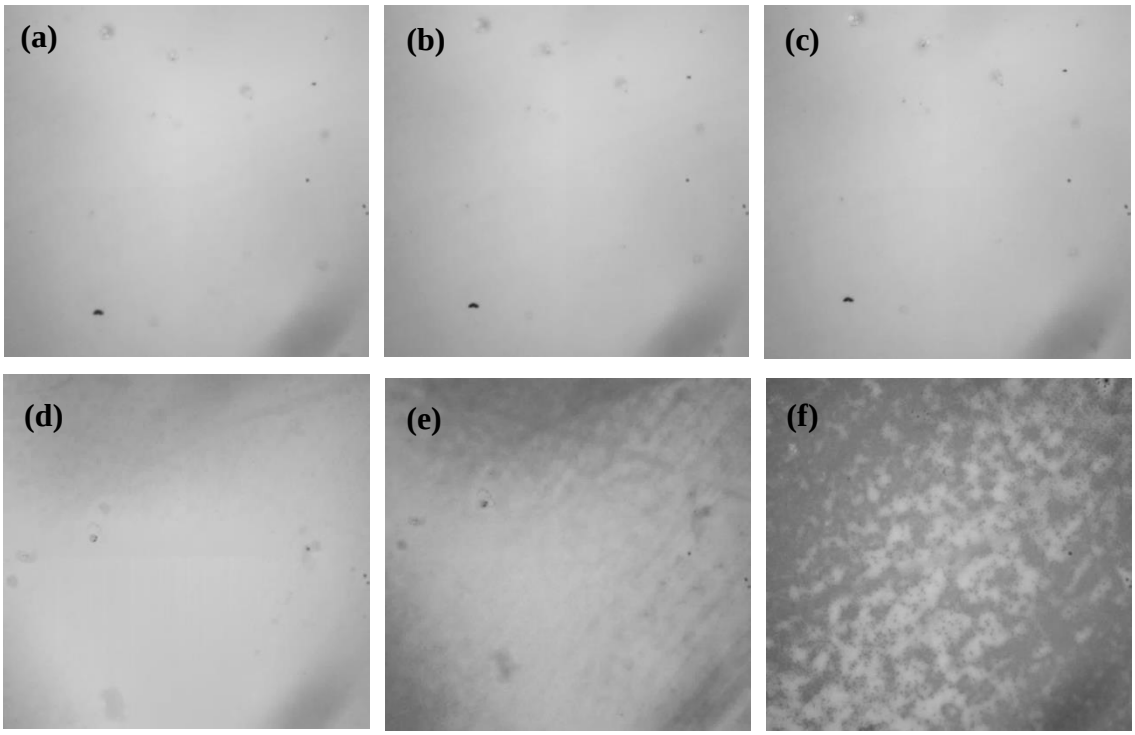

Figure 7.2: Optical Microscopy images of PMMA/SAN 50/50 at (a) 20ºC, (b) 120ºC, (c) 200 ºC, (d) 230 ºC, (e) 250ºC and (f) 262 ºC. Initial phase separation can be observed at 230 ºC and the blend is fully separated and dewetted at 262 ºC.

The temperature of phase separation for PMMA/SAN blends depends heavily on the % acrylonitrile (AN) present in the SAN copolymer. Previous studies[188] have shown that PMMA/SAN blends are only miscible when AN content is between 9 and 34%. This effect is known as a miscibility window. Additionally, an AN content of between 10 to 26 wt% results in a polymer phase separation temperature that is potentially higher than the decomposition temperature of the two polymers. This resulted in being unable to observe phase separation before the samples decomposed. The SAN copolymer used in our experiments contained 26 wt% AN, which resulted in a phase separation temperature in PMMA/SAN (50/50) of approximately 230 ^{o}C (Figure 7.2).

Additionally, various studies on PMMA/SAN blends have observed dewetting occurring on a similar time scale to phase separation in ultrathin films[190, 349, 350]. When the polymer blend film dewets from the substrate into droplets, phase separation can more rapidly occur within these droplets. This interplay of dewetting and phase separation mechanisms has generally only been observed in films with a thickness lower than ~50 nm.[349] However, the temperatures required for phase separation of the blend studied is significantly lower (~175 ^{o}C). The higher temperatures reached in this experiment caused dewetting as the blend phase separated, as observed in the microscopy image at 250 ^{o}C. Full phase separation and dewetting of the film from the silica substrate is observed in the pure blend at 262 ^{o}C.

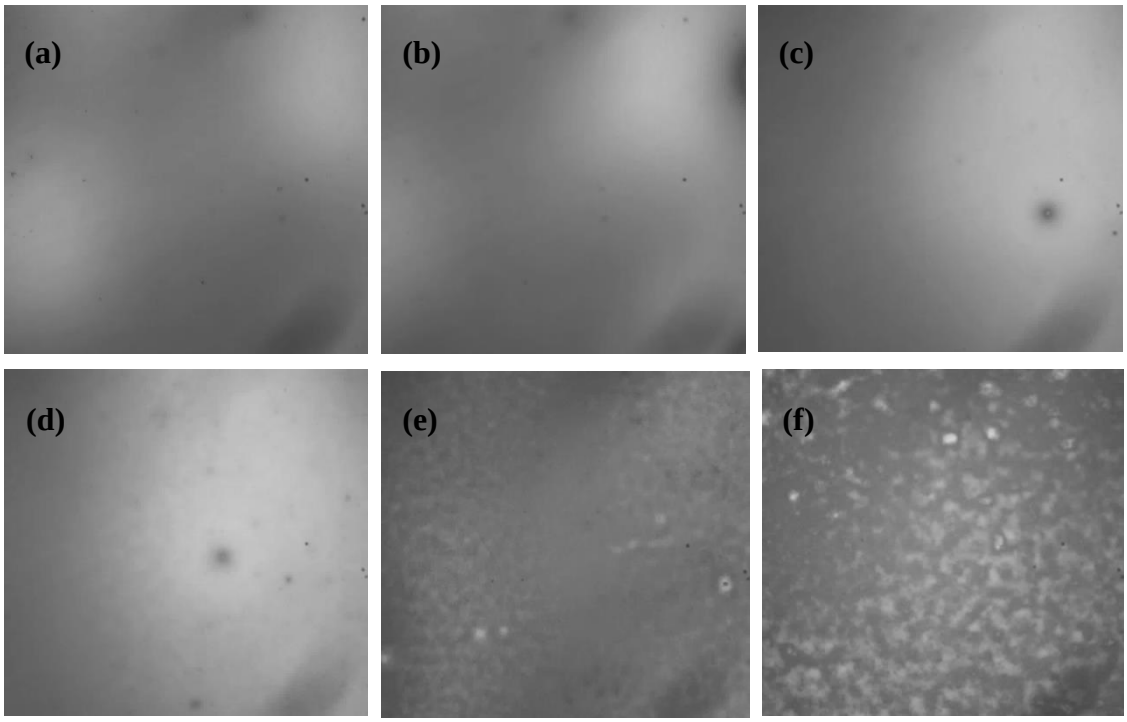

Figure 7.3: Optical Microscopy images of PMMA/SAN/MEK-ST 50/50/1 at (a) 20^{o}C, (b) 120^{o}C, (c) 200 ^{o}C, (d) 250^{o}C, (e) 270 ^{o}C and (f) 295 ^{o}C. Phase separation occurs at 250 ^{o}C and full phase separation and dewetting occurs at temperatures > 270 ^{o}C.

Upon addition of 1 wt% MEK-ST silica, both phase separation and dewetting temperatures are affected (Figure 7.3). The PMMA/SAN/MEK-ST (50/50/1) blend sample starts to phase separate at 250 ^{o}C, 20 ^{o}C higher than the observed phase separation in the blend without nanoparticles. Full phase separation and dewetting behaviour occurs at temperatures $\geq$ 270 ^{o}C. A similar increase in phase separation temperature has been observed in the literature for PMMA/SAN blends containing 3% silica nanoparticles[183].

Potential explanations for the increase in phase separation temperature include the formation of a surface layer around the nanoparticles due to the formation of hydrogen bonds between the silica and PMMA. This results in a loss of entropy and a significant change in the effective composition of the polymer blend, thereby leading to an increase in phase separation temperature[197]. A study on the effect of silica on the kinetics of phase separation of PMMA/SAN also found that domain growth and the kinetics of demixing were slowed down by the presence of silica nanoparticles[191], affecting the observed phase separation temperatures.

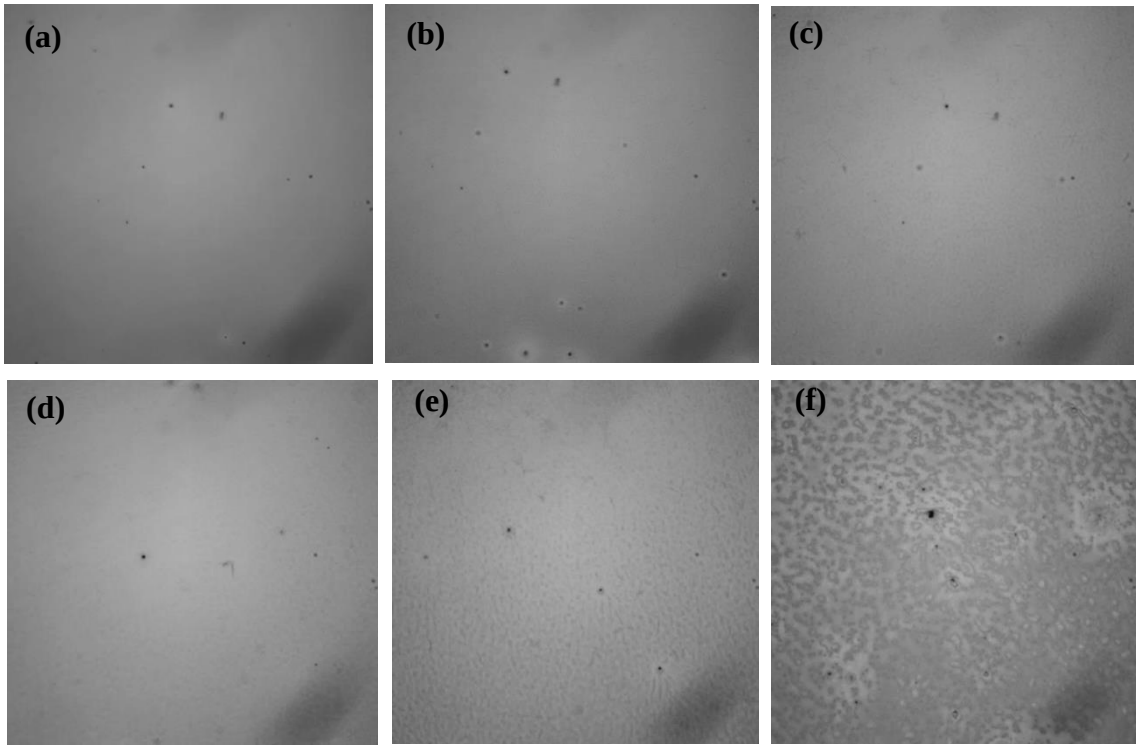

Figure 7.4: Images of PMMA/SAN/MEK-ST 50/50/5 at (a) 20^{o}C, (b) 200 ^{o}C, (c) 220^{o}C, (d) 240 ^{o}C, (e) 255 ^{o}C and (f) 270 ^{o}C. Phase separation occurs at 220 ^{o}C and full phase separation and dewetting occurs at 270 ^{o}C.

The literature on the effect of spherical nanoparticles on PMMA/SAN blends has generally shown an increase in phase separation temperature. However, when a

higher loading of silica was added to the same PMMA/SAN blend (5 wt%), the phase separation temperature of the film decreased significantly (Figure 7.4). The thin film starts to phase separate at ~220 ^{o}C, a 10 ^{o}C decrease compared to the pure blend. The film is also significantly dewetted at 270 ^{o}C, and the dewetting effect is greater than in either the pure blend or the 1 wt% silica blend at a similar temperature.

The loading of nanoparticles used in the polymer blend is therefore an important factor in the phase separation behaviour. Decreased phase separation temperatures have been observed in other polymer blends based on filler concentration. For example, in a PVA/PMMA blend with Aerosil fumed silica, the opposite effect has been observed: decreased phase separation temperature at low silica content, increased phase separation at high silica concentration[345]. The authors posited that the effect was due to diminishing polymer-silica interactions.

It is currently uncertain why the addition of a higher loading of silica decreases the phase separation temperature in this study. Additional investigations using more blends with different silica concentrations and polymer blend compositions are therefore required to fully understand the unusual result obtained from this experiment.

Two grafted-PMMA/SAN blends were also investigated using optical microscopy. However, the samples were significantly dewetted before heating (Figure 7.5), greatly affecting the microscopy measurements, and the second sample (30/70/5) also appears phase separated and inhomogeneous (Figure 7.6). AFM measurements (Appendix C) on these samples confirm that the grafted-PMMA MEK-ST 30/70/2 sample is homogeneous and thus a one phase blend. Whilst some further dewetting occurs at 270 ^{o}C in the 30/70/2 composition, it is impossible to determine visually whether or not the sample is also phase separating.

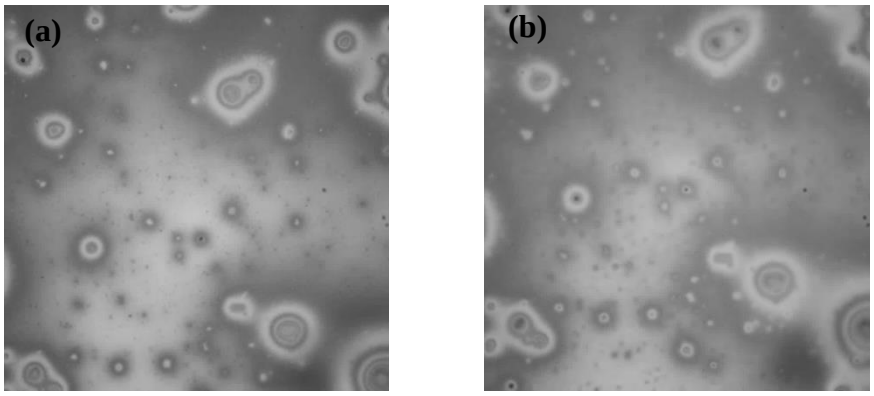

Figure 7.5: Optical microscopy images of grafted-PMMA/SAN 30/70/2 at (a) 120 ^{o}C, (b) 270 ^{o}C

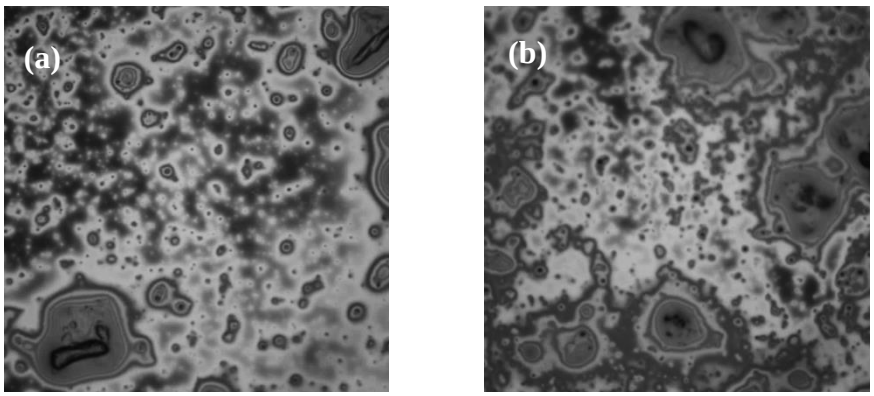

Figure 7.6: Optical microscopy images of grafted-PMMA/SAN 30/70/5 at (a) 100 ºC and (b) 270 ºC showing the films are significantly dewetted.

7.2.3 SANS measurements

SANS measurements on various PMMA/SAN blends (Table 7.2) were carried out using SANS2D (ISIS). The samples were measured at temperatures between 120 and 160 ºC.

Table 7.2: PMMA/SAN blend composition for SANS measurements

Blend	**Composition**	
d_8PMMA/SAN/MEK-ST		30/70/1
d_5PMMA^{syn}/SAN/MEK-ST	30/70/0	30/70/5
Grafted-d_8PMMA 17.3 MEK-ST/SAN		30/70/5

Notation: $d_{\#}$ = number of deuterium atoms, syn = syndiotactic, Unless otherwise stated, the PMMA samples are atactic.

7.2.3.1 Background subtraction

For polymer blends, the background is subtracted by taking a proportion by volume fraction of the hydrogenated and deuterated polymer component background scattering. The incoherent background was calculated from the measured deuterated PMMA background by taking the average of the constant plateau value reached at high *Q* (see Section 2.3.2). This method is suitable for the data from the SANS2D instrument due to the large *Q* range used in the experiment (0.004 to 1.8 Å^{-1}), as a constant plateau is reached in the high *Q* range of all the blends measured. An example of the incoherent background of d_5PMMA^{iso} at a given temperature measured is shown in Figure 7.7.

The pure hydrogenated polymer is considered to be entirely incoherent due to the large amount of hydrogen atoms in the polymer. Normally, a background sample of the hydrogenated polymer would be measured at the same time as the blend sample and

then directly subtracted from the blend scattering. However, the SAN polymer background was not measured due to limited beam time. The background for the hydrogenated polymer was therefore calculated using a weighted proportion of a hydrogenated polystyrene background used in Chapter 5 to account for the 26% of AN present in the copolymer.

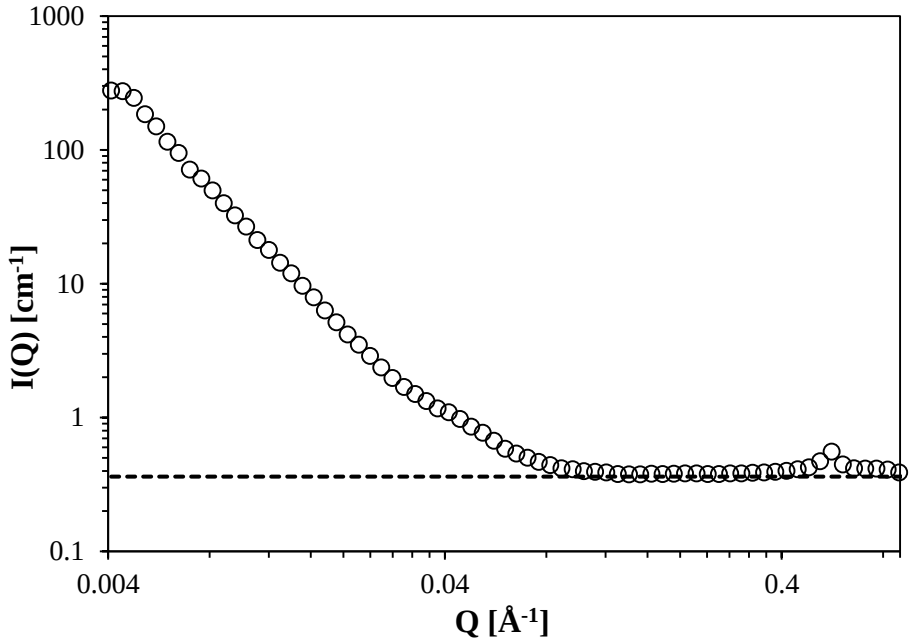

Figure 7.7: Example of incoherent background calculation (dashed line) on d_5^{iso}PMMA at 25 °C. The additional scattered intensity is due to coherent scattering from the deuterium atoms present.

Figure 7.8 shows an example of the different components of the background subtraction in the PMMA/SAN blend samples, with the calculated incoherent backgrounds from the pure polymer components (dashed lines). In all the blend samples measured, a high level of additional forward scattering is seen at low Q (<0.01 Å^{-1}) that cannot be modelled with an RPA fit. Therefore, for the preliminary analysis of these polymer blends, an additional Porod scattering background was also subtracted to remove this extraneous scattering (dotted line).

The inset graph of Figure 7.8 shows the coherent scattering, I_{coh}, after subtraction of the incoherent scattering from the hydrogeneous and deuterated components (□). When an additional Porod component is subtracted (○), the overall scattered intensity is affected at Q < 0.018 Å^{-1} only. This subtraction therefore eliminates the additional scattering only and allows for an easier and more accurate least squares fit of the rest of the curve.

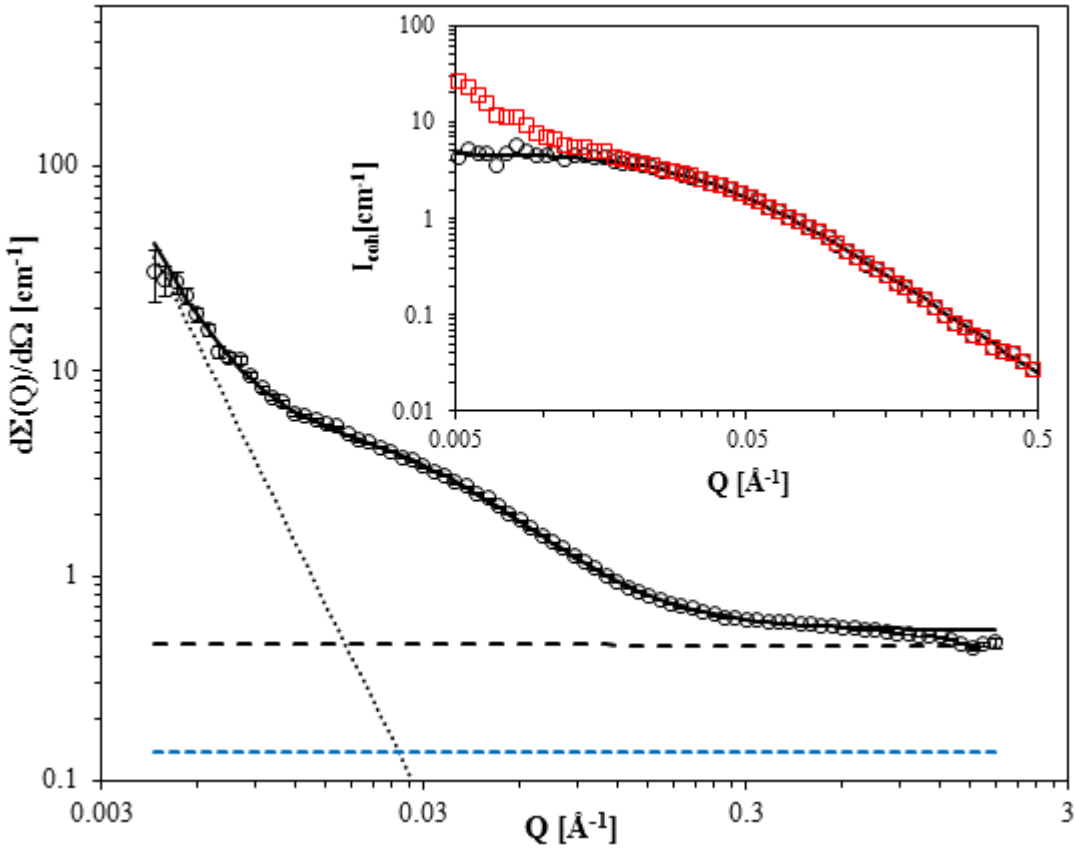

Figure 7.8: Example of the background subtraction in a PMMA/SAN blend at 120 ºC: raw data (○), the RPA fit (solid line), the volume fraction weighted hydrogenated background scattering (- - -), the volume fraction weighted deuterated background component (– – –), and a calculated additional Porod contribution (·····). The inset shows the difference between the scattered intensity when just the incoherent scattering from the polymers is subtracted (□) and when an additional Porod scattering is subtracted (○).

7.2.3.2 Random Phase Approximation analysis

The PMMA/SAN blends were measured between 120 ºC and 160 ºC, below the temperature for phase separation seen in microscopy experiments and therefore entirely in the one phase region. The data were analysed using the random phase approximation (RPA) (See Section 2.3.6 for details). Various parameters of the RPA fit were fixed using prior knowledge of the polymers: molecular weight, polydispersity, volume fractions and scattering length densities. Only the interaction parameter χ and radius of gyration were allowed to vary. An additional background coefficient is used in the fit to adjust the fixed background as the temperature increases.

The expected weight average radius of gyration values, $R_{g,w}$, for the two components within the blend were calculated using literature values[351] of mean square end-to-end distance, $\langle r^2 \rangle$, and the relationship between R_g^2 and $\langle r^2 \rangle$ (Equation 1.3). The $R_{g,w}$ value for SAN is an approximate $R_{g,w}$, calculated using an intermediate value

between polystyrene and poly(acrylonitrile). The radius of gyration was therefore only allowed to vary within reasonable limits around these calculated values during the fitting process.

The RPA fits at various temperatures for d_5PMMA^{syn}/SAN 30/70 and d_5PMMA^{syn}/SAN/MEK-ST 30/70/5 are shown in Figure 7.9 and Figure 7.10 respectively. The RPA models the data well up to Q = 0.5 Å^{-1}. Although the data appear to be reaching a plateau at this value, the scattered intensity starts to decreases again, reaching a shallow minimum and then starting to increase again. An attempt to model this decrease with the RPA analysis results in a poor fit for the rest of the scattered curve. It is uncertain whether the decrease is due to an instrument or detector error during the experiment, or a real effect in the sample. Therefore, the decrease at high Q was ignored in preliminary analysis and fits only applied at Q < 0.5 Å^{-1}.

The calculated and experimental $R_{g,w}$ and χ parameters obtained for each temperature are listed in Table 7.3. The χ parameter for the pure blend is between -0.010 – 0.14, which is consistent with the literature value of -0.01 for an atactic PMMA/SAN blend[352]. The error in the χ parameter is determined from the experimental error in measured blend composition and I(Q).

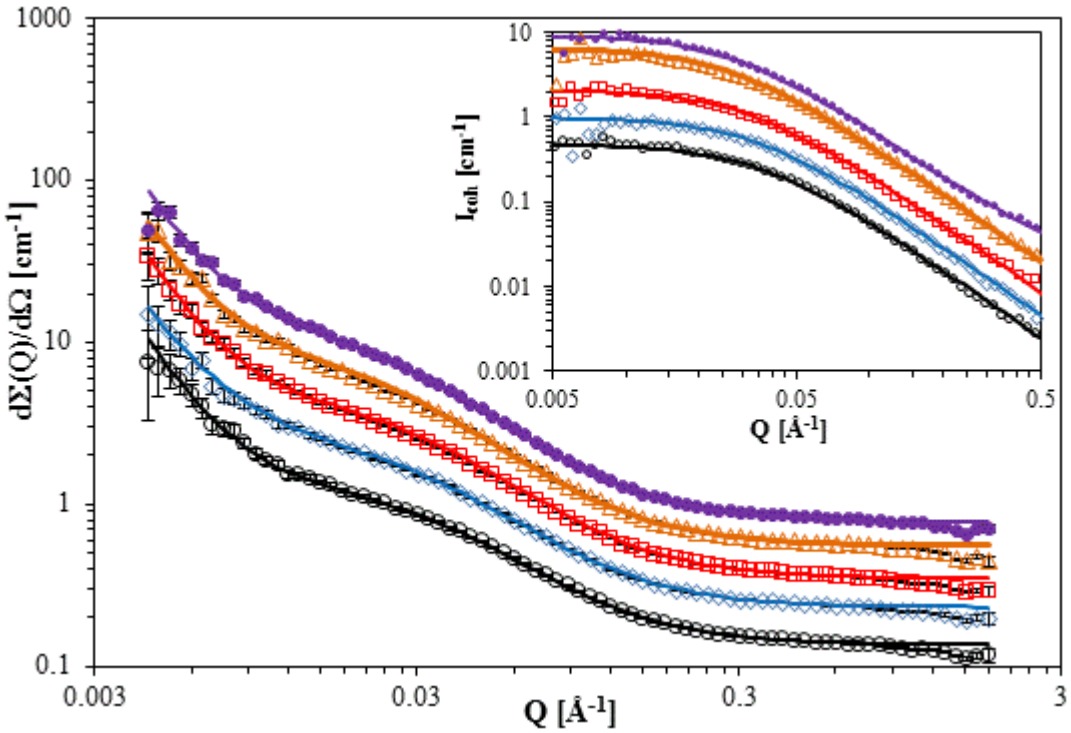

Figure 7.9: Experimental data and RPA fits (solid lines) of d_5PMMA^{syn}/SAN 30/70 at 120 ºC (o), 130 ºC (◊), 140 ºC (□), 150 ºC (Δ), and 160 ºC (●). Curves have been shifted vertically for clarity. Inset: RPA fit of the coherent scattering only, with all background scattering subtracted.

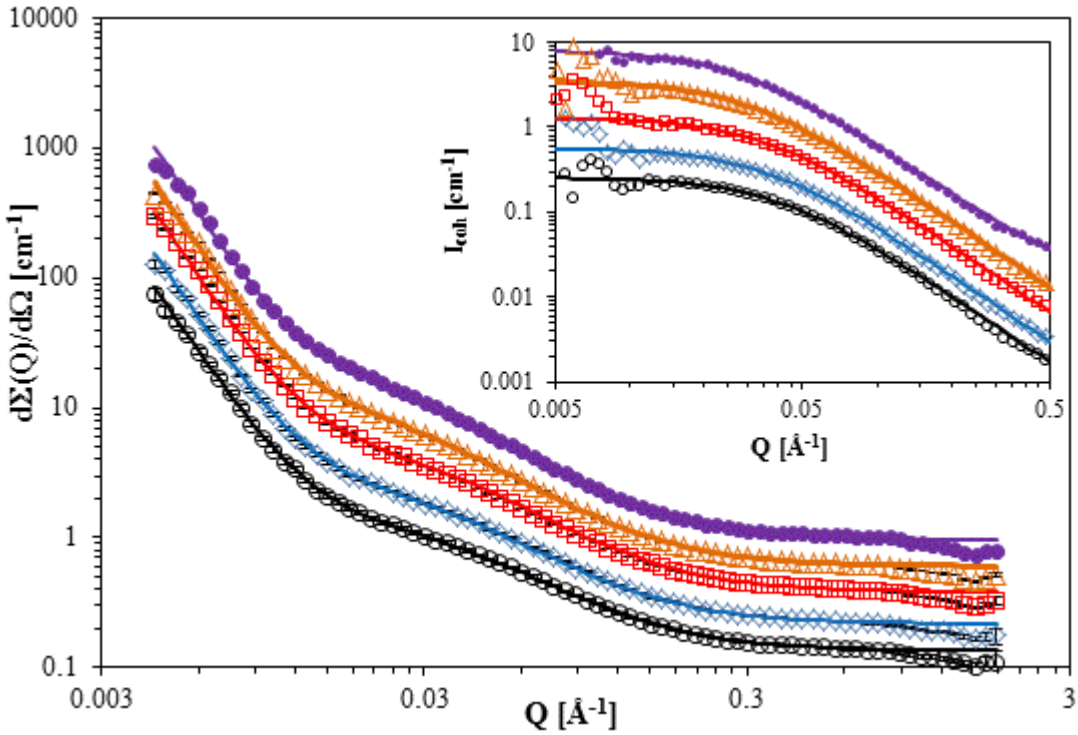

Figure 7.10: Experimental data and RPA fits (solid lines) of d_5PMMA^{syn}/SAN/MEK-ST 30/70/5 at 120 ºC (o), 130 ºC (◊), 140 ºC (□), 150 ºC (Δ), and 160 ºC (●). Curves have been shifted vertically for clarity. Inset: RPA fit of the coherent scattering only, with all background and silica scattering subtracted.

Table 7.3: RPA fitting parameters for PMMA/SAN blends with and without silica.

Blend	T /ºC	Calc. $R_{g,w}$ /Å		Exp. $R_{g,w}$ /Å		χ
		H	D	H	D	
d_5PMMA^{syn}/SAN	120			87	149	-0.0135 ± 0.0021
30/70	130			86	157	-0.0128 ± 0.0021
	140	85	138	84	167	-0.0121 ± 0.0017
	150			88	198	-0.0115 ± 0.0016
	160			87	184	-0.0107± 0.0014
d_5PMMA^{syn}/SAN/MEK-ST	120			81	124	-0.0125 ± 0.0012
30/70/5	130			84	133	-0.0110 ± 0.0011
	140	85	138	84	125	-0.0094 ± 0.0008
	150			84	150	-0.0087 ± 0.0008
	160			86	149	-0.0074 ± 0.0007

The $R_{g,w}$ values obtained are consistent with the calculated values, with a general trend of increasing $R_{g,w}$ with increasing temperature. The $R_{g,w}$ values of the two polymer components are correlated[101], but the least squares analysis allows them to vary independently, leading to the non-systematic increase seen. The $R_{g,w}$ values obtained for

the blend containing nanoparticles are consistently lower than those obtained for the pure polymer blend.

The temperature dependence of χ for the blend with and without silica nanoparticles was then determined by producing plots of χ against $1/T$ (Figure 7.11). The addition of 5 wt% silica results in a slight increase in χ across the experimental temperature range. This could be due to slight changes in the scattering that are not subtracted with a simple silica background subtraction, or the silica destabilising the mixed polymer blend. A linear fit of the data according to the adjusted Flory-Huggins theory gives the following temperature dependences:

$$\chi(\mathrm{T})_{\mathrm{PMMA/SAN}} = 0.0028\ (\pm 0.0006) - \frac{1.29 \pm 0.082}{\mathrm{T}}$$

$$\chi(\mathrm{T})_{\mathrm{PMMA/SAN/MEK-ST}} = 0.0076\ (\pm 0.0007) - \frac{2.41(\pm 0.103)}{\mathrm{T}} \qquad \textbf{(7.1)}$$

The thermodynamic stability of the blend decreases more rapidly with increasing temperature than the pure d_5PMMA^{syn}/SAN blend, therefore leading to the decreased phase separation temperature observed in the optical microscopy measurements for the same blend. A similar PMMA/SAN blend containing 5 wt% fumed silica in the literature exhibited a decrease in χ compared to the blend without silica nanoparticles and therefore an increase in phase separation temperature and miscibility[353].

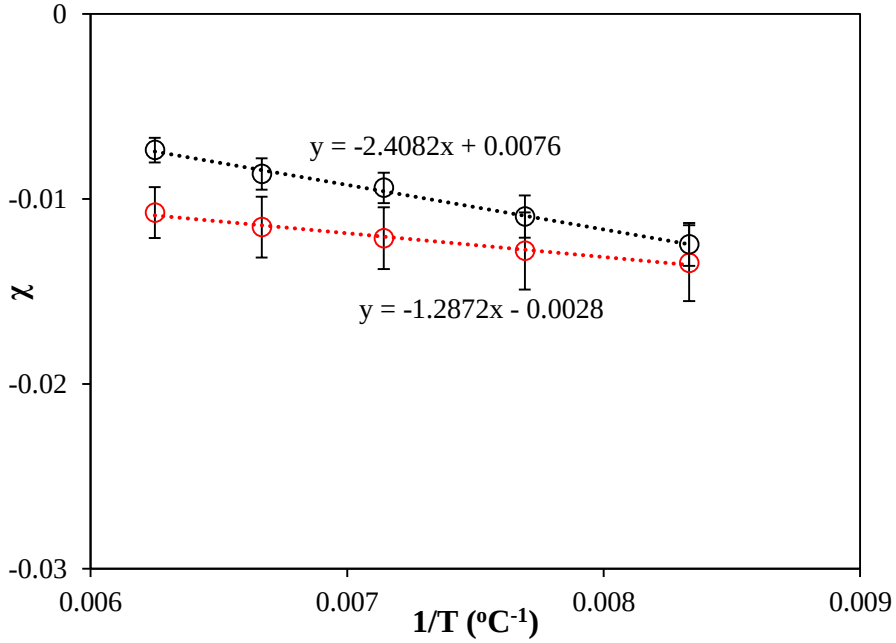

Figure 7.11: Temperature dependence of χ for d_5PMMA^{syn}/SAN 30/70 (O) and d_5PMMA^{syn}/SAN/MEK-ST 30/70/5 (□). The dotted lines were obtained by linear fits of the data.

A grafted d_8-PMMA-MEK-ST/SAN blend was also measured, however currently there is no suitable model for the $P_D(Q)$ in RPA Equation 2.69, i.e. there is currently no model of the scattering from the grafted-d_8-PMMA-MEK-ST component from the analysis in Chapter 5. Although the data of grafted samples were analysed in Chapter 5, a suitable model was not found for samples in the bulk that exhibit a shoulder peak in the scattered intensity. There is a clear double step in scattered intensity of the blend in the low to intermediate Q range ($0.01 < Q < 0.05$ Å^{-1}). An attempt was made to fit the data with the RPA equation used for the linear polymers (Figure 7.12) using the calculated $R_{g,w}$ values and a variable χ. The double step cannot be modelled using this fit, and fitting either step on its own results in a poor fit.

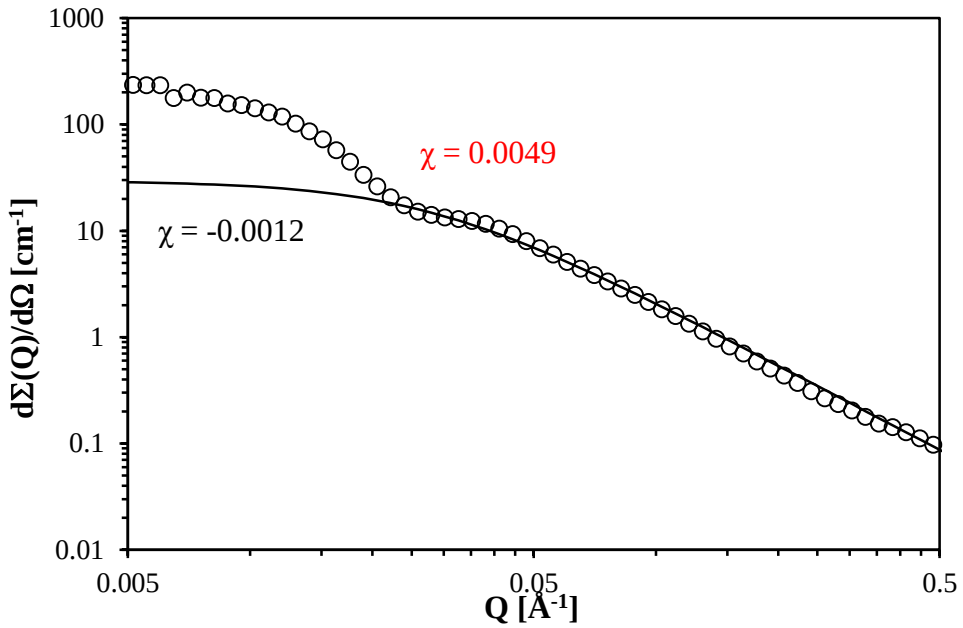

Figure 7.12: Coherent scattering from grafted-d_8-PMMA-MEK-ST/SAN after subtraction of incoherent background. The lines show two attempted RPA fits, with fixed R_g and variable χ only.

The various components of the blend and a comparison of the scattering from a blend made with grafted d_8-PMMA-MEK-ST and non-grafted d_8-PMMA and MEK-ST are shown in Figure 7.13. Qualitatively, the scattering at $Q > 0.05$ Å^{-1} is similar to that of the dispersed sample. The additional scattering at low Q may be at least partially due to the same interparticle correlations that cause the large shoulder peak in the grafted d_8-PMMA-MEK-ST sample. Furthermore, multiple "bumps" in this scattering curve are potentially indicative of partial sphere or core-shell scattering present in the grafted nanocomposite when blended with another polymer. Further analysis and measurements on grafted samples are required to understand the cause of the formation of these peaks in the scattered intensity.

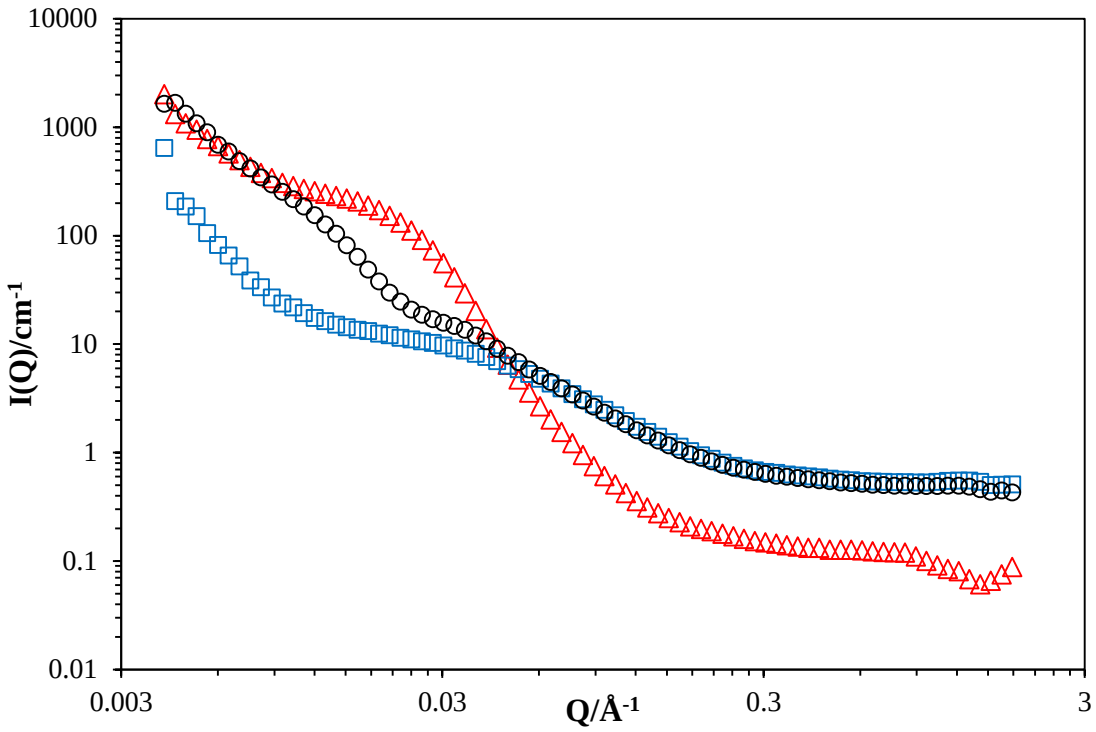

Figure 7.13: Comparison of scattered intensity of grafted-d_8-PMMA-MEK-ST/SAN 30/70/5 (○), d_8-PMMA-MEK-ST/SAN 30/70/1 (□) and grafted-d_8-PMMA-MEK-ST (Δ) at 120 °C.

7.3 PMMA/SCPE/silica blends

PMMA/SCPE is a partially miscible blend, dependent on the extent of chlorination of the SCPE, that has been studied primarily by Higgins *et al.* using various neutron scattering techniques[354, 355]. Solvent-chlorinated polyethylene (SCPE) is an amorphous, randomly chlorinated analogue of poly(vinyl chloride) (PVC). Two tactic forms of PMMA were used (syndiotactic and isotactic) to study the effect of tacticity on blends with and without silica nanoparticles.

7.3.1 Glass transition measurements

Preliminary glass transition measurements were carried out on polymer blends without silica nanoparticles to determine if DSC is an appropriate technique to study the miscibility of PMMA/SCPE blends. Similarly to the PMMA/SAN samples, the use of DSC for PMMA/SCPE blends is often limited. The T_g of SCPE is highly variable depending on the percentage chlorination; Higgins *et al.* reported that while SCPE[56] (i.e. 56% chlorinated) has a T_g of 44 °C, SCPE[63] (i.e. 63% chlorinated) has a Tg of 116 °C.[355] The various tactic forms of PMMA also have different T_g values. Whilst the syndiotactic PMMA and SCPE[63] samples used in this experiment have a T_g difference of nearly 40°C, the T_g of the isotactic PMMA is within 20 °C of SCPE[63] (Table 7.4).

The ^{syn}PMMA/SCPE blend showed a sharp single transition with a lower glass transition than predicted by Flory-Fox theory (76 ^{o}C compared to calculated 89 ^{o}C, likely due to plasticisation presence effect of solvent). When the blend is fully separated, two distinct glass transitions are seen (Figure 7.14). Thus DSC is a suitable technique for determining the miscibility of atactic and syndiotactic PMMA/SCPE blends.

Table 7.4: Glass transition temperatures of pure polymers and blends

Polymer	M_w /g mol^{-1}	T_g /^{o}C	Range /^{o}C	ΔC_p / J g^{-1} ^{o}C^{-1}	T_m /^{o}C
hPMMA	90,000	117.9	13.8	0.373	-
d_5^{iso}PMMA	250,000	53.1	9.3	0.299	-
(after heating at 100 ^{o}C)		51.6	11.0		110
d_5^{syn}PMMA [ref ^{348}]	250,000	107	-	-	-
SCPE[63]	210,000	70.6	17.1	0.379	-
d_5^{iso}PMMA/SCPE 56/44		66.2	26.8	0.278	-
d_5^{iso}PMMA/SCPE 56/44		1) 58.4	9.4	0.178	-
(two phase)		2) 72.7	8.3	0.087	-
^{syn}PMMA/SCPE 50/50		76.2	8.0	0.266	-
^{syn}PMMA/SCPE 50/50		1) 64.4	7.9	0.201	-
(two phase)		2)123.1	18.5	0.155	-

Notation: syn = syndiotactic, iso = isotactic. All blend compositions are using weight fractions.

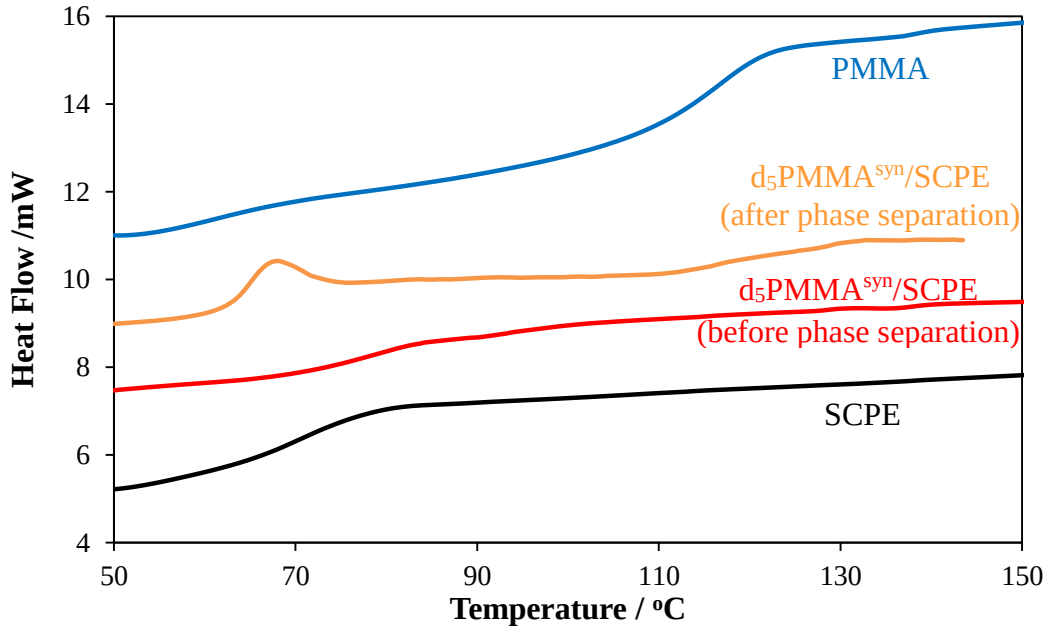

Figure 7.14: DSC traces of PMMA, SCPE and the d_5PMMA^{syn}/SCPE 50/50 blend before and after phase separation. The curves have been shifted vertically for clarity.

In the ^{iso}PMMA/SCPE blend, the one phase system shows a very broad (~27 °C) single transition, whereas the fully phase separated sample shows two mostly distinct T_gs (Figure 7.15). This suggests that the PMMA/SCPE blend may only be partially miscible when isotactic PMMA is used. However, the T_g values of the pure polymer components are only ~17-18 °C apart, thus is it difficult to definitively determine miscibility of this blend from DSC measurements.

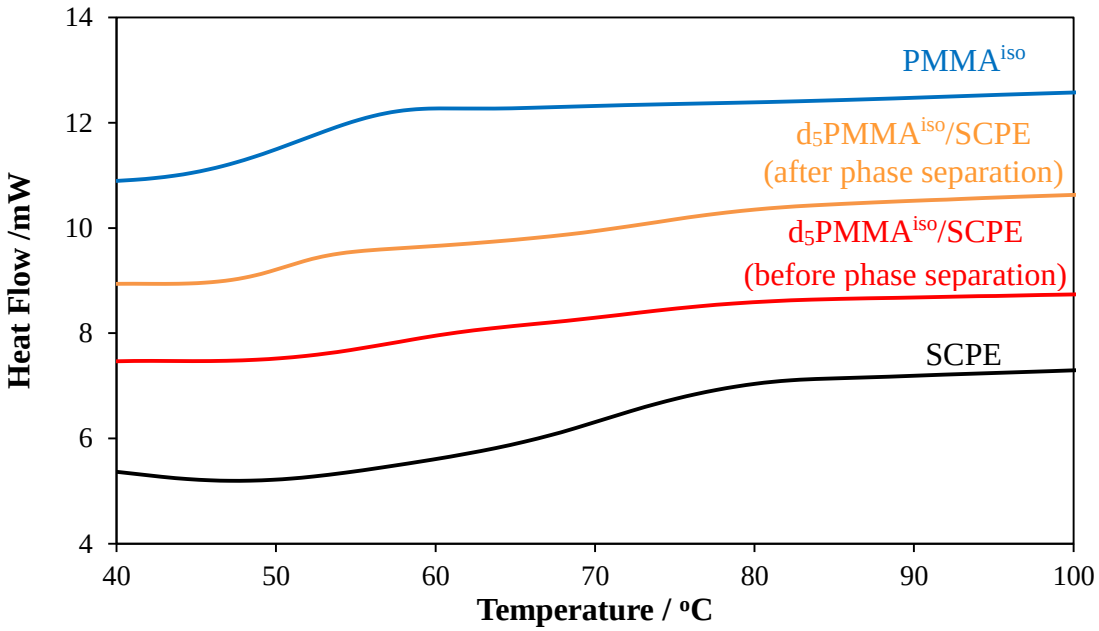

Figure 7.15: DSC traces of d_5PMMA^{iso}, SCPE and the d_5PMMA^{iso}/SCPE 56/44 blend before and after phase separation. The curves have been shifted vertically for clarity

7.3.2 Optical microscopy measurements

The PMMA/SCPE blend samples for optical microscopy were treated in the same way as the PMMA/SAN samples. The literature phase separation temperature of PMMA/SCPE is 130 – 140 °C,[348, 356] however the neutron experiments on this blends give a phase separation temperature closer to 160 °C (Section 7.3.3). It has previously been reported that PMMA/SCPE blends are optically clear even at phase separation temperatures[356]. In the optical microscopy experiments, the PMMA/SCPE film remained clear up to 270 °C, well above the phase separation temperature of the blend (Figure 7.16). This is a common problem in blends where the refractive indices of the constituent polymers are similar (<0.01 difference), leading to insufficient contrast to observe phase separation by optical measurements[101]. The microscopy images also show no apparent change in homogeneity when 1 wt% and 5 wt% colloidal MEK-ST silica is added, and the films exhibit the same optical clarity after phase separation

(Figure 7.17 and Figure 7.18). Additional AFM measurements in Appendix C show the same apparent homogeneity of the samples. It is therefore not possible to determine the effect of silica on blend miscibility using optical microscopy. However, changes in the dewetting behaviour could still be observed.

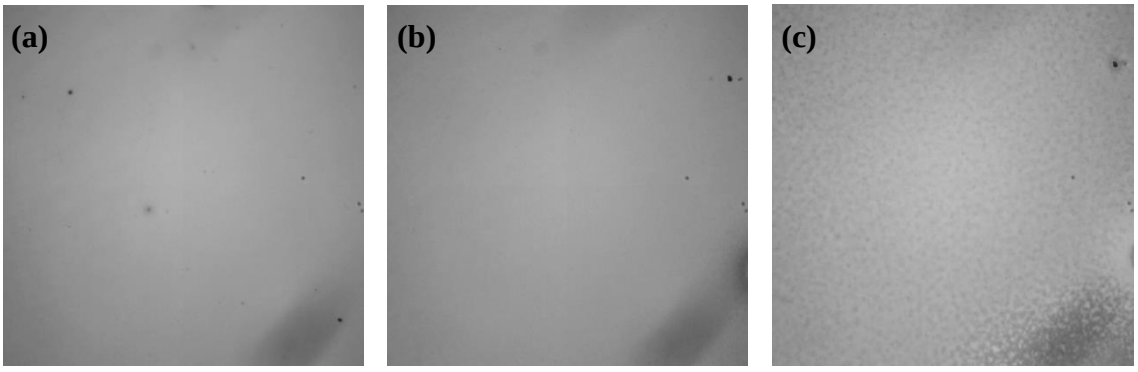

Figure 7.16: Optical microscopy images of PMMA/SCPE 50/50 at (a) 200 ºC, (b) 270 ºC and (c) 290 ºC. Dewetting of the blend can be seen at 290 ºC.

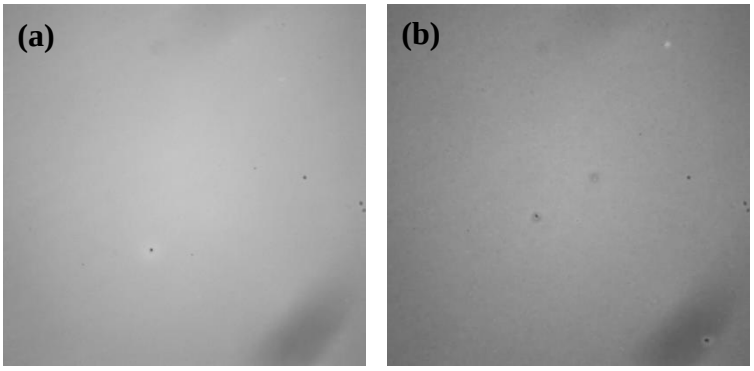

Figure 7.17: Optical microscopy images of PMMA/SCPE/MEK-ST 50/50/1 at (a) 200 ºC and (b) 290 ºC, showing little dewetting even at 290 ºC.

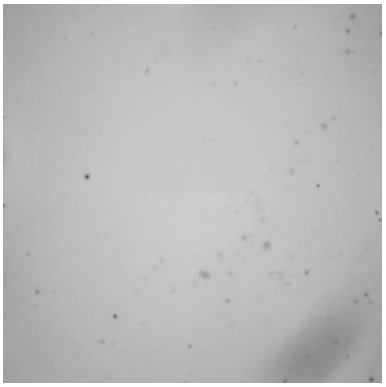

Figure 7.18: Optical microscopy image of PMMA/SCPE/MEK-ST 50/50/5 at 20 ºC.

Dewetting of the pure PMMA/SCPE blend occurred as the temperature reached 290 ºC. Upon addition of a small amount of silica nanoparticles (1 wt%), dewetting of

the thin film is suppressed, as shown by the clear difference in the morphology at 290 ^{o}C for the blend with silica nanoparticles (Figure 7.17). Suppression of dewetting in thin films upon addition of nanoparticles has been observed in the literature for pure polymer films containing nanoparticles such as PS and polybutadiene (PB) films containing fullerene nanoparticles[357].

7.3.3 SANS measurements

SANS measurements on PMMA/SCPE blends with and without silica nanoparticles were carried out in the melt on the SANS2D instrument. Two types of PMMA were used in the blends: isotactic (iso) and syndiotactic (syn). The details of the samples are given in Table 7.5. The following sections deal with the analysis of the one phase region, the two phase region and phase separation of these blends, as well as the semi-crystalline behaviour found in the d_5PMMA^{iso} sample.

Table 7.5: PMMA/SCPE blend composition for SANS measurements

Blend	Composition	
d_5PMMA^{syn}/SCPE^{63}/MEK-ST	50/50/0	50/50/1
d_5PMMA^{iso}/SCPE^{63}/MEK-ST	56/44/0	

Notation: $d_{\#}$ = number of deuterium atoms, syn = syndiotactic, iso = isotactic.

7.3.3.1 Backgrounds and incoherent background subtraction

The incoherent background scattering subtraction was carried out as described in Section 7.2.3.1., using volume fraction weighted scattered intensity from the measured or calculated hydrogenated and deuterated backgrounds. The experimentally measured backgrounds were d_5PMMA^{iso} and SCPE. Whilst d_5PMMA^{syn} was also used to make blends, due to sample and beam time constraints only the isotactic background was measured. Similarly to the PMMA/SAN blends, additional forward scattering at low *Q* values is seen in the blend samples, which may be due to scattering from voids in the sample. This scattering was subtracted using an additional Porod contribution, as shown in Figure 7.8 for PMMA/SAN blends.

Upon measuring the d_5PMMA^{iso} background, evidence of semi-crystalline behaviour was discovered (see Appendix C for detailed analysis). Polymer crystallisation can be suppressed when the polymer is blended, often due to interactions

between the polymer components such as hydrogen bonding[358]. The miscibility of a blend can also be affected by the crystallinity of the polymer, as crystallisation of one component within a miscible blend can cause phase segregation[359]. Therefore the semi-crystalline behaviour of d_5PMMA^{iso} may be an important factor in the miscibility of PMMA^{iso}/SCPE blends with and without silica nanoparticles.

7.3.3.2 PMMA^{iso}/SCPE blend

The PMMA^{iso}/SCPE blend was measured at temperatures from 25 °C to 165 °C (Figure 7.19). Qualitatively, the SANS results show that the sample is phase-separated even at low temperatures. Although the sample is clear to the eye when cast onto slides and DSC measurements showed a single broad T_g, the blend is not a one-phase mixture. The tacticity of PMMA has been shown to affect miscibility in other blends, as atactic and syndiotactic PMMA are partially miscible with PVC, but isotactic PMMA/ PVC is almost entirely immiscible[360]. However, it may be the case that the blend is partially miscible, but the process of hot pressing caused phase separation in the sample. The samples were hot pressed using the same temperature and method as the PMMA^{syn}/SCPE sample, however if the phase separation temperature is significantly lower than in PMMA^{syn}/SCPE, phase separation may have occurred during processing.

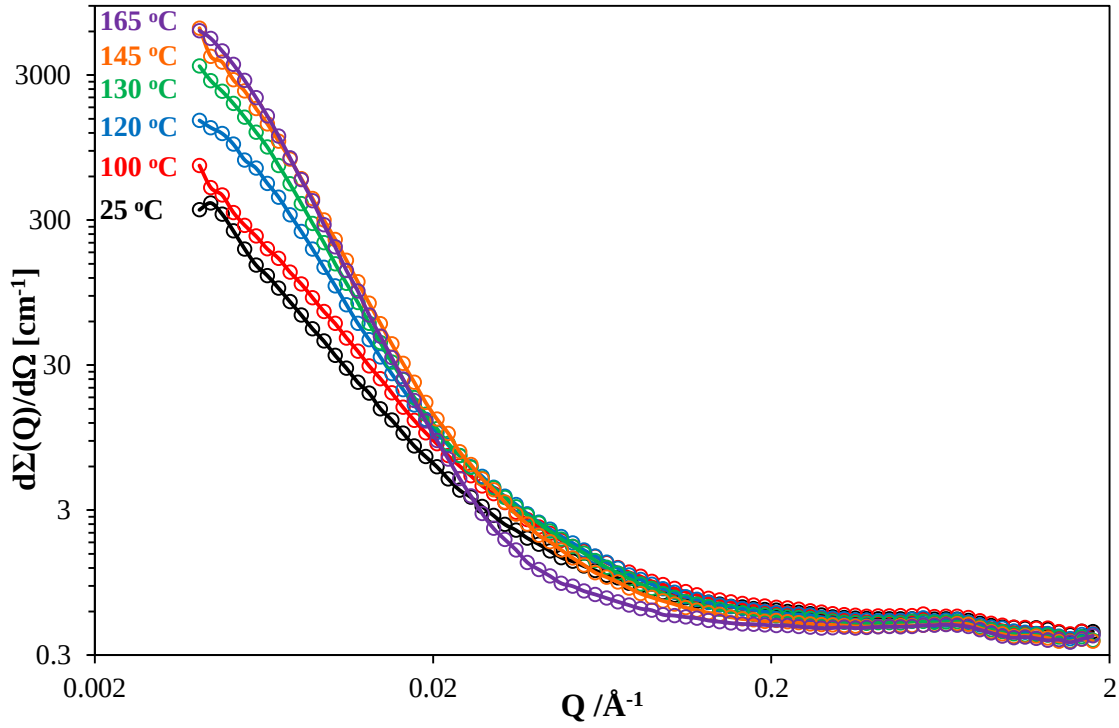

Figure 7.19: Scattered intensity of the PMMA^{iso}/SCPE 56/44 blend at temperatures ranging from 25 to 165 °C

The scattering was analysed using a simple Porod law equation for a two-phase blend. However, the Porod exponent had to be set as a variable in order to fit the data, as the slope is <4 at low temperatures. As the temperature increases, the blend phase separates more and the phase boundary sharpens leading to the expected *Q* dependence of -4. The blend system therefore obeys the Porod law at ≥ 150 ^{o}C. The Porod exponents are listed in Table 7.6.

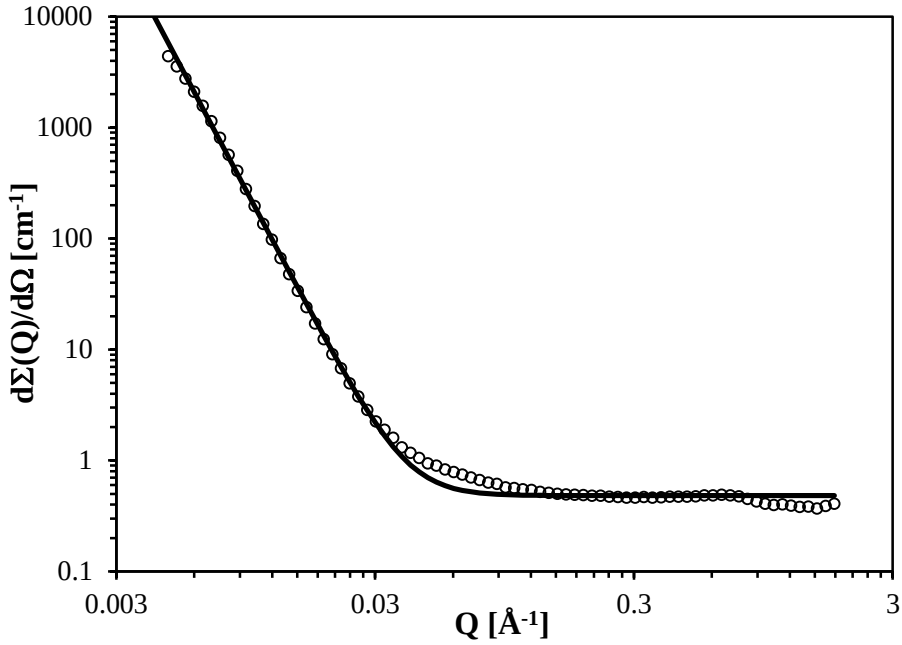

Figure 7.20: The log-log plot of PMMA^{iso}/SCPE at 165 ^{o}C showing a Porod law fit.

Table 7.6: Porod exponents for PMMA^{iso}/SCPE at different temperatures

Sample	Temperature / ^{o}C	Porod exponent
PMMA^{iso}/SCPE	25	2.80
	100	2.77
	110	2.80
	120	3.43
	130	3.86
	145	3.96
	155	4.24
	165	4.41

Despite the PMMA^{iso}/SCPE blend sample being phase separated throughout the experiment, there is no evidence of the crystallisation peak that is present in the

PMMA^{iso} background sample. There was also no evidence of a melting peak during the DSC measurements (Section 7.3.1). Therefore blending isotactic PMMA with SCPE inhibits crystallisation of the PMMA.

Although a sample of PMMA^{iso}/SCPE/MEK-ST was prepared, the immiscibility of the blend lead to the decision not to measure the sample on SANS2D and instead concentrate on the miscible PMMA^{syn}/SCPE blend.

7.3.3.3 PMMA^{syn}/SCPE blend

While the PMMA^{iso}/SCPE^{63} blend proved to be immiscible, the ^{syn}PMMA/SCPE^{63} has been shown through T_g measurements to be a fully miscible blend. Therefore, the prepared blend with 1 wt% silica was also measured to evaluate the effect of silica on the miscibility and phase separation temperature.

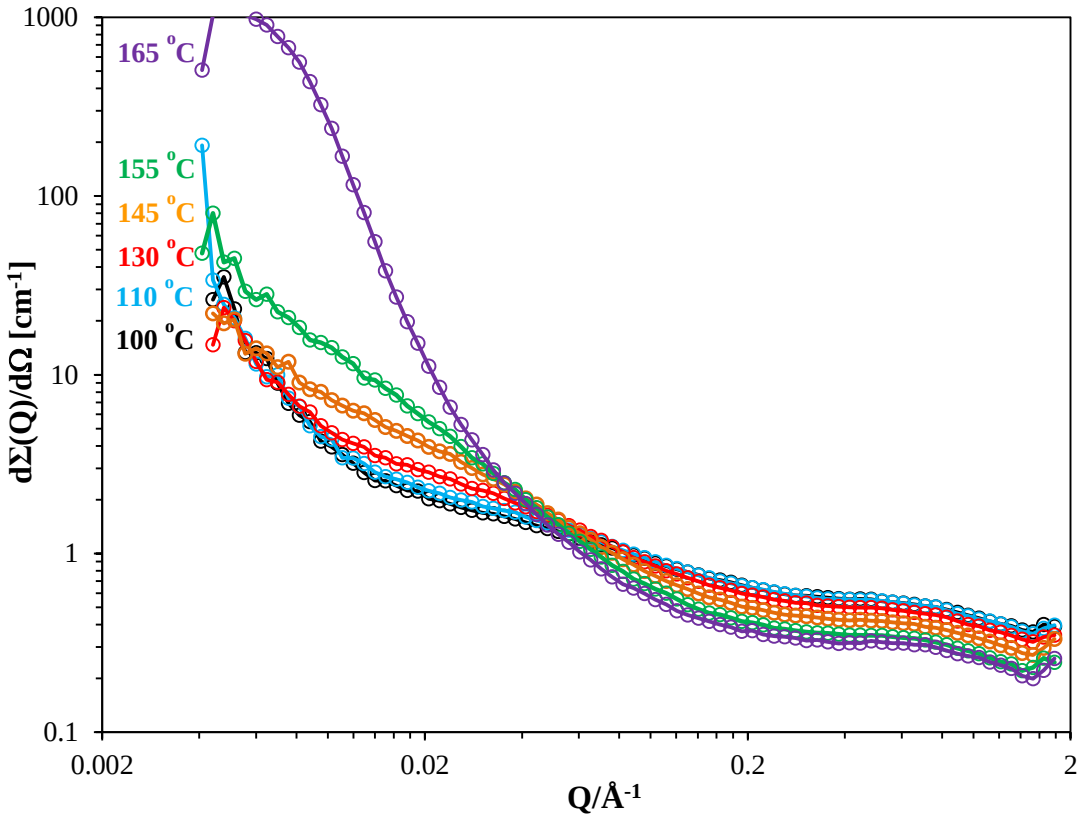

Figure 7.21: Scattered intensity for PMMA^{syn}/SCPE 50/50 blend at temperatures 100 °C to 165 °C.

Qualitatively, the sample with and without silica are quite similar. The pure PMMA^{syn}/SCPE^{63} blend, shown in Figure 7.21, phase separates between 155 and 165 °C. However, the sample containing 1 wt% silica phase separates in the region of 150 – 160 °C (Figure 7.22). Without additional evidence from microscopy measurements, it is

difficult to determine whether the phase separation temperature decreases slightly or is unchanged. If there is an effect on the phase separation temperature, it is relatively small compared to the PMMA/SAN blends (<10 ºC).

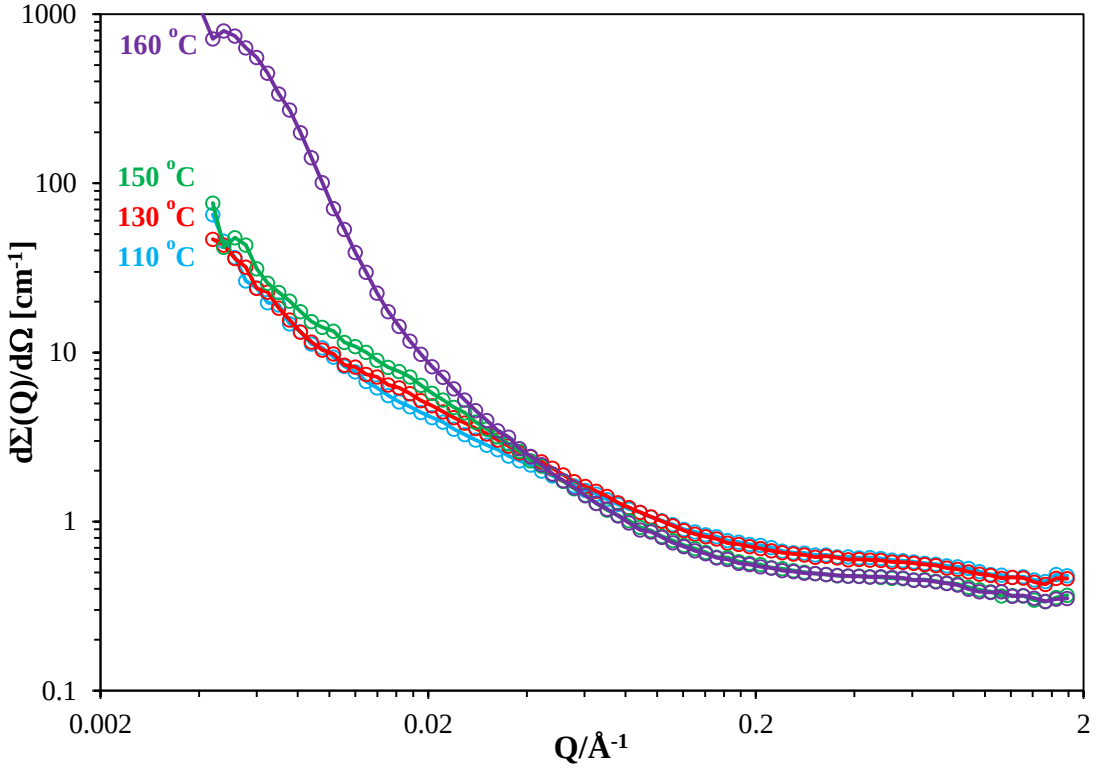

Figure 7.22: Scattered intensity for PMMA^{syn}/SCPE/MEK-ST 50/50/1 blend at temperatures 110 ºC to 160 ºC.

The data were then analysed using the RPA equation as per the PMMA/SAN blends. The RPA fits at various temperatures for d_5PMMA^{syn}/SCPE 50/50 and d_5PMMA^{syn}/SCPE/MEK-ST 50/50/1 are shown in Figure 7.23 and Figure 7.24 respectively. The RPA models the data well up to Q = 0.5 Å^{-1} for both samples.

The calculated and experimental $R_{g,w}$ and χ parameters obtained for each temperature are listed in Table 7.7. There is no literature value for $\langle r^2 \rangle$ for SCPE, therefore the value for PVC was used instead[351] to calculate an approximate expected value for $R_{g,w}$. As the χ parameter is dependent on many factors, such as composition and molecular weight, the error in the χ parameter in Table 7.7 is determined from the experimental error in blend composition, molecular weight and I(Q). The χ parameter for PMMA/SCPE is consistent with a weakly interacting LCST blend. The obtained $R_{g,w}$ values are consistent with the calculated values and showing increasing $R_{g,w}$ values with increasing temperature.

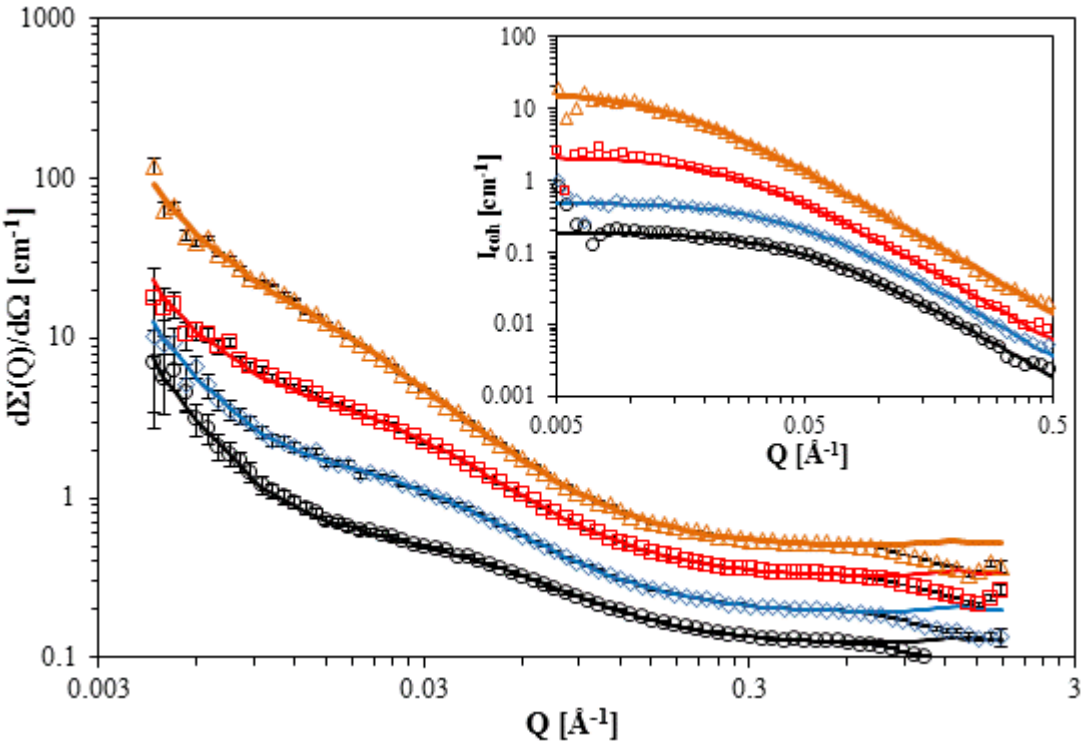

Figure 7.23: Experimental data and RPA fits (solid lines) of d_5PMMA^{syn}/SCPE 50/50 at 120 ºC (o), 130 ºC (◊), 145 ºC (□) and 155 ºC (Δ). Curves have been shifted vertically for clarity. Inset: RPA fit of the coherent scattering only, with all background incoherent scattering subtracted.

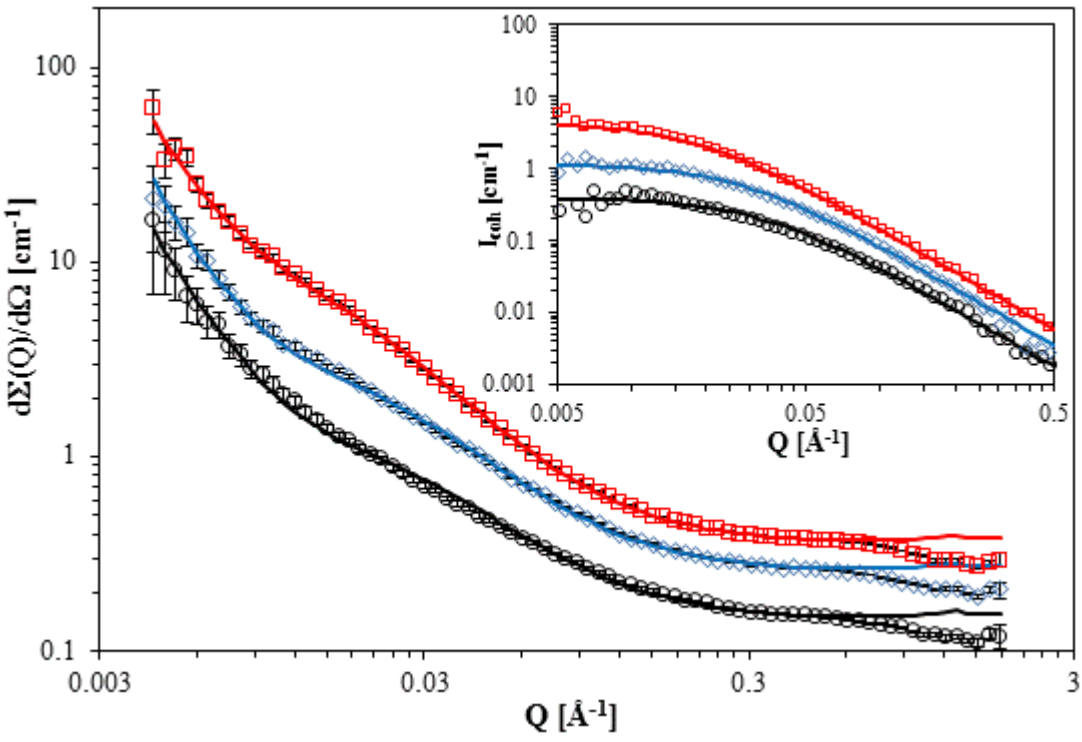

Figure 7.24: Experimental data and RPA fits (solid lines) of d_5PMMA^{syn}/SCPE/MEK-ST 50/50/1 at 110 ºC (o), 130 ºC (◊) and 150 ºC (□). Curves have been shifted vertically for clarity. Inset: RPA fit of the coherent scattering only, with all background incoherent and silica scattering subtracted.

Table 7.7: RPA fitting parameters for PMMA/SCPE blends with and without silica.

Blend	T /°C	Calc. $R_{g,w}$ /Å		Exp. $R_{g,w}$ /Å		χ
		H	D	H	D	
$d_5PMMA^{syn}/SCPE^{63}$	100			202	130	-0.042 ± 0.007
	110			203	130	-0.035 ± 0.007
	120			211	135	-0.028 ± 0.006
	125	~220	138	213	137	-0.025 ± 0.005
	130			215	139	-0.021 ± 0.004
	135			227	148	-0.016 ± 0.005
	145			235	154	-0.009 ± 0.003
	155			263	169	-0.003 ± 0.001
$d_5PMMA^{syn}/SCPE^{63}$/MEK-ST	110			211	147	-0.013 ± 0.003
	130	~220	138	215	146	-0.009 ± 0.002
	150			241	153	-0.004 ± 0.001

The temperature dependence of χ is shown in Figure 7.25 for both samples measured. Upon addition of silica nanoparticles, the interaction parameter increases significantly across the experimental temperature range, showing that the silica weakens the interactions between the two polymers. The experimental data do not vary linearly with $1/T$ as expected from the Flory-Huggins theory (Equation 1.25)). A simple polynomial gives a better fit for the temperature dependence of χ for the blend both with and without silica nanoparticles, although it is more difficult to assign physical meaning to the obtained parameters[361].

The addition of silica greatly increases χ but also decreases the temperature dependence of χ, as evidenced by the much shallower slope. Both the linear and polynomial fits are converging in the temperature range between 155 – 165 °C, where the phase separation of both blends occurs. This explains why the phase separation temperature of the blend is relatively unaffected by the addition of silica, despite the significant change in χ observed.

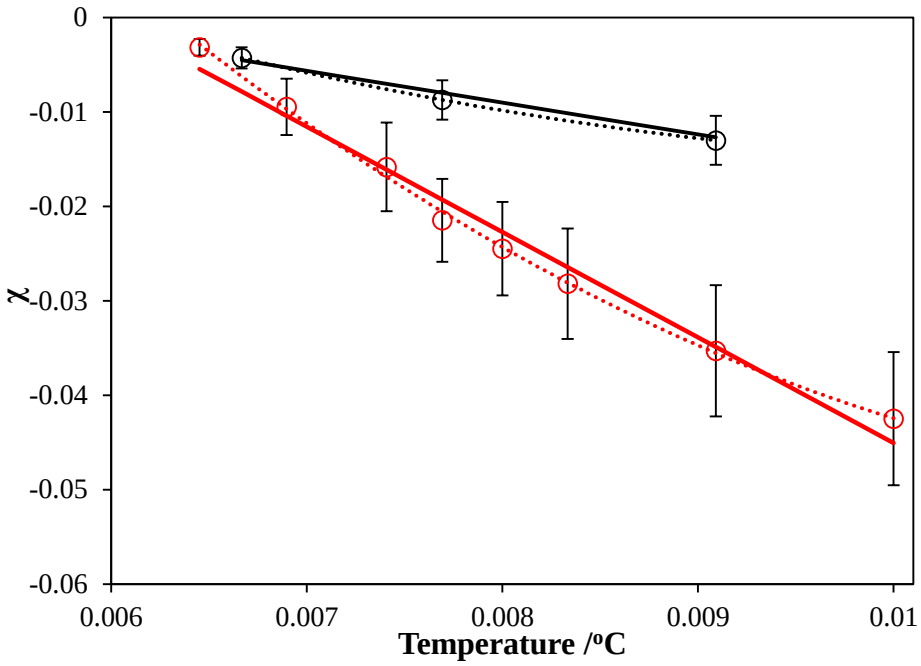

Figure 7.25: The temperature dependence of χ for d_5PMMA^{syn}/SCPE 50/50 (O) and d_5PMMA^{syn}/SCPE/MEK-ST 50/50/1 (□). The solid lines were obtained by linear fits of the data, the dotted lines show the second degree polynomial equation fit

7.4 Conclusions

Preliminary measurements and analysis on the effect of nanoparticles on miscible polymer blends, PMMA/SAN and PMMA/SCPE, were presented in this chapter. Glass transition measurements proved inconclusive for PMMA/SAN and PMMA^{iso}/SCPE blends, due to the pure polymers having T_g values within 20 °C of each other. However, microscopy and SANS measurements have provided more useful information on the phase separation behaviour of the blends measured. Despite the preliminary nature of the study thus far, some important conclusions and areas of interest for future research have already been identified.

7.4.1 PMMA/SAN blends

The initial microscopy results on PMMA/SAN blends containing dispersed silica nanoparticles show significant changes in both the phase separation temperature and dewetting behaviour upon addition of silica. At low loadings of silica (1 wt%), the phase separation temperature increased by 20 °C and dewetting behaviour was seen at higher temperatures than the pure blend. This behaviour has been observed in PMMA/SAN blends containing silica nanoparticles in the literature[183]. However, at higher loadings (5 wt%) the behaviour is completely different: the phase separation

temperature decreases by 10 ºC and extensive dewetting occurs at lower temperatures than expected. The destabilisation of the PMMA/SAN/MEK-ST 50/50/5 blend is further evidenced from the SANS analysis, as the RPA fit of the blend shows a consistent increase in the Flory interaction parameter, χ, across all temperatures measured. The temperature dependence of χ also increased compared to the pure blend, leading to the observed decrease in phase separation temperature. Therefore, the concentration of nanoparticles is an important factor in the miscibility of polymer blends containing these fillers.

The microscopy study of the phase separation temperature of grafted PMMA-MEK-ST/SAN blends is currently inconclusive, due to significant dewetting of the film on the silica substrate. Analysis of the SANS measurements are also hindered by the appearance of shoulder peaks that require more complex analysis than the current RPA model for pure blends and blends containing dispersed silica.

7.4.2 PMMA/SCPE blends

In PMMA/SCPE blends, optical microscopy is unable to observe the phase separation temperature behaviour due to the similar refractive indices of the two component polymers. However, OM images have shown that dewetting behaviour is suppressed in the sample upon addition of a small amount (1 wt%) of silica nanoparticles, a behaviour seen in other polymer nanocomposite thin films in the literature.

The SANS measurements have shown that $PMMA^{iso}$/SCPE is less miscible than $PMMA^{syn}$/SCPE, as the sample was at least partially phase separated at all temperatures measured. When the sample is heated, the blend interfaces sharpen and the sample tends to obeying Porod's law. However, despite the blend being phase separated, there is evidence that blending with SCPE inhibits crystallisation of the isotactic PMMA.

The $PMMA^{syn}$/SCPE blend is fully miscible, and has a phase separation temperature between 155 - 165 ºC. Upon addition of 1 wt % silica, the phase separation temperature is between 150 – 160 ºC, therefore showing either no change or a slight decrease. The one-phase behaviour of the blend with and without silica was analysed using the RPA model, showing that the interaction parameter, χ, of the blend containing silica nanoparticles is significantly higher than the pure blend, with a decreased temperature dependence. Therefore, the addition of even a small amount of silica nanoparticles decreases the interactions between the two polymer components and

hinders miscibility of this polymer blend. However, the considerably decreased temperature dependence leads to the χ values of the two samples converging between 155 – 165 ^{o}C, thus showing that the phase separation temperature of the blends is relatively unaffected by the presence of silica, unlike the PMMA/SAN blend.

Chapter 8. Conclusions and Future Work

8.1 Introduction

The structure and dynamics of chain-grafted polymer nanocomposites has been studied using a range of experiments and a wide variety of techniques. In this thesis, extensive SANS analysis of the structural behaviour of two types of polymer nanocomposites in solution has been reported. QENS and rheological measurements comprise the bulk results on the chain dynamics of polymer nanocomposites, complemented with glass transition and physical ageing results. The key findings of the work presented in this thesis are summarised below.

8.2 Conclusions

8.2.1 Polymer-silica nanocomposites

A structural study of various polymer-silica nanocomposites (PS, PMMA, PBA) was carried out using SANS, SAXS and DLS measurements. Contrast matching experiments on PMMA samples showed that grafting the polymer chains to the surface of colloidal nanoparticle silica (MEK-ST) has little effect on the conformation of the chains in comparison to the analysed pure PMMA sample. The obtained R_g and correlation length values obtained from fits of the data were consistent with the pure polymer chains, regardless of the silica loading (3 to 18 wt%). This is consistent with the recent general trend in the literature on other polymer nanocomposites[114]. Dispersed polymer systems made with MEK-ST particles could also be modelled by assuming the chains are not affected by the presence of small, spherical nanoparticles.

In the contrast matching experiments on samples containing fumed silica, there was evidence of slight perturbation of the polymer chains, but they still generally followed Gaussian statistics and typical linear polymer behaviour. However, significantly additional scattering is seen in the non-contrast matched solutions of both dispersed and grafted fumed silica hybrid particles that could not be modelled. This could be due to agglomeration of the silica nanoparticles or the polymer-silica hybrid particles, or an additional scattering component from polymer-particle interactions. The aggregated structure of the fumed silica nanoparticles therefore results in structural effects not seen in the colloidal silica samples.

The dynamic behaviour of polymer-silica samples was also studied using various techniques. Glass transition measurements showed no change or a slight decrease in T_g when silica nanoparticles are dispersed in the polymer matrix, and a significantly increased T_g in grafted polymer nanocomposites, suggesting decrease chain mobility in these nanocomposites. Enthalpy relaxation measurements showed decelerated ageing in grafted SAN/PS-silica samples and little change in ageing rate for dispersed nanocomposites, consistent with the T_g results obtained.

The addition of silica particles to PBA also significantly increases the viscosity and dynamic moduli of the polymer matrix. The greatest effect is seen upon addition of fumed silica. The increase in these properties cannot be sufficiently modelled using the classical equations for calculating the composite viscosities and dynamic moduli, such as the Einstein-Batchelor equation or Guth-Gold equation. Therefore a more complex equation or computational modelling is required to fully understand the mechanisms behind this reinforcement effect.

QENS measurements of PBA-A300 nanocomposites showed a significant decrease in chain mobility compared to pure PBA, with no evidence of a bound layer of immobile chains around the silica. TTS analysis of the QENS data suggest a loss in free volume, potentially caused by the formation of a filler network through bridging polymer chains which could account for the observed decrease in chain dynamics. The reduction in free volume was also observed in the rheological measurements on the dynamic moduli of the dispersed aggregated silica samples. Only the aggregated silica samples show this behaviour, the dispersed and grafted samples prepared with colloidal silica show the same temperature dependence and free volume as the pure PBA.

8.2.2 Polystyrene-fullerene stars

In chapter 4, a series of SANS experiments of PS-C60 stars in various solvents (good solvents toluene and benzene, and theta solvent cyclohexane) were reported. The core-star model was successfully applied to the data in benzene and cyclohexane. The resulting R_g values from the model fit were found to be larger than the values calculated for equivalent pure polymer stars, especially in the smaller stars (2k arms). Scaling analysis shows that this could be due to the presence of an area of extended chains around the fullerene core, resulting from the sharp boundary between the chains and the fullerene.

The samples in toluene could not be modelled with the core-star model due to excluded volume effects. Scaling analysis using the Daoud-Cotton model showed the small deviations in the structure of PS-C60 stars compared to pure polymer stars. Guinier and Zimm analysis provided R_g values that confirmed that the polymer arms are slightly extended. This result was confirmed by DLS measurements, as obtained hydrodynamic radius values for the PS-C60 stars in toluene were larger than the equivalent linear polymers, contradictory to pure polymer stars which have smaller R_h values.

The dynamics of PS-C60 stars were studied using glass transition, rheological and QENS measurements (Chapter 6). The results from all of these experiments consistently showed that the chain dynamics of these samples are not the same as pure polymer stars: they show total molecular weight dependence rather than arm molecular weight dependence. This results in dynamic properties that are more similar to those of a linear polystyrene than a pure polystyrene star of the same total molecular weight, e.g. similar viscoelastic behaviour and T_g values. This behaviour has currently only been seen in the literature in polymer stars with very low molecular weight arms[338]. The unusual dynamics are due to the chains being tethered to the fullerene core, leading to the whole star being seen as a single dynamic unit.

8.2.3 Polymer blends containing silica nanoparticles

A preliminary study of the phase separation and miscibility of polymer blends (PMMA/SAN and PMMA/SCPE) containing dispersed silica nanoparticles was reported in Chapter 7. The phase separation temperature was determined by optical microscopy for PMMA/SAN 30/70 blends containing 0, 1 and 5 wt% MEK-ST silica. The concentration of silica proved to be a significant factor; the addition of 1 wt% silica increased the phase separation temperature, however 5 wt% silica decreased the phase separation significantly by ~ 20 ^{o}C. This shows that dispersing high loadings of silica can destabilise a blend.

SANS measurements on the two blends were carried out at various temperatures and the one-phase scattering curves were analysed. RPA analysis of the PMMA/SAN/MEK-ST sample containing 5 wt% silica corroborated the results from the microscopy measurements: a small increase in the Flory-Huggins parameter, χ, indicating decreased miscibility and a greatly increased temperature dependence of χ

which leads to a lower phase separation temperature. The analysis of $PMMA^{syn}$/SCPE/MEK-ST scattered intensity showed that addition of even 1 wt% silica could lower the miscibility of the blend. Significantly increased χ values were obtained for the PMMA/SCPE/MEK-ST sample compared to the pure PMMA/SCPE. However, the temperature dependence of χ was greatly decreased, leading to both blends phase separating in the region of 155 to 165 ^{o}C and therefore little to no effect on the phase separation temperature. Overall, the addition of silica to these two blends leads to lower miscibility. This is likely due to the presence of silica nanoparticles decreasing the interactions between the two polymer components.

8.3 Future work

8.3.1 Polymer-silica nanocomposites

The SANS study of dispersed and grafted polymer-silica showed that colloidal silica has little effect on the structure of the polymer chains. However, the effect of fumed silica is much less clear. Further analysis of the data is required, as well as more SANS or SAXS measurements examining the structure of the filler within these nanocomposites. Additionally, more dilute solution measurements on polymer-silica samples could be carried out, as the majority of the data collected was in the semi-dilute region. However, reliable preparation of soluble grafted deuterated polymer-silica samples is required, as deuterated monomers are prohibitively expensive. A project student has recently successfully utilised an NMRP method[362] to synthesise soluble polystyrene-silica nanocomposites, allowing for more solution measurements.

Additional QENS measurements on PBA-silica samples are also to be considered. The PBA-silica nanocomposites studied by QENS were made using fumed silica only. In chapter 5, the structural study of fumed versus colloidal silica samples showed that only fumed silica has an effect on the structural behaviour. However, the rheological results on PBA-MEK-ST nanocomposites showed a significant increase in the viscosity. The physical ageing of polymer grafted nanocomposites containing colloidal silica showed greatly decelerated ageing (PS, SAN), indicating potential effects of grafting chains from colloidal silica on segmental dynamics.

The rheological data on the PBA-silica samples also requires more quantitative analysis in order to give more insight into the origin of the large increase in modulus. A

program to model the data using the Christensen-Lo model and other more complex models is being provided via a collaboration with Dr. Guido Raos.[171]

8.3.2 Polystyrene-fullerene stars

There is still a lot of scope for future work on studying the chain dynamics of the PS-fullerene system. The unusual total molecular weight dependence behaviour and any additional effect of the fullerene core on dynamics could be studied by neutron spin-echo (NSE). NSE is an ideal technique for studying the relaxations and diffusive motions of polymeric materials on longer time scales than QENS measurements. Therefore, NSE measurements would obtain information on the single-chain dynamics of these systems in the melt and extend the present study of the dynamics of PS-C60 stars.

8.3.3 Polymer nanocomposite blends

The study on polymer blends is still in the preliminary stages, and therefore there is large scope for future work on polymer blends containing nanoparticles. In terms of data collection on the blends measured, more AFM measurements are required to determine changes in the morphology upon phase separation on the nanometre scale of the blends when silica particles are present in the system (see Appendix A for preliminary AFM measurements). These results and other techniques such as TEM would determine if the silica nanoparticles preferentially segregate into one of the polymer phases during or after phase separation

The chapter focused primarily on dispersed polymer nanocomposites, due to the insolubility of many of the prepared grafted polymer nanocomposites. Therefore, the development of a successful NMRP route for synthesising soluble grafted polymer nanocomposites allows for future studies on such systems. Along with grafted PMMA-silica samples for comparison with the dispersed PMMA/SAN and PMMA/SCPE blends measured, grafted PS-silica could be used to make PS/PVME blends, a commonly studied polymer blend, for analysis on the effect of grafting on the miscibility of polymer blends.

Another avenue of future research is changing the type of silica used in the polymer blends. The initial measurements have concentrated entirely on using colloidal silica (MEK-ST). However, the results in chapters 5 and 6 have clearly shown that it is

the fumed silica with the aggregated structure that has the largest effect on the structure and dynamics of polymer chains. The effect of dispersing fumed silica on phase separation has been investigated previously using primarily rheology and microscopy, on both miscible[185] and immiscible[363, 364] polymer blends. However, the effect of grafting well-defined chains to fumed silica on polymer blends requires more extensive study[365], and there is little work on comparing grafted fumed silica nanocomposites to dispersions. The effect of grafting and dispersing fumed silica on phase separation could be investigated to provide more of an insight on the effect of filler size and structure on polymer blends.

Appendix A. Structure of polymer nanocomposites

DLS analysis of the mini-emulsion synthetic method

The synthesis of the grafted polymer-silica nanocomposites utilises a mini-emulsion process from the literature that was designed to prevent macroscopic gelation and cross-linking by keeping monomers isolated in small droplets[40]. The characteristic feature of mini-emulsions is the stability of the droplets in the suspensions.

DLS was employed to monitor the size of the droplets over time to determine the stability of the mini-emulsion over time. Monitoring mini-emulsion droplet size by DLS has disadvantages. Accurate DLS requires higher dilution than a typical mini-emulsion mixture, however diluting the emulsion can destabilise it[366]. Other techniques that do not require dilution, such as SANS, are more effective, but less practical in terms of availability of equipment. The DLS measurements carried out in this project were done without dilution, as the actual size of the droplets is not critical, only any change in the size observed over time.

From the preliminary measurements shown in Figure A.1 (a) on butyl acrylate, although the peaks are very broad due to the high concentration present, it is clear that over time the size of the droplets is changing dramatically in an unstable mini-emulsion. The lack of stability causes cross-linking, which reduces the solubility of the grafted samples. The ratio of [M]:[I]:[catalyst] was adjusted for styrene and the mini emulsion measured over time (Figure A.1 (b)). Whilst the mini-emulsion is more stable than previously, after 24 hours the mixture had visibly phase separated.

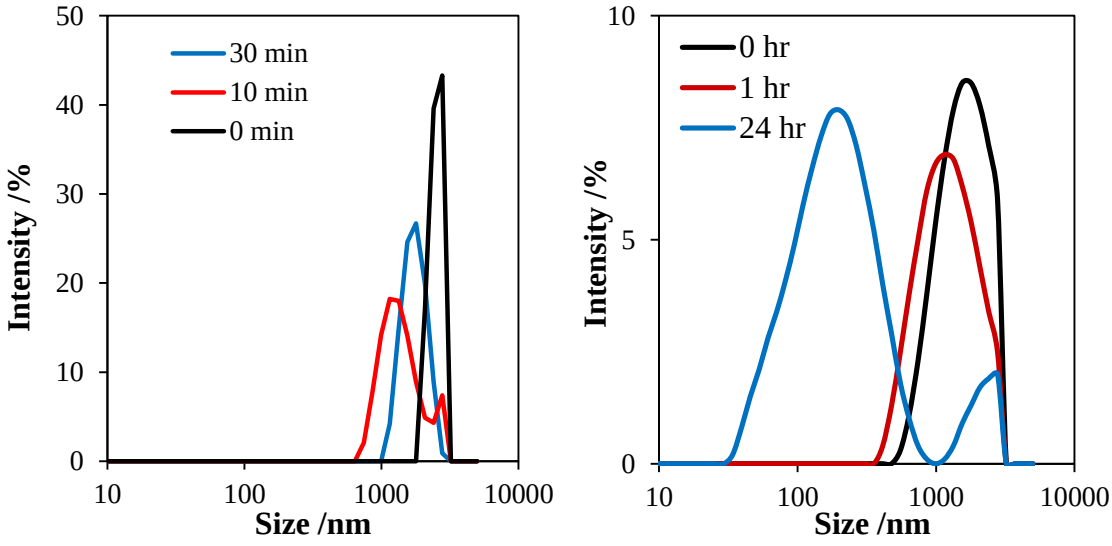

Figure A.1: Radius of droplets within a mini-emulsion of water and (a) butyl acrylate at 0, 30 and 60 mins and (b) styrene at 0, 1 and 24 hours.

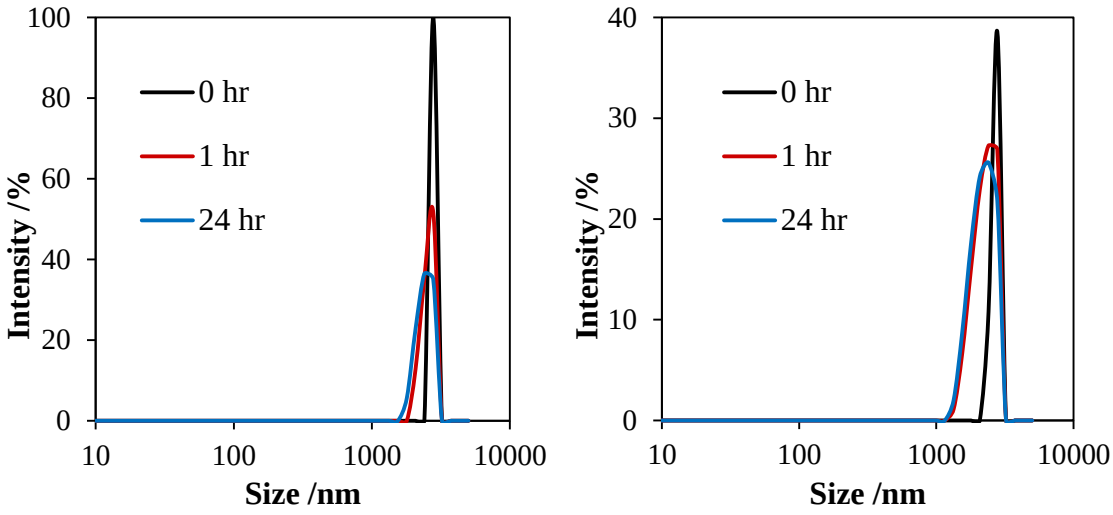

Figure A.2: Radius of droplets within a mini-emulsion containing styrene and (a) A300 silica particles and (b) Ludox silica particles at 0, 1 and 24 hours.

Surprisingly, the mini-emulsions containing silica particles are more stable than mini-emulsions without, showing only a broadening of the droplet peak over the course of 24 hours (Figure A.2). Whilst the new polymer-silica mini emulsion results are promising, the addition of solid silica nanoparticles introduces a different problem, as solid silica-initiator particles are difficult to uniformly disperse in the medium. If not sufficiently dispersed, the silica could lead to different rates of polymerisation within the mini emulsion[40] which could lead to cross-linking and insolubility in polymer-silica nanocomposite.

DLS measurements on grafted PMMA-silica hybrid particles in solution

Grafted PMMA-silica samples were measured by DLS in toluene or MEK solution (Figure A.3). The samples were primarily measured without filtering them first. While this could result in the presence of dust or large aggregates in the samples measured, filtration caused aggregation and lead to the loss of the unimer signal in the DLS data.

The DLS results show a unimer hydrodynamic radius of ~11 – 19 nm, for samples attached to both colloidal silica and 10 nm for fumed silica (Table A.1). TEM images on similar samples showed that the aggregated structure of fumed silica can break down during polymerisation[31]. The DLS measurements also showed the formation of larger aggregates in solution, with an R_h of approximately 250 – 300 nm. In the grafted-PMMA 9 H5, the aggregate peak at ~127 nm corresponds to the size of

the fumed silica. However, the peak is very broad (Figure A.4), suggesting also the presence of larger aggregates, as in the MEK-ST nanocomposites.

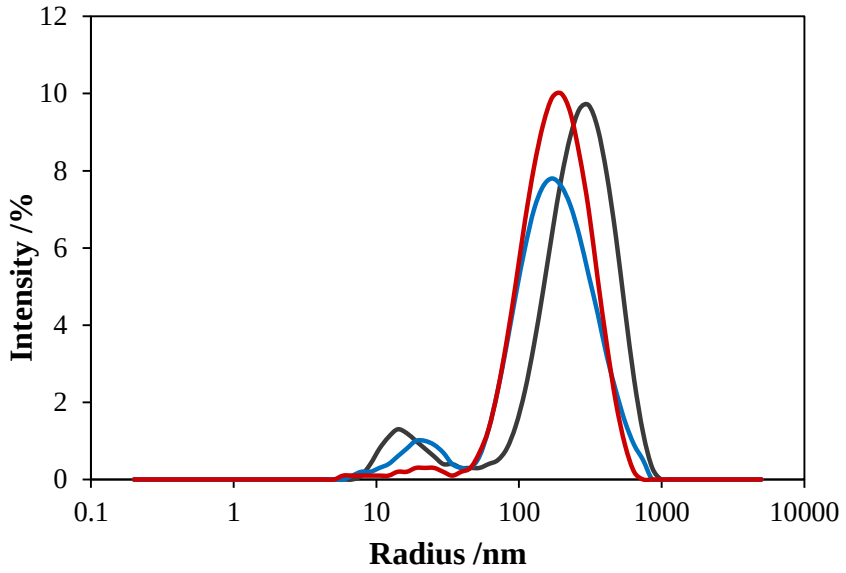

Figure A.3: Particle size distribution of grafted-PMMA MEK-ST nanocomposites at (orange) 3 wt%, (blue) 6 wt% and (red) 18 wt % silica

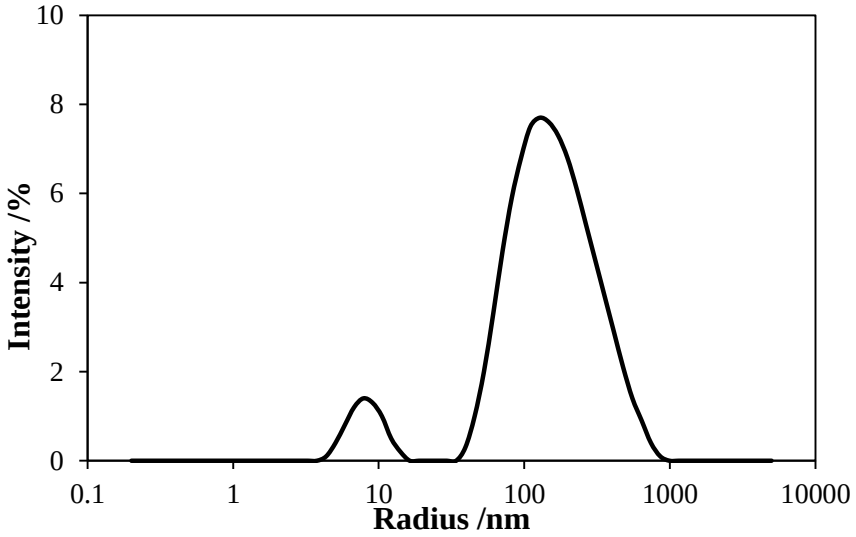

Figure A.4: Particle size distribution of grafted-PMMA 9 H5 nanocomposite

Table A.1: Dynamic Light Scattering results for PMMA-silica samples

Sample	R_h unimer /nm	R_h aggregate /nm
grafted-PMMA 3 MEK-ST	14.6	292
grafted-PMMA 6 MEK-ST	11.1	310
grafted-PMMA 18 MEK-ST	18.8	229
grafted-PMMA 9 H5	10.0	127

Notation: ## = wt % of silica measured by elemental analysis

Kratky plots for additional linear and star polymers

The 105k HPS sample (Figure A.5) shows the typical behaviour for linear polymers, whereas the 2k HStar sample (Figure A.6) shows the maximum seen in star polymers[200].

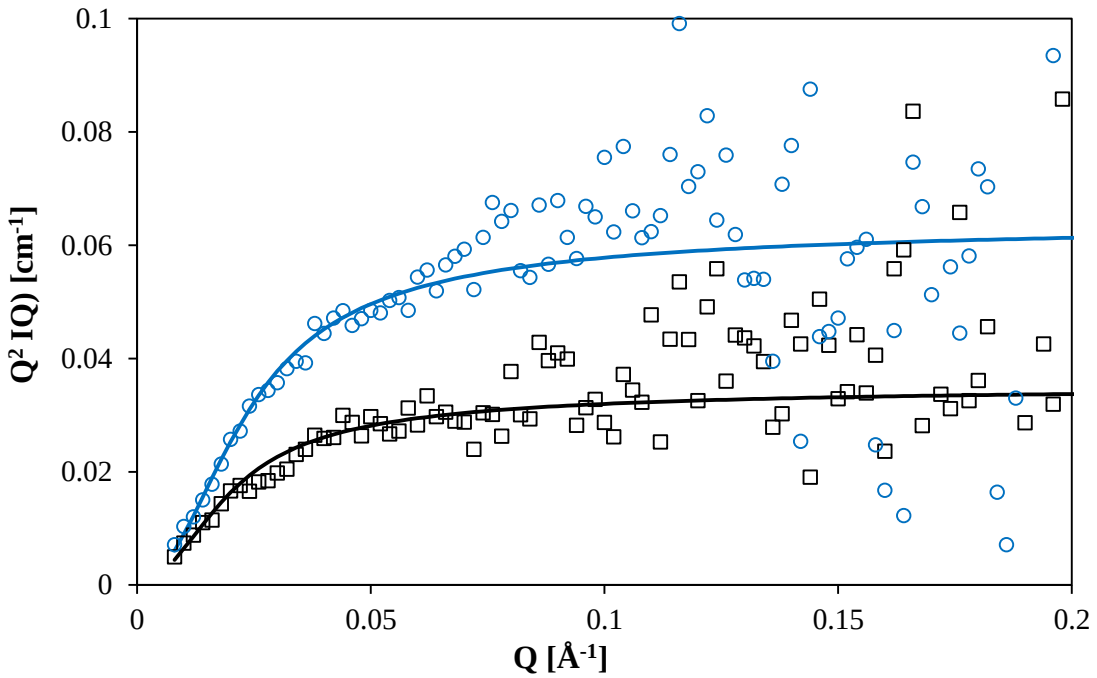

Figure A.5: Kratky plot for the linear 105k HPS sample measured on LOQ at 1 wt% (□) and 2 wt% (o) in benzene, with calculated lines from the Debye model.

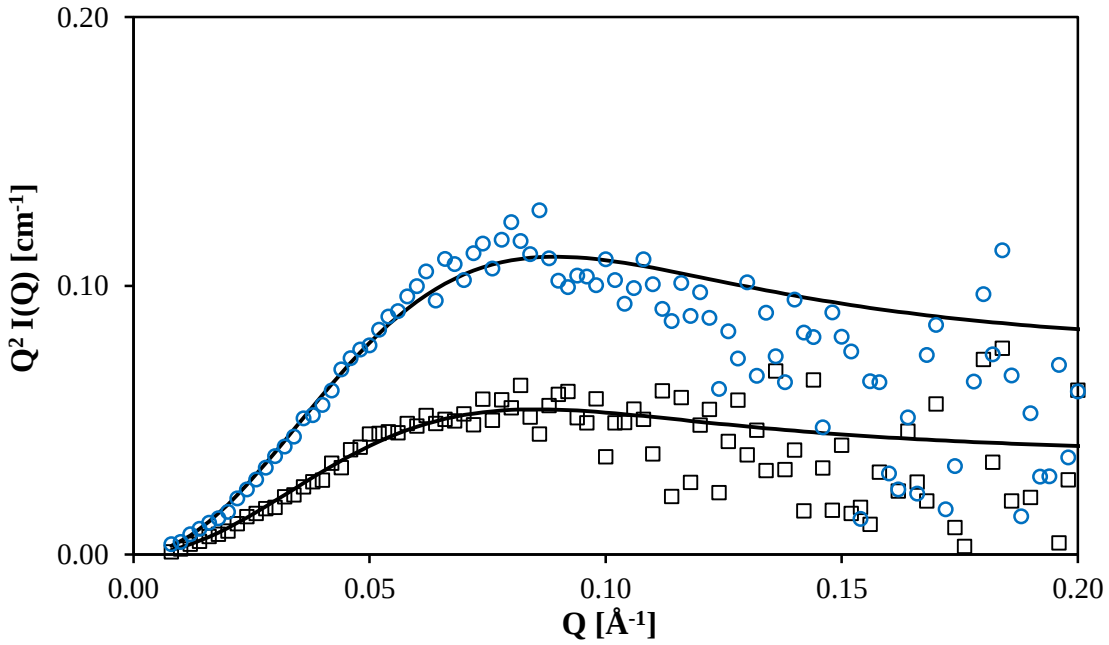

Figure A.6: Kratky plot for 2k HStar sample measured on LOQ at 1 wt% (□) and 2 wt% (o) in benzene, along with calculated lines from the star model (Equation (2.58)).

Core-star model fits of PS-C60 stars in cyclohexane

The core-star model (Equation (4.5)) fits of hydrogenated PS-fullerene stars in cyclohexane at non-theta temperatures are shown below. The model fits the data well at all temperatures and concentrations.

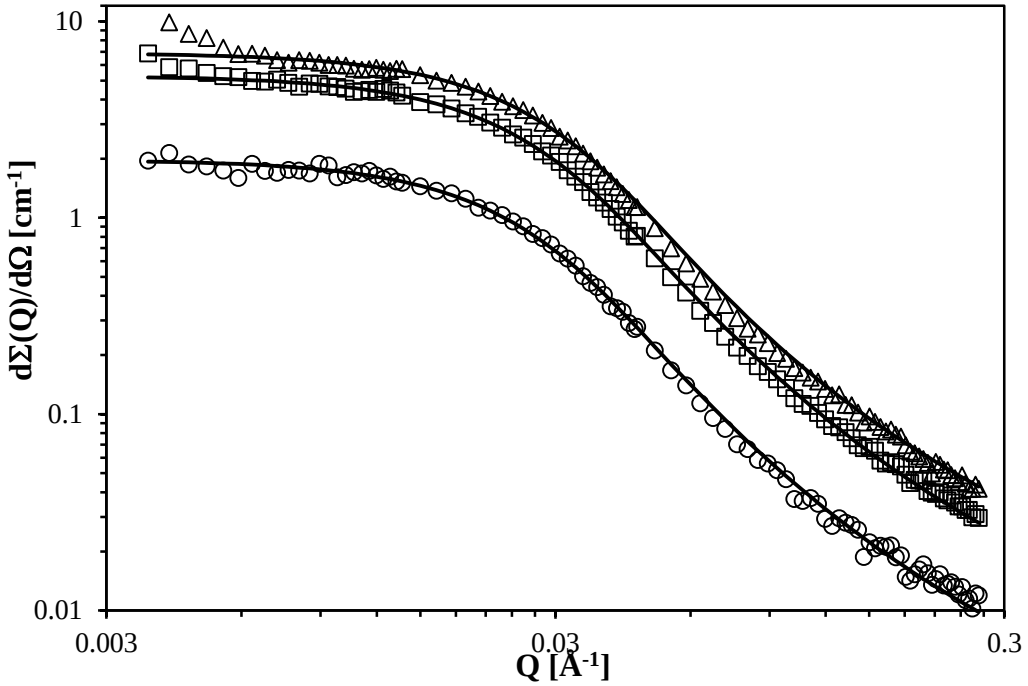

Figure A.7: Core-star model fits on a log-log scale for 16k HStar data at 50 ºC and 0.5 wt% (○), 1 wt% (□) and 2 wt% (Δ) concentration in d-cyclohexane solution

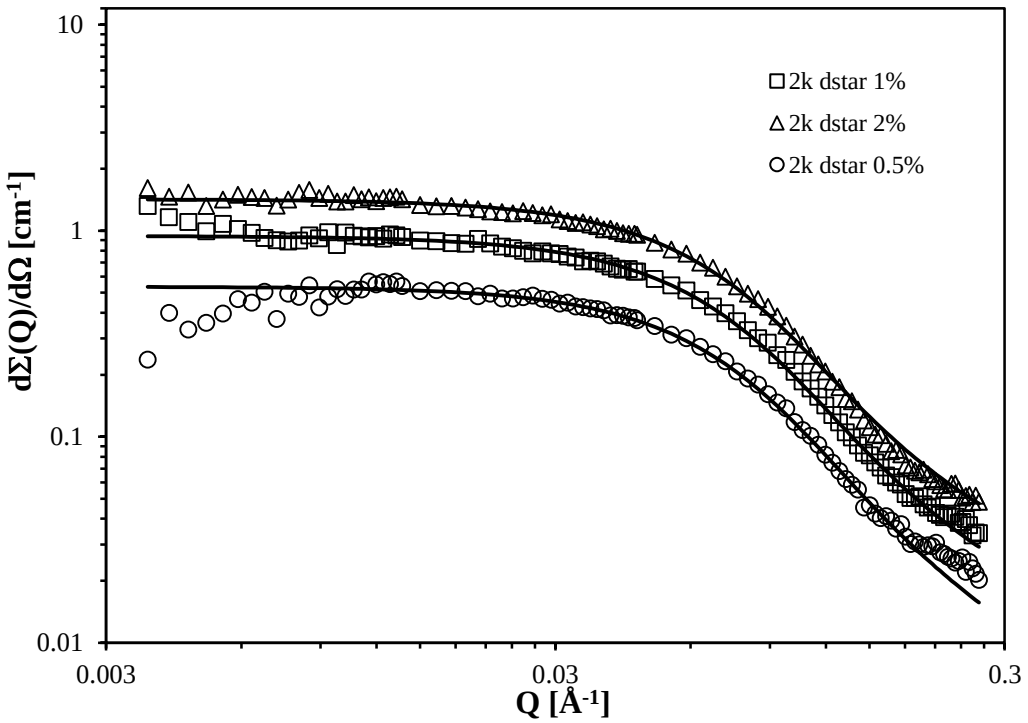

Figure A.8: Core-star model fits on a log-log scale for 2k HStar data at 30 ºC and 0.5 wt% (○), 1 wt% (□) and 2 wt% (Δ) concentration in d-cyclohexane solution

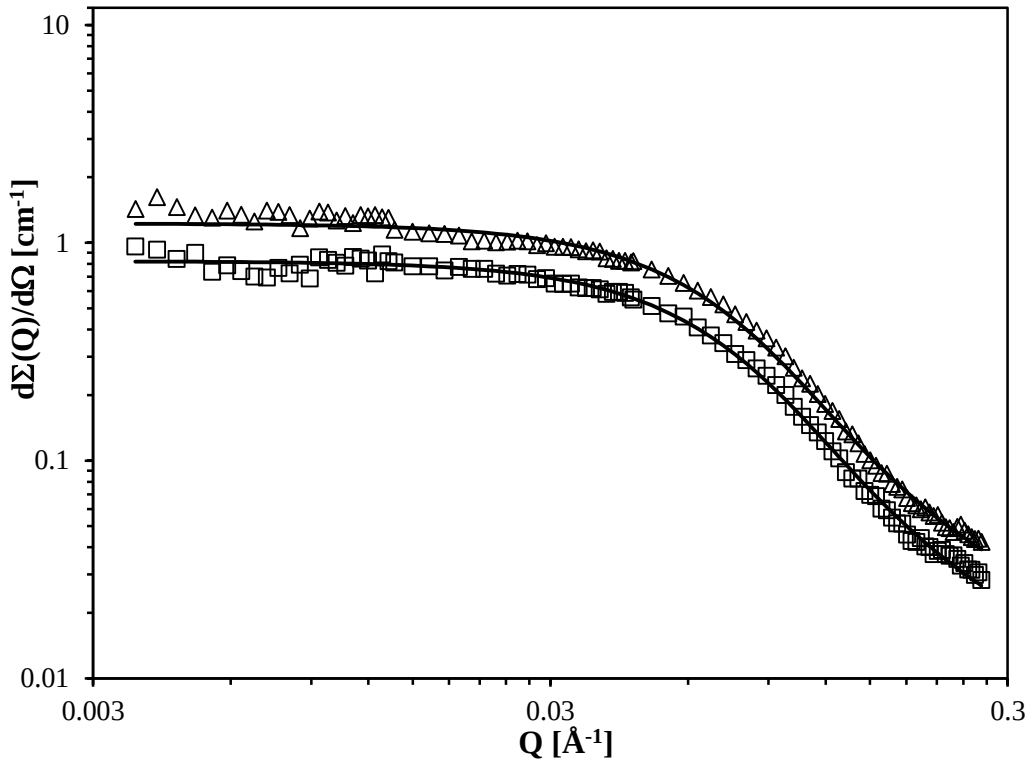

Figure A.9: Core-star model fits on a log-log scale for 2k HStar data at 50 ºC and 0.5 wt% (○), 1 wt% (□) and 2 wt% (Δ) concentration in d-cyclohexane solution

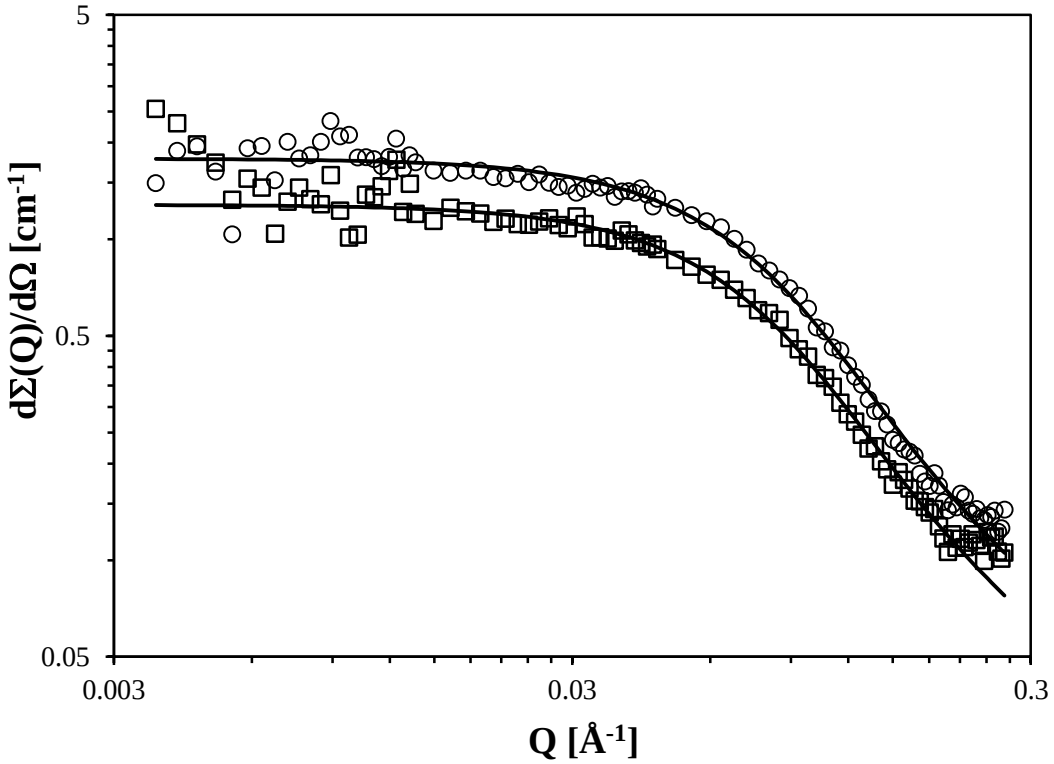

Figure A.10: Core-star model fits on a log-log scale for 2k DStar in cyclohexane at 30 ºC (○) and 40 ºC (□) with the calculated curve from the core-star model.

Guinier and Zimm plots

The Zimm plot of 16k HStar is shown below (Figure A.11), clearly showing that as the concentration increases to 5 wt%, the data points no longer line up with the data from the lower concentrations, leading to inaccurate results if used in the calculation.

Calculated Guinier plots for the core-star model was used to determine the range for which the Guinier plot is a reliable method of calculating the R_g value of the PS-C60 samples (Figure A.12). The Guinier plot start to deviate from linearity at R_g = 50 Å.

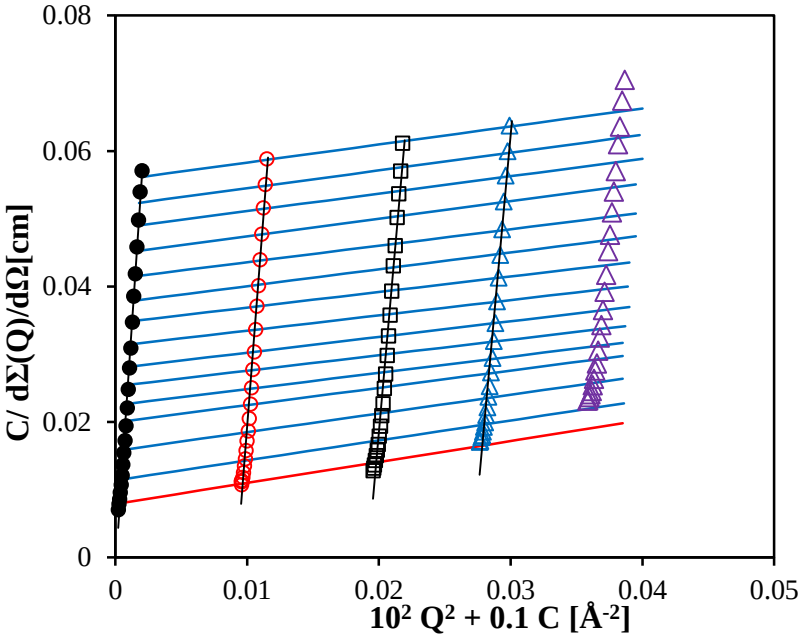

Figure A.11: Zimm plot of 16k HStar at 1 wt% (○), 2 wt% (□), 3 wt% (Δ) and 5 wt % (◊). The filled symbols show the extrapolated C = 0 values.

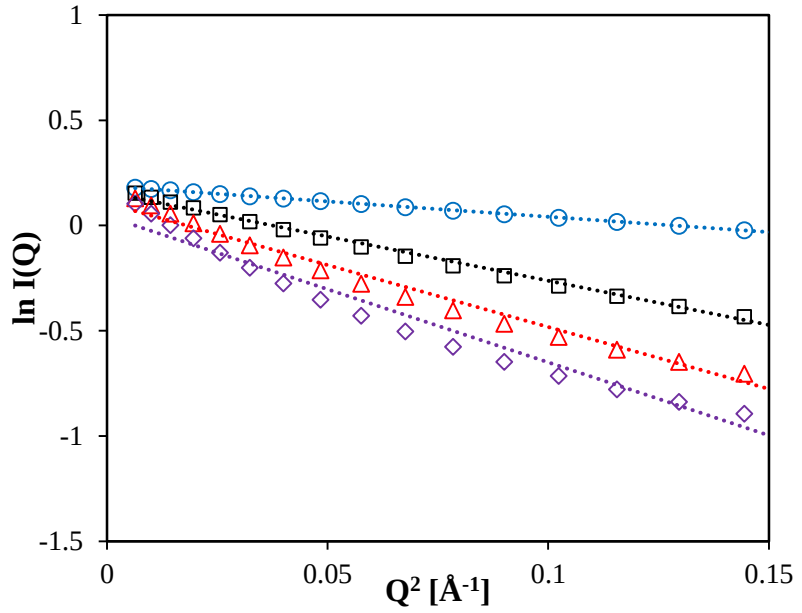

Figure A.12: Calculated Guinier plots from calculated intensity of the core-star model for PS-C60 samples using different R_g values: 20 Å (○), 40 Å (□), 50Å (Δ) and 60 Å (◊).

Modelling of SAXS data of fumed silica nanoparticles

The SAXS data of A300 and H5 particles were analysed using the MassSurfaceFractal model used for the SANS data.

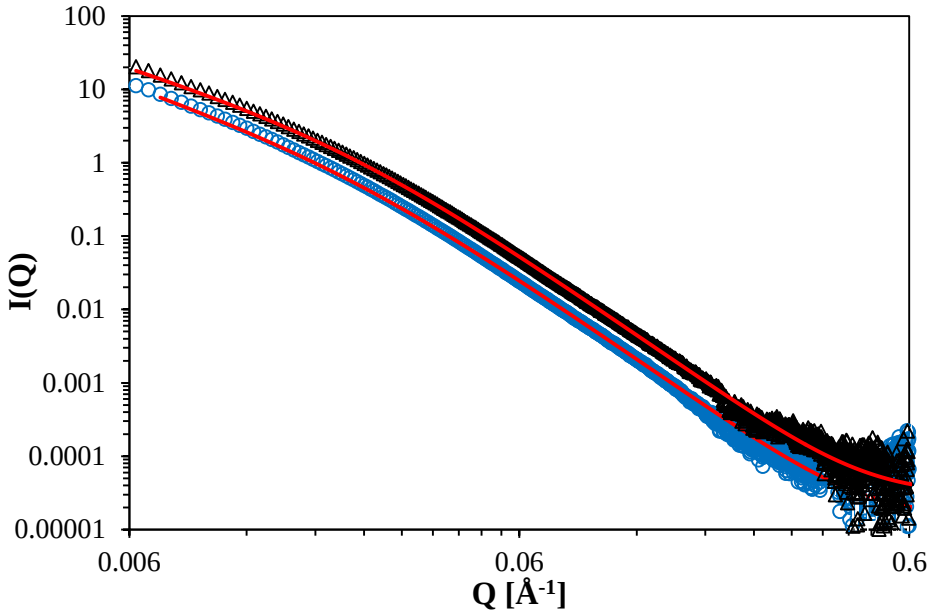

Figure A.13: MassSurfaceFractal model fits of A300 (○) and H5 (Δ) particles.

Subtraction of silica scattering from SAXS data

The fractal model for aggregated silica was subtracted from the overall scattered intensity of a grafted PS sample. The resulting intensity does not resemble that of a linear polymer chain and cannot be modelled with a Debye function.

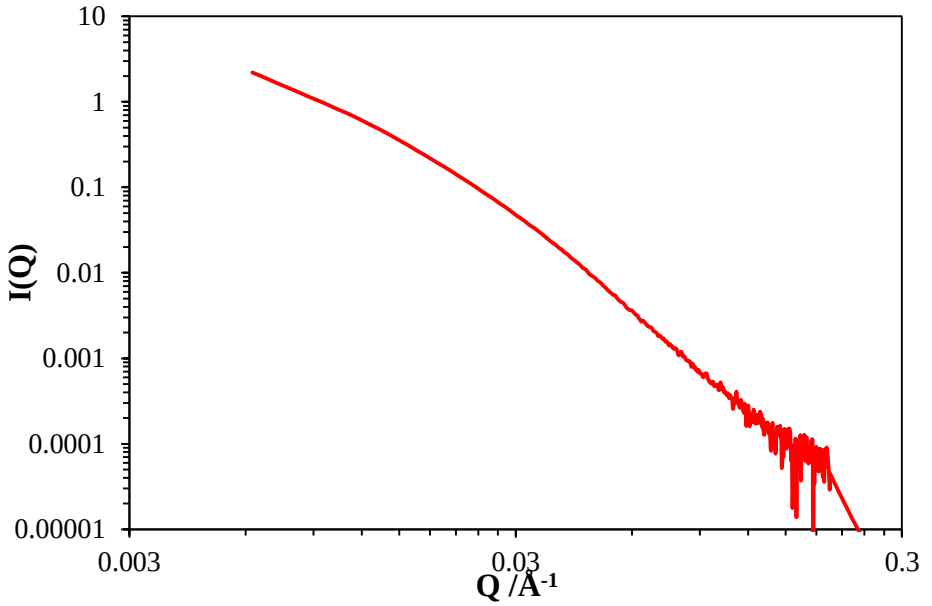

Figure A.14: SAXS intensity profile of grafted-PS 16.5 H5 (red) after subtraction of the silica scattering.

Appendix B. Dynamics of polymer nanocomposites

TTS master curves for Ludox and A300 samples

The horizontally shifted master curves for PBA-silica samples containing colloidal Ludox or fumed A300 particles are shown below. The obtained curves are similar to those obtained for MEK-ST and H5 particles respectively.

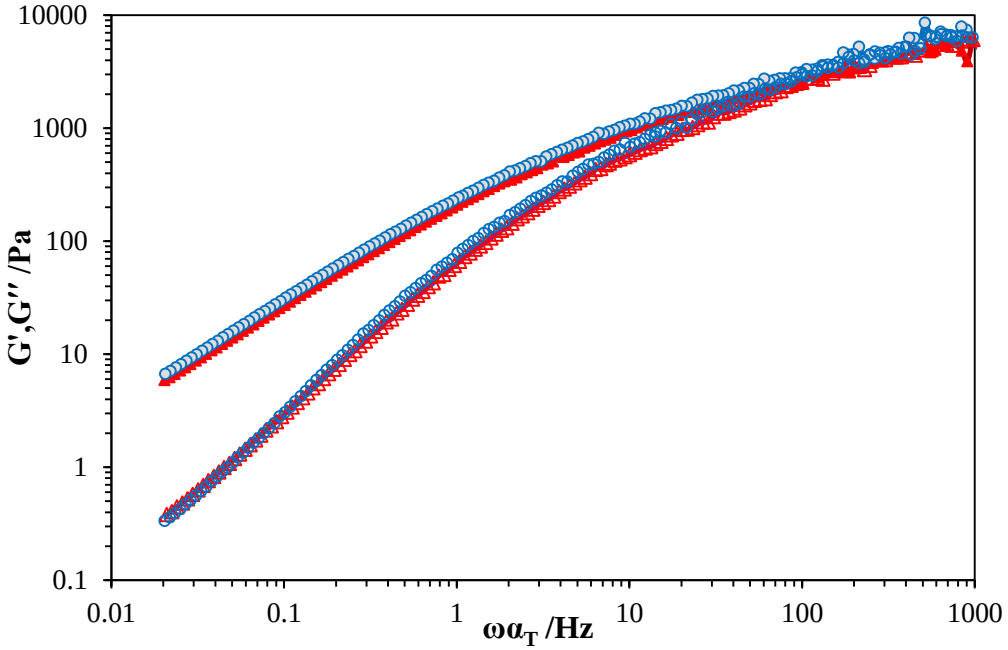

Figure B.1: Comparison of master curves of elastic modulus G′ (empty symbols) and viscous modulus G′′ (filled symbols) for dispersed-PBA 5.2 MEK-ST (Δ) and dispersed-PBA 5.5 Ludox (○).

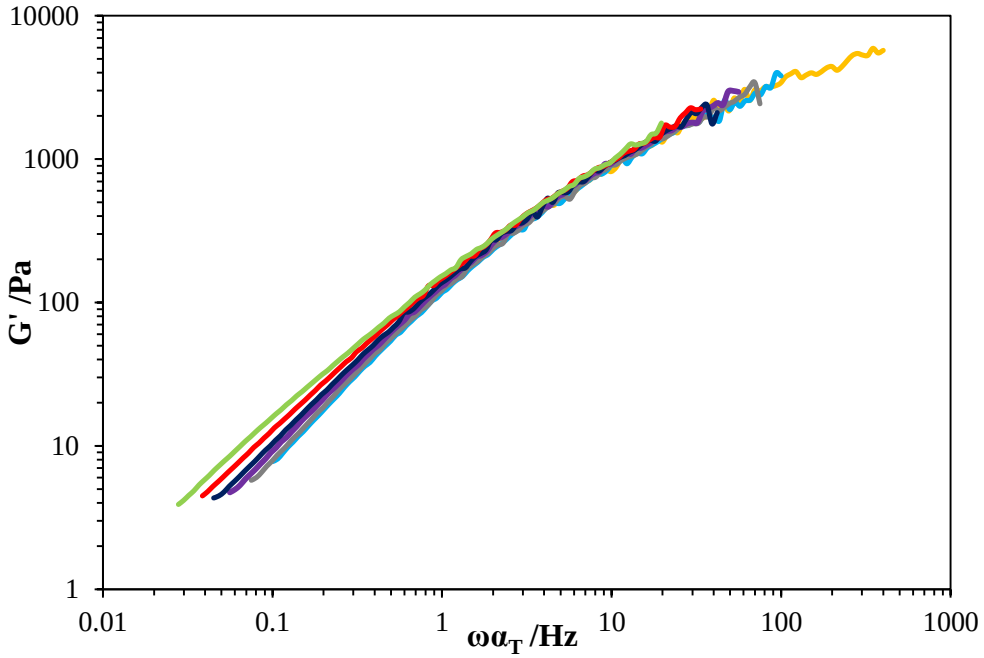

Figure B.2: Horizontally shifted *G′* curves for dispersed-PBA 5.3 A300 sample at temperatures between 20 and 80 ºC. The curves show the same breakdown in the TTS principle at low frequencies that is observed in the dispersed-PBA 5.2 Cab H5 sample.

Appendix C. Polymer Blends

AFM measurements on PMMA/SAN blends

The surface phase morphologies of PMMA/SAN, PMMA/SAN/MEK-ST and grafted PMMA-MEK-ST/SAN thin films were characterised by tapping-mode atomic force microscopy (TM-AFM) after vacuum oven drying at 100 ^{o}C. The TM-AFM measurements were carried out at ambient temperature in air using an Innova AFM and probe. The height and phase images are shown below.

The AFM measurements show that even though the surface of the cast film with silica particles appears homogeneous, on a nanometre to micron level scale the topography and phase of the blend changes when silica is added. Despite significant dewetting seen in the OM images, the grafted 30/70/2 blend sample has a similar phase image to the dispersed 30/70/1 blend sample.

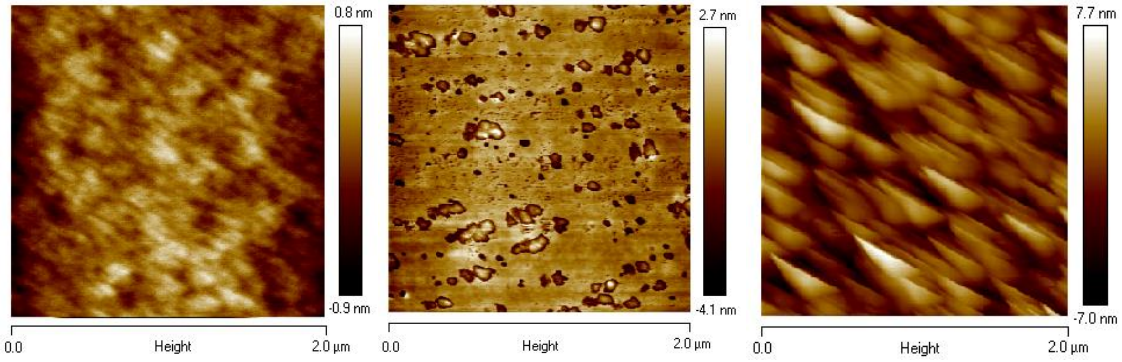

Figure C.1: TM-AFM height images for PMMA/SAN 30/70 (left), PMMA/SAN/MEK-ST 30/70/1 (middle) and PMMA/SAN/MEK-ST 70/30/5 (right)

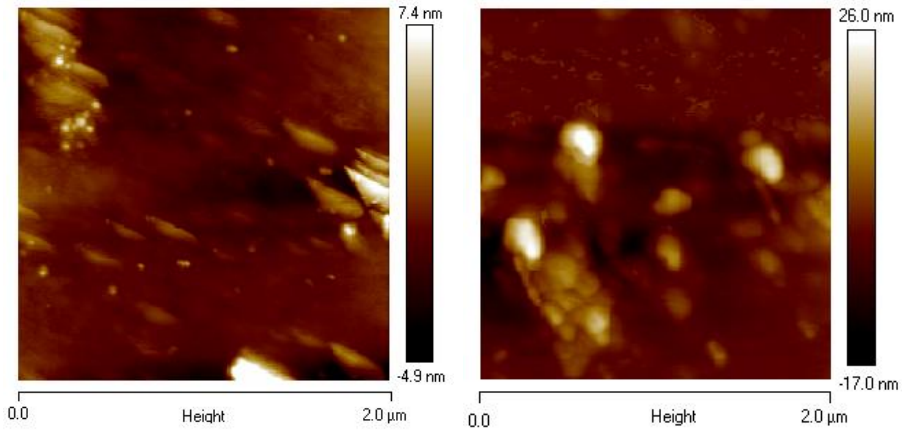

Figure C.2: TM-AFM height images for GPMMA-MEK-ST/SAN 30/70/2 (left) and GPMMA-MEK-ST/SAN 70/30/5 (right)

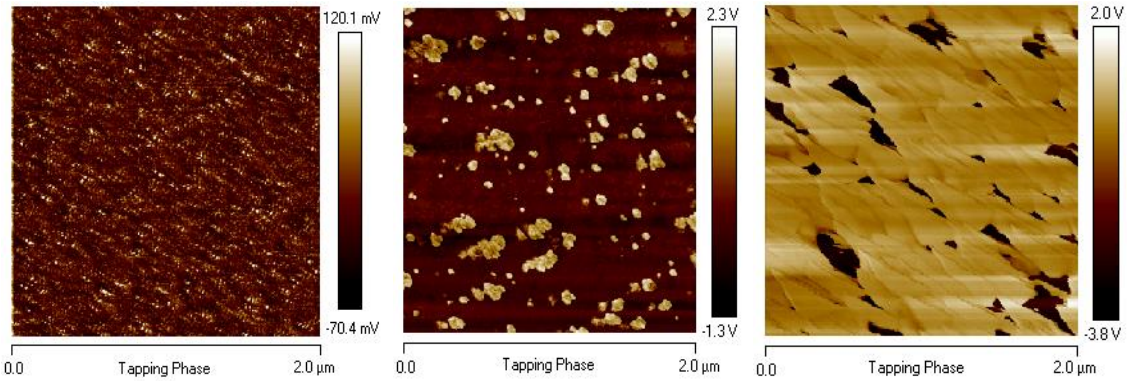

Figure C.3: TM-AFM phase images for PMMA/SAN 30/70 (left), PMMA/SAN/MEK-ST 30/70/1 (middle) and PMMA/SAN/MEK-ST 70/30/5 (right)

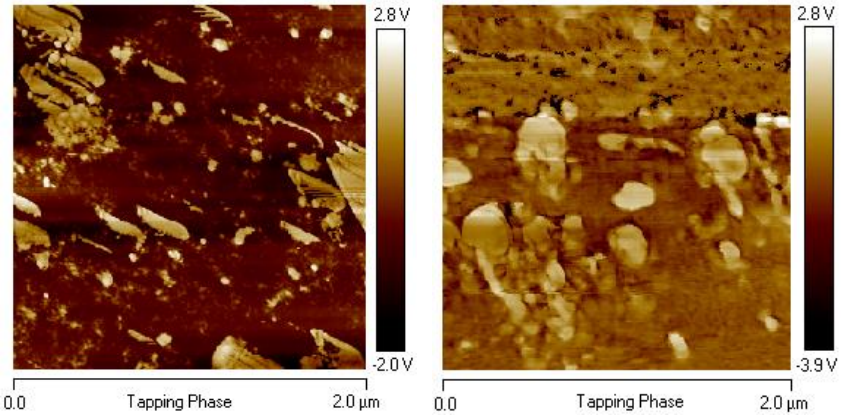

Figure C.4: TM-AFM phase images for GPMMA-MEK-ST/SAN 30/70/2 (left) and GPMMA-MEK-ST/SAN 70/30/5 (right)

AFM measurements were only carried out on the blends before phase separation due to time and experimental constraints. The next step in these measurements is to measure phase separated thin films made by annealing above the phase separation temperature for a minimum of 24 hours.

AFM measurements on PMMA/SCPE blends

Solvent cast films of PMMA/SCPE and PMMA/SCPE/MEK-ST blends were vacuum oven dried at 100 ^{o}C and characterised in the one-phase region by TM-AFM measurements. The height and phase images are shown below. The phase images are similar to those obtained for the PMMA/SAN blends with and without nanoparticles, showing that atactic PMMA and SCPE are miscible. The next stage is to phase separate the thin films and observe the changes in phase morphology in the two-phase region. Unlike optical microscopy, phase separation may be observable with AFM.

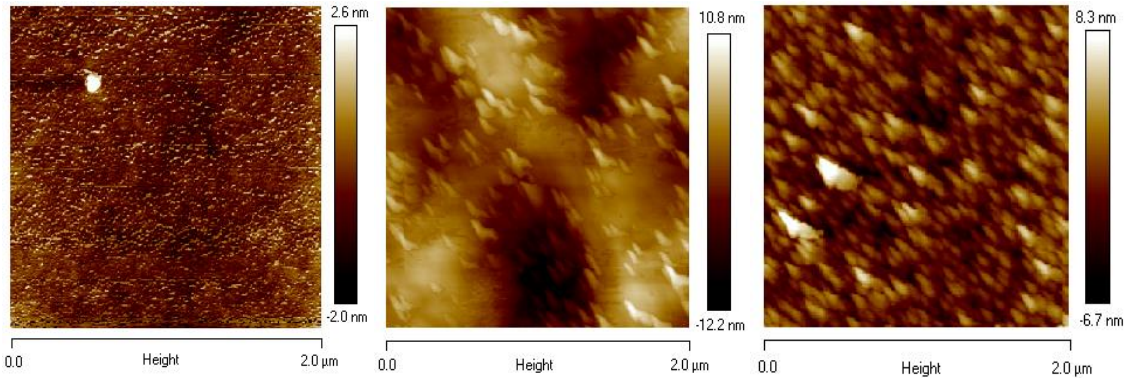

Figure C.5: TM-AFM height images for PMMA/SCPE 30/70 (top left), PMMA/SCPE/MEK-ST 30/70/1 (top right) and PMMA/SCPE/MEK-ST 70/30/5 (bottom)

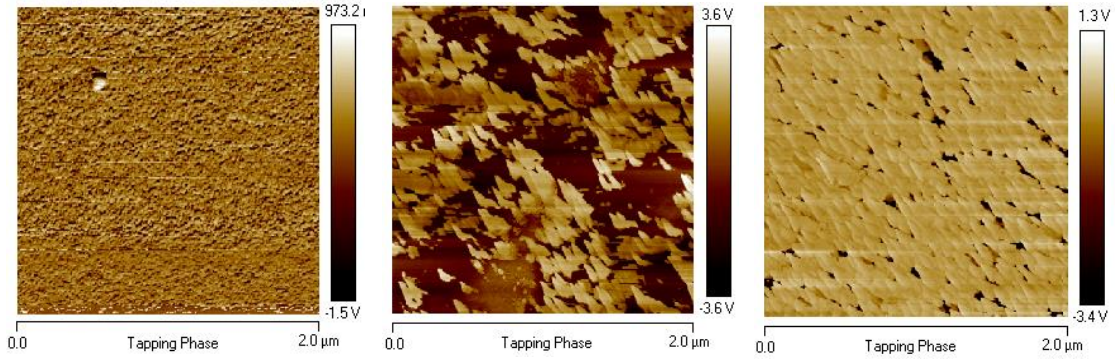

Figure C.6: TM-AFM phase images for PMMA/SCPE 30/70 (top left), PMMA/SCPE/MEK-ST 30/70/1 (top right) and PMMA/SCPE/MEK-ST 70/30/5 (bottom)

Semi-crystalline behaviour of d_5PMMA^{iso}

There is evidence of the formation of lamellae, i.e. a peak appearing at intermediate *Q* values (between 0.01 - 0.1 $Å^{-1}$), in the d_5PMMA^{iso} background sample when heated above 100 ^oC (Figure C.7). This semi-crystalline behaviour was also observed by DSC measurements of a sample after being heated at 100 ^oC for 24 hours (Figure C.8).

The crystallinity of the sample observed in SANS measurements was firstly analysed using a Lorentz correction (inset in Figure C.7) to calculate the d-spacing (305 and 356 Å for 100 ^oC and 120 ^oC respectively). Then, the scattered intensity was converted into the correlation function using Equation (C.1) and a Matlab front-end provided by Prof. David Bucknall:

$$\gamma(r) = \frac{1}{2\pi^2}\int_0^\infty q^2 I(q)\cos(qr)\,dq \qquad \textbf{(C.1)}$$

The correlation function is shown in Figure C.9 and allows direct analysis without the need for a model function[199]. Analysis of the correlation function showed that the d_5PMMA sample is approximately 30% crystalline.

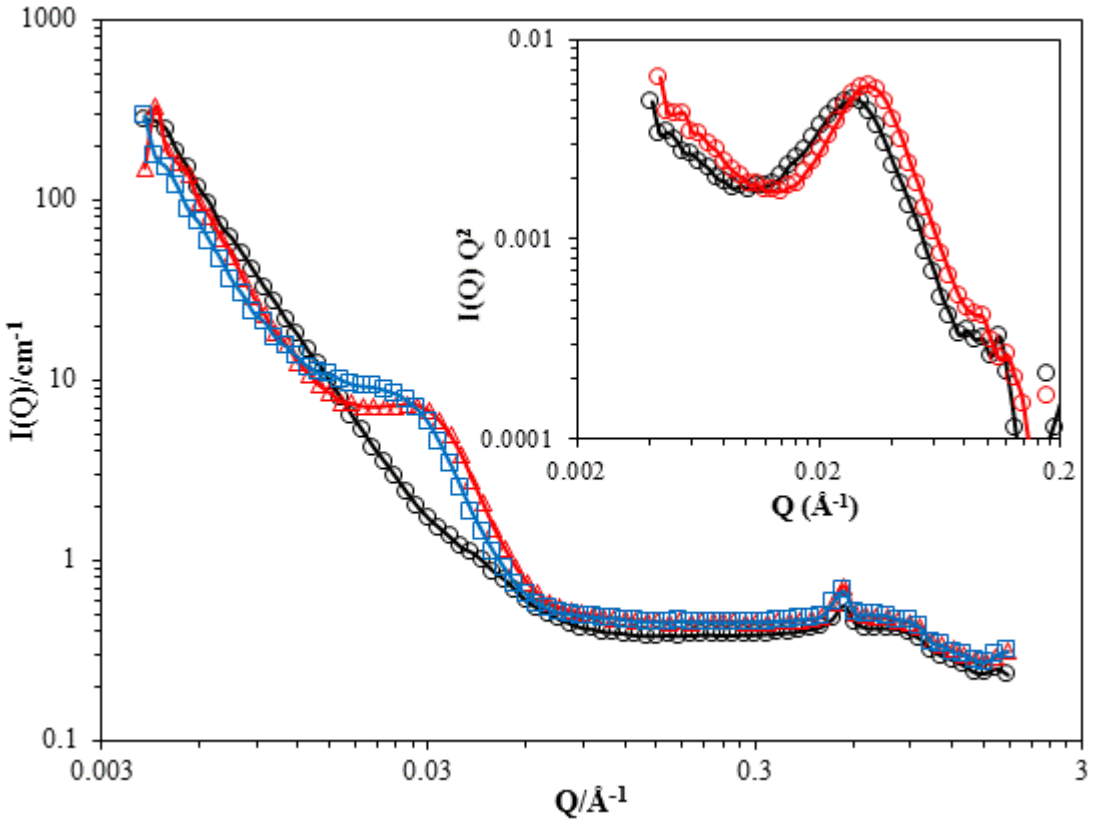

Figure C.7: Scattered intensity of the d_5PMMA^{iso} background at 25 ºC (o), 100 (Δ) and 120 ºC (□). Inset shows the Lorentz corrected SANS intensity at 100 ºC (red) and 120 ºC (black).

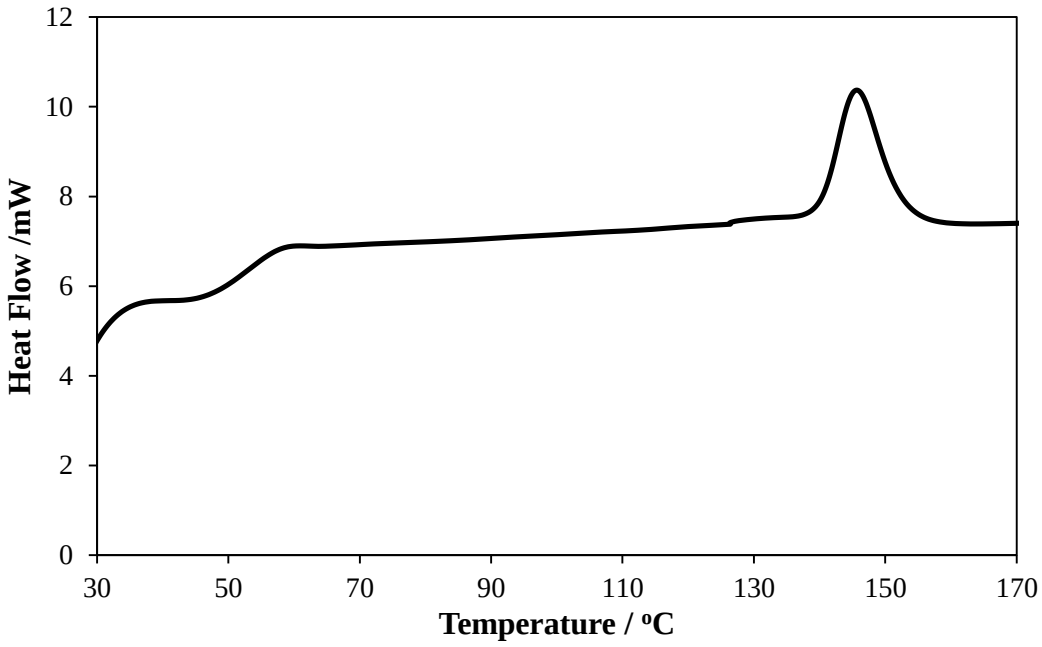

Figure C.8: DSC trace of d_5PMMA^{iso} after being heated for 24 hours at 100 ºC.

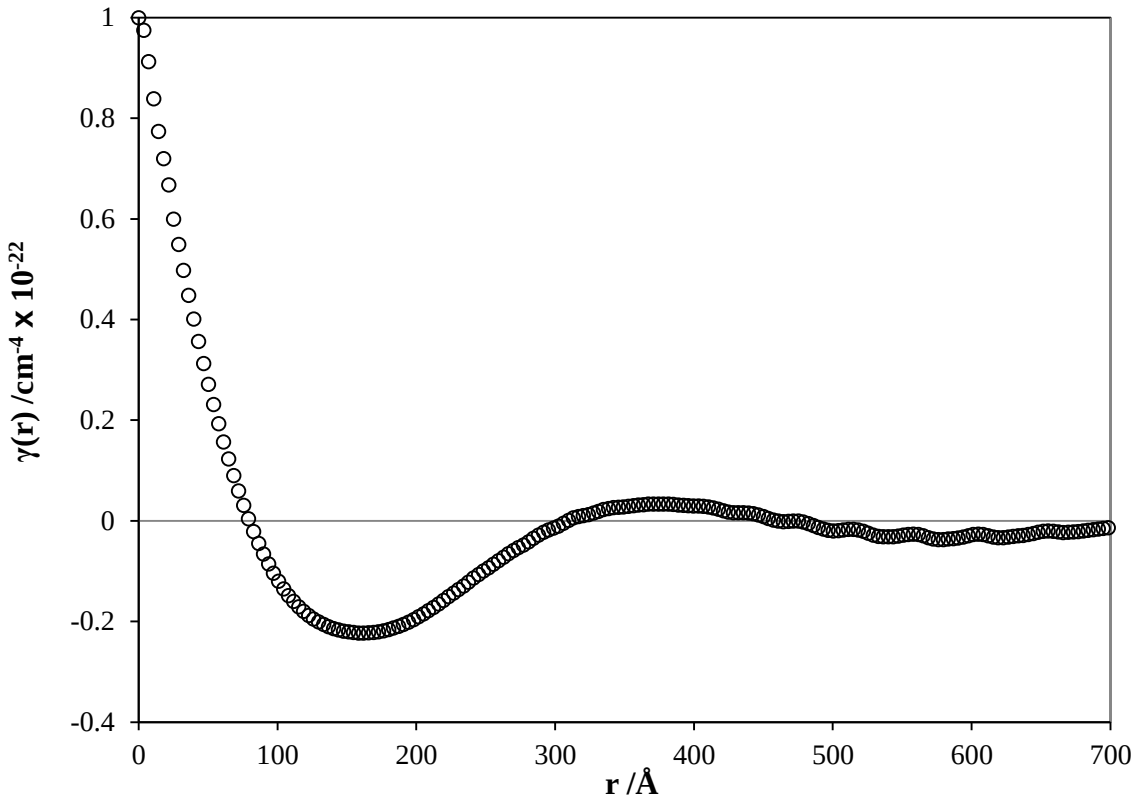

Figure C.9: Correlation function of d_5^{iso}PMMA at 120 ºC.

REFERENCES

1. T. Nann and W. M. Skinner, *ACS Nano*, 2011, **5**, 5291-5295.
2. I. Capek, *Adv. Colloid Interface Sci.*, 2009, **150**, 63-89.
3. J. P. Harris, A. E. Hess, S. J. Rowan, C. Weder, C. A. Zorman, D. J. Tyler and J. R. Capadona, *J. Neural Eng.*, 2011, **8**.
4. K. Davis, F. M. Sayler and M. G. Bakker, *Abstracts of Papers of the American Chemical Society*, 2011, **241**.
5. Y. Kasirga, A. Oral and C. Caner, *Polym. Compos.*, 2012, **33**, 1874-1882.
6. W. Chen, X. Tang, J. Considine and K. T. Turner, *J. Adhes. Sci. Technol.*, 2011, **25**, 581-596.
7. L. H. Baekeland, *Ind. Eng. Chem.*, 1909, **1**, 149-161.
8. E. C. Case, *Science (New York, N.Y.)*, 1925, **61**, 543-544.
9. A. Balazs, T. Emrick and T. Russell, *Science*, 2006, **314**, 1107-1110.
10. A. P. Alivisatos, *Science*, 1996, **271**, 933-937.
11. H. E. Miltner, N. Watzeels, C. Block, N. A. Gotzen, G. Van Assche, K. Borghs, K. Van Durme, B. Van Mele, B. Bogdanov and H. Rahier, *Eur. Polym. J.*, 2010, **46**, 984-996.
12. M. M. Demir, P. Castignolles, U. Akbey and G. Wegner, *Macromolecules*, 2007, **40**, 4190-4198.
13. J. P. Gann and M. Yan, *Langmuir*, 2008, **24**, 5319-5323.
14. S. Yoshio, J. Tatami, T. Yamakawa, T. Wakihara, K. Komeya, T. Meguro, K. Aramaki and K. Yasuda, *Carbon*, 2011, **49**, 4131-4137.
15. N. Mandzy, E. Grulke and T. Druffel, *Powder Technol.*, 2005, **160**, 121-126.
16. C. Sauter, M. A. Emin, H. P. Schuchmann and S. Tavman, *Ultrason. Sonochem.*, 2008, **15**, 517-523.
17. J. Sun and L. Gao, *Carbon*, 2003, **41**, 1063-1068.
18. P.-C. Ma, N. A. Siddiqui, G. Marom and J.-K. Kim, *Composites Part A*, 2010, **41**, 1345-1367.
19. S. Thomas, D. Rouxel and D. Ponnamma, *Spectroscopy of Polymer Nanocomposites*, Elsevier Science, 2016.
20. F. Dalmas, J.-Y. Cavaillé, C. Gauthier, L. Chazeau and R. Dendievel, *Compos. Sci. Technol.*, 2007, **67**, 829-839.

21. M. Monti, A. Terenzi, M. Natali, I. Gaztelumendi, N. Markaide, J. M. Kenny and L. Torre, *J. Appl. Polym. Sci.*, 2010, **117**, 1658-1666.

22. A. Karatrantos, N. Clarke and M. Kröger, *Polymer Reviews*, 2015, 00-00.

23. A. El Harrak, G. Carrot, J. Oberdisse, J. Jestin and F. Boue, *Polymer*, 2005, **46**, 1095-1104.

24. F. Boon, S. Desbief, L. Cutaia, O. Douheret, A. Minoia, B. Ruelle, S. Clement, O. Coulembier, J. Cornil, P. Dubois and R. Lazzaroni, *Macromol. Rapid Commun.*, 2010, **31**, 1427-1434.

25. J. Jeon, V. Panchagnula, J. Pan and A. V. Dobrynin, *Langmuir*, 2006, **22**, 4629-4637.

26. J. W. Ostrander, A. A. Mamedov and N. A. Kotov, *J. Am. Chem. Soc.*, 2001, **123**, 1101-1110.

27. S. C. Tjong, *Mater. Sci. Eng., R*, 2006, **53**, 73-197.

28. K. Matyjaszewski and J. Spanswick, *Mater. Today*, 2005, **8**, 26-33.

29. Y. Huang, Q. Liu, X. Zhou, S. Perrier and Y. Zhao, *Macromolecules*, 2009, **42**, 5509-5517.

30. A. Kraft, V. Arrighi and N. Grima, *Polym. Mater. Sci. Eng*, 2008, **98**, 687.

31. M. Khlifa, PhD Thesis, Heriot-Watt University, 2013.

32. J. S. Wang and K. Matyjaszewski, *J. Am. Chem. Soc.*, 1995, **117**, 5614-5615.

33. M. Kato, M. Kamigaito, M. Sawamoto and T. Higashimura, *Macromolecules*, 1995, **28**, 1721-1723.

34. W. Tang and K. Matyjaszewski, *Macromolecules*, 2006, **39**, 4953-4959.

35. C.-H. Peng, J. Kong, F. Seeliger and K. Matyjaszewski, *Macromolecules*, 2011, **44**, 7546-7557.

36. N. V. Tsarevsky and K. Matyjaszewski, *Chem. Rev.*, 2007, **107**, 2270-2299.

37. W. Jakubowski and K. Matyjaszewski, *Macromolecules*, 2005, **38**, 4139-4146.

38. K. Min, H. Gao and K. Matyjaszewski, *J. Am. Chem. Soc.*, 2006, **129**, 10521.

39. W. Jakubowski, K. Min and K. Matyjaszewski, *Macromolecules* 2006, **39**, 39.

40. L. Bombalski, K. Min, H. C. Dong, C. B. Tang and K. Matyjaszewski, *Macromolecules*, 2007, **40**, 7429-7432.

41. Y. Zhao and S. Perrier, *Macromolecules*, 2007, **40**, 9116-9124.

42. R. Merget, T. Bauer, H. U. Kupper, S. Philippou, H. D. Bauer, R. Breitstadt and T. Bruening, *Archives of Toxicology*, 2002, **75**, 625-634.

43. W. Stöber, A. Fink and E. Bohn, *J. Colloid Interface Sci.*, 1968, **26**, 62.

44. Y. Huang, Q. Liu, X. Zhou, S. b. Perrier and Y. Zhao, *Macromolecules*, 2009, **42**, 5509-5517.

45. D. A. Savin, J. Pyun, G. D. Patterson, T. Kowalewski and K. Matyjaszewski, *J. Polym. Sci., Part B: Polym. Phys.*, 2002, **40**, 2667-2676.

46. A. Rungta and B. C. Benicewicz, *Polymer Preprints*, 2011, **52**, 511-512.

47. J. Pietrasik, H. C. Dong and K. Matyjaszewski, *Macromolecules*, 2006, **39**, 6384-6390.

48. J. C. Chen, M. Hu, W. D. Zhu and Y. P. Li, *Appl. Surf. Sci.*, 2011, **257**, 6654-6660.

49. E. Badamshina and M. Gafurova, *J. Mater. Chem.*, 2012, **22**, 9427-9438.

50. M. Moniruzzaman and K. I. Winey, *Macromolecules*, 2006, **39**, 5194-5205.

51. A. Tuteja, P. M. Duxbury and M. E. Mackay, *Macromolecules*, 2007, **40**, 9427-9434.

52. J. Zhou, *J. Mol. Graphics Modell.*, 2015, **61**, 102-106.

53. R. Dattani, R. Michels, A. J. Nedoma, R. Schweins, P. Westacott, K. Huber and J. T. Cabral, *Macromolecules*, 2014, **47**, 6113-6120.

54. E. Samulski, J. M. Desimone, M. Hunt Jr, Y. Menceloglu, R. Jarnagin, G. York, K. Labat and H. Wang, *Chem. Mater.*, 1992, **4**, 1153-1157.

55. V. Weber, M. Duval, Y. Ederle and C. Mathis, *Carbon*, 1998, **36**, 839-842.

56. D. Uhrig, G. C. Morar, M. Goswami, J. Huang, B. G. Sumpter, J. Zhou, S. M. Kilbey and D. L. Pickel, *Macromolecules*, 2013, **46**, 7451-7457.

57. H. Zou, S. S. Wu and J. Shen, *Chem. Rev.*, 2008, **108**, 3893-3957.

58. G.-L. Zhuang, H.-H. Tseng and M.-Y. Wey, *Int. J. Hydrogen Energy*, 2014, **39**, 17178-17190.

59. T. Meyer, S. Prause, S. Spange and M. Friedrich, *J. Colloid Interface Sci.*, 2001, **236**, 335-342.

60. C.-C. Chang and W.-C. Chen, *Chem. Mater.*, 2002, **14**, 4242-4248.

61. Y.-l. Su, *React. Funct. Polym.*, 2006, **66**, 967-973.

62. J. Jang, J. Ha and B. Lim, *Chem. Commun.*, 2006, 1622-1624.

63. H. C. Wong, Z. Li, C. H. Tan, H. Zhong, Z. Huang, H. Bronstein, I. McCulloch, J. T. Cabral and J. R. Durrant, *ACS nano*, 2014, **8**, 1297-1308.

64. D. Mühlbacher, M. Scharber, M. Morana, Z. Zhu, D. Waller, R. Gaudiana and C. Brabec, *Adv. Mater.*, 2006, **18**, 2884-2889.

65. V. Arrighi and J. M. G. Cowie, *Polymers: Chemistry and Physics of Modern Materials*, Third edn., Taylor & Francis Group, Boca Raton, 2008.

66. J. Mark, K. Ngai, W. Graessley, L. Mandelkern, E. T. Samulski, J. Koenig and G. D. Wignall, *Physical Properties of Polymers*, 3rd edn., Cambridge University Press, 2004.

67. P. J. Flory, *Principles of Polymer Chemistry*, Cornell University Press, 1953.

68. P. Flory and M. Volkenstein, Wiley Online Library, Editon edn., 1969.

69. L. H. Sperling, *Introduction to physical polymer science*, John Wiley & Sons, 2005.

70. P. Debye, *J. Chem. Phys*, 1946, **14**, 636-639.

71. W. Kuhn, *Kolloid-Zeitschrift*, 1934, **68**, 2-15.

72. A. Rudin, *Elements of Polymer Science & Engineering: An Introductory Text and Reference for Engineers and Chemists*, Elsevier Science, 1998.

73. P. J. Flory, *J. Chem. Phys.*, 1949, **17**, 303-310.

74. R. H. Colby, *Rheol. Acta*, 2010, **49**, 425-442.

75. D. Ballard, G. Wignall and J. Schelten, *Eur. Polym. J.*, 1973, **9**, 965-969.

76. J. Cotton, D. Decker, H. Benoit, B. Farnoux, J. Higgins, G. Jannink, R. Ober, C. Picot and J. Des Cloizeaux, *Macromolecules*, 1974, **7**, 863-872.

77. B. H. Zimm and W. H. Stockmayer, *J. Chem. Phys.*, 1949, **17**, 1301-1314.

78. A. Boothroyd and R. Ball, *Macromolecules*, 1990, **23**, 1729-1734.

79. M. Doi and S. F. Edwards, *The theory of polymer dynamics*, Oxford University Press, 1988.

80. J. D. Ferry, *Viscoelastic Properties of Polymers*, 3rd edn., Wiley, New York, 1980.

81. M. F. Lai, J. Li and J. J. Liu, *J. Therm. Anal. Calorim.*, 2005, **82**, 293-298.

82. A. Henry and G. Safford, *J Polym Sci A2*, 1969, **7**, 433-462.

83. T. Hayakawa and K. Adachi, *Polym. J.*, 2000, **32**, 845-848.

84. M. Gaborieau, R. Graf, S. Kahle, T. Pakula and H. W. Spiess, *Macromolecules*, 2007, **40**, 6249-6256.

85. A. Kulik and K. Prins, *Polymer*, 1993, **34**, 4635-4641.

86. J. Zhao, Y. H. Chin, Y. Liu, A. A. Jones, P. T. Inglefield, R. P. Kambour and D. M. White, *Macromolecules*, 1995, **28**, 3881-3889.

87. A. V. Lyulin, N. K. Balabaev and M. Michels, *Macromolecules*, 2002, **35**, 9595-9604.

88. B. Vorselaars, A. V. Lyulin and M. Michels, *Macromolecules*, 2007, **40**, 6001-6011.

89. S. Arrese-Igor, A. Arbe, B. Frick and J. Colmenero, *Macromolecules*, 2011, **44**.

90. P. E. Rouse Jr, *J. Chem. Phys*, 1953, **21**, 1272-1280.

91. B. H. Zimm, *J. Chem. Phys*, 1956, **24**, 269-278.

92. F. Bueche, *J. Chem. Phys*, 1954, **22**, 603-609.

93. P. De Gennes, *Macromolecules*, 1976, **9**, 587-593.

94. T. McLeish, *Advances in physics*, 2002, **51**, 1379-1527.

95. P.-G. de Gennes, *J. Chem. Phys.*, 1971, **55**, 572-579.

96. P.-G. De Gennes, *Introduction to polymer dynamics*, CUP Archive, 1990.

97. C. Adams, L. Hutchings, P. Klein, T. McLeish and R. Richards, *Macromolecules*, 1996, **29**, 5717-5722.

98. P. De Gennes, *Journal de Physique*, 1975, **36**, 1199-1203.

99. S. Milner and T. McLeish, *Macromolecules*, 1997, **30**, 2159-2166.

100. L. A. Utracki, *Polymer Blends Handbook*, Kluwer Academic Pub, 2002.

101. A. I. Isayev, *Encyclopedia of Polymer Blends: Volume 1: Fundamentals*, John Wiley & Sons, 2010.

102. K. R. Sharma, *Polymer Thermodynamics: Blends, Copolymers and Reversible Polymerization*, CRC Press, 2011.

103. W. Cui, J. Kerres and G. Eigenberger, *Sep. Purif. Technol.*, 1998, **14**, 145-154.

104. L. A. Goettler and J. J. Scobbo, in *Polymer blends handbook*, Springer, Editon edn., 2014, pp. 1433-1458.

105. T. G. Fox, *Bull Am Phys Soc*, 1956, **1**, 123-135.

106. G. Beaucage, S. Sukumaran, S. Clarson, M. Kent and D. Schaefer, *Macromolecules*, 1996, **29**, 8349-8356.

107. M. Brereton, E. Fischer, C. Herkt-Maetzky and K. Mortensen, *J. Chem. Phys.*, 1987, **87**, 6144-6149.

108. G. H. Fredrickson, A. J. Liu and F. S. Bates, *Macromolecules*, 1994, **27**, 2503-2511.

109. J. Kressler, N. Higashida, K. Shimomai, T. Inoue and T. Ougizawa, *Macromolecules*, 1994, **27**, 2448-2453.

110. H. Saito, D. Tsutsumi and T. Inoue, *Polym. J.*, 1990, **22**, 128-134.

111. C. C. Han, B. J. Bauer, J. C. Clark, Y. Muroga, Y. Matsushita, M. Okada, Q. Tran-cong, T. Chang and I. C. Sanchez, *Polymer*, 1988, **29**, 2002-2014.

112. G. Beaucage, R. Stein and R. Koningsveld, *Macromolecules*, 1993, **26**, 1603-1608.

113. A. Tuteja, P. M. Duxbury and M. E. Mackay, *Phys. Rev. Lett.*, 2008, **100**.

114. A. Banc, A.-C. Genix, C. Dupas, M. Sztucki, R. Schweins, M.-S. Appavou and J. Oberdisse, *Macromolecules*, 2015, **48**, 6596-6605.

115. A. I. Nakatani, W. Chen, R. G. Schmidt, G. V. Gordon and C. C. Han, *Polymer*, 2001, **42**, 3713-3722.

116. N. Jouault, F. Dalmas, S. Said, E. Di Cola, R. Schweins, J. Jestin and F. Boue, *Phys. Rev. E*, 2010, **82**.

117. W.-S. Tung, V. Bird, R. J. Composto, N. Clarke and K. I. Winey, *Macromolecules*, 2013, **46**, 5345-5354.

118. S. Sen, Y. Xie, S. Kumar, H. Yang, A. Bansal, D. Ho, L. Hall, J. Hooper and K. Schweizer, *Phys. Rev. Lett.*, 2007, **98**.

119. A. C. Genix, M. Tatou, A. Imaz, J. Forcada, R. Schweins, I. Grillo and J. Oberdisse, *Macromolecules*, 2012, **45**, 1663-1675.

120. M. K. Crawford, R. J. Smalley, G. Cohen, B. Hogan, B. Wood, S. K. Kumar, Y. B. Melnichenko, L. He, W. Guise and B. Hammouda, *Phys. Rev. Lett.*, 2013, **110**.

121. C. Chevigny, D. Gigmes, D. Bertin, J. Jestin and F. Boue, *Soft Matter*, 2009, **5**, 3741-3753.

122. N. Jouault, F. Dalmas, S. Said, E. Di Cola, R. Schweins, J. Jestin and F. Boue, *Macromolecules*, 2010, **43**, 9881-9891.

123. C. Picot, F. Audouin and C. Mathis, *Macromolecules*, 2007, **40**, 1643-1656.

124. V. Lebedev, G. Torok and L. Vinogradova, *J. Macromol. Sci. B. Phys.*, 2013, **52**, 1736-1755.

125. S. Kaufman, W. Slichter and D. Davis, *J. Polym. Sci. Part A: Polym. Phys*, 1971, **9**, 829-839.

126. A. Papon, K. Saalwächter, K. Schäler, L. Guy, F. Lequeux and H. Montes, *Macromolecules*, 2011, **44**, 913-922.

127. D. Fragiadakis, P. Pissis and L. Bokobza, *Polymer*, 2005, **46**, 6001-6008.

128. S. E. Harton, S. K. Kumar, H. C. Yang, T. Koga, K. Hicks, E. Lee, J. Mijovic, M. Liu, R. S. Vallery and D. W. Gidley, *Macromolecules*, 2010, **43**, 3415-3421.

129. S. Gagliardi, V. Arrighi, R. Ferguson and M. Telling, *Physica B: Condens. Matt.*, 2001, **301**, 110-114.

130. J. M. Kropka, V. Garcia Sakai and P. F. Green, *Nano Lett.*, 2008, **8**, 1061-1065.

131. F. Du, R. C. Scogna, W. Zhou, S. Brand, J. E. Fischer and K. I. Winey, *Macromolecules*, 2004, **37**, 9048-9055.

132. P. Akcora, S. K. Kumar, V. G. Sakai, Y. Li, B. C. Benicewicz and L. S. Schadler, *Macromolecules*, 2010, **43**, 8275-8281.

133. D. Fragiadakis, L. Bokobza and P. Pissis, *Polymer*, 2011, **52**, 3175-3182.

134. S. Gam, J. S. Meth, S. G. Zane, C. Chi, B. A. Wood, M. E. Seitz, K. I. Winey, N. Clarke and R. J. Composto, *Macromolecules*, 2011, **44**, 3494-3501.

135. D. Cangialosi, V. M. Boucher, A. Alegria and J. Colmenero, *J. Chem. Phys.*, 2011, **135**.

136. A. P. Holt, J. R. Sangoro, Y. Wang, A. L. Agapov and A. P. Sokolov, *Macromolecules*, 2013, **46**, 4168-4173.

137. A. Sanz, M. Ruppel, J. F. Douglas and J. T. Cabral, *J. Phys.: Condens. Matter*, 2008, **20**.

138. K. Chrissopoulou, S. Anastasiadis, E. Giannelis and B. Frick, *J. Chem. Phys.*, 2007, **127**, 144910.

139. K. Chrissopoulou and S. H. Anastasiadis, *Soft Matter*, 2015, **11**, 3746-3766.

140. F. W. Starr, T. B. Schroder and S. C. Glotzer, *Physical Review E*, 2001, **64**.

141. M. Mizuno, K. Nakamura, T. Konishi and K. Fukao, *J. Non-Cryst. Solids*, 2011, **357**, 594-597.

142. S. K. Fullerton-Shirey and J. K. Maranas, *J. Phys. Chem. C*, 2010, **114**, 9196-9206.

143. S. Amanuel, A. N. Gaudette and S. S. Sternstein, *J. Polym. Sci., Part B: Polym. Phys.*, 2008, **46**, 2733-2740.

144. J. S. Meth, S. G. Zane, C. Chi, J. D. Londono, B. A. Wood, P. Cotts, M. Keating, W. Guise and S. Weigand, *Macromolecules*, 2011, **44**, 8301-8313.

145. V. Pryamitsyn and V. Ganesan, *Macromolecules*, 2010, **43**, 5851-5862.

146. L. X. Xu, F. Xu, F. Chen, J. T. Yang and M. Q. Zhong, *J. Nanomater.*, 2012, 10.

147. H. Koerner, E. Opsitnick, C. A. Grabowski, L. F. Drummy, M.-S. Hsiao, J. Che, M. Pike, V. Person, M. R. Bockstaller and J. S. Meth, *J. Polym. Sci., Part B: Polym. Phys.*, 2016, **54**, 319-330.

148. A. Sanz, H. C. Wong, A. J. Nedoma, J. F. Douglas and J. T. Cabral, *Polymer*, 2015, **68**, 47-56.

149. G. Tsagaropoulos and A. Eisenberg, *Macromolecules*, 1995, **28**, 6067-6077.

150. L. Chen, K. Zheng, X. Tian, K. Hu, R. Wang, C. Liu, Y. Li and P. Cui, *Macromolecules*, 2009, **43**, 1076-1082.

151. G. Tsagaropoulos and A. Eisenberg, *Macromolecules*, 1995, **28**, 396-398.

152. C. G. Robertson, C. J. Lin, M. Rackaitis and C. M. Roland, *Macromolecules*, 2008, **41**, 2727-2731.

153. V. M. Boucher, D. Cangialosi, A. Alegria, J. Colmenero, I. Pastoriza-Santos and L. M. Liz-Marzan, *Soft Matter*, 2011, **7**, 3607-3620.

154. N. R. Cameron, J. M. G. Cowie, R. Ferguson and I. McEwan, *Polymer*, 2000, **41**, 7255-7262.

155. A. L. Flory, T. Ramanathan and L. C. Brinson, *Macromolecules*, 2010, **43**, 4247-4252.

156. V. M. Boucher, D. Cangialosi, A. Alegria, J. Colmenero, J. Gonzalez-Irun and L. M. Liz-Marzan, *Soft Matter*, 2010, **6**, 3306-3317.

157. D. Cangialosi, V. M. Boucher, A. Alegría and J. Colmenero, *Soft Matter*, 2013, **9**, 8619.

158. V. M. Boucher, D. Cangialosi, A. Alegria and J. Colmenero, *Macromolecules*, 2010, **43**, 7594-7603.

159. J. Cho, M. S. Joshi and C. T. Sun, *Compos. Sci. Technol.*, 2006, **66**, 1941.

160. P. Dittanet and R. A. Pearson, *Polymer*, 2013, **54**, 1832-1845.

161. H. M. Smallwood, *J. Appl. Phys.*, 1944, **15**, 758-766.

162. G. Heinrich and M. Kluppel, *Adv. Polym. Sci.*, 2002, **160**, 1-44.

163. N. Dutta, N. R. Choudhury, B. Haidar, A. Vidal, J. Donnet, L. Delmotte and J. Chezeau, *Polymer*, 1994, **35**, 4293-4299.

164. S. S. Sternstein and A. J. Zhu, *Macromolecules*, 2002, **35**, 7262-7273.

165. R. A. Vaia and J. F. Maguire, *Chem. Mater.*, 2007, **19**, 2736-2751.

166. P. Akcora, S. K. Kumar, J. Moll, S. Lewis, L. S. Schadler, Y. Li, B. C. Benicewicz, A. Sandy, S. Narayanan, J. Illavsky, P. Thiyagarajan, R. H. Colby and J. F. Douglas, *Macromolecules*, 2010, **43**, 1003-1010.

167. M. Kluppel, *J. Phys.: Condens. Matter*, 2009, **21**.

168. M. Du, J. H. Gong and Q. Zheng, *Polymer*, 2004, **45**, 6725-6730.

169. B. J. Ash, D. F. Rogers, C. J. Wiegand, L. S. Schadler, R. W. Siegel, B. C. Benicewicz and T. Apple, *Polym. Compos.*, 2002, **23**, 1014-1025.

170. V. Kovacevic, M. Leskovac and S. L. Blagojevic, *J. Adhes. Sci. Technol.*, 2002, **16**, 1915-1929.

171. G. Raos, *Macromol. Theory Simul.*, 2003, **12**, 17-23.

172. N. Jouault, P. Vallat, F. Dalmas, S. Said, J. Jestin and F. Boue, *Macromolecules*, 2009, **42**, 2031-2040.

173. D. Zhao, S. Ge, E. Senses, P. Akcora, J. Jestin and S. K. Kumar, *Macromolecules*, 2015, **48**, 5433-5438.

174. A. Metzner, *J. Rheol.*, 1985, **29**, 739-775.

175. D. H. Cole, K. R. Shull, P. Baldo and L. Rehn, *Macromolecules*, 1999, **32**, 771-779.

176. G. Galgali, C. Ramesh and A. Lele, *Macromolecules*, 2001, **34**, 852-858.

177. Q. Zhang and L. A. Archer, *Macromolecules*, 2004, **37**, 1928-1936.

178. M. Fereydoon, S. H. Tabatabaei and A. Ajji, *Polym. Eng. Sci.*, 2014, **54**, 2617-2631.

179. E. T. Kopesky, T. S. Haddad, R. E. Cohen and G. H. McKinley, *Macromolecules*, 2004, **37**, 8992-9004.

180. M. E. D. Mackay, Tien T. Tuteja, Anish Ho, Derek L. Van Horn, Brooke Kim, Ho-Cheol Hawker, Craig J., *Nat. Mater.*, 2003, **2**, 762-766.

181. A. Tuteja, M. E. Mackay, C. J. Hawker and B. Van Horn, *Macromolecules*, 2005, **38**, 8000-8011.

182. S. Jain, J. G. P. Goossens, G. W. M. Peters, M. van Duin and P. J. Lemstra, *Soft Matter*, 2008, **4**, 1848.

183. J. Gao, C. Huang, N. Wang, W. Yu and C. Zhou, *Polymer*, 2012, **53**, 1772-1782.

184. A. Gharachorlou and F. Goharpey, *Macromolecules*, 2008, **41**, 3276-3283.

185. Y. S. Lipatov, A. Nesterov, T. Ignatova and D. Nesterov, *Polymer*, 2002, **43**, 875-880.

186. G. Wu, T. Miura, S. Asai and M. Sumita, *Polymer*, 2001, **42**, 3271-3279.

187. V. V. Ginzburg, *Macromolecules*, 2005, **38**, 2362-2367.

188. M. Suess, J. Kressler and H. W. Kammer, *Polymer*, 1987, **28**, 957-960.

189. M. E. Fowler, J. W. Barlow and D. R. Paul, *Polymer*, 1987, **28**, 2145-2150.

190. J. C. You, Y. G. Liao, Y. F. Men, T. F. Shi, L. J. An and X. H. Li, *Macromolecules*, 2011, **44**, 5318-5325.

191. H.-J. Chung, A. Taubert, R. Deshmukh and R. J. Composto, *EPL (Europhysics Letters)*, 2004, **68**, 219.

192. C. Huang, J. Gao, W. Yu and C. Zhou, *Macromolecules*, 2012, **45**, 8420-8429.

193. L. T. Vo and E. P. Giannelis, *Macromolecules*, 2007, **40**, 8271-8276.

194. Y.-C. Chua, A. Chan, H.-C. Wong, J. S. Higgins and J. T. Cabral, *Macromolecules*, 2010, **43**, 9578-9582.

195. G. P. Kar, A. Bharati, P. Xavier, G. Madras and S. Bose, *Phys. Chem. Chem. Phys.*, 2015, **17**, 868-877.

196. G. P. Kar, P. Xavier and S. Bose, *Phys. Chem. Chem. Phys.*, 2014, **16**, 17811-17821.

197. P. Xavier, P. Rao and S. Bose, *Phys. Chem. Chem. Phys.*, 2016, **18**, 47-64.

198. D. S. Sivia, *Elementary Scattering Theory*, Oxford University Press, Oxford, 2011.

199. R.-J. Roe, *Methods of X-ray and neutron scattering in polymer science*, Oxford University Press, New York, 2000.

200. J. S. Higgins and H. C. Benoit, *Polymers and Neutron Scattering*, Oxford University Press, Oxford, 1994.

201. M. Bée, *Quasielastic neutron scattering*, Adam Hilger, Bristol, 1988.

202. G. L. Squires, *Introduction to the Theory of Thermal Neutron Scattering*, Dover Publications, 1978.

203. V. F. Sears, *Neutron news*, 1992, **3**, 26-37.

204. L. Van Hove, *Phys. Rev.*, 1954, **95**, 249.

205. A. P. R. Eberle and L. Porcar, *Curr. Opin. Colloid Interface Sci.*, 2012, **17**, 33-43.

206. V. T. Lebedev, G. Torok and L. V. Vinogradova, *Polym. Sci. Ser. A*, 2013, **55**, 65-74.

207. I. Grillo, in *Soft matter characterization*, Springer, Editon edn., 2008, pp. 723-782.

208. H. Hayashi, P. J. Flory and G. D. Wignall, *Macromolecules*, 1983, **16**, 1328-1335.

209. M. Rawiso, R. Duplessix and C. Picot, *Macromolecules*, 1987, **20**, 630-648.

210. A. Maconnachie, *Polymer*, 1984, **25**, 1068-1072.

211. A. Guinier and G. Fournet, *Small angle X-rays*, Wiley, New York, 1955.

212. H. Benoit, *C. R. Hebd. Seances Acad. Sci.*, 1957, **245**, 2244-2247.

213. B. Hammouda, in *Polymer Characteristics*, Springer, Editon edn., 1993, pp. 87-133.

214. *SasView*, http://wwww.sasview.org/.

215. L. Willner, O. Jucknischke, D. Richter, J. Roovers, L. L. Zhou, P. M. Toporowski, L. J. Fetters, J. S. Huang, M. Y. Lin and N. Hadjichristidis, *Macromolecules*, 1994, **27**, 3821-3829.

216. W. D. Dozier, J. S. Huang and L. J. Fetters, *Macromolecules*, 1991, **24**, 2810-2814.

217. B. H. Zimm, *J. Chem. Phys*, 1948, **16**, 1093-1099.

218. O. Kratky, *Pure Appl. Chem.*, 1966, **12**, 483-524.

219. S. Gagliardi, V. Arrighi, R. Ferguson, A. Dagger, J. Semlyen and J. Higgins, *J. Chem. Phys*, 2005, **122**, 064904.

220. B. Hammouda, *Macromol. Theory Simul.*, 2012, **21**, 372-381.

221. P. De Gennes, *Journal de Physique*, 1970, **31**, 235-238.

222. P. Debye and A. Bueche, *J. Appl. Phys.*, 1949, **20**, 518-525.

223. G. Porod, *Colloid Polym. Sci.*, 1951, **124**, 83-114.

224. Y. Osada and A. Khokhlov, *Polym. Gels Networks*, Taylor & Francis, 2001.

225. S. K. Kumar, N. Jouault, B. Benicewicz and T. Neely, *Macromolecules*, 2013, **46**, 3199-3214.

226. B. Frick and L. Fetters, *Macromolecules*, 1994, **27**, 974-980.

227. V. Arrighi, J. Higgins, A. Burgess and G. Floudas, *Polymer*, 1998, **39**, 6369-6376.

228. B. Frick, J. Combet and L. Van Eijck, *Nucl. Instrum. Methods Phys. Res., Sect. A*, 2012, **669**, 7-13.

229. C. Chen, J. K. Maranas and V. García-Sakai, *Macromolecules*, 2006, **39**, 9630-9640.

230. V. Arrighi, F. Ganazzoli, C. Zhang and S. Gagliardi, *Phys. Rev. Lett.*, 2003, **90**, 058301.

231. A. Chahid, A. Alegria and J. Colmenero, *Macromolecules*, 1994, **27**, 3282-3288.

232. D. Richter, M. Monkenbusch, J. Allgeier, A. Arbe, J. Colmenero, B. Farago, Y. C. Bae and R. Faust, *J. Chem. Phys*, 1999, **111**, 6107-6120.

233. D. Richter, B. Ewen, B. Farago and T. Wagner, *Phys. Rev. Lett.*, 1989, **62**, 2140.

234. G. Allen, J. S. Higgins, A. Maconnachie and R. E. Ghosh, *J. Chem. Soc. Faraday Trans.*, 1982, **78**, 2117-2130.

235. W. Paul, G. Smith, D. Y. Yoon, B. Farago, S. Rathgeber, A. Zirkel, L. Willner and D. Richter, *Phys. Rev. Lett.*, 1998, **80**, 2346.

236. K. Ngai, J. Colmenero, A. Alegria and A. Arbe, *Macromolecules*, 1992, **25**, 6727-6729.

237. R. Ferguson, V. Arrighi, I. McEwen, S. Gagliardi and A. Triolo, *J. Macromol. Sci. Part B: Phys.*, 2006, **45**, 1065-1081.

238. S. M. King, http://www.isis.stfc.ac.uk/instruments/loq/loq2470.html.

239. R. K. Heenan, http://www.isis.stfc.ac.uk/instruments/sans2d/sans2d3000.html, Accessed 28/09/15.

240. ILL,https://www.ill.eu/instruments-support/instruments-groups/instruments/d22/description/instrument-layout/, Accessed 29/09/15.

241. G. Nagy, http://www.psi.ch/sinq/sansii/description, Accessed 29/09/15.

242. ILL, https://www.ill.eu/instruments-support/instruments-groups/yellowbook/.

243. R. K. Heenan, http://www.isis.stfc.ac.uk/instruments/iris/documents/iris-documents4694.html, Accessed 29/09/15.

244. J. C. Mareque Rivas, R. Torres Martin de Rosales and S. Parsons, *Dalton Trans.*, 2003, 2156.

245. J. Xia and K. Matyjaszewski, *Macromolecules*, 1999, **32**, 2434.

246. M. Li, K. Min and K. Matyjaszewski, *Macromolecules*, 2004, **37**, 2106.

247. J. D. Tong and R. Jerome, *Macromolecules*, 2000, **33**, 1479-1481.

248. K. Matyjaszewski, Y. Nakagawa and C. B. Jasieczek, *Macromolecules*, 1998, **31**, 1535-1541.

249. B. Schmaltz, C. Mathis and M. Brinkmann, *Polymer*, 2009, **50**, 966-972.

250. B. Hammouda, D. L. Ho and S. Kline, *Macromolecules*, 2004, **37**, 6932-6937.

251. M. Daoud and J. P. Cotton, *Journal De Physique*, 1982, **43**, 531-538.

252. C. M. Marques, D. Izzo, T. Charitat and E. Mendes, *Eur. Phys. J. B.*, 1998, **3**, 353-358.

253. L. J. Fetters, N. Hadjichristidis, J. S. Lindner and J. W. Mays, *J. Phys. Chem. Ref. Data*, 1994, **23**, 619-640.

254. W. Brown and T. Nicolai, *Colloid. Polym. Sci.*, 1990, **268**, 977-990.

255. K. F. Freed, *Renormalization Group Theory of Macromolecules*, Wiley Interscience, New York, 1987.

256. G. S. Grest, L. J. Fetters, J. S. Huang and D. Richter, *Adv. Chem. Phys.*, 1996, **94**, 67-163.

257. J. E. Mark, *Physical Properties of Polymers Handbook*, Woodbury, New York, 1996.

258. L. Willner, O. Jucknischke, D. Richter, B. Farago, L. Fetters and J. Huang, *EPL*, 1992, **19**, 297.

259. X. Li, C. Do, Y. Liu, L. Sánchez-Diáz, G. Smith and W.-R. Chen, *J. Appl. Crystallogr.*, 2014, **47**, 1901-1905.

260. V. Lebedev, G. Török and L. Vinogradova, *Polym. Sci. Ser. A*, 2011, **53**, 537-545.

261. D. Richter, B. Farago, L. J. Fetters, J. S. Huang and B. Ewen, *Macromolecules*, 1990, **23**, 1845-1856.

262. M. Mishra and S. Kobayashi, *Star and hyperbranched polymers*, CRC Press, 1999.

263. A. Einstein, *Ann. der Physik*, 1905, **17**, 549.

264. R. Pecora, *Dynamic light scattering: applications of photon correlation spectroscopy*, Springer Science & Business Media, 2013.

265. N. Khasat, R. W. Pennisi, N. Hadjichristidis and L. J. Fetters, *Macromolecules*, 1988, **21**, 1100-1106.

266. J. Roovers, L. L. Zhou, P. M. Toporowski, M. van der Zwan, H. Iatrou and N. Hadjichristidis, *Macromolecules*, 1993, **26**, 4324-4331.

267. H. Sasabe, *Hyper-structured Molecules I: Chemistry, Physics and Applications*, Gordon and Breach Science Publishers, 1999.

268. P. Somasundaran, *Encyclopedia of Surface and Colloid Science*, CRC Press, 2006.

269. D. Vlassopoulos, G. Fytas, T. Pakula and J. Roovers, *J. Phys.: Condens. Matter*, 2001, **13**, R855.

270. S. P. Singh, C.-C. Huang, E. Westphal, G. Gompper and R. G. Winkler, *J. Chem. Phys*, 2014, **141**, 084901.

271. K. Nusser, S. Neueder, G. J. Schneider, M. Meyer, W. Pyckhout-Hintzen, L. Willner, A. Radulescu and D. Richter, *Macromolecules*, 2010, **43**, 9837-9847.

272. A. Guinier and G. Fournet, *Small-angle scattering of X-rays*, John Wiley & Sons Inc., New York, 1955.

273. A. J. Hurd, D. W. Schaefer and J. E. Martin, *Phys. Rev. A*, 1987, **35**, 2361.

274. X. Sheng, D. Xie, C. Wang, X. Zhang and L. Zhong, *Colloid. Polym. Sci.*, 2016, **294**, 463-469.

275. P. Wiltzius, *Phys. Rev. Lett.*, 1987, **58**, 710-713.

276. T. Jesionowski, *Colloids. Surf., A.*, 2003, **222**, 87-94.

277. D. W. Schaefer and A. J. Hurd, *Aerosol Sci. Technol.*, 1990, **12**, 876-890.

278. C. J. Kim, K. Sondergeld, M. Mazurowski, M. Gallei, M. Rehahn, T. Spehr, H. Frielinghaus and B. Stühn, *Colloid Polym. Sci.*, 2013, **291**, 2087-2099.

279. D. W. Janes, J. F. Moll, S. E. Harton and C. J. Durning, *Macromolecules*, 2011, **44**, 4920-4927.

280. G. Beaucage, *J. Appl. Crystallogr.*, 1995, **28**, 717-728.

281. J. Hyeon-Lee, G. Beaucage, S. E. Pratsinis and S. Vemury, *Langmuir*, 1998, **14**, 5751-5756.

282. A. P. Holt, P. J. Griffin, V. Bocharova, A. L. Agapov, A. E. Imel, M. D. Dadmun, J. R. Sangoro and A. P. Sokolov, *Macromolecules*, 2014, **47**, 1837-1843.

283. B. Hammouda, *J. Appl. Crystallogr.*, 2010, **43**, 1474-1478.

284. A. Botti, W. Pyckhout-Hintzen, D. Richter and E. Straube, *Physica A*, 2002, **304**, 230-234.

285. M. K. Corbierre, N. S. Cameron, M. Sutton, K. Laaziri and R. B. Lennox, *Langmuir*, 2005, **21**, 6063-6072.

286. J. Jancar, J. Douglas, F. W. Starr, S. Kumar, P. Cassagnau, A. Lesser, S. S. Sternstein and M. Buehler, *Polymer*, 2010, **51**, 3321-3343.

287. H. C. Wong, A. Sanz, J. F. Douglas and J. T. Cabral, *J. Mol. Liq.*, 2010, **153**, 79-87.

288. G. Carrot, S. Diamanti, M. Manuszak, B. Charleux and I. P. Vairon, *J. Polym. Sci., Part A: Polym. Chem.*, 2001, **39**, 4294-4301.

289. A. Kraft, V. Arrighi and N. Grima, *Abstracts of Papers of the American Chemical Society*, 2008, **235**.

290. A. Sargsyan, A. Tonoyan, S. Davtyan and C. Schick, *Eur. Polym. J.*, 2007, **43**, 3113-3127.

291. N. Jouault, J. F. Moll, D. Meng, K. Windsor, S. Ramcharan, C. Kearney and S. K. Kumar, *Acs Macro Lett.*, 2013, **2**, 371-374.

292. J. B. Hooper and K. S. Schweizer, *Macromolecules*, 2006, **39**, 5133-5142.

293. J. Colmenero, A. Arbe, A. Alegria, M. Monkenbusch and D. Richter, *J. Phys.: Condens. Matter*, 1999, **11**, A363.

294. R. Z. Li, *Mater. Sci. Eng., A*, 2000, **278**, 36-45.

295. M. van Gurp and J. Palmen, *Xiith International Congress on Rheology, Proceedings*, 1996, 134-135.

296. M. Khlifa, *Synthesis of polymer grafted silica nanoparticles: effect of grafting on mechanical reinforcement*, PhD Thesis, Heriot-Watt University, 2013.

297. S. R. Raghavan and S. A. Khan, *J. Colloid Interface Sci.*, 1997, **185**, 57-67.

298. L. Shan, Y. Tian, J. Jiang, X. Zhang and Y. Meng, *Colloids. Surf., A.*, 2015, **464**, 1-7.

299. S. A. Khan and N. J. Zoeller, *J. Rheol.*, 1993, **37**, 1225-1235.

300. B. J. Anderson and C. F. Zukoski, *Macromolecules*, 2008, **41**, 9326-9334.

301. A. Einstein, *Annalen der physik*, 1906, **4**, 371-381.

302. J. M. Dealy and K. F. Wissburn, *Melt Rheology and its role in Plastics Processing: Theory and Applications*, Van Nostrand Reinhold, New York, 1990.

303. G. K. Batchelor and J. T. Green, *J. Fluid Mech.*, 1972, **56**, 401-427.

304. Q. Zhang and L. A. Archer, *Langmuir*, 2002, **18**, 10435-10442.

305. I. M. Krieger and T. J. Dougherty, *Transactions of The Society of Rheology (1957-1977)*, 1959, **3**, 137-152.

306. S. A. Madbouly, J. U. Otaigbe, A. K. Nanda and D. A. Wicks, *Macromolecules*, 2007, **40**, 4982-4991.

307. A. M. Wierenga and A. P. Philipse, *Colloids. Surf., A.*, 1998, **137**, 355-372.

308. Y. S. Song, *Rheol. Acta*, 2006, **46**, 231-238.

309. H. Wang, S. Hoa and P. Wood-Adams, *J. Appl. Polym. Sci.*, 2006, **100**, 4286-4296.

310. T. Hanemann, *Ceram. Int.*, 2008, **34**, 2099-2105.

311. R. D. Sudduth, *J. Appl. Polym. Sci.*, 1993, **48**, 37-55.

312. P. S. Stephanou, V. G. Mavrantzas and G. C. Georgiou, *Macromolecules*, 2014, **47**, 4493-4513.

313. M. Van Gurp and J. Palmen, *Rheol. Bull.*, 1998, **67**, 5-8.

314. C. Triebel and H. Muenstede, *Polymer*, 2011, **52**, 1596-1602.

315. T. A. Vilgis, *Polymer*, 2005, **46**, 4223-4229.

316. G. Allegra, G. Raos and M. Vacatello, *Prog. Polym. Sci.*, 2008, **33**, 683-731.

317. E. Guth and O. Gold., *Phys. Rev.*, 1938, **53**.

318. E. Guth, *J. Appl. Phys.*, 1945, **16**, 20-25.

319. A. I. Medalia, *J. Colloid Interface Sci.*, 1970, **32**, 115-&.

320. A. I. Medalia, *Rubber Chem. Technol.*, 1972, **45**, 1171-1194.

321. L. E. Nielsen, *J. Appl. Phys.*, 1970, **41**, 4626-4627.

322. A. Vassiliou, D. Bikiaris and E. Pavlidou, *Macromol. React. Eng.*, 2007, **1**, 488-501.

323. Y. H. Song and Q. A. Zheng, *Polymer*, 2010, **51**, 3262-3268.

324. R. Christensen and K. Lo, *J. Mech. Phys. Solids*, 1979, **27**, 315-330.

325. J. M. G. Cowie and R. Ferguson, *Macromolecules*, 1989, **22**, 2312-2317.

326. J. M. G. Cowie and R. Ferguson, *Macromolecules*, 1989, **22**, 2307-2312.

327. J. M. G. Cowie and V. Arrighi, *Polymer Physics: From Suspensions to Nanocomposites and Beyond*, 2010.

328. R. Ruggerone, V. Geiser, S. D. Vacche, Y. Leterrier and J.-A. E. Manson, *Macromolecules*, 2010, **43**, 10490-10497.

329. G. V. Samsonov, *The Oxide Handbook*, Second edn., IFI/Plenum Data Company, New York, 1982.

330. H. K. Nguyen, M. Labardi, S. Capaccioli, M. Lucchesi, P. Rolla and D. Prevosto, *Macromolecules*, 2012, **45**, 2138-2144.

331. S. S. Lee, C. S. Lee, M. H. Kim, S. Y. Kwak, M. Park, S. Lim, C. R. Choe and J. Kim, *J. Polym. Sci., Part B: Polym. Phys.*, 2001, **39**, 2430-2435.

332. R. R. Madathingal and S. L. Wunder, *Thermochim. Acta*, 2011, **526**, 83-89.

333. R. D. Priestley, P. Rittigstein, L. J. Broadbelt, K. Fukao and J. M. Torkelson, *J. Phys.: Condens. Matter*, 2007, **19**, 205120.

334. A. Lee and J. D. Lichtenhan, *Macromolecules*, 1998, **31**, 4970-4974.

335. P. Rittigstein and J. M. Torkelson, *J. Polym. Sci., Part B: Polym. Phys.*, 2006, **44**, 2935-2943.

336. J. Roovers and P. Toporowski, *J. Appl. Polym. Sci.*, 1974, **18**, 1685-1691.

337. A. Kisliuk, Y. Ding, J. Hwang, J. Lee, B. Annis, M. Foster and A. Sokolov, *J. Polym. Sci. Part B: Polym. Phys.*, 2002, **40**, 2431-2439.

338. W. Choi, J. W. Chung and S.-Y. Kwak, *Polymer*, 2015, **79**, 91-98.

339. V. A. Bershtein, V. M. Egorov, V. N. Zgonnik, E. Y. Melenevskaya and L. V. Vinogradova, *J. Therm. Anal. Calorim.*, 2000, **59**, 23-31.

340. G. G. Vogiatzis and D. N. Theodorou, *Macromolecules*, 2014, **47**, 387-404.

341. V. Lebedev, G. Török, L. Cser, D. Orlova, V. Bershtein, V. Zgonnik, E. Y. Melenevskaya and L. Vinogradova, *Appl. Phys. A*, 2002, **74**, s475-s477.

342. L. J. Fetters, A. D. Kiss, D. S. Pearson, G. F. Quack and F. J. Vitus, *Macromolecules*, 1993, **26**, 647-654.

343. O. O. Mykhaylyk, C. M. Fernyhough, M. Okura, J. P. A. Fairclough, A. J. Ryan and R. Graham, *Eur. Polym. J.*, 2011, **47**, 447-464.

344. J. Kennedy and S. Jacob, *Acc. Chem. Res.*, 1998, **31**, 835-841.

345. A. Nesterov, Y. S. Lipatov, V. Horichko and O. Gritsenko, *Polymer*, 1992, **33**, 619-622.

346. W. Z. Li, R. M. A. l'Abee and J. G. P. Goossens, *Macromol. Chem. Phys.*, 2013, **214**, 2705-2715.

347. N. Cameron, J. M. G. Cowie, R. Ferguson, J. L. G. Ribelles and J. M. Estelles, *Eur. Polym. J.*, 2002, **38**, 597-605.

348. V. Arrighi, J. S. Higgins, A. N. Burgess and W. S. Howells, *Macromolecules*, 1995, **28**, 4622-4630.

349. Y. Liao, J. You, T. Shi, L. An and P. K. Dutta, *Langmuir*, 2007, **23**, 11107-11111.

350. H. Wang and R. J. Composto, *Europhys. Lett.*, 2000, **50**, 622-627.

351. L. Fetters, D. Lohse and R. Colby, in *Physical properties of polymers handbook*, Springer, Editon edn., 2007, pp. 447-454.

352. K. Hahn, B. Schmitt, M. Kirschey, R. Kirste, H. Salie and S. Schmitt-Strecker, *Polymer*, 1992, **33**, 5150-5166.

353. Y. Huang, S. Jiang, G. Li and D. Chen, *Acta Mater.*, 2005, **53**, 5117-5124.

354. M. L. Fernandez, J. S. Higgins, J. Penfold, C. Shackleton and D. J. Walsh, *Polymer*, 1990, **31**, 2146-2151.

355. G. Floudas and J. S. Higgins, *Polymer*, 1992, **33**, 4121-4128.

356. R. G. Hill, P. E. Tomlins and J. S. Higgins, *Macromolecules*, 1985, **18**, 2555-2560.

357. K. A. Barnes, A. Karim, J. F. Douglas, A. I. Nakatani, H. Gruell and E. J. Amis, *Macromolecules*, 2000, **33**, 4177-4185.

358. T. Honma, T. Senda and Y. Inoue, *Polym. Int.*, 2003, **52**, 1839-1846.

359. G. Crevecoeur and G. Groeninckx, *Macromolecules*, 1991, **24**, 1190-1195.

360. E. Vorenkamp, G. Ten Brinke, J. Meijer, H. Jager and G. Challa, *Polymer*, 1985, **26**, 1725-1732.

361. N. Schuld and B. A. Wolf, *J. Polym. Sci., Part B: Polym. Phys.*, 2001, **39**, 651-662.

362. C. Bartholome, E. Beyou, E. Bourgeat-Lami, P. Chaumont, F. Lefebvre and N. Zydowicz, *Macromolecules*, 2005, **38**, 1099-1106.

363. L. Elias, F. Fenouillot, J.-C. Majesté, P. Alcouffe and P. Cassagnau, *Polymer*, 2008, **49**, 4378-4385.

364. L. Elias, F. Fenouillot, J.-C. Majesté and P. Cassagnau, *Polymer*, 2007, **48**, 6029-6040.

365. A. Karim, D.-W. Liu, J. Douglas, A. Nakatani and E. Amis, *Polymer*, 2000, **41**, 8455-8458.

366. F. J. Schork, Y. Luo, W. Smulders, J. P. Russum, A. Butte and K. Fontenot, *Adv. Polym. Sci.*, 2005, **175**, 129-255.